Modelling Interactions Between Vegetation and Tropospheric Ozone

Michael John Hollaway

Submitted in accordance with the requirements for the degree of
Doctor of Philosophy

The University of Leeds
School of Earth and Environment
September 2012

Declaration of Authorship

The candidate confirms that the work submitted is his own, except where work which has formed part of jointly-authored publications has been included. The contribution of the candidate and the other authors to this work has been explicitly indicated below. The candidate confirms that appropriate credit has been given within the thesis where reference has been made to the work of others.

Chapter 4 is based on the publication: **Hollaway, M.J., Arnold, S.R., Challinor, A.J. and Emberson, L.D. 2012. Intercontinental trans-boundary contributions to ozone-induced crop yield losses in the Northern Hemisphere, Biogeosciences, 9,271–292, doi: 10.5194/bg–9–271–2012.** The candidate performed all of the model runs, analysis and interpretation of the results and wrote the text. S.R. Arnold devised the concept of the model experiments and provided assistance in data analysis and interpretation and editing of text. L.D. Emberson and A.J. Challinor provided discussion of the metrics used in this analysis and putting the results into wider context.

Acknowledgements

I would first like to extend my utmost thanks and gratitude to my supervisors Steve Arnold, Martyn Chipperfield and Bill Collins for their guidance, help, support and patience over the last 4 years. This thesis would not have come close to coming together without them. I am particularly grateful to Steve for always taking the time to provide comments on the essays I've left on his desk over the past few years.

I would also like to thank Gerd Folberth, Andy Challinor, Mohit Dalvi, Stephen Sitch, and Lisa Emberson for their advice and input over the duration of this project. For extensive help with IDL and for always being willing to answer "just one quick question", I would like to thank Nigel Richards. The members of my research group and the biosphere atmosphere group (BAG) also deserve a mention for many interesting and helpful scientific discussions over the years.

Everybody in SEE and ICAS have made the last 4 years an amazing experience. First mention must go to everybody in the old dungeon and all the people in office 10.126 past and present. In particular Chris W, Dave T, Ryan H, Mr Stamper, Matty P and Nigel R deserve a mention for making up the best ever office cricket and stairway badminton team. We'll get these sports in the Olympics yet! Mention must also go to everyone at the weekly footy sessions including James P for his annoying yet ingenious psyche-out tactics when I'm clean through on goal and Ben Parkes who provides the world's best demonstration of a two-footed challenge crossed with a pirouette. A thank you must also go to to everyone who I've shared a pint with over the years, and especially to Bradley JS and Tim B who never fail to encourage just one more drink (even when the missus does not approve!).

Last, but by no means least, I would like to say a massive thank you to Sarah who has always kept a smile on my face during the writing of this thesis, for always encouraging me to keep going when the going got tough and also for letting me near a kitchen again after the infamous "Chicken with all the spices in my cupboard on it served with Super Noodles" incident.

Finally a big thank you must go to my parents for their support and encouragement not only over the last four years but in everything that I do and for casually laughing when they explain that their son is still in education and WILL get a real job soon. And also

to my little brother Robbie, for making sure I always try my best at what I do, even if it means being a “fake doctor”!

This project has been funded by the UK Natural Environment Research Council (NERC) and the UK Met Office.

Abstract

In this thesis, the TOMCAT and HadGEM2-ES models are used to improve the understanding of the complex interactions between tropospheric ozone and the global biosphere. The focus is on the impacts of surface ozone on crops, impacts of land surface vegetation changes on tropospheric ozone and the effects of vegetation ozone damage on tropospheric chemistry through changes in dry deposition and BVOC emissions. This thesis presents the first estimates of the impact of ozone precursor emissions from each of the northern hemisphere's major industrialised regions (N America, SE Asia and Europe) on crop yields globally and in continents downwind of each region. Using a range of ozone crop damage metrics, 100 % reductions in SE Asian anthropogenic NO_x emissions tend to produce the greatest global reduction in crop production losses (42.3-95.2 %). A 100 % reduction in N American anthropogenic NO_x emissions produces the largest transboundary impact, resulting in European production loss reductions of between 14.2 % and 63.2 %. Pre-industrial model tropospheric ozone distributions are shown to be sensitive to the model vegetation coverage and representation of biosphere atmosphere processes. Simulations with HadGEM2-ES indicate a pre-industrial ozone burden which ranges from 200.4 Tg to 220.9 Tg with the variation resulting from differences in the model land vegetation distribution, the CO_2 mixing ratio the vegetation was exposed to and the model climate setup. The change in pre-industrial to present day ozone burden ranged from 71.9 Tg to 92.5 Tg translating into an estimated radiative forcing of 0.227 Wm^{-2} to 0.244 Wm^{-2}. The response of ozone concentrations to land cover changes is greater than the response to changes in the CO_2 mixing ratio the vegetation is exposed to. The ozone distribution is shown to be more sensitive to changes in the rates of isoprene emissions than to changes in dry deposition processes. The effects of ozone damage have a self limiting effect on ozone and NO_y dry deposition leading to a rise in surface ozone concentrations. Depending on plant sensitivity to ozone damage, mean total stomatal uptake was shown to decline by 0.22 to 0.42 $mmolO_3m^{-2}$ resulting in average surface ozone concentrations rising by 0.02 to 0.03 ppbv, with local increases of up to 14 ppbv. The effects of ozone damage on photosynthesis is to reduce isoprene emissions, producing slight drops in ozone over the more polluted regions offsetting the rise in concentrations due to the dry deposition effect. The inclusion of both effects resulted in a net rise in surface ozone concentrations indicating the dry deposition response to ozone damage dominates over the effects on isoprene emissions.

Contents

List of Figures

List of Tables

Abbreviations

AOT40	**A**ccumulated **O**ver a **T**hreshold of **40** ppbv
AQSs	**A**ir **Q**uality **S**tandards
BVOC	**B**iogenic **V**olatile **O**rganic **C**ompounds
CASTNET	**C**lean **A**ir **S**tatus and **T**rends **Net**work
CLM	**C**ommunity **L**and **M**odel
CMIP5	**C**limate **M**odel **I**ntercomparison **P**rogram #**5**
CPL	**C**rop **P**roduction **L**oss
EMEP	**E**uropean **M**onitoring and **E**valuation **P**rogramme
FACE	**F**ree **A**ir CO_2 **E**nrichment
GPP	**G**ross **P**rimary **P**roductivity
HadGEM2-ES	**Had**ley **C**entre **G**lobal **E**nvironment **M**odel version **2**-**E**arth **S**ystem
iBVOC	**i**nteractive **B**iogenic **V**olatile **O**rganic **C**ompounds
IGBP	**I**nternational **G**eosphere-**B**iosphere **P**rogramme
IPCC	**I**ntergovernmental **P**anel on **C**limate **C**hange
LAI	**L**eaf **A**rea **I**ndex
MOSES II	**M**et **O**ffice **S**urface **E**xchange **S**cheme **II**
PFT	**P**lant **F**unctional **T**ype
RYL	**R**elative **Y**ield **L**oss
SOA	**S**econdary **O**rganic **A**erosol
SRES	**S**pecial **R**eport on **E**missions **S**cenario
TRIFFID	**T**op-Down **R**epresentation of **I**nteractive **F**oliage and **F**lora **I**ncluding **D**ynamics
UKCA	**U**nited **K**ingdom **C**hemistry and **A**erosols
UTLS	**U**pper **T**roposphere **L**ower **S**tratosphere
UV	**U**ltra **V**iolet

VOC	**V**olatile **O**rganic **C**ompounds
WDCGG	**W**orld **D**ata **C**entre for **G**reenhouse **G**ases

Chapter 1

Introduction and Motivation

1.1 Motivation

In recent decades the topic of climate change has had increasing attention drawn towards it, in particular the rise in the mean global surface temperature since the onset of the industrial revolution at the turn of the nineteenth Century. This rise in temperature has been attributed to the elevated levels of greenhouse gases in the atmosphere which trap outgoing long wave radiation from the Earth's surface. Figure 1.1 shows that since the start of the pre-industrial era (1750) anthropogenic activity has led to an estimated net radiative forcing of $1.6\,\mathrm{Wm}^{-2}$ which has resulted in a rise in mean global surface temperature of 0.74°C (IPCC, 2007).

Carbon dioxide (CO_2) is the longest lived of the greenhouse gases and has been the focus of efforts to alleviate the effects of anthropogenic induced climate change. However, focus is also now turning towards the shorter lived greenhouse gases such as methane (CH_4) and tropospheric ozone. This is because reductions in their emissions, or in the case of tropospheric ozone emissions of its precursor species, can lead to quicker responses in their atmospheric concentrations due to shorter atmospheric lifetimes than CO_2. Recent work by Shindell et al. (2012) indicated that 14 technical (e.g. clean burning biomass stoves) and regulatory (e.g. Banning agricultural waste burning and high emitting vehicles) targeting short lived greenhouse gases could reduce the projected mean global warming by 0.5°C by 2050. These strategies also avoid 0.7 to 4.7 million annual premature deaths from outdoor air pollution and lead to increases in annual crop yields by 30 to 135 million

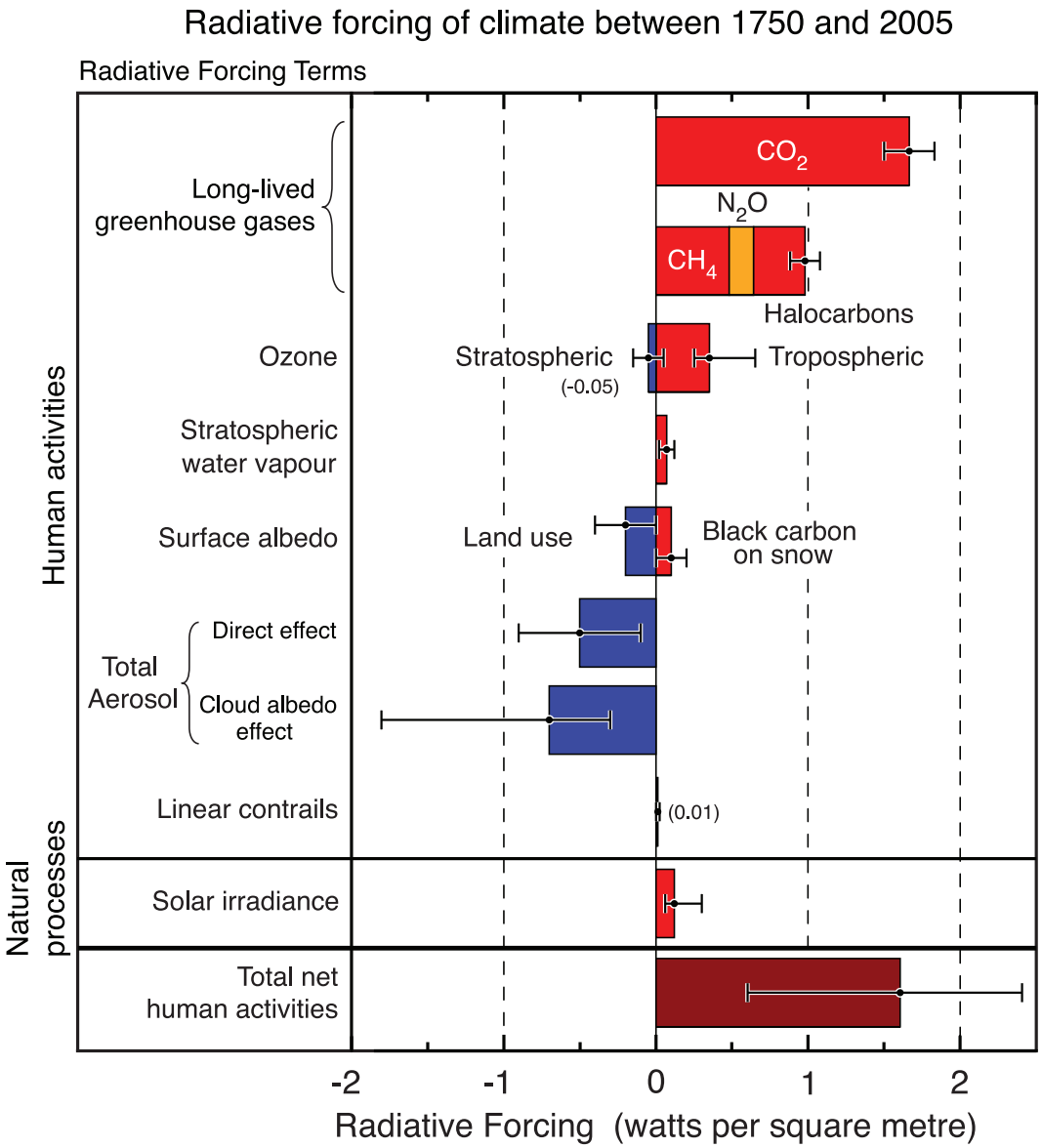

FIGURE 1.1: Summary of the principal components of the radiative forcing of climate change. The values represent the forcings in 2005 relative to the start of the industrial era (around 1750). The error bars indicate the level of uncertainty around each respective value. Taken from Forster et al. (2007)

metric tons due to ozone reductions in 2030 and beyond (Shindell et al., 2012). Therefore understanding the processes that control the concentrations of these short lived greenhouse gases in the atmosphere is essential to developing strategies to alleviate their impact on global warming.

Tropospheric ozone is not only a global air pollution problem (Fowler et al., 2008) but is also a strong greenhouse gas contributing $0.35\,\mathrm{Wm}^{-2}$ (with an uncertainty range of $0.25\,\mathrm{Wm}^{-2}$ to $0.65\,\mathrm{Wm}^{-2}$) to the net positive radiative forcing attributed to anthropogenic

activity (Figure 1.1). Ozone is produced insitu in the troposphere through a sequence of sunlight driven reactions involving nitrogen oxides (NO_x encompassing both NO and NO_2) and volatile organic compounds (VOCs) or carbon monoxide (CO) (Crutzen et al., 1999). Since the pre-industrial period, anthropogenic emissions of NO_x, CO, methane (CH_4), and other VOCs have led to increased ambient ozone over many regions (Prather et al., 2001).

These rising levels of ozone are not only due to increases in local precursor emissions but can also result from the long range transport of ozone and its precursors from continents thousands of kilometres away. Many observational and modelling studies have quantified contributions to regional surface ozone concentrations from import of ozone and its precursors from continental regions upwind (Dentener et al., 2010; Derwent et al., 2004; Hudman et al., 2004; Parrish et al., 2010). These studies have inferred contributions of between 2 and 10 ppbv to surface ozone in western Europe and western North (N) America from ozone precursor emissions in N America and Asia, respectively. European emissions also impact surface ozone in South East (SE) Asia by 0.2 to 3.5 ppbv (Duncan and Bey, 2004; Fiore et al., 2009; Wild et al., 2004).

Higher levels of tropospheric ozone have also been shown to be a global air pollution problem for human health (Avol et al., 1998; Bell et al., 2005, 2004) and to have harmful impacts on vegetation (Fuhrer and Achermann, 1994; Jager et al., 1996; USEPA, 1996) with reductions in yield and deterioration in crop quality observed during field experiments (Fuhrer, 2009). Ozone induced crop yield reductions have been suggested to lead to economic loss and to threaten global food security (Wang and Mauzerall, 2004). Damage to plants and visible leaf injury are typically caused when vegetation is exposed to ozone concentrations that exceed 40 ppbv with the associated economic costs of this damage of several billion dollars per year over the United States, the European Union and East Asia (Ashmore, 2005; Sitch et al., 2007; Wang and Mauzerall, 2004).

The effects of ozone exposure on plants have been linked to reduced rates of photosynthesis (Ashmore, 2005; Fiscus et al., 2005; Karnosky et al., 2005; Pell et al., 1997) which induces closure of the tiny pores (stomata) in the surfaces of leaves leading to a reduction in trace gas exchange with the atmosphere. This has important implications for the climate system as vegetation regulates both the carbon and hydrological cycles on both regional and global scales through the exchange of carbon and water between plants and the atmosphere (Bonan, 2008). It has been estimated by Sitch et al. (2007) that effects

of ozone damage on stomatal conductance reduces the rate of CO_2 uptake leading to a rise in atmospheric CO_2 concentrations. These reductions in stomatal uptake also affect the uptake of other reactive trace species in the atmosphere including ozone itself with this path providing an important contribution to the dry deposition of ozone to the land surface (Smith et al., 2000). Photosynthesis also plays a vital role in controlling isoprene emissions from vegetation which itself has been shown to play an important role in driving atmospheric chemistry (Pacifico et al., 2009; Sharkey et al., 2007). These complex interactions between the biosphere and tropospheric ozone provide important contributions to the global ozone budget (Wild, 2007).

As the observational constraints on the controlling terms of the ozone budget are currently poor, global atmospheric models are currently used to estimate the magnitude of each term. Many of these models produce a reasonable representation of the seasonality and distribution of tropospheric ozone when compared to observational data, however the relative importance of the major controlling sources and sinks vary between models. In relation to biosphere tropospheric ozone interactions, the processes of dry deposition and biogenic isoprene emissions occur on temporal and spatial scales that are often smaller than the coarse resolutions of these models and are therefore highly parametrised with large amounts of uncertainty associated with them. Further to this the effects of ozone damage to vegetation are currently not included in the present generation of atmospheric models.

Therefore impacts of including the effects in model simulations needs to be considered in order to fully understand the effects and feedbacks of changing the tropospheric ozone distribution in past, present and future climates. They also need to be considered to estimate the response of the biosphere to future, warmer climates and to understand the response of global crop yields to the implementation of air quality legislation that will introduce emissions controls on ozone precursor species.

1.2 Aims of this thesis

The main aim of this thesis is to improve the understanding of the complex interactions between tropospheric ozone and the global biosphere in order to estimate the effects and

feedbacks of changing tropospheric ozone under past, present and future climates on atmospheric composition and air quality. To achieve this both a chemical transport model (TOMCAT) and a coupled chemistry-climate model (HadGEM2-ES) are used. The specific aims are:

1. **Quantify the intercontinental trans-boundary contributions of the emissions of ozone precursors to ozone induced crop yield losses in the northern hemisphere.** The TOMCAT model is used to quantify the intercontinental contributions to ozone-induced crop yield losses, due to anthropogenic NO_x emissions from North (N) America, South East (SE) Asia and Europe. A range of ozone exposure metrics are used to determine crop yield losses with the aim to determine how the use of different metrics impacts the overall conclusions.

2. **Quantify the impact of pre-industrial to present day land cover changes on the pre-industrial tropospheric ozone distribution and the associated impact of these changes on the estimated radiative forcing.** The HadGEM2-ES model is used to separately assess the impacts of changes in land cover, climate and atmospheric CO_2 on the dry deposition of ozone and its precursors, and on biogenic isoprene emissions and the resultant impact on the estimated pre-industrial tropospheric ozone distribution. The impact of how these variations influence the estimate of changes in radiative forcing since the pre-industrial period are also investigated.

3. **Investigate the effects of ozone vegetation damage on tropospheric composition through its effects on dry deposition and isoprene emissions.** The HadGEM2-ES model is used to quantify for the first time the impact of ozone vegetation damage on reactive trace gas deposition and the subsequent feedback on atmospheric ozone concentrations. The model interactive isoprene emissions scheme is also used to quantify the first estimate of the feedback on isoprene emissions, of ozone damage through the plant photosynthesis response to ozone exposure.

1.3 Thesis layout

Chapter 2 provides an overview of the structure and composition of the atmosphere along with the key chemical and physical processes that occur. The trace species of ozone is

described along with the key processes which govern its atmospheric budget. Chapter 2 also provides an overview of the current understanding of interactions between tropospheric ozone and vegetation, the damage that this gas can cause to plants and the potential feedbacks these can have on atmospheric composition and chemistry. Chapter 3 provides an overview of the TOMCAT and HadGEM2-ES atmospheric models used in this thesis along with the evaluation of these models against surface site, aircraft and ozonesonde data. Chapter 3 also discusses the implementation and evaluation of an updated dry deposition scheme in the TOMCAT model. Chapter 4 presents estimates of the impact of ozone precursor emissions from each of the northern hemisphere's major industrialised regions on crop yields globally and in continents downwind of each region. Chapter 5 investigates the impacts of changing the prescribed model land cover on the simulated pre-industrial tropospheric ozone burden and associated pre-industrial to present day radiative forcing. Chapter 6 quantifies the impact of ozone vegetation damage on reactive trace gas deposition and the subsequent feedbacks on atmospheric ozone concentrations. The effects of ozone damage on isoprene emissions through the plant photosynthesis response to ozone damage is also quantified in this Chapter. Finally a summary of all of the results is presented in Chapter 7 along with a discussion of how they address the aims set out in Section 1.2. Chapter 7 also presents suggestions for future work.

Chapter 2

Background and current understanding of interactions between vegetation and tropospheric ozone

2.1 Introduction

This chapter will provide a brief summary of the Earth's atmosphere outlining its overall structure and composition and the chemical and physical process that occur. The chapter will then go on to discuss the trace species of ozone in more detail, in particular, its role in the troposphere and the chemical processes that occur in this lowest layer of the atmosphere. The ozone budget will be described including important sources and sinks and the role that ozone plays as a greenhouse gas and its contribution to climate change. Finally the chapter will discuss the current understanding of how ozone interacts with the biosphere, the damage that this gas can cause to vegetation and the potential feedbacks these interactions can have on the atmosphere and ultimately the climate. The present treatment of these interactions in atmospheric models will be highlighted including areas that require further investigation.

2.2 The Earth's atmosphere

The Earth's atmosphere is a thin layer consisting of a mixture of gases, which surrounds the surface of the planet and extends out into space for approximately 100km. The mass of the atmosphere is estimated at 5 x 10^{18} kg (Wayne, 2000). However, since atmospheric pressure and density decrease approximately exponentially with height, the majority of the Earth's atmosphere lies near the surface, with half of the mass lying below 5.5km and roughly 99% of the mass lying below 30km. The atmosphere is made up of primarily molecular nitrogen (N_2) which comprises approximately 78% of the total mass and molecular oxygen (O_2) which accounts for 21%. The remaining 1% is made up of a number of trace species which include ozone (O_3), carbon dioxide (CO_2), methane (CH_4), argon (Ar), neon (Ne) and a number of different biogenic and anthropogenic volatile organic compounds (VOCs). Water Vapour (H_2O) is also an important constituent of the atmosphere however its concentrations are highly variable dependant upon temperature and pressure.

The force exerted by the weight of the atmosphere is known as the atmospheric pressure and this falls off exponentially with increasing height due to the effects of gravity and temperature (Figure 2.1). The atmosphere is divided into 4 layers with these determined by the way that temperature varies with height from the surface to the top of the atmosphere. It is shown in Figure 2.1 that from the surface up to an altitude of approximately 18km, the temperature decreases from a maximum of about 288K at the surface to about 225K. This region of the atmosphere is known as the troposphere and is where a significant number of chemical and physical processes and feedbacks occur that can have important implications on atmospheric composition and climate. The troposphere is also directly in contact with the Earth's surface where exchange of trace species between the atmosphere and the land surface can occur.

Above the troposphere sits the stratosphere which is characterised by an increase of temperature with height and is also the location of the ozone layer which acts to filter out harmful ultra-violet (UV) rays from the incoming solar radiation. The stratosphere plays an important role in the budgets of trace species in troposphere with stratospheric-tropospheric exchange providing significant input of species such as ozone into the upper troposphere (Wild, 2007).

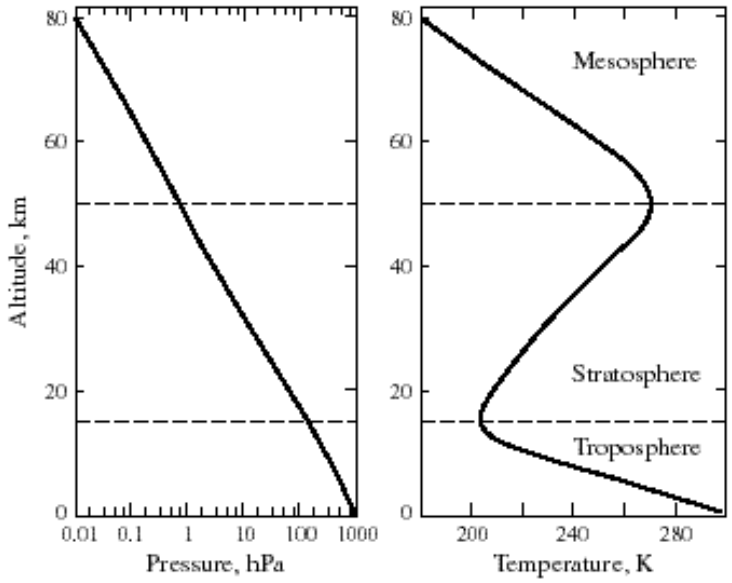

FIGURE 2.1: Typical pressure (left panel) and temperature (right panel) vertical profiles in the atmosphere at 30 °N for March. Taken from Jacob (1999)

Finally the upper atmosphere consists of the mesosphere and the thermosphere. In the mesosphere, above an altitude of approximately 50 km, the heating of the air is dominated by cooling processes and temperature begins to fall off with height again (Wayne, 2000). The lowest temperatures in the atmosphere are found at the mesopause (the boundary between the mesosphere and the thermosphere) above which temperature once again begins to rise with increasing altitude (Figure 2.1).

2.3 Transport processes in the atmosphere.

Atmospheric transport is the term given to the micro (small) and macro (large) scale processes which move air parcels carrying trace gas molecules through the atmosphere. Therefore upon emission into the atmosphere, trace gases are transported away from their sources and are ultimately mixed throughout the atmosphere. Three major processes that play a strong role in atmospheric transport are advection, convection and boundary layer mixing.

2.3.1 Advection

Advection is the horizontal movement of air molecules by wind which can transport trace gas molecules and aerosols both short and long distances through the atmosphere. Winds are generated as a result of pressure gradient forces and flow from high to low pressure with the strength of the wind determined by the magnitude of the gradient. This can lead to air pollutants being transported long distances and impacting air quality in regions thousands of kilometres downwind from the emission source. Due to strong cyclogenesis and frontal activity over eastern parts of North America and Asia, trace gases can be lifted into the free troposphere once emitted and transported eastwards on the prevailing westerly winds at mid-latitudes (Stohl, 2001). This results in the transport of air pollutants from North America across the Atlantic to Europe and from East Asia across the Pacific to North America. The transport of European emissions to Asia is less efficient due to a paucity of strong cyclogenesis and frontal activity over central and eastern Europe (Stohl, 2001).

This is important in relation to ozone pollution, as this long range transport of ozone and its precursor species contributes between 2 and 10 ppbv to surface ozone concentrations in western Europe and western N America from emission sources of ozone precursors in N America and Asia respectively (Dentener et al., 2010; Derwent et al., 2004; Hudman et al., 2004; Parrish et al., 2010).

2.3.2 Convection

Convection is the process which involves the rapid vertical transport of air molecules, trace gases and aerosols in the atmosphere. There are two types of convection, free and forced convection. Free convection is induced by solar heating of the Earth's surface which is conducted to air molecules, making them buoyant and causing the air to rise. Free convection is stronger in the tropics where incoming solar radiation is higher and surface temperatures are typically higher. Conversely, free convection is weaker at the poles where surface temperatures are lower. Forced convection is induced by a number of processes and can be influenced by the land surface as well as converging and diverging horizontal winds. Convection is an important process as it can lead to the transport of trace pollutants out of the boundary layer and into the free troposphere where they can be advected.

2.3.3 Boundary layer mixing

The Planetary boundary layer, is the layer of air within the troposphere that is directly in contact with the Earth's surface. The depth of the boundary layer varies diurnally from a depth of a few 100 metres during the night up to a peak of about 1-2 km during the afternoon (Jacob, 1999). Due to a number of factors, including the characteristics of the underlying land surface and the rate of solar heating, the boundary layer is well mixed due to turbulent and rapid mixing of air close to the Earth's surface. This results in species emitted from the surface being fairly rapidly mixed throughout the boundary layer over a couple of days. The boundary layer is capped by a subsidence inversion which leads to slower transport of air out of the boundary layer, with ventilation of air to the free troposphere taking approximately one week (Jacob, 1999). At night, the land surface cools due to lack of solar heating which results in the formation of a temperature inversion near to the surface under calm conditions. This suppresses vertical mixing of trace gases, trapping them near to the surface allowing concentrations to build up. Finally, the dry deposition of many trace species (including ozone and its precursors) occurs in the boundary layer.

2.4 An overview of background tropospheric chemistry

After pollutants have been emitted to the atmosphere, they are also affected by a large number of chemical reactions and processes that can impact their concentrations along with the physical transport processes. This section provides an overview of the key chemical species which will be discussed in this thesis along with the chemical reactions they undergo in the troposphere. Table 2.1 summarises the typical concentrations of each species along with the lifetime in the atmosphere.

2.4.1 Ozone

In recent decades tropospheric ozone has emerged as a global air pollution problem (Fowler et al., 2008) along with being identified as an important greenhouse gas, with current estimates of a contribution of 0.25-0.65 Wm^{-2} to the global radiative forcing attributed to anthropogenic activity since the pre-industrial era (Forster et al., 2007). As shown in

TABLE 2.1: Volume mixing ratios and tropospheric lifetimes of key trace species. Volume mixing ratios are reported for 2 tropospheric regions (Jacobson, 2002).

		Volume Mixing Ratio (ppbv)		
Species	Chemical Formula	Clean Troposphere	Polluted Troposphere	Lifetime
Ozone	O_3	10-100	10-350	≈22 days[a]
Nitric Oxide	NO	0.005-0.1	0.05-300	≈1 day[b]
Nitrogen Dioxide	NO_2	0.01-0.3	0.2-200	≈1 days[b]
Carbon Monoxide	CO	40-200	2000-10000	≈2 months[c]
Methane	CH_4	1800	1800-2500	7.8-10.3 years[d]
PAN	$CH_3CO \cdot O_2NO_2$	0.002-0.1	10-35	1 hour-5 months[e]

[a] Mean lifetime from 25 model simulations (Stevenson et al., 2006) [b] Mean lifetime of NO_x (Jacob, 1999) [c] Mean lifetime for oxidation by OH (Jacob, 1999) [d] Mean lifetime for oxidation by OH (Lawrence et al., 2001) [e] Mean lifetime varies with temperature between 1h at 298 K and ≈5m at 250 K (Singh, 1987)

Table 2.1 ozone concentrations in the troposphere lie in the range 10-100 ppbv in clean air environments and 10-350 ppbv in polluted air. The lifetime of ozone in the atmosphere is approximately 22 days with principal sinks of chemical destruction and dry deposition to the land surface. One key sink is the photodissociation of ozone and the formation of the hydroxyl radical (OH) from the the resultant products which results in ozone being identified as a significant driver of tropospheric chemistry (Crutzen et al., 1999).

The chemistry of the troposphere is largely driven by UV radiation of wavelengths shorter than 340 nm which have sufficient energy to dissociate an ozone molecule into O_2 and electronically exited oxygen $O(^1D)$ (Michelsen et al., 1994). A large proportion of the $O(^1D)$ become collisionally deactivated and react with O_2 to reform ozone (Equation 2.4) however the remainder have the required energy to react with water vapour H_2O to produce 2 OH radicals (Crutzen et al., 1999).

$$O_3 + h\nu \rightarrow O(^1D) + O_2(\lambda < 340\,nm) \tag{2.1}$$

$$O(^1D) + H_2O \rightarrow 2OH \tag{2.2}$$

The OH radicals have been termed the detergents of the atmosphere (Crutzen et al., 1999) as they are highly reactive and react with the majority of trace gases emitted from both natural and anthropogenic activities. The average concentration of OH in the troposphere is around 10^6 molecules cm^{-3} (Krol et al., 1998; Prinn et al., 1995) which is low relative to other trace species however the OH radical initiates almost all of the oxidation processes in the atmosphere. The efficiency of reaction of trace gases with the OH radical also determines their atmospheric lifetimes. In addition to OH two other important species exist in the atmosphere that are initiators of atmospheric oxidation, these being the nitrate radical (NO_3) and ozone. Both of these species play an important role in chemical processes in the atmosphere as outlined below.

Ozone is classed as a secondary air pollutant in that it is not directly emitted into the atmosphere instead being produced in-situ in the troposphere through a sequence of sunlight-driven photochemical reactions involving nitrogen oxides (NO_x, encompassing both NO and NO_2) and VOCs or CO (Crutzen et al., 1999). Ozone is produced by the photodissociation of nitrogen dioxide (NO_2) which yields nitric oxide (NO) and atomic oxygen (O). This atomic oxygen then goes on to react with molecular oxygen (O_2) to produce ozone. However, ozone can then go on to react with NO to reform NO_2 and O_2. This series of reactions forms what is known as a null cycle as the overall result is zero net production of ozone and is commonly known as the photostationary state (Equations 2.3 to 2.5). The photolysis of NO_2 is the only known method of producing ozone in the troposphere (Wayne, 2000).

$$NO_2 + h\nu \rightarrow O + NO(\lambda < 424\,nm) \tag{2.3}$$

$$O + O_2 + M \rightarrow O_3 + M \tag{2.4}$$

$$O_3 + NO \rightarrow NO_2 + O_2 \tag{2.5}$$

NO_x has a relatively short lifetime in the atmosphere of approximately one day with the main sink in the troposphere during the daytime being the oxidation of NO_2 by the OH radical to produce nitric acid (HNO_3) which is highly soluble in water and is readily removed by the process of wet deposition (Jacob, 1999).

$$NO_2 + OH + M \rightarrow HNO_3 + M \tag{2.6}$$

During the night, in the absence of sunlight, the photolysis of NO_2 does not occur (Equation 2.3) and the reaction of ozone with NO dominates (Equation 2.5) resulting in a net sink of ozone and the conversion of the majority of NO_x into NO_2. The NO_2 then goes onto react with ozone to form the nitrate radical (NO_3) which subsequently reacts with NO_2 to produce dinitrogen pentoxide (N_2O_5). At higher temperatures, N_2O_5 can thermally dissociate back into its constituent products NO_3 and NO_2 (Equation 2.9). Alternatively, N_2O_5 reacts heterogeneously with H_2O on particle surfaces to form HNO_3, leading to the removal of NO_x from the atmosphere.

$$NO_2 + O_3 \rightarrow NO_3 + O_2 \tag{2.7}$$

$$NO_3 + NO_2 + M \rightarrow N_2O_5 + M \tag{2.8}$$

$$N_2O_5 + M \rightarrow NO_3 + NO_2 + M \tag{2.9}$$

$$N_2O_5 + H_2O(aerosol) \rightarrow 2HNO_3 \tag{2.10}$$

When NO_x is present in the atmosphere, the presence of CO, CH_4 and VOCs can result in the net production of ozone through the oxidation of these species by the OH radical. However, as shown by Figure 2.2, the production of ozone is not linearly related to the concentrations of these species. The thick black line in Figure 2.2 represents the separation of the NO_x- and hydrocarbon- limited regimes. To the left of the line lies the NO_x limited regime where ozone concentrations will increase with rising NO_x levels and are insensitive to changes in hydrocarbon levels. To the right of the line is the hydrocarbon limited regime where ozone concentrations respond to changes in both NO_x and hydrocarbons with a response of rising ozone with rising hydrocarbons and decreasing ozone with increasing NO_x.

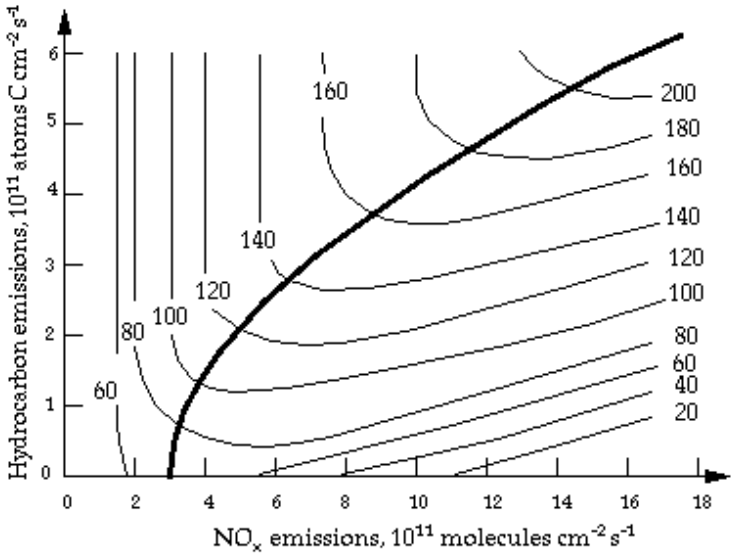

FIGURE 2.2: Ozone concentrations (ppbv) as a function of NO_x and hydrocarbon emissions. Taken from (Jacob, 1999).

This non-linear response of ozone is important when implementing air quality control strategies to control ozone pollution as the chemical regime for ozone production needs to be considered when deciding which precursor to implement the strategies for (Jacob, 1999). For example, if the regime is hydrocarbon limited, applying emissions reductions to NO_x will lead to a small response in ozone concentrations even for a large change in NO_x. Reductions in NO_x may also potentially result in enhanced ozone concentrations.

2.4.2 Carbon monoxide

CO is a major pollutant in the atmosphere and plays an important role in the chemical production of ozone in the troposphere. It is primarily released into the atmosphere through fossil fuel combustion and biomass burning (largely associated with tropical agriculture over regions such as Central and Southern Africa (Andreae, 1991; Hao et al., 1990; Matichuk et al., 2007)) with a large source also coming from the oxidation of methane (Jacob, 1999) as shown in Table 2.2. The majority of CO in the present day troposphere is of anthropogenic origin (Table 2.2) with the dominating sink shown to be oxidation by OH. This results in CO having an atmospheric lifetime that is very seasonally dependent, though typically the lifetime is approximately 2 months (Table 2.1). Therefore CO is not well mixed in the atmosphere with surface concentrations ranging from 50-300 ppbv in remote regions to several ppmv in polluted urban areas where CO is considered to be hazardous to human health.

TABLE 2.2: Present Day Global budget of CO (Jacob, 1999).

	Range of estimates (Tg CO yr^{-1})
SOURCES	**1800-2700**
Fossil fuel combustion / industry	300-550
Biomass burning	300-700
Vegetation	60-160
Oceans	20-200
Oxidation of methane	400-1000
Oxidation of other hydrocarbons	200-600
SINKS	**2100-3000**
Tropospheric oxidation by OH	1400-2600
Stratosphere	∼100
Soil uptake	250-640

The oxidation of CO by reaction with OH is important as when NO_x is present it can result in the formation of ozone. When CO reacts with OH it produces a single hydrogen atom and CO_2. The single hydrogen atom then goes on to react rapidly with O_2 to produce the peroxy radical HO_2. As the second stage of the reaction is very rapid, the oxidation reaction can be written as follows:

$$CO + OH(+O_2) \rightarrow CO_2 + HO_2 \tag{2.11}$$

The HO_2 formed then proceeds to react with NO to reproduce NO_2 and OH, thus making the cycle catalytic in nature (Equation 2.12). This reaction is rapidly followed by the photolysis of NO_2 and the formation of ozone (Equations 2.3 to 2.4). This effectively breaks the photostationary state by producing NO_2 from NO without the loss of ozone with the net result being the production of ozone.

$$HO_2 + NO \rightarrow OH + NO_2 \tag{2.12}$$

The HO_2 can also react with itself to produce H_2O_2 which is a temporary reservoir species for HO_x ($OH+HO_2$). Photolysis of H_2O_2 can subsequently occur to yield 2 OH radicals (Equation 2.14) or H_2O_2 can react with OH to produce one HO_2 radical and H_2O (Equation 2.15), with the result of this reaction being the loss of one HO_x molecule. H_2O_2 is also highly soluble and can therefore be scavenged by precipitation and be lost through the process of wet deposition thus removing two HO_x molecules from the atmosphere.

$$HO_2 + HO_2 \rightarrow H_2O_2 + O_2 \tag{2.13}$$

$$H_2O_2 + h\nu \rightarrow OH + OH \tag{2.14}$$

$$H_2O_2 + OH \rightarrow HO_2 + H_2O \tag{2.15}$$

2.4.3 Methane

A similar pathway also exists in the atmosphere for the oxidation of CH_4 by OH which can affect the formation of ozone in the troposphere as well as provide an important source of CO (Table 2.2). This oxidation pathway is the principal sink of CH_4 resulting in a

relatively long atmospheric lifetime of CH_4 of 7.8–10.3 years (Table 2.1). However, due to the high concentrations of CH_4 in the troposphere (1800-2500 ppbv (Table 2.1)) its oxidation still plays a significant role in atmospheric chemistry. CH_4 is oxidised by OH to produce CH_3 and H_2O (Equation 2.16). The CH_3 then goes on to react rapidly with O_2 to produce the methylperoxy radical (CH_3O_2) (Equation 2.17). In conditions where NO concentrations are high CH_3O_2 can react with NO to produce the methoxy radical (CH_3O) and NO_2 (Equation 2.18) which can then go on to form ozone through the series of reactions shown by equations 2.3 to 2.4.

$$CH_4 + OH \rightarrow CH_3 + H_2O \tag{2.16}$$

$$CH_3 + O_2 + M \rightarrow CH_3O_2 + M \tag{2.17}$$

$$CH_3O_2 + NO \rightarrow CH_3O + NO_2 \tag{2.18}$$

A very rapid reaction can occur between CH_3O and O_2 to yield formaldehyde (HCHO) and HO_2. Due to the speed of this reaction it is often combined with Equation 2.18 to:

$$CH_3O_2 + NO + O_2 \rightarrow HCHO + HO_2 + NO_2 \tag{2.19}$$

In conditions where NO concentrations are very low the CH_3O_2 radical formed in Equation 2.17 can react with HO_2, NO_2 or another CH_3O_2 radical. In the case of reaction with HO_2, the products are methyl hydroperoxide CH_3OOH and O_2 (Equation 2.20), with the high solubility of CH_3OOH leading to dissolution in cloud droplets which can lead to the removal of HO_x from the troposphere through wet deposition (Wayne, 2000).

$$CH_3O_2 + HO_2 \rightarrow CH_3OOH + O_2 \tag{2.20}$$

Formaldehyde (HCHO) is a typical product formed during the oxidation of hydrocarbons and itself undergoes 2 main reactions in the atmosphere, one being reaction with OH and the other being photolysis. The photolysis of HCHO has two possible pathways (Equations 2.21 and 2.22) which both can yield active radicals which can further oxidise CO and CH_4 or play a role in ozone pollution through NO to NO_2 conversion.

$$HCHO + h\nu \rightarrow H + HCO \tag{2.21}$$

$$HCHO + h\nu \rightarrow H_2 + CO \tag{2.22}$$

The first photolysis pathway (Equation 2.21) leads to the formation of H and HCO. Both of these products can re-enter the HO_x chain with the H atom reacting rapidly with O_2 to form HO_2 (as shown in Section 2.4.2) and HCO reacting with O_2 to form CO and HO_2. The second pathway (Equation 2.22) leads to the formation of CO and H_2. The other possible reaction pathway for HCHO is reaction with OH which results in the formation of HCO and H_2O (Equation 2.23).

$$HCHO + OH \rightarrow HCO + H_2O \tag{2.23}$$

All reaction pathways of HCHO result in the formation of CO and the recycling of HO_x molecules showing why the oxidation pathways of CH_4 are important to the CO budget (Table 2.2) as well as ozone formation (Wayne, 2000).

2.4.4 Volatile organic compounds

The oxidation pathways that exist for CH_4 also have their analogues that apply to higher hydrocarbons, which can have important implications for ozone formation and NO_x and HO_x cycling in the troposphere. For the general case, a hydrocarbon (RH) is oxidised by reaction with OH which results in the formation of an alkyl (R) radical and H_2O. This R radical then reacts rapidly with O_2 to form a peroxy radical (RO_2). As the reaction with O_2 is very fast the reaction sequence can be written as follows (Wayne, 2000):

$$OH + RH + O_2 \rightarrow RO_2 + H_2O \tag{2.24}$$

The RO_2 radical can then react with NO to form NO_2 and an oxy- radical (RO) (Equation 2.25). Two further reaction pathways can occur for the RO radical, it can either decompose into a daughter alkyl (R') and an aldehyde (R"CHO) (Equation 2.26) or it can react with O_2 to yield a ketone species (R'R"CO) and HO_2 (Equation 2.27). The HO_2 will further react with NO to produce NO_2 and OH (Equation 2.12) which confirms the oxidation sequence as a chain process. The aldehyde and ketone species can be photolysed as seen for formaldehyde (Equations 2.21 and 2.22) or they can take part in further oxidation in thermal reactions.

$$RO_2 + NO \rightarrow RO + NO_2 \tag{2.25}$$

$$RO \rightarrow R' + R"CHO \tag{2.26}$$

$$RO + O_2 \rightarrow R'R"CHO + HO_2 \tag{2.27}$$

One such reaction is the oxidation of acetaldehyde (CH_3CHO) by OH to form CH_3CO (Equation 2.28) which then reacts with O_2 to produce the peroxyacetyl radical ($CH_3CO \cdot O_2$) (Equation 2.29). An important reaction step involving $CH_3CO \cdot O_2$ and NO_2 can take place resulting in the formation of peroxyacetyl nitrate (PAN) which is an important reservoir species for NO_x (Section 2.4.6).

$$CH_3CHO + OH \rightarrow CH_3CO + H_2O \tag{2.28}$$

$$CH_3CO + O_2 \rightarrow CH_3CO{\cdot}O_2 \tag{2.29}$$

$CH_3CO \cdot O_2$ can also react with NO to produce NO_2 and the $CH_3CO \cdot O$ (Equation 2.30) radical which can then fragment to yield CH_3 and CO_2 (Equation 2.31). The CH_3 radical is able to further take part in NO_x and HO_x cycling with important implications for ozone and CO production (Section 2.4.3).

$$CH_3CO{\cdot}O_2 + NO \rightarrow CH_3CO{\cdot}O + NO_2 \tag{2.30}$$

$$CH_3CO{\cdot}O \rightarrow CH_3 + CO_2 \tag{2.31}$$

The final result of each OH-VOC oxidation cycle is the conversion of two NO molecules to NO_2 molecules which plays an important role in ozone production (Section 2.4.1).

2.4.5 Isoprene

Isoprene (2-methyl-1,3-butadiene,C_5H_8) is a hydrocarbon emitted from vegetation and plays an important role in the production of ozone in the troposphere. Isoprene is quantitatively the most important of a wide range of biogenic volatile organic compounds (BVOCs) with an estimated global annual emission of around 400–600 $TgCyr^{-1}$ (Arneth et al., 2008; Pacifico et al., 2009). Approximately 90 % of isoprene emissions are from terrestrial vegetation (Pacifico et al., 2009). Isoprene is a highly reactive gas and consequently has a very short lifetime in the atmosphere. Its major sinks are reaction with nitrate (NO_3), OH and ozone with typical reaction lifetimes of 0.8 h, 1.7 h and 1.3 days respectively (Seinfeld and Pandis, 1998).

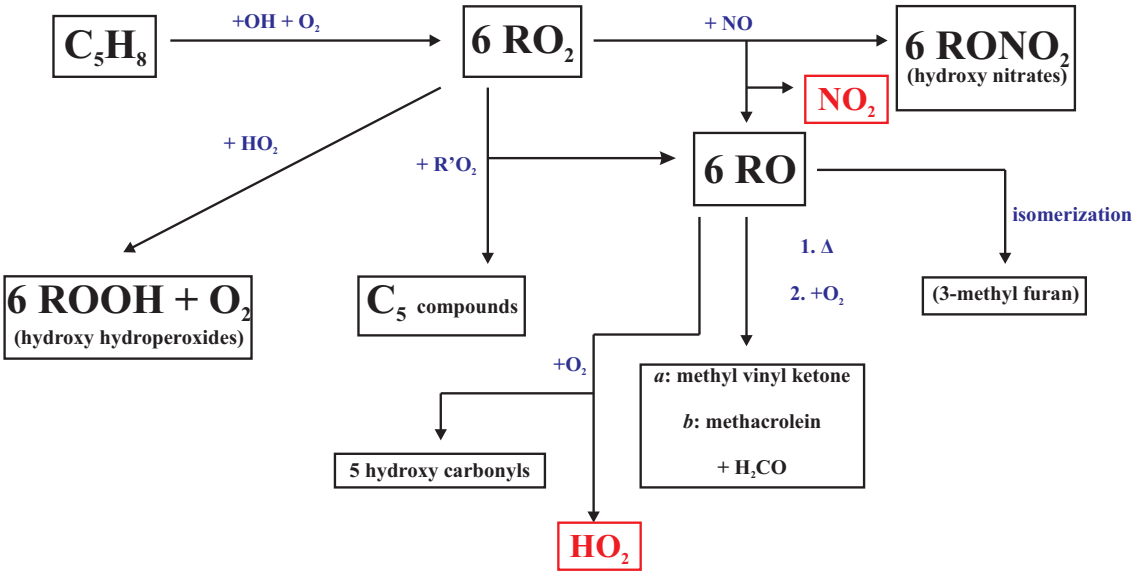

FIGURE 2.3: Simplified schematic of the OH-oxidation of isoprene. The key oxidation products at each step are shown in black text. Blue text indicates the key chemical reaction steps involved in the oxidation process. Finally red text indicates steps in the process where cycling of NO_x and HO_x occur. The numbers preceding each product indicate the number of different compounds that can be formed at each stage in the oxidation chain. See text for details.

The oxidation pathway of isoprene by OH plays an integral role in atmospheric chemistry through its effect on ozone formation and NO_x and HO_x cycling. The initial attack of isoprene by OH can yield four different radical adducts. If each of these is represented as R, the isoprene oxidation chain will proceed as shown in Equation 2.32 (Wayne, 2000).

$$\mathrm{R} \xrightarrow{+\mathrm{O_2}} \mathrm{RO_2} \xrightarrow{+NO} \mathrm{RO} \xrightarrow{+\mathrm{O_2}} \mathrm{HO_2} + \mathrm{HCHO} + \mathrm{carbonyl} \tag{2.32}$$

Two of these radical adducts are allylic (delocalized free electron) which leads to the production of two peroxy radicals RO_2 with the addition of oxygen resulting in a total of six possible reaction pathways as outlined in Figure 2.3. In the presence of high NO_x, RO_2 can react with NO (Equation 2.25) to produce NO_2 leading to ozone formation. Further reactions of RO can occur with O_2 leading to formation of HO_2 and a ketone species (Equation 2.27). Finally, HO_2 can react further react with NO leading to NO_2 formation and the generation of the OH radical (Equation 2.12). This completes the chain by enhancing ozone formation whilst recycling the OH radical. As long as there is a carbon-hydrogen bond in the resultant ketone species from the reaction of RO with O_2, the resulting hydrocarbon can take part in further cycles to further enhance ozone formation (Sharkey et al., 2007). To add to the complexity of the chemistry, the RO_2 radicals formed in the initial stages of the oxidation process not only react with NO as shown in Equation 2.32 but also with HO_2 (yielding hydroxy hydroperoxides and oxygen) and all other RO_2 species present as highlighted in Figure 2.3. The net effect of this oxidation chain is the formation of a large number of ozone molecules from the oxidation of a single isoprene molecule. Overall in high NO_x environments, the net effect of isoprene oxidation is the maintenance of high OH concentrations through OH recycling, the removal of BVOCs and the net production of ozone.

Two products of isoprene oxidation that have been observed in laboratory studies are the unsaturated carbonyl compounds methacrolein (CH_2=C(CH_3)CHO) and methyl vinyl ketone $CH_3COCH=CH_2$ (Figure 2.3) (Wayne, 2000). Both of these species can undergo further oxidation in the atmosphere and can also by photolysed. A key process involves the oxidation of methacrolein which yields a peroxy radical (CH_2=C(CH_3)C(O)$\dot{O}_2$) which can add to NO_2 to form peroxymethacryloyl nitrate (MPAN), as shown in Equation 2.33. This species is analogous to PAN (Section 2.4.6) and has tropospheric concentrations of up to 10-30 % of that of PAN itself (Wayne, 2000). As the only source of MPAN is through the oxidation chain of isoprene, its presence in the atmosphere is a strong indicator of recent ozone formation from hydrocarbons of biogenic origin rather than anthropogenic.

$$CH_2{=}C(CH_3)C(O)\dot{O}_2 + NO_2 \rightarrow CH_2{=}C(CH_3)C(O)\dot{O}_2NO_2 \quad (2.33)$$

Presently there is large uncertainty in the understanding of the OH-oxidation pathway. Field measurements at sites in the Amazon have shown that isoprene concentrations above the forest canopy are lower than those implied by measurements at leaf level (Greenberg et al., 2004). However, OH concentrations were observed to be higher than expected at the estimated magnitude of isoprene emission if the sink of isoprene was through the OH-oxidation pathway (Butler et al., 2008; Carslaw et al., 2001; Ganzeveld et al., 2008; Hofzumahaus et al., 2009; Karl et al., 2007; Kuhn et al., 2007; Lelieveld et al., 2008; Tan et al., 2001; Thornton et al., 2002). It was suggested by Lelieveld et al. (2008) that the high levels of OH were maintained whilst isoprene was removed through the recycling of OH through the oxidation pathway. However, when this mechanism was included in a chemistry-climate model, the estimated isoprene mixing ratios were shown to be unrealistically low (Butler et al., 2008). It has also been suggested that OH recycling could possibly take place without reactions involving NO_2 (Hofzumahaus et al., 2009). This would result in isoprene removal without an increase in ozone production and would produce isoprene mixing ratios that are in agreement with the observations. This uncertainty needs to be considered when modelling the impacts of how isoprene emissions from vegetation impact atmospheric chemistry.

The response of ozone concentrations to an increase in isoprene emissions also depends on the local NO_x distribution in a given region. In relatively polluted urban environments where NO_x and OH concentrations are high, isoprene will act as an ozone source. Conversely, in unpolluted low NO_x regions, isoprene can react directly with ozone itself and higher emissions can result in a net ozone sink. Overall, this non-linear dependence of the response of ozone and OH concentrations to isoprene emissions leads to high levels of uncertainty when accounting for the emissions of isoprene and its subsequent oxidation in atmospheric models.

2.4.6 Reactive nitrogen

The role of NO_x has been shown to be very important in the distribution of ozone in the troposphere and the oxidation rates of CO, CH_4 and other higher level hydrocarbons (Sections 2.4.1 to 2.4.4). However due to its relatively short lifetime in the atmosphere compared to the rate of atmospheric redistribution, concentrations were thought to be low in regions remote from anthropogenic sources (Wayne, 2000). As shown in Section 2.4.1 NO_x can be locked up in the reservoir species HNO_3 however this is readily removed by wet deposition which results in loss of NO_x from the troposphere, meaning this reservoir is only temporary and does not result in high levels of transport to remote regions.

NO_x can however be locked up in another reservoir species known as peroxyacetyl nitrate (PAN). This can be formed during the thermal reaction of acetaldehyde CH_3CHO with OH, which yields the peroxyacetyl radical $CH_3CO \cdot O_2$ (Equation 2.29). Through the addition of NO_2, PAN ($CH_3CO \cdot O_2NO_2$) is formed.

$$CH_3CO{\cdot}O_2 + NO_2 \leftrightharpoons CH_3CO{\cdot}O_2NO_2 \tag{2.34}$$

PAN is important as it is in thermal equilibrium with its precursor species (Wayne, 2000) with the equilibrium shifted towards the right at cooler temperatures and the left at higher temperatures. PAN has a lifetime of around one hour at a temperature of 298 K with this increasing to five months at temperatures of 250 K (Table 2.1). Therefore if PAN is injected into air above the boundary layer it will be subject to cooler temperatures than at the surface and will be relatively stable. This allows PAN (and its analogue species) to remain in the atmosphere for weeks and be transported long distances with the equilibrium of Equation 2.34 shifting to the left if subsidence of PAN occurs and it is transferred to warmer temperatures where it will break up to release NO_2. This can lead to the removal of reactive nitrogen from high emissions regions and redistribution to remote areas (Moxim et al., 1996) which can impact ozone concentrations in these remote regions. There is increasing evidence from a number of modelling and observational studies that long range transport of ozone and its precursor species (including PAN) from high emissions regions such as North America and Asia are impacting ozone concentrations in regions downwind

(Cooper et al., 2010; Dentener et al., 2010; Derwent et al., 2004; Hudman et al., 2004; Parrish et al., 2010).

2.5 Vegetation – tropospheric ozone Interactions

Vegetation plays an important role in the climate system through modulating the surface water- and energy-balance and through the emission of greenhouse gases (CO_2, CH_4 and N_2O) to the atmosphere (Denman et al., 2007). Vegetation regulates both the carbon and hydrological cycles on both regional and global scales through the exchange of carbon and water between plants and the atmosphere (Bonan, 2008). These processes are typically closely coupled, with tiny pores in the surfaces of leaves known as stomata controlling the amount of CO_2 entering the leaf for the photosynthesis and the amount of water exiting the leaf (evapotranspiration). Evapotranspiration from forests has been shown to have a strong impact on precipitation rates with a recent study showing that for more than 60 % of the tropical land surface (30 °S to 30 °N), air that has passed over extensive vegetation produces at least twice as much rain as air that has passed over little vegetation (Spracklen et al., 2012).

In addition to this impact on the carbon and hydrological cycles, vegetation can have two major types of impacts on the atmosphere. Firstly vegetation can have biophysical effects through modifying the properties of the land surface. These impacts include modifying the surface albedo which leads to changes in the radiation balance affecting temperatures on a local and regional scale. For example, the boreal forests located at high latitudes in the northern hemisphere, have a dark canopy (low albedo) which covers over the snow covered land surface (high albedo) resulting in greater absorption of sunlight and a warming of the climate. This effect has been predicted to cause a warming of the global climate by 0.8 ° C (Bala et al., 2007). Vegetation also modifies the roughness length of the land surface depending upon the vegetation type and stage of growth. This can impact the flow of air over the vegetated surfaces as well as affecting the rate of dry deposition of trace species (Ganzeveld and Lelieveld, 1995).

Secondly, plants can have biogeochemical feedbacks on the atmosphere through emissions of trace gas and aerosol species which can alter atmospheric composition. These species include BVOC compounds such as isoprene which can have important implications for

atmospheric chemistry as discussed in Section 2.4.5. Finally, the rate of stomatal uptake by plants leaves plays an important role controlling the exchange of trace gases with the atmosphere, including ozone again leading to feedbacks on atmospheric composition and chemistry.

This biogeochemical feedback on ozone concentrations is important to consider due to its role as a greenhouse gas and a global air pollution problem (Fowler et al., 2008). Ozone has also been observed through field experiments to result in cellular damage inside the leaves of plants leading to yield reduction and deterioration in crop quality (Fuhrer, 2009). This can impact photosynthetic rates and induce stomatal closure in plants with resultant reductions in trace gas exchange with the atmosphere. This section provides an overview of the key interactions between vegetation and tropospheric ozone, including the role of vegetation in the ozone budget, the impacts of ozone damage on photosynthesis, the resultant effects on stomatal conductance and the feedbacks of ozone damage on atmospheric composition and chemistry.

2.5.1 Role of dry deposition in the ozone budget.

The total amount of ozone in the atmosphere is controlled by the complex interaction of a number of processes. The major sources of ozone are chemical production due to the oxidation of VOCs and CO in the presence of NO_x (Sections 2.4.2, 2.4.4 and 2.4.5) and downwards transport from the stratosphere where ozone concentrations are much higher than in the troposphere. The major sinks of ozone are chemical destruction by reactions with OH and HO_2 and photodissociation (Equation 2.1) and dry deposition to the land surface. There are currently large uncertainties in the magnitudes of these budget terms and observational constraints on them are currently poor (Wild, 2007). Global chemistry transport models have been used to estimate the ozone budget with a summary of 33 published model CTM studies shown in Table 2.3.

Most of these CTMs produce a reasonable reproduction of the seasonality and distribution of tropospheric ozone based upon climatological ozone sonde observations however the relative importance of the major controlling sources and sinks vary between models. In addition to this the resolution of these CTMs is often too coarse to resolve many of the chemical and dynamical processes that make up the budget terms as these occur

TABLE 2.3: Mean global ozone budget from 33 published model studies (Wild, 2007)

Budget Term	**Range of estimates (Tg O_3 yr^{-1})**
Chemical Production	3948 ±761
Chemical loss	3745 ±554
Production - Loss	245 ±346
Stratosphere–troposphere exchange	636 ±273
Dry Deposition	902 ±255
Burden	**307 ±38**

on much smaller temporal and spatial scales. Therefore these are often parametrised in global models introducing additional uncertainty into the estimates of the budget terms. Therefore it is necessary to represent these processes as consistently and accurately as possible in global models to provide the best estimate of the ozone budget terms and to assess the sensitivity of each term to dynamical and chemical changes.

One such important process is the dry deposition of ozone to the land surface which accounts for a mean global sink of 902 Tg O_3 yr^{-1}. The rate of dry deposition to a given surface is controlled by 3 major processes. The first is the transport of the trace gas from the well mixed boundary layer to the immediate vicinity of the absorbing surface (Smith et al., 2000). This is determined primarily through the level of turbulent diffusion (Monteith, 1973) which itself is dependant on the wind velocity and the roughness length of the underlying surface. The second process is the transport of the trace species through the thin viscous quasi-laminar boundary layer of air close to the absorbing surface. This occurs by the process of molecular diffusion and is dependant on the physical properties of the depositing trace gas. The final process is the removal of the trace gas from the atmosphere by sticking to the absorbing surface. The rate of this process is dependant upon both the physical and chemical properties of the land surface itself. For the case of a vegetated surface the removal of ozone can occur through the combination of a number of pathways. Ozone can react with the epicuticular waxes on a leaf surface and stick to the leaf cuticles or it can diffuse through the open stomata and react with tissues within the leaf structure (Smith et al., 2000). There is also a small amount of uptake by exposed soil around the plant.

The rate of stomatal uptake is determined by the degree of opening of the stomatal apertures in the leaves of plants which respond to changes in environmental controls such as light, temperature and ambient CO_2 concentrations (Jones, 1998; Schroeder et al., 2001).

Changes in these environmental controls can also impact the rate of photosynthesis which is closely linked to the degree of opening of the stomata, generally referred to as the stomatal conductance (Cox et al., 1999).

2.5.2 Photosynthesis and stomatal conductance

The process of photosynthesis plays an important role in the carbon cycle as it controls the exchange of CO_2 between the atmosphere and the biosphere, with atmosphere-biosphere interactions dominating over the geochemical parts of the carbon cycle. Approximately 150 PgC are transferred each way per year which results in the conversion of approximately 20 % of the CO_2 content of the atmosphere annually (Wayne, 2000). Photosynthesis accounts for the removal of CO_2 from the atmosphere and respiration and decay account for the release of CO_2 back into the atmosphere.

The overall process of photosynthesis involves the CO_2, H_2O and light which leads to the reduction of CO_2 to form carbohydrates and molecular oxygen O_2. The process can be represented stoichiometrically by Equation 2.35 (Jacob, 1999),

$$n\mathrm{CO_2} + n\mathrm{H_2O} \xrightarrow{light} (\mathrm{CH_2O})_n + n\mathrm{O_2} \tag{2.35}$$

where $(CH_2O)_n$ is the stoichiometric approximation of carbohydrate which constitutes biomass material used for growth in plants and is subsequently allocated to the leaves, stems, roots and storage organs within the plant. The process of photosynthesis involves a complex cycle of intermediate steps with an enzyme known as Rubisco (Ribulose-1,5-bisphosphate carboxylase oxygenase) playing an integral role. Rubisco is the world's most abundant protein and is known as a CO_2 acceptor which catalyses the process of carboxylation, the first stage of photosynthesis (Lack and Evans, 2005).

The rate of photosynthesis is dependant upon the amount of incoming solar radiation, the concentration of CO_2 and the availability of H_2O with the stomatal pores controlling the rate at which these enter the leaf. During photosynthesis the plants must maintain the correct degree of stomatal opening such that the required amount of CO_2 enters the leaf

to sustain the rate of carbon fixation but at the same time must reduce the rate of water loss through the open stomata. This is an issue for plants operating the C3 photosynthesis pathway which is so named due to the carboxylation stage involving the formation of two C3 sugars (Lack and Evans, 2005). To adapt to this problem, some plants (particularly those in arid environments where water stress can be a common occurrence) have adopted the C4 pathway where they minimize water loss and maximise CO_2 usage. This pathway involves the fixation of CO_2 to give 4-carbon compounds at the end of the process (Lack and Evans, 2005). The overall result of the C4 pathway is to increase the efficiency of CO_2 reducing the need of the stomata to open widely, reducing water loss. Consequently, the rate of photosynthesis is strongly linked to stomatal conductance and changes in one can have significant impacts on the other and vice-versa. This results in a linear relationship between the 2 processes (Cox et al., 1999).

Photosynthesis also plays an important role in the process of isoprene synthesis and emission from leaves (Arneth et al., 2007; Niinemets et al., 1999; Pacifico et al., 2011) along with other environmental controls such as ambient air temperature and CO_2 concentrations. Therefore changes in the rate of photosynthesis can affect the rate of isoprene emissions which can result in important impacts on atmospheric composition and chemistry (Section 2.4.5).

2.5.3 Impacts of vegetation damage by ozone exposure

Ozone has been observed to have harmful impacts on vegetation (Fuhrer and Achermann, 1994; Jager et al., 1996; USEPA, 1996) with field experiments showing exposure of crops to ozone to result in yield reduction and deterioration of crop quality (Fuhrer, 2009). Damage to plants and visible leaf injury are typically caused when vegetation is exposed to ozone concentrations that exceed 40 ppbv with the associated economic costs of this damage of several billion dollars per year over the United States, the European Union and East Asia (Ashmore, 2005; Sitch et al., 2007; Wang and Mauzerall, 2004). This critical value is generally used to derive European Air Quality Standards (AQSs) with respect to vegetation with the AOT40 (accumulated exposure over a threshold of 40 ppbv) employed to relate ozone exposure to impacts on vegetation growth and crop yields (EEA, 1999). It has however been accepted that concentrations of ozone below the 40 ppbv value are less important in terms of plant damage but are still able to cause some reduction in

yield (Heck and Colwing, 1997). It is also widely acknowledged that the impacts of ozone on plants are more closely related to the flux of ozone through the open stomata rather than exposure in the atmosphere (Emberson et al., 2000; Fuhrer et al., 1992; Musselman and Massman, 1999). This flux of ozone is controlled by the stomatal conductance and determines the amount of ozone that enters the leaf structure.

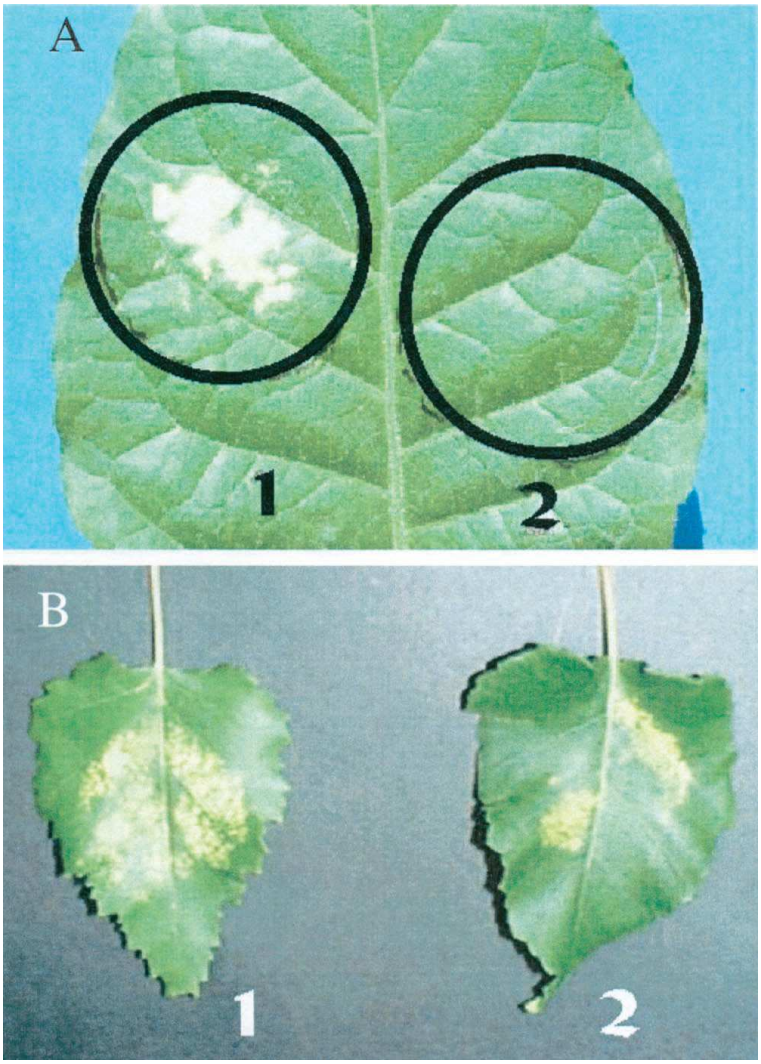

FIGURE 2.4: Ozone damage in Tobacco (**A**) and Birch (**B**) leaves exposed to 300 ppbv of ozone for 3 hours (**1**) or to 300 ppbv of ozone and 3 ppmv of isoprene for 3 hours (**2**). Taken from (Loreto et al., 2001)

Once ozone enters the aqueous environment of the leaf structure it can generate OH, O_2^- (superoxide) and H_2O_2 through a series of several mechanisms and reaction pathways (Byvoet et al., 1995). These products are toxic to plants and can result in high rates of oxidation in the leaf structure leading to necrosis of cell tissue and the formation of necrotic lesions on the surfaces of leaves (Pell et al., 1997). It has also been considered

that when these species interact with the plant cells, they might provide the signal(s) that initiates programmed cell death within the plant (Greenberg et al., 1994). Evidence of such lesions is shown in Figure 2.4 which shows the effects of exposing tobacco and birch leaves to 300 ppbv of ozone for period a of 3 hours. These concentrations are however much higher than experienced at the surface in the atmosphere, however visible damage can still occur at ambient atmospheric ozone concentrations (Ashmore, 2005).

Temperature can also play a role in the effects of ozone damage on plants. At high temperatures, exposure to elevated ozone concentrations causes the peroxidation (oxidative degradation) and denaturation (loss of protein structure) of membrane lipids (Ederli et al., 1997; Maccarrone et al., 1992; Pell et al., 1997; Ranieri et al., 1996; Wellburn and Wellburn, 1996). This can result in damage to the plants cellular structure which, as reported by Loreto et al. (2001) causes an almost complete collapse of the mesophyll of tobacco leaves with the disappearance of palisade and spongy tissues observed as well as the formation of abundant empty spaces. This overall effect leads to the plant reallocating the products of photosynthesis to detoxify the leaf tissues and repair the damaged cells rather than for growth resulting in smaller leaves and less allocation of carbon to other plant organs. This lowers crop yields and the amount of carbon locked up in the biosphere. The effects of ozone damage can also lead to direct damage of the stomatal guard cells which can affect their ability to open and close the stomata which leads to changes in stomatal conductance (Sitch et al., 2007).

In addition to this direct damage to plant cells, exposure to ozone can also result in the degradation of the Rubisco protein (Section 2.5.2) within the leaves of the plant. Pell et al. (1997) have observed that in the presence of ozone, Rubisco frequently does not reach peak concentration and is lost more rapidly. As Rubisco is integral in the first stage of photosynthesis, a reduction in its concentration leads to reduced carboxylation efficiency and a decline in the rate of carbon assimilation by photosynthesis (Ashmore, 2005; Fiscus et al., 2005; Karnosky et al., 2005; Pell et al., 1997). As photosynthesis has been linearly linked to the stomatal conductance (Cox et al., 1999) the reduced rate due to ozone damage will lead to lower rates of stomatal conductance. It has also been indicated that the impact of ozone damage on stomatal conductance is primarily due to this drop in photosynthetic rate rather than direct damage to the stomatal guard cells (Sitch et al., 2007). This drop in stomatal conductance can have important feedbacks on

atmospheric composition by affecting the rate of uptake of trace gases by dry deposition leading to potential climate impacts. It was estimated by Sitch et al. (2007) that effects of ozone damage on stomatal conductance reduces the rate of CO_2 uptake leading to a rise in atmospheric CO_2 concentrations. This indirect radiative forcing by ozone effects on plants is estimated to be greater than the direct radiative forcing caused by tropospheric ozone itself (Sitch et al., 2007).

The reduction in the rate of photosynthesis as a result of ozone exposure can also feedback to atmospheric composition through changes in isoprene emissions due to the strong link between the rates of the 2 processes (Arneth et al., 2007; Niinemets et al., 1999; Pacifico et al., 2011). Present understanding of the impact of elevated atmospheric ozone concentrations on isoprene emissions is highly uncertain with recent studies only quantifying the effect on a limited number of plant species with contrasting results (Calfapietra et al., 2008; Pinelli and Tricoli, 2004; Tiiva et al., 2007; Velikova et al., 2005). During ozone fumigation experiments isoprene emissions were observed to decrease for *P. tremuloides* (Aspen) (Calfapietra et al., 2008) and *Q. pubescens* (Downy Oak) (Velikova et al., 2005) under high atmospheric ozone concentrations. However Pinelli and Tricoli (2004) showed that emissions from *Q. pubescens* were in fact stimulated under intermediate ozone exposure (190 ppbv as opposed to 300 ppbv under high ozone concentrations) and Tiiva et al. (2007) showed that elevated ozone concentrations had zero statistically significant effects on isoprene emissions from a boreal peatland. It should be noted however that in these studies the ozone concentrations the plants were exposed to were much higher than standard ambient concentrations at surface level typically found in the atmosphere. These studies are also only based upon certain plant species on local to regional scales. No study has attempted to quantify the impact of ozone damage on isoprene emissions on a global and continental scale and the subsequent feedback on tropospheric ozone concentrations.

Isoprene has also been shown to prevent visible damage to vegetation caused by exposure to ozone (Loreto et al., 2001; Loreto and Velikova, 2001) and therefore the emission of isoprene by a plant could indicate resistance to ozone damage (Sharkey et al., 2007). This prevention of visible leaf damage is shown in Figure 2.4 by the leaves marked in panel 2 which were fumigated with air containing 3 ppmv of isoprene in addition to 300 ppbv of ozone. For the tobacco leaf, the lesions on the leaf surface are no longer evident with the presence of isoprene and for Birch the area of the leaf that appears bleached is significantly

less than on the leaf fumigated with ozone alone. Isoprene can also prevent measurable losses in photosynthetic capacity by ozone and other reactive oxygen species (Affek and Yakir, 2002; Penuelas and Llusia, 2002; Penuelas et al., 2005; Velikova et al., 2004) and therefore it has been indicated that isoprene emissions may be stimulated by enhanced ozone concentrations due to this potential defence mechanism.

2.6 Current treatment of ozone damage in atmospheric models

As discussed in Section 2.5.1, in order to understand the ozone budget it is necessary to represent the individual processes controlling the main budget terms as consistently and accurately as possible. This is particularly important to consider when using atmospheric models to simulate the evolution of ozone, its budget and those of other trace species in past, present and future climates. Figure 2.5 summarises the main interactions and feedbacks between tropospheric ozone, the biosphere and the climate system indicating that the links between ozone and the biosphere currently have high levels of uncertainty associated with them and are often highly parametrised in both CTM and coupled chemistry-climate models.

The dry deposition of ozone to vegetated surfaces through the stomata has been modelled for individual plant species to quantify the rate of ozone uptake (Emberson et al., 2000; Karlsson et al., 2004) and is currently included in atmospheric models (Giannakopoulos et al., 1999; Smith et al., 2000). However, these processes are often scaled up from individual plant level to canopy level and over broad vegetation categories rather than individual species. This can introduce uncertainty into the estimates of the rate of dry deposition to the biosphere (Figure 2.5). The current generation of global climate models however do not take into account the effects of ozone damage and the resultant feedbacks on tropospheric ozone concentrations through impacts on dry deposition processes and isoprene emissions due to the effects of ozone damage on photosynthesis.

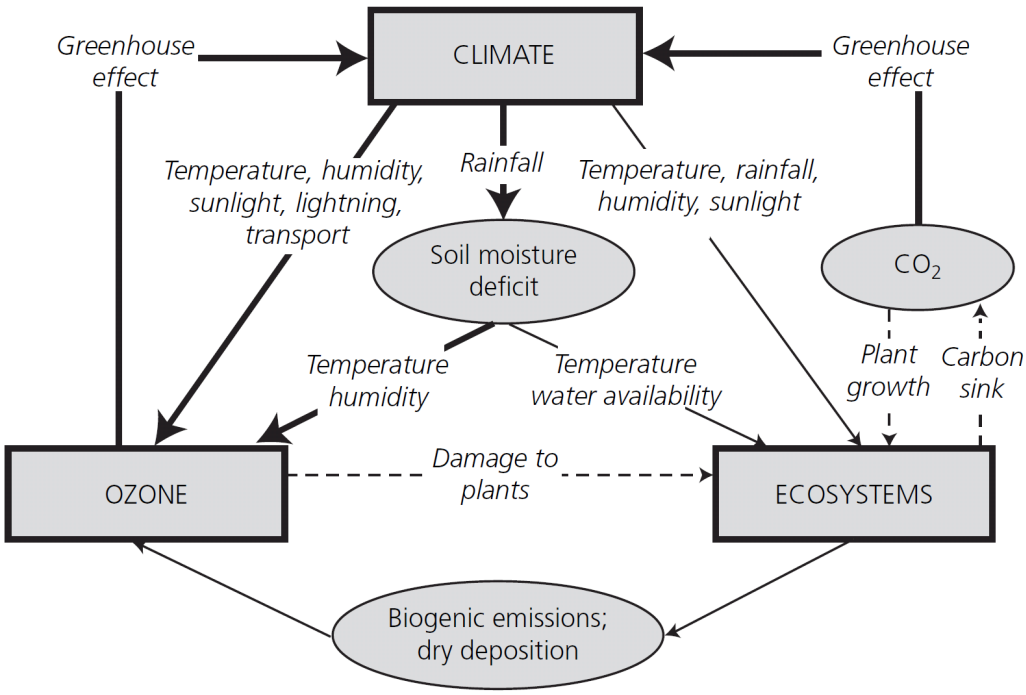

FIGURE 2.5: Interactions between tropospheric ozone, the biosphere (ecosystems) and the climate system. Thick solid lines indicate processes that are well understood and represented in CTM and coupled chemistry-climate models. Thin solid lines show processes that are understood but for which uncertainties exist and are only partially represented in models and are often highly parametrised. Thin dashed lines indicate links that are recognised as important but are not generally included in models. Taken from Fowler et al. (2008)

2.7 Recent modelling studies of the effects of ozone damage

2.7.1 Impact of ozone damage on climate through land-carbon sink

A recent study by Sitch et al. (2007) modelled the indirect radiative forcing of climate change through the effects of ozone damage on the land carbon sink. This study employed a flux based approach to modelling ozone damage and implemented an empirical relationship between the rate of photosynthesis and stomatal conductance. The mechanistic approach employed assumes a suppression of net leaf photosynthesis that varies proportionally to the stomatal flux when it is over a critical threshold. This threshold depends on the sensitivity of the plants to ozone damage. The scheme adopted by Sitch et al. (2007) also allows the complex interactions between the effects of both CO_2 and ozone on stomatal uptake to be modelled. This scheme was then implemented into the MOSES-TRIFFID (Met Office Surface Exchange Scheme – Top-Down Representation of Interactive Foliage

and Flora Including Dynamics) land surface scheme. In this study, the STOCHEM model was used to generate ozone distributions for past, present and future climates with the future ozone projections following the Intergovernmental Panel on Climate Change (IPCC) Special Report on Emissions Scenarios (SRES) A2 scenario. These ozone fields were then used to drive the modified MOSES-TRIFFID land scheme offline to simulate the effects of ozone damage on climate through feedbacks on the land carbon sink.

During the course of the time period 1900–2100 surface ozone concentration increases were estimated to reduce land-carbon storage storage accumulation by between 143 PgC and 263 PgC. The associated radiative forcing by 2100 due to the resultant build up in atmospheric CO_2 concentrations was estimated to be 0.62 Wm^{-2} and 1.09 Wm^{-2} for the low and high plant sensitivity runs respectively. This so called indirect radiative forcing due to increases in ozone is greater than the direct radiative forcing ozone is predicted to cause by 2100 in its role as a greenhouse gas (0.89 Wm^{-2}). This study however did not consider the impacts of ozone damage on the dry deposition of other trace gases such as ozone itself and the subsequent feedbacks on atmospheric composition and chemistry.

2.7.2 Modelling photosynthesis and transpiration responses to ozone damage

Another recent study by Lombardozzi et al. (2012) has drawn attention to the possibility that photosynthesis and stomatal conductance may not be as tightly correlated as previously thought particularly under chronic ozone exposure. Lombardozzi et al. (2012) presents results from a land model modified to account for this potential decoupling. The land surface model was run offline with exposure of vegetation to a constant ambient ozone concentration of 100 ppbv. The results presented by Lombardozzi et al. (2012) suggest that modifying the stomatal conductance directly rather than indirectly through the impact of ozone damage on photosynthesis acts to reduce the effect of ozone exposure on gross primary productivity (GPP) and transpiration processes. This could therefore indicate higher stomatal conductances under chronic ozone exposure than predicted using the scheme used by Sitch et al. (2007). However, the results presented by Lombardozzi et al. (2012) have only been modelled for a single plant type (tulip poplar) whereas the simulations preformed by Sitch et al. (2007) were evaluated against and broadly agreed with observations from the Aspen free air CO_2 enrichment (FACE) experiments covering

the 5 plant functional types (PFTs) in the MOSES-TRIFFID land surface model. Both studies however concluded that the predicted responses of plants to ozone exposure is higher in the tropics than the mid-latitude regions suggesting higher sensitivity in these regions to small changes in surface ozone concentrations.

2.8 Summary

This Chapter has provided an overview of the present understanding of the key interactions between the biosphere and tropospheric ozone highlighting the key role that these interactions play in both the tropospheric ozone budget and the overall climate system. It has long been established that ozone damage to vegetation plays a key role in affecting the exchange of trace gases with potentially many important air quality and climate feedbacks. As well as resulting in direct damage to plant tissue the effects of ozone exposure can also lead to inhibition of photosynthesis which can reduce the amount of CO_2 locked up in the land carbon sink (Sitch et al., 2007). In addition to this, the reduction in photosynthesis can lead to reduced stomatal uptake by plants leading to a reduction in the dry deposition of ozone and its precursor species setting up a potential positive feedback loop. Reduced rates of photosynthesis can also potentially affect isoprene emissions which plays a key role in tropospheric chemistry (Pacifico et al., 2009). Finally, the associated reduction in stomatal uptake can also limit evapotranspiration processes and surface run off resulting in potential climate impacts through the hydrological cycle (Lombardozzi et al., 2012).

These processes are however not currently represented in atmospheric models and no previous work has quantified the impact of ozone vegetation damage on reactive trace gas deposition and the subsequent feedback on atmospheric ozone concentrations. Therefore further work is required to investigate the impact of including these ozone damage parametrisations in the current generation of models in order to gain a better understanding of these effects on local, regional and global scales. There are also large uncertainties associated with the representation of biosphere-atmosphere processes in atmospheric models that play a key role in the ozone budget (e.g. The uncertainty in BVOC emissions lies in the range 400-600 Tg yr^{-1} (Pacifico et al., 2009) and the uncertainty in dry deposition lies in the range 647-1157 Tg O_3 yr^{-1} (Wild, 2007)). This points towards the need of better observational data of these processes in order to constrain them and limit the

uncertainty associated with their representation in models. As highlighted by Wild (2007) observational constraints of the key ozone budget terms is currently very poor with limited spatial and temporal coverage, and of the budget terms only influx of ozone from the stratosphere has been adequately estimated from observations. In this thesis, these processes will be investigated using both the TOMCAT chemical transport model (CTM) and the HadGEM2-ES Earth system (ES) model which are described in detail in Chapter 3.

Chapter 3

Model Description and Evaluation

3.1 Introduction

This chapter provides a full description of both the TOMCAT chemical transport model (CTM) and the HadGEM2-ES Earth System (ES) model and how they will be used to perform the model runs in this thesis. The first part gives an overview of the dynamics, advection and chemistry schemes used by each model, including a detailed description of the new ozone damage (OzDAM) scheme in HadGEM2-ES. The second part addresses the implementation of an updated dry deposition scheme into TOMCAT. Finally, the last part of this chapter addresses the evaluation of both models with observational data.

3.2 The TOMCAT chemical transport model (CTM)

TOMCAT is a global 3D CTM that is forced using meteorological data from the European Center for Medium Range Weather Forecasts (ECMWF) and uses detailed advection and chemistry schemes to model past or present atmospheres. The model is used to simulate both tropospheric and stratospheric chemistry and is described in detail by Chipperfield (2006).

3.2.1 Horizontal model grid

As described in Chipperfield (2006), the horizontal model grid size in TOMCAT is not fixed and can be variable in nature, which is usually determined by available computer resources. The grid is Eulerian in nature and extends from pole to pole, with regular spacing in the longitudinal direction and irregular spacing in the latitudinal direction. The ECMWF analyses are generally read in as spectral coefficients and are then converted to grid-point fields by a spectral transform which can be done onto any prescribed latitudinal grid using pre-tabulated integrals of the associated Legendre functions (Chipperfield, 2006). This means that the model is not restricted to the usual Gaussian latitudes. For the model runs performed in this thesis, the TOMCAT CTM will be run at T42 resolution with 128 grid cells in the longitude direction and 64 grid cells in the latitude direction. This equates to an approximate spacing of 2.8 degrees between the centre of each each grid box.

3.2.2 Model vertical coordinates

The TOMCAT CTM defines its vertical grid using hybrid σ-p levels defined by Equation 3.1. The model levels follow the terrain near the surface (σ) and follow pure pressure levels at higher altitudes in the atmosphere, typically above approximately 100 hPa.

$$p_{\mathrm{k}+\frac{1}{2}} = Ap_0 + Bp_{\mathrm{s}} \tag{3.1}$$

In Equation 3.1, k is the model level, p_0 is the reference pressure (10^5 pa), p_{s} is the surface pressure and A and B are altitude varying coefficients used to define p levels. The model has 31 p levels covering the entire troposphere and the lower parts of the stratosphere up to a pressure of 10 hPa.

3.2.3 Model advection schemes

TOMCAT uses the conservation of second-order moments advection scheme (Prather, 1986) which aims to provide the most accurate transport of tracer species around the

model domain, whilst providing the compromise on all of the desired properties of conservation, monotonicity, low numerical diffusion and low dispersion (Chipperfield, 2006). Another important consideration is that the advection scheme should preserve tracer-tracer correlations and total family abundances, i.e. the advection should not be specific to any one tracer species.

Chipperfield (2006) highlights that this Eulerian finite volume is used separately for advection in the x, y and z directions based on mass fluxes averaged over the interfaces of the model grid. Advantage of this scheme include that is has exact mass conservation and low numerical diffusion however disadvantages include that it is not monotonic (of an ordered system of sets).

3.2.4 Model boundary layer mixing schemes

TOMCAT has the option of parametrizing vertical turbulent mixing in the planetary boundary layer (PBL) using two different schemes. The first is a local first order approach where the diffusion coefficient is calculated from the Richardson number (Louis, 1979). This provides a reasonable representation of vertical PBL mixing in a neutral or relatively stable boundary layer. However as discussed by Wang et al. (1999), for an unstable and convective boundary layer the vertical scale of the largest turbulent eddies are similar to the depth of the PBL itself. This leads to the development of counter gradient transport in the PBL and results in large-eddy motion that has a strong non-local character which depends on parameters including surface heat flux, surface temperature and surface constituent flux (Holstag and Boville, 1993). This nonlocal nature of trace gas transport is not accounted for using a local diffusion scheme (Louis, 1979) and can result in the build up of trace species close to a surface emission source leading to unrealistic surface concentrations (Wang et al., 1999). Additionally, this can result in limited transport of trace species out of the PBL.

The second PBL mixing parametrisation in TOMCAT uses the scheme of Holstag and Boville (1993). The inclusion of this scheme in TOMCAT follows the method of Wang et al. (1999) which describes the implementation of the scheme into a similar CTM. This non-local scheme accounts for counter gradient transport which can develop in an unstable and convective boundary layer. In this non-local scheme, the upward pumping of surface

emitted tracer species is carried out by the coupling between surface heat flux, cloud convection and large scale vertical motion (Wang et al., 1999). As discussed in Chipperfield (2006), the non-local scheme gives much stronger transport out of the PBL than the local scheme and provides tropospheric tracer distributions that provide a better match to observational data. For the model runs performed in this Thesis, TOMCAT is run using the non-local scheme of Holstag and Boville (1993) in order to provide the most accurate representation of the transport of ozone and its precursor species.

3.2.5 Model convection scheme

TOMCAT uses a parametrisation of convection based around a mass-flux scheme (Tiedtke, 1989). This scheme includes cumulus updraughts in the vertical column, the turbulent and organized entrainment of air from the background environment into the cloud domain and finally the organized and turbulent detrainment of air from within the cloud into the background environment. The scheme utilised in TOMCAT is the same as that described by Tiedtke (1989) however includes several key differences as discussed in Stockwell and Chipperfield (1999).

Firstly, mid-level convection and convective downdraughts are not included. Secondly, there is no organized entrainment of environmental air into the cloud domain above the cloud base. Finally, the test for moisture convergence in the TOMCAT scheme (a prerequisite for convection when using the Tiedtke (1989) scheme) is determined differently and only for the subcloud layer which results in a different cloud-base mass-flux calculation from that described by Tiedtke (1989). In addition to the Tiedtke scheme, TOMCAT also includes the subgrid scale subsidence of environmental air (mesoscale downdraughts induced by convection) within the same model timestep in order to maintain mass balance in the vertical column (Stockwell and Chipperfield, 1999).

3.2.6 Chemistry scheme

The TOMCAT tropospheric chemistry scheme includes methane, NO_x, C2-C3 VOCs, isoprene photochemistry, and detailed schemes for gas phase chemistry (Law et al., 1998). A full description of the current chemistry scheme used in the model can be found in Arnold et al. (2005), with the chemical species contained in the standard model chemistry scheme

listed in Table 3.1. The standard chemical scheme in the model represents 23 advected tracer species (individual species or chemical families). Chemical tracer species that are short-lived (e.g. OH) are not advected and are assumed to be in a photochemical steady-state (Arnold et al., 2005). For H_2O the model field is taken from the ECMWF analyses that are used to force the model.

TABLE 3.1: Chemical Species in the standard TOMCAT CTM chemistry scheme[a]

Category	Species
Shorter-lived species	O_x(= O_3 + $O(^3P)$ + $O(^1D)$), H_2O_2, NO_x(= NO + NO_2), NO_3, N_2O_5, HNO_3, HO_2NO_2, HONO, $MeCO_3NO_2$, $EtCO_3NO_2$, $MeONO_2$, HCHO, MeOOH, MECHO, Me_2CO, C_2H_6, EtOOH, EtCHO, C_3H_8, n-PrOOH, i-PrOOH
Steady-state	OH, HO_2, MeO_2, EtO_2, $MeCO_3$, $EtCO_3$, n-PrOO, i-PrOO, $MeCOCH_2OO$, $MeCOCH_2OOH$
Source gases	CH_4, CO
Fixed	O_2, N_2, H_2, CO_2
Analyses	H_2O

[a] Me = CH_3, Et = C_2H_5, Pr = C_3H_7

Time-dependent chemical rate equations are solved using the ASAD atmospheric chemistry integration package (Carver et al., 1997). This self-contained chemistry package and reaction database allows the use of chemical families which reduces the number of tracers that need to be transported in the model thus permitting the use of less costly integration packages in terms of computer resources required. This also reduces the stiffness of chemical equations and has the advantage of reducing the amount of computing resources required at each model timestep for the integration of tropospheric chemistry.

In addition to the standard TOMCAT chemistry scheme, the version used to perform the model experiments in this thesis contains additional chemical tracer species and chemical reactions from the Mainz Isoprene Mechanism (MIM) described by Poschl et al. (2000).

The MIM utilizes 16 organic species and 44 chemical reactions with the majority of the reactions comprising combinations of the major reactions of the Master Chemical Mechanism (MCM) by Jenkin et al. (1997). This allows TOMCAT to represent the chemistry of isoprene, its oxidation products and the related photooxidants, of which a number play an important role in the ozone budget. The MIM species are shown in Table 3.2. Poschl et al. (2000) showed that for a variety of key atmospheric tracers (including O_3, OH, CO, CH_3O_2H, and PAN) the MIM was able to produce a good approximation (within 10%) of the MCM in a box model intercomparison. Therefore the inclusion of the MIM in TOMCAT allows the quantification of the effects of isoprene on key tracer species such as ozone by reducing the uncertainty associated with the strongly condensed and simplified mechanisms that are usually utilised in 3D global modelling studies.

TABLE 3.2: Species in the MIM (Poschl et al., 2000)

	Chemical Formula	Species
	C_5 compounds	
1	C_5H_8	isoprene
2	ISO_2	peroxy radicals from C_5H_8 + OH
3	ISO_2H	β-hydroxyhydroperoxides from ISO_2 + HO_2
4	ISON	β-hydroxyalkylnitrates from ISO_2 + NO and alkylnitrates from C_5H_8 + NO_3
	C_4 compounds	
5	MACR	methacrolein, methylvinylketone and other C_4 carbonyls
6	$MACRO_2$	peroxy radicals from MACR + OH
7	$MACRO_2H$	hydroperoxides from $MACRO_2$ + HO_2
8	MPAN	peroxymethacryloynitrate and other higher peroxyacylnitrates
	C_3compounds	
9	HACET	hydroxyacetone and other C_3 ketones
10	MGLY	methylglyoxal and other C_3 aldehydes
	C_2 and C_1 compounds	
11	CH_3CO_3	peroxyacetyl radical
12	PAN	peroxyacetylnitrate
13	CH_3CO_3H	peroxyacetic acid
14	CH_3COOH	acetic acid
15	NALD	nitrooxyacetaldehye
16	HCOOH	formic acid

For photolysis rates TOMCAT makes use of the scheme of Hough (1988). This code utilizes 203 wavelength bins from 121 nm to 850 nm with the photolysis rates calculated at each model timestep using model profiles of temperature and ozone in the calculation of

cross sections, quantum yields, and solar flux, where appropriate (Arnold et al., 2005). A climatological cloud field is also specified for the photolysis calculations. This field varies on a seasonal basis and provides the photolysis scheme with percentage cloud coverage of low, medium and high level clouds along with the heights of the cloud tops and bottom for each cloud type in each model grid box.

3.2.7 Wet and dry deposition

Wet and dry deposition processes are important sink pathways for several trace gases and aerosols in the troposphere, particularly ozone and its precursor species. Dry deposition is a complex process that depends upon the meteorological conditions near the surface, the physical and chemical characteristics of the chemical species being deposited and finally the nature of the surface the species are being deposited upon. TOMCAT utilises the simple dry deposition scheme described by Giannakopoulos et al. (1999) which assumes that the rate of deposition r_{d} can be expressed as a function of the dry deposition velocity V_{d} as follows:

$$r_{\mathrm{d}} = \frac{V_{\mathrm{d}}}{H}, \tag{3.2}$$

where H is the height of the lowest model level. The current dry deposition scheme in TOMCAT accounts for 37 tracer species (Table 3.3), including ozone and its major precursors. The dry deposition velocity at 1 m height is determined for each model grid cell based upon the underlying surface type (of which there are 4 categories: Forest, grass/shrub/crop, water and ice), the local time of day and the local season. Roughness length is used to classify land into each category with the exception of ice which is determined using a simple seasonal parametrisation. The dry deposition velocity is then obtained from a look up table based upon these characteristics.

In order to simulate the process of dry deposition loss, a parametrization is employed to extrapolate the dry deposition velocities from 1 m height to the middle of the lowest model grid box. This parametrization is described by Bernsten and Isaksen (1997) and performs

TABLE 3.3: TOMCAT CTM dry deposited tracer species [a]

Category	Species
Shorter-lived species	O_3, NO, NO_2, NO_3, N_2O_5, HO_2NO_2, HNO_3, H_2O_2, HCHO, MeOOH, HONO, EtOOH, Me_2CO, MeCHO, n-PrOOH, i-PrOOH, EtCHO, O_3S, NO_xS, HNO_3S, NO_yS, MeOH
Steady-state	$MeCOCH_2OOH$
Source gases	CO
MIM species	ISO_2H, ISON, MACR, $MACRO_2H$, HACET, MGLY, NALD, HCOOH, $MeCO_3H$, $MeCO_2H$, PAN, PPAN, MPAN

[a] Me = CH_3, Et = C_2H_5, Pr = C_3H_7

the extrapolation using the vertical diffusion coefficient calculated in the model boundary layer scheme. The formula of Bernsten and Isaksen (1997) is as follows:

$$V_{\mathrm{d}}(z_2) = V_{\mathrm{d}}(z_1)\frac{1}{1+\frac{V_{\mathrm{d}}(z_1)}{DC}} \tag{3.3}$$

In Equation 3.3 $V_{\mathrm{d}}(z_2)$ is the dry deposition velocity at the mid point of the lowest model layer, $V_{\mathrm{d}}(z_1)$ is the dry deposition velocity at 1 m height and DC is the vertical diffusion coefficient at the lowest model layer in m^2s^{-1}. The value of DC depends upon the wind velocity, surface roughness and the stability of the boundary layer, therefore its variation with season and time of day can provide significant variation in the calculation of $V_{\mathrm{d}}(z_2)$. This can impact the dry deposition lifetimes of tracer and aerosol species.

For wet deposition the model utilizes the scheme described by Giannakopoulos et al. (1999) which links the removal frequency of the wet deposited species to the profile of specific humidity. The episodic removal of species is also taken into account by the inclusion of a storm cycle. As described by Giorgi and Chameides (1985) this cycle is a modified first-order rainout parametrization that is a function of the species' solubility and takes

into account the intermittent nature of atmospheric wet removal. The model accounts for convective precipitation using the scheme of Tiedtke (1989). Effective Henry's law coefficients H_{eff} are read into the model for each wet deposited species (Table 3.4).

TABLE 3.4: TOMCAT CTM wet deposited tracer species [a]

Category	Species
Shorter-lived species	H_2O_2, NO_3, N_2O_5, HNO_3, HO_2NO_2, HONO, HCHO, MeOOH, EtOOH, n-PrOOH, i-PrOOH, HNO_3S, NO_yS, MeOH
Steady-state	HO_2, MeO_2, $MeCOCH_2OOH$
MIM species	ISO_2H, ISON, $MACRO_2H$, HACET, MGLY, HCOOH, $MeCO_3H$, $MeCO_2H$

[a] Me = CH_3, Et = C_2H_5, Pr = C_3H_7

3.2.8 Emissions

Anthropogenic emissions of carbon monoxide, methane, NO_x formaldehyde and hydrocarbons are prescribed using the IPCC AR5 emissions set for the year 2000 (Lamarque et al., 2010). Biomass burning emissions are obtained from the Global Fire Emissions Database version 2 (GFED2) described by van der Werf et al. (2006) as climatological monthly means. In addition biogenic emissions are taken from the POET (Precursors of Ozone and their Effects in the Troposphere) database, used as described by Emmons et al. (2010). TOMCAT also calculates NO_x emissions from lightning sources (Stockwell et al., 1999). Finally, biogenic isoprene emissions are included from Guenther et al. (1995). The emissions of the key tracer species are prescribed as monthly means on a 1° x 1° emissions grid. Table 3.5 shows the mean annual emissions of the tracer species emitted used by TOMCAT.

TABLE 3.5: TOMCAT annual total emissions fluxes

Species	Emissions ($Tgyr^{-1}$)
CO	1207
CH_4	301[a]
NO_x	141
CH_3CHO	6.8
CH_3COCH_3	32
HCHO	9.0
CH_3OH	31
C_2H_2	4.8
C_2H_4	18
C_2H_6	7.2
C_3H_8	7.2
C_5H_8	570.1

[a] CH_4 emissions total is for anthropogenic sources only.

3.3 The HadGEM2 Earth System model

The HadGEM2 (Hadley Centre Global Environment Model version 2) Earth System (ES) model is a coupled general circulation model (GCM) that couples together atmospheric and oceanic processes along with interactions of these processes with the Earth's surface, to simulate and understand the evolution of climate. This understanding includes biogeochemical feedbacks between the biosphere, the atmosphere and the ocean. Unlike CTMs, GCMs derive their own meteorological fields online using a series of physical and dynamical equations to determine model dynamics and the water cycle. As described by Jones et al. (2011), HadGEM2-ES represents interactive land and ocean carbon cycles along with an interactive tropospheric chemistry scheme which simulates the evolution of atmospheric composition and the interaction of trace gas species with each other and atmospheric aerosols. For the purposes of this thesis, the HadGEM2-ES model is run in the atmosphere only configuration (HadGEM2-A) which decouples the ocean processes from the atmospheric component.

HadGEM-ES includes the fully interactive United Kingdom Chemistry and Aerosols scheme (UKCA). The model fields that would normally come from the ocean model are supplied in the form of mean climatological variables. The land surface and hydrology schemes also include exchange processes with the atmosphere allowing changing atmospheric composition to feedback on the interaction of trace gases with vegetated surfaces and the resultant

effect this has on the underlying vegetation. This also allows the feedbacks of a changing land surface on atmospheric composition to be quantified. The following sections of this chapter provide an overview of the key model components that are investigated in this thesis (Collins et al., 2011; Jones et al., 2011; Martin et al., 2011).

3.3.1 Horizontal and vertical coordinates

The horizontal grid for the atmospheric component of HadGEM2 is based upon the underlying physical model in the predecessor climate model HadGEM1 as described by Jones et al. (2011). The horizontal grid in the atmospheric component of HadGEM2 has a resolution of 1.25° in the latitude and 1.875° in the longitude direction, termed as N96 resolution. As discussed by Pope and Stratton (2002), this higher horizontal resolution has been shown to improve some aspects of the model's climatology as well as improving the model's ability to resolve smaller scale features and its representation of dynamics.

For the model vertical grid of HadGEM2's atmospheric component, a Charney-Phillips vertical grid is utilized (Martin et al., 2006). The model has 38 vertical levels which extend from the surface up to an altitude of approximately 39 km which encompasses the entirety of the troposphere and the lower portion of the stratosphere. The Charney-Phillips vertical grid is a hybrid height grid which represents the true height above a surface at mean sea level. The boundary heights of each model level depend on the surface orographic height for the first 29 levels and then follow a constant real height above this (Martin et al., 2006). This results in an approximate resolution of 100 m in the lowest 2.5 km of the atmosphere with this falling to around 1 km in the upper troposphere.

3.3.2 Underlying ocean model

As an Earth system model, HadGEM2-ES also has an underlying ocean model that can be fully coupled to the atmospheric model allowing oceanic and atmospheric processes to interact and feedback on one another. This ocean model provides sea surface temperature and sea ice fields to the atmospheric component as well as the ocean component of the carbon cycle. The ocean model also provides the emissions of di-methyl sulphide (DMS) from phytoplankton. As described briefly by Collins et al. (2011), the ocean model has a latitude-longitude grid with a zonal resolution of 1° everywhere and a meridional resolution

of 1° between the poles and 30° latitude, which increases smoothly up to 1/3° at the equator. The ocean model has 40 vertical levels which are not evenly spaced. In the HadGEM2-A configuration of the model, the ocean component is switched off and the required carbon cycle, sea surface temperature, sea ice and DMS emissions fields are read in as climatological monthly means from ancillary files.

3.3.3 HadGEM2 model advection scheme

For the advection of all prognostic variables with the exception of density, HadGEM2 makes use of a semi-implicit semi-Langrangian time integration scheme (Davies et al., 2005). These SLT schemes are advantageous as they can be used in high resolution models without the need of a very short model time step. In order to overcome the non-conservative nature of SLT schemes, which is considered important in longer climate model runs, the continuity equation is treated using a semi-implicit Eurlerian scheme (Johns et al., 2006) along with the application of the conservation constraint of Priestley (1993) in SLT advection. This ensures dry mass conservation and improves tracer species conservation.

3.3.4 UKCA chemistry scheme

The version of HadGEM2 used in this thesis makes use of the extended chemistry version of the UK Community Chemistry and Aerosol (UKCA) scheme which features approximately 300 chemical reactions and accounts for 83 chemical species. The scheme includes tropospheric CH_4-NO_x-CO-O_3 chemistry (O'Connor et al., 2011) which is representative of the tropospheric background. The scheme also includes simplified isoprene reactions (Folberth et al., 2006) which are based around the Mainz Isoprene Mechanism (as described in section 3.2.6). The scheme in its implementation of non-methane hydrocarbons (NMHC), takes into account the photochemical oxidation pathways of NMHCs and non-methane volatile organic compounds (NMVOC) from both anthropogenic and natural sources along with their photochemical oxidation products (Folberth et al., 2006).

The emissions of chemical species from all anthropogenic sources and the majority of natural sources are provided to UKCA as external forcing fields (Jones et al., 2011). UKCA however runs interactively with the large scale hydrology scheme used in HadGEM2

in order to obtain methane emissions from wetlands (Collins et al., 2011) with biogenic emission of isoprene, a lumped monoterpene species, acetone and methanol provided online by an interactive BVOC emissions model (as described in section 3.3.7.2). Interactive NO_x emissions from lightning are also included in UKCA and are calculated based upon the scheme of Price and Rind (1993). Ozone concentrations in the stratosphere are prescribed according to climatology from the CMIP5 database as the version of UKCA used does not account for halogen chemistry that is relevant to the stratosphere (Collins et al., 2011).

The interactive gas-phase chemistry of UKCA provides the model aerosol scheme with oxidants (HO_2, H_2O_2 and O_3) and nitric acid (HNO_3) which results in the depletion of H_2O_2 and HNO_3 from the gas phase. The interactive nature of UKCA also has the advantage of allowing the feedback of three dimensional ozone and methane fields to the model radiation scheme permitting the modelling of the radiative feedbacks of changes in these tracer species. In previous models the methane field had been implemented into the radiation scheme as a single value over the whole globe and at all model altitudes (Collins et al., 2011). The CLASSIC aerosol scheme is used (Bellouin et al., 2011), which is a mass based aerosol scheme with natural (dust, sea salt and secondary organic aerosol) and anthropogenic (sulphate and black and organic carbon from fossil fuels) and biomass burning emissions.

The UKCA chemistry scheme utilises the offline Cambridge 2D-photolysis model (Law and Pyle, 1993a,b) which is based on the two-streamed approach of Hough (1988) (Section 3.2.6). Photolysis rates are pre-calculated offline and then read in by UKCA and interpolated in space and time at each model grid box (with no variability with clouds and aerosols). The extended UKCA chemistry scheme includes 45 photolysis reactions. For certain reactions (e.g. in the case of organic hydroperoxides) a scaled photolysis rate is used rather than the pre-calculated rate. Finally the model makes use of an interactive dry deposition scheme which is based upon the resistance analogy derived by Wesely (1989) (Section 3.3.6).

3.3.5 Land surface exchange scheme

The land surface exchange scheme in HadGEM2 is the Met Office Surface Exchange Scheme version II (MOSES II (Essery et al., 2003)) which calculates the exchange of heat, moisture,

momentum and CO_2 between the land surface and the atmosphere. These fluxes are important to consider in global climate models as they govern the exchange of water and carbon between the biosphere and the atmosphere. Variations in these fluxes can also result in changes to vegetation stomatal conductance which itself is important in controlling the exchange of trace gases (including ozone and its precursor species) with the atmosphere.

In HadGEM2, the MOSES II scheme complements the Top-Down Representation of Interactive Foliage and Flora Including Dynamics (TRIFFID) vegetation dynamics model (Cox, 2001; Cox et al., 2000). The land surface classification in each gridbox is represented as a combination of the coverage of TRIFFID's 5 vegetation categories (broadleaf tree, needleleaf tree, C3 grasses, C4 grasses and shrubs) known as plant functional types (PFTs) and 4 non-vegetation categories (urban, inland water, soil and ice). Vegetation coverage can either be modelled using TRIFFID or can be prescribed from offline datasets. In this Thesis, the model land cover is prescribed from a dataset representative of historical changes in land use as processed for the CMIP5 (Hurtt et al., 2011). This data was derived from the present-day climatology IGBP dataset (Loveland et al., 2000) and reconstructions of anthropogenic land-use from the HYDE3 dataset (Klein Goldewijk et al., 2010). This provides coverage from the pre-industrial period through to the present day.

Leaf phenology is modelled on a daily basis using TRIFFID (Cox, 2001) which determines the evolution of leaf area index (LAI) for each vegetation PFT. The canopy height, roughness length and canopy water capacity are parametrised based upon LAI (Essery et al., 2001). The canopy conductance of each PFT type is calculated based upon temperature, incoming solar radiation, soil moisture availability, humidity deficit, CO_2 concentration and vegetation type and is calculated online using a photosynthesis model (Cox, 2001; Cox et al., 1998). The ability of plants to access moisture at each model soil level, is determined by a root density distribution which varies exponentially with depth (Thornley and Johnson, 1990). The canopy conductance controls the rate of evapotranspiration from vegetation as well as playing an important role in driving the rate of dry deposition of trace species to the land surface (Section 3.3.6).

3.3.6 Dry deposition in HadGEM2

For the treatment of dry deposition of tracer species in HadGEM2, the UKCA scheme uses an adaptation of the Wesely (1989) dry deposition scheme which has been previously implemented into the STOCHEM model as described by Sanderson et al. (2006). The dry deposition fluxes for gas phase species and aerosols are calculated using the a 'big leaf' model (Smith et al., 2000) which uses a multiple resistance analogy to quantify the 3 main phases of the dry deposition process. As described in Chapter 2, Section 2.5.1, the 3 resistances to uptake to a given surface are the aerodynamic resistance (r_{a}), the quasi-laminar boundary layer resistance (r_{b}) and the surface resistance (r_{c}).

The dry deposition $D_{\mathrm{g}}(z)$ flux of a tracer species from a fixed height in the atmosphere, z, is a product of the gas concentration at that height ($\chi(z)$) and the deposition velocity of the given species to the underlying surface ($V_{\mathrm{g}}(z)$).

$$D_{\mathrm{g}}(z) = \chi(z) V_{\mathrm{g}}(z) \tag{3.4}$$

Equation 3.4 assumes that the gas concentration at the level of the absorbing surface is zero and that the deposition velocity of the tracer species is independent of its atmospheric concentration. The deposition velocity itself depends upon the aerodynamic resistance in the boundary layer near to the absorbing surface ($r_{\mathrm{a}}(z)$, which varies with height and depends upon the wind velocity and aerodynamic roughness of the surface (Smith et al., 2000)), the quasi-laminar boundary layer resistance (r_{b}) and the bulk canopy resistance ((r_{c}), which depends upon the chemical and physical properties of the underlying surface). These resistances are treated in series with the deposition velocity being equal to the reciprocal of the total resistance.

$$V_{\mathrm{g}}(z) = \frac{1}{r_{\mathrm{a}}(z) + r_{\mathrm{b}} + r_{\mathrm{c}}} \tag{3.5}$$

If the underlying surface type is vegetation, the r_c term is a combination of the resistances of potential pathways of trace species uptake by the vegetation type. These include, the uptake of gases through the tiny pores in the leaves (stomata), the uptake through the leaf surface or cuticles and the uptake through the soil. For species such as ozone and SO_2 the bulk canopy resistance is calculated as the combination of the resistances to the above pathways in parallel (Equation 3.6).

$$r_c = \frac{1}{1/r_{\text{stomata}} + 1/r_{\text{leafsurface}} + 1/r_{\text{soil}}} \tag{3.6}$$

This bulk resistance term also varies according to the tracer species being deposited and its nature of uptake by vegetation. For example, for the deposition of NO_2, the uptake through the stomata is the dominant sink pathway, leading to the bulk surface resistance being equated to the stomatal resistance. For certain species that are not readily deposited to vegetation such as HNO_3, the bulk canopy resistance term is assumed to be zero (Smith et al., 2000). In HadGEM2-ES the following species are dry deposited to vegetation through the stomatal pathway: ozone, NO_2, PAN, PPAN, MPAN, ONITU, SO_2 and NH_3.

3.3.7 Ozone damage and interactive BVOC code in HadGEM2

In addition to the standard interactive dry deposition scheme in HadGEM2, the version used in this thesis had the effect of ozone damage on the stomatal conductance of vegetation incorporated into the dry deposition scheme of UKCA in the HadGEM2 GCM. As discussed by Ashmore (2005) and Sitch et al. (2007), ozone causes visible leaf injury and plant damage leading to the reduction in crop quality and yields, particularly when the surface ozone concentration is greater than 40 ppbv. As discussed in Chapter 2, the representation of the interactions between the impact of ozone on plants and the resultant feedbacks on ozone deposition and the carbon cycle are not presently accounted for in global climate models, with few global modelling studies assessing the impact of tropospheric ozone on plant production and global land carbon storage (Felzer et al., 2005). Sitch et al. (2007) highlighted the importance of including this effect of ozone damage

on the stomatal uptake of trace gas species to quantify the indirect radiative forcing impact of elevated surface ozone concentrations on climate change through the land carbon sink. This study showed that the inclusion of ozone damage effects on vegetation could potentially double the effective radiative forcing due to increases in tropospheric ozone. Therefore it is important to consider the parametrisations developed by Sitch et al. (2007) in the HadGEM2 model used in this thesis and investigate the potential impacts of ozone damage on atmospheric composition and the resultant feedbacks on air quality and climate. Adapting this scheme for use in HadGEM2 was done by Dr. Gerd Folberth and Professor Stephen Sitch. The quantification of the impacts of ozone damage on reactive trace gas deposition and isoprene emissions and the feedbacks on atmospheric composition was done as part of this thesis and the first results are discussed in Chapter 6.

In addition to the inclusion of the ozone damage parametrisations in HadGEM2, the model is run with an interactive BVOC (iBVOC) emissions scheme (Pacifico et al., 2011) in order to calculate online biogenic emissions of isoprene, a lumped monoterpene species, acetone and methanol. This scheme yields total global emissions of 431.6 $\mathrm{TgCyr^{-1}}$ of isoprene, 105.6 $\mathrm{TgCyr^{-1}}$ of monoterpenes, 77.9 $\mathrm{TgCyr^{-1}}$ of methanol and 18.6 $\mathrm{TgCyr^{-1}}$ of acetone when the model is set up for present day conditions. The inclusion of this scheme allows vegetation - atmospheric chemistry interactions and feedbacks to be simulated including the feedback of changing GPP and photosynthesis on isoprene emissions which play an important role in modulating tropospheric ozone and methane (Hofzumahaus et al., 2009).

3.3.7.1 Ozone damage parametrisation

In order to account for the effect of ozone damage on stomatal conductance and the resultant feedbacks on CO_2 uptake by vegetation, photosynthetic processes and net primary production in vegetation, a parametrisation based upon the flux of ozone through the plants' stomata was adopted. This flux-gradient approach was developed by Sitch et al. (2007) and assumes a suppression of net leaf photosynthesis that varies proportionally to the stomatal ozone flux when it is above a critical threshold.

The scheme implements an empirical relationship between stomatal conductance and photosynthesis. This allows the direct effect of ozone damage to be parametrised which accounts for the resultant ozone impact on photosynthesis (Ashmore, 2005) which in itself

can lead to a reduction in stomatal conductance. This is because if the rate of photosynthesis is reduced, the plant will close its stomata as a lower flux of CO_2 and water is required to enter the leaves to sustain the lower rate of photosynthesis. The stomatal conductance of the leaf also provides a feedback to the flux of ozone into the leaf thus completing the feedback loop. Based upon this, the scheme used by Sitch et al. (2007) requires a consistent series of equations that link all of these effects. The scheme adopted here also allows the complex interactions between the effects of CO_2 and ozone uptake on stomatal conductance to be accounted for and thus the impact of an increase in either gas on the other.

Therefore the extent to which higher CO_2 levels can limit stomatal conductance (Gedney et al., 2006) can be accounted for which acts to potentially protect the plant from ozone damage due to a lower ozone flux into the leaves. The opposite effect can also be accounted for with this model in that the damage ozone causes to the plant can act to reduce the stomatal conductance and thus limit the terrestrial uptake of CO_2.

The mechanism derived by Sitch et al. (2007) modifies the net rate of photosynthesis (A_{P}) by applying an ozone uptake or exposure factor (F) which is calculated as follows.

$$A = A_P F \tag{3.7}$$

Where the ozone exposure factor F is determined from Equation 3.8 (Pleijel et al., 2004).

$$F = 1 - aUO_{>FO3crit} \tag{3.8}$$

In Equation 3.8, the ozone exposure factor (F) represents the fractional reduction in plant production, $UO_{>FO3crit}$ represents the instantaneous uptake rate of ozone when the stomatal flux of ozone is over a critical threshold F_{O3crit} which is specific to each PFT type in HadGEM2 (Table 3.6). Finally, the parameter a accounts for the fractional reduction of photosynthesis with ozone uptake by leaves which again is PFT specific and represents the

sensitivity of each PFT type to ozone damage (Table 3.6). These parameters are calibrated in the ozone damage parametrisation using data from open-top chamber experiments based on the exposure of young trees to elevated ozone concentrations (Karlsson et al., 2004). A high and low parametrisation is chosen for each of the five PFT types in HadGEM2-ES (broadleaf tree, needleleaf tree, C3 grass, C4 grass and shrub) to represent species that are sensitive and less sensitive to the effects of ozone exposure (Sitch et al., 2007).

TABLE 3.6: Ozone exposure parameters for the ozone damage effect on stomatal uptake (Sitch et al., 2007)

Parameter	Broadleaf Tree	Needleaf tree	C3 Grass	C4 Grass	Shrub
F_{O3crit}(nmol m^{-2} s^{-1})	1.6	1.6	5.0	5.0	1.6
High a (mmol^{-1} m^{-2})	0.15	0.075	1.40	0.735	0.10
Low a (mmol^{-1} m^{-2})	0.04	0.02	0.25	0.13	0.03

The instantaneous leaf uptake rate of ozone by the leaf is calculated as shown by Equation 3.9 which when combined with Equation 3.8 relates the ozone exposure factor to the flux of ozone into the leaf structure as shown in Equation 3.10.

$$UO_{>FO3crit} = max[(F_{O3} - F_{O3crit}), 0.0] \tag{3.9}$$

$$F = 1 - amax[(F_{O3} - F_{O3crit}), 0.0] \tag{3.10}$$

This critical threshold of ozone stomatal flux for damage takes into account the different responses of various types of vegetation to ozone damage based upon their tolerance to the effects of ozone exposure. The stomatal flux of ozone into the leaf is calculated based upon the molar concentration at reference level (in this case the canopy height of the underlying vegetation), the aerodynamic and boundary layer resistances between the reference height and the leaf surface and the stomatal conductance of ozone (Sitch et al., 2007).

$$F_{O3} = \frac{[O_3]}{R_a + [\frac{\kappa_{O3}}{g_l}]} \tag{3.11}$$

Where F_{O3} is the flux of ozone to the stomata (nmol O_3 m^{-2} s^{-1}), [O_3] is the molar concentration at reference level (nmol m^{-3}), R_a is the aerodynamic and boundary layer resistance between the leaf surface and the reference level (s m^{-1}), g_l is the leaf conductance for H_2O (m s^{-1}) and κ_{O_3} is the ratio of leaf resistance for ozone to the leaf resistance for water vapour ($\kappa_{O_3} = 1.67$).

As the stomatal conductance is a linear function of the net rate of photosynthesis, A, (Cox et al., 1999) the ozone exposure factor (F) can be used to account for the impact of ozone damage on stomatal uptake based on equation 3.7 as follows.

$$g_l = g_p F \tag{3.12}$$

In this case, g_p is the leaf stomatal conductance without the impact of ozone damage. Finally Sitch et al. (2007) used the set of equations 3.10, 3.11 and 3.12 to produce a quadratic in F that can be solved analytically during the model run to parametrise the complex set of feedbacks that result from the ozone damage suffered by vegetation.

3.3.7.2 Interactive BVOC (iBVOC) emissions

The iBVOC emissions scheme incorporated into the HadGEM2 model is described by Pacifico et al. (2011) and is based upon the scheme adopted by Arneth et al. (2007). The scheme is based on a biochemical model for the emission of isoprene developed by Niinemets et al. (1999). In this model the emission of isoprene is dependent on the electron requirement for isoprene synthesis.

All of the isoprene that is emitted is assumed to be synthesised in the chloroplasts of the plants' leaves and that photosynthetic electron transport (J) is calculated as follows (Equation 3.13):

$$J = \frac{(A_J + R_D)(4C_I + 8\Gamma)}{C_I - \Gamma}, \tag{3.13}$$

where A_J is leaf level net photosynthesis, R_D is leaf level dark respiration, C_I is the internal leaf CO_2 concentration and Γ is the photorespiration compensation point. Niinemets et al. (1999) assume that isoprene emission is nicotinamide adenine dinucleotide phosphate (NADPH) limited. The NADPH requirement per CO_2 mole assimilated is 1.17 times higher for isoprene synthesis than it is for sugar synthesis and the requirement that 6 CO_2 molecules must be assimilated to release one molecule of isoprene, results in rate of photosynthetic electron transport to sustain isoprene synthesis and emission at the leaf level (I_l) as follows (Niinemets et al., 1999).

$$J_{isoprene} = \frac{6I_l(4.67C_I + 9.33\Gamma)}{C_I - \Gamma} \tag{3.14}$$

$J_{isoprene}$ is the rate of photosynthetic electron transport required to sustain isoprene synthesis and I_l is the isoprene emission rate at leaf level and is calculated as in Equation 3.15:

$$I_l = \varepsilon \frac{(A_J + R_D)(4C_I + 8\Gamma)}{6(4.67C_I + 9.33\Gamma)}, \tag{3.15}$$

where ε is the isoprene emission factor. The scheme described by Pacifico et al. (2011) assigns values of ε which are specific to each plant functional type (PFT) and for the leaf level when under standard conditions (Table 3.7). These standard conditions are described as a temperature (T_{st}) of 30°C, photosynthetically active radiation of 1000 $\mu molm^{-2}s^{-1}$ and a CO_2 atmospheric concentration of 370 ppmv (Arneth et al., 2007; Guenther et al., 1995). When these PFT specific emissions factors (IEF) are used, leaf level isoprene emissions (I_l) are calculated as follows:

$$I_l = IEF\frac{(A_J + R_D)}{(A_J)_{st} + R_{D_{st}}} f_T \cdot f_{\mathrm{CO}_2}. \tag{3.16}$$

TABLE 3.7: Emissions factors used by iBVOC emissions scheme (μgC g^{-1} h^{-1})

BVOC emissions factor	Broadleaf Tree	Needleaf tree	C3 Grass	C4 Grass	Shrub
IEF	35.00	12.00	16.00	8.00	20.00
$EF_{terpene}$	0.40	2.40	0.80	0.80	0.80
$EF_{methanol}$	0.60	0.90	0.60	0.90	0.57
$EF_{acetone}$	0.18	0.21	0.12	0.08	0.20

In equation 3.16 T is the air temperature and st refers to the variable under standard conditions. The empirical factors f_{T} and f_{CO_2} are representative of the effect of temperature and CO_2 inhibition on isoprene synthesis and emission and are calculated as follows (Pacifico et al., 2011):

$$f_T = min[e^{a_T(T-T_{st})}; 2.3], \tag{3.17}$$

$$f_{\mathrm{CO}_2} = \frac{C_{I_{st}}}{C_I}. \tag{3.18}$$

In equation 3.17 the empirical factor a_{T} is set to a value of 0.1K and accounts for the higher temperature optimum of isoprene synthesis compared to that of the rate of electron transport (Pacifico et al., 2011). The term f_{T} simulates the effect of differences in the short term response of carbon assimilation and isoprene emission to a change in temperature. An example of this is the higher temperature optimum of isoprene synthase (Monson et al., 1992). Arneth et al. (2007) included the empirical factor f_{CO_2} in order to account for the modelling of the inhibition of isoprene emission with higher atmospheric CO_2 concentrations. In the isoprene emissions model, the isoprene is not stored in the leaf structure (Sanadze, 2004) therefore the emitted isoprene at leaf level is analogous of the rate of isoprene synthesis.

As electron transport is not explicitly simulated in the HadGEM2 photosynthesis scheme, it is assumed that rate of net photosynthesis (A) is a reasonable approximation to the electron transport dependent rate of net photosynthesis. Therefore the canopy isoprene emission rate (I) is given as follows:

$$I = IEF\frac{(A_{canopy} + R_{D_{canopy}})}{A_{st} + R_{D_{st}}} f_T \cdot f_{\mathrm{CO_2}} \tag{3.19}$$

In this equation the isoprene emission rate is scaled up from leaf level to canopy level using the canopy level net photosynthesis (A_{canopy}) and canopy level dark respiration ($R_{D_{canopy}}$). This equation shows the strong link between the processes of photosynthesis and isoprene production (Delwiche and Sharkey, 1993) as well as taking into account the effect of CO_2 inhibition on stomatal uptake and thus the resulting effect on isoprene emission ($f_{\mathrm{CO_2}}$) along with accounting for the fact that the peak rate of photosynthesis occurs at a lower temperature than the peak rate at which isoprene synthesis occurs (f_{T}).

The iBVOC emissions scheme also provides interactive emissions for a lumped monoterpene species, acetone and methanol. The emissions of these species are calculated based upon the model leaf area index (LAI) which can be used as a proxy for photosynthetic primary production and vegetation growth. For theses species it is also assumed that there is no storage of the BVOCs in the leaf structure and all that are produced are emitted directly into the atmosphere through the plant stomata. A PFT specific emissions factor is once again applied for each BVOC with the canopy level emissions rate calculated as follows:

$$BVOC_{EMS} = EF_{BVOC} \cdot f_{T_{terp}} \cdot LAI, \tag{3.20}$$

where EF is the PFT specific emission factor for each emitted BVOC (Table 3.7) and $f_{T_{terp}}$ is the empirical factor which represents the effect of temperature on the emission of the respective BVOC species. In this case a lumped terpene $f_{T_{terp}}$ is applied to monoterpenes, acetone and methanol.

3.4 Model development

This section provides an overview of the updates made to the TOMCAT model as part of model development work performed for this thesis. As discussed in Chapter 2, feedback processes between the atmosphere and biosphere regarding the uptake and impacts of tropospheric ozone are currently highly parametrised in CTMs. The model development in this thesis focuses on the implementation of an updated dry deposition scheme into the TOMCAT CTM, focusing on updating the land use classification scheme and the land/sea ice parametrisation used by the model to determine the dry deposition rates of tracer species.

3.4.1 Developing an updated dry deposition scheme for the TOMCAT CTM - updating the land use scheme

The model development work involved updating the land classification scheme used in the TOMCAT CTM to determine the underlying land surface for the calculation of tracer specific dry deposition rates. As discussed in Chapter 2, the dry deposition of a tracer species is an important sink pathway, particularly for ozone where it can account for up to approximately a quarter of the sink of ozone through chemical loss (Wild, 2007). It is shown by Ganzeveld and Lelieveld (1995) and Giannakopoulos et al. (1999), that the physical and chemical properties of the land surface play an important role in determining the surface resistance (r_c) which in turn impacts the dry deposition velocity to that surface type (Equation 3.5). Ganzeveld and Lelieveld (1995) indicate that the dry deposition of ozone and NO_x is by and large mainly controlled by the surface resistance term. This in itself is dependent upon the resistance of ozone uptake by soil (r_{soil}) and vegetation (r_{veg}). For ozone, the uptake by vegetation is essentially determined by the transfer through the leaf stomata, as uptake through the leaf cuticle is very small with a large resistance term (10^5 sm^{-1} as adopted by Ganzeveld and Lelieveld (1995)). With respect to uptake of ozone by soil, typical resistance values to uptake range from 50 to 1000 sm^{-1} (Galbally and Roy, 1980; Stocker et al., 1993; Wesely, 1989; Wesely et al., 1981) which can vary temporally depending upon soil moisture content and soil temperature.

Ozone deposits to water surfaces much less readily than it does to land surfaces with typical surface resistances over sea and fresh water falling within the range of 1000 to

2000 sm^{-1}. As roughness lengths tend to be lower over water than they do over land, the aerodynamic resistance term also tends to be greater acting to further inhibit ozone uptake. The surface resistance term is still however shown to dominate over the aerodynamic resistance (Lenschow et al., 1982). Ozone has also been shown to deposit less readily to ice and snow covered surfaces (Galbally and Roy, 1980; Wesely et al., 1981) with typical resistance values similar to the higher end of the range for water adopted in the deposition schemes of CTMs.

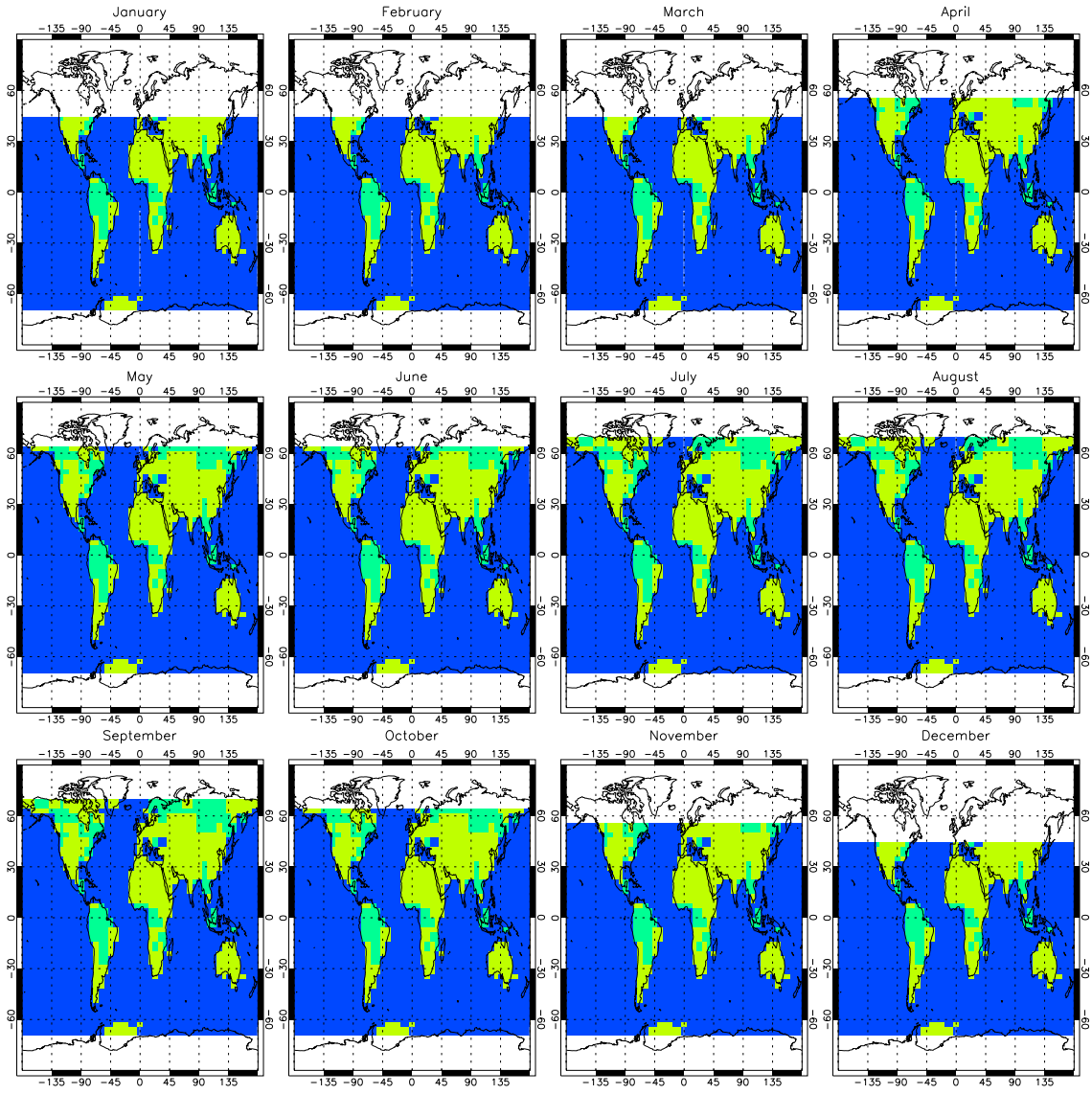

FIGURE 3.1: Standard fixed land classification map used in TOMCAT at T42 resolution with seasonal land/sea ice fields. Blue = water, Dark Green = Forest, Light Green = Grass/shrub/crop, and White = Ice.

In section 3.2.7 it was shown that TOMCAT uses a simple parametrisation based on the roughness length to classify the land cover in a given model gridbox into one of 3 land

categories. These land categories are, water, forest, and grass/crop/shrub and are fixed throughout the year with no seasonal variation (Figure 3.1). Figure 3.1 also shows the simple sea/land ice parametrisation used to determine the fourth land use category of ice/snow.

TABLE 3.8: TOMCAT dry deposition velocities (cm s^{-1}) for ozone, NO_x and CO based upon time of year and season.

		Summer		Winter	
	Surface Type	Day	Night	Day	Night
O_3[a]	Water	0.05	0.05	0.05	0.05
	Forest	0.85	0.30	0.65	0.25
	Grass/crop/shrub	0.65	0.25	0.65	0.25
	Desert/Bare ground	0.18	0.18	0.18	0.18
	Snow/Ice	0.05	0.05	0.05	0.05
NO[b]	Water	0.00	0.00	0.00	0.00
	Forest	0.14	0.01	0.01	0.01
	Grass/crop/shrub	0.10	0.01	0.01	0.01
	Desert/Bare ground	0.01	0.01	0.01	0.01
	Snow/Ice	0.00	0.00	0.00	0.00
NO_2	Water	0.02	0.02	0.02	0.02
	Forest	0.83	0.04	0.06	0.04
	Grass/crop/shrub	0.63	0.06	0.07	0.06
	Desert/Bare ground	0.03	0.03	0.03	0.03
	Snow/Ice	0.01	0.01	0.01	0.01
CO[c]	Water	0.00	0.00	0.00	0.00
	Forest	0.03	0.03	0.03	0.03
	Grass/crop/shrub	0.03	0.03	0.03	0.03
	Desert/Bare ground	0.03	0.03	0.03	0.03
	Snow/Ice	0.00	0.00	0.00	0.00

[a] Based upon Ganzeveld and Lelieveld (1995) as inferred by Giannakopoulos (1998) with the exception of snow and ice which are taken directly from Ganzeveld and Lelieveld (1995). Modified to Guang's values as described by Zhang et al. (2003), [b] Inferred from NO_2 - see Giannakopoulos (1998), [c] See Giannakopoulos (1998).

The TOMCAT land categories shown in Figure 3.1 show a very coarse resolution in land cover over the majority of the globe including classifying a number of island and coastal regions as water rather than land. For example, over Europe, northern parts of the UK are classified as water along with southern parts of Italy and Ireland. The same issue occurs over Indonesia and the island nations in the Caribbean region. This could lead to an underestimation of the predicted rate of dry deposition in these model grid boxes, as the dry deposition velocities used by TOMCAT to determine deposition to water are significantly lower than those to the land surface for ozone and other key tracer species such as NO_x (Table 3.8).

Additionally, the simple seasonal sea/land ice parametrisation utilised by TOMCAT could also result in the misrepresentation of dry deposition velocities at a number of locations. The scheme is highly parametrised and defines a threshold latitude of which any model grid box north of this latitude in the Northern Hemisphere (or in the case of the Southern Hemisphere south of this threshold latitude) the underlying land category is classified as ice/snow, irrespective of the land use type defined by the roughness length. This threshold latitude is seen to vary with the month of the year in order to parametrise the seasonality of ice growth and retreat in both the Arctic and Antarctic regions (Figure 3.1).

This would therefore result in locations being classed as completely covered in snow/ice throughout the winter months whereas in reality there would only be partial ice/coverage during the winter season at locations in northern parts of Europe and North America with the majority of surfaces being largely covered in vegetation or bare soil if vegetation has died back during the winter season. As the deposition velocities of ozone and associated tracer gases (Table 3.8) to ice surfaces is slower than that to vegetated surfaces and bare soil, this could result in an underestimate of the rate of deposition of ozone leading to a potential positive winter bias in surface concentrations. Finally, the standard dry deposition scheme in TOMCAT does not utilize the desert/bare ground category only classifying land points as either forest or shrub/grass/crop. This can also lead to the miscalculation of dry deposition rates over a number of regions where desert is the predominant land category such as Saharan Africa.

The TOMCAT land use map was updated using output from the NCAR (National Center for Atmospheric Research) Community Land Model (CLM). This new CLM vegetation map (Figure 3.2) was read into the model at 0.5 by 0.5 degree resolution and then regridded to TOMCAT's horizontal model resolution. The desert category was also included. The CLM provides land coverage over 16 categories including several vegetation types and these were transferred into the TOMCAT land types. The CLM land types are derived from 1 km resolution satellite data (Bonan et al., 2002). The coverage of the CLM tree land types are determined from the 1 km University of Maryland tree cover dataset and the coverage of the other vegetation categories are inferred from the 1 km IGBP DISCover dataset (Bonan et al., 2002).

The coverage of each TOMCAT land type was determined as a combination of the coverage of the CLM land types as shown in Table 3.9. Water coverage is defined as the percentage

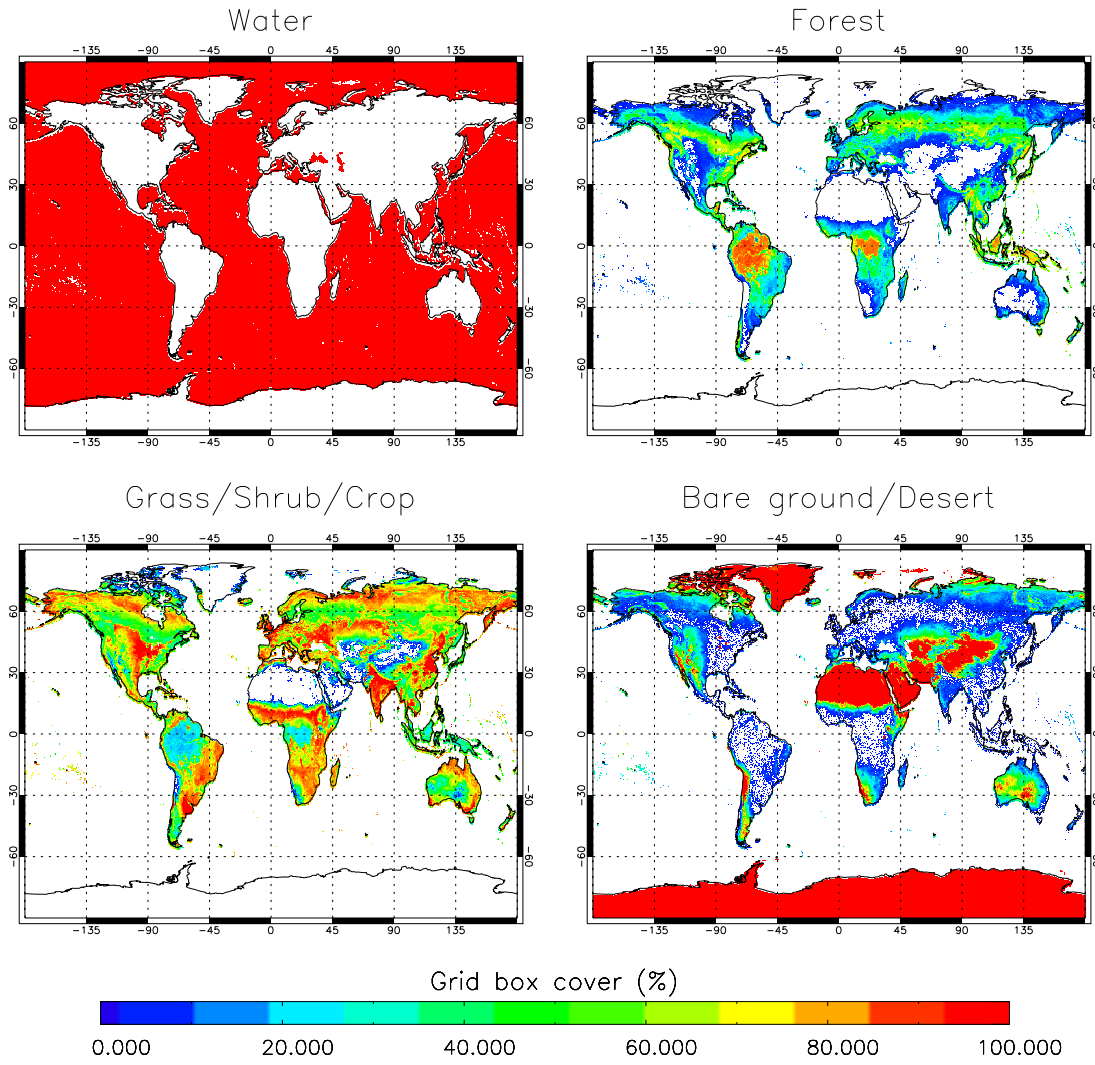

FIGURE 3.2: Updated fixed land classification map used in TOMCAT based upon NCAR CLM output.

of a grid box not covered by any of the CLM land types. The dry deposition rate of each of the 37 tracer species (that are dry deposited in TOMCAT) was then determined as previously based upon time of day, time of year and the underlying land type. However, in the updated scheme the model no longer uses roughness lengths to categorize each grid box into a single land use type. The updated scheme calculates the dry deposition velocity based upon the fractional cover of each land category in each land grid box, as shown by equation 3.21.

$$V_{\mathrm{d}} = \sum_{n=1}^{4} V_{dn} \times LC_n \tag{3.21}$$

Where V_{d} is the mean dry deposition velocity for a given model grid box, n is the land surface type (where 1=Water, 2=forest, 3=Grass/Shrub/Crop and 4=Desert/Bare ground), V_{dn} is the species specific dry deposition velocity to surface category n (Table 3.8) and LC_{n} is the fractional area of the grid box covered by land type n.

TABLE 3.9: Transfer of CLM land categories onto TOMCAT land types.

TOMCAT land type	CLM Category
Forest	Needleleaf evergreen tree (temperate), Needleleaf evergreen tree (boreal), Needleleaf deciduous tree, Broadleaf evergreen tree (tropical), Broadleaf evergreen tree (temperate), Broadleaf deciduous tree (tropical), Broadleaf deciduous tree (temperate), Broadleaf deciduous tree (boreal)
Grass/shrub/crop	Broadleaf evergreen shrub, Broadleaf deciduous shrub (temperate), Broadleaf deciduous shrub (boreal), C3 grass (arctic), C3 grass (non-arctic), C4 grass, Corn
Desert/Bare Ground	Bare Ground

An updated seasonal sea/land ice parametrisation was also added to the model based upon the respective fields utilised by the CLM model to represent ice coverage. This data is represented in two forms with a glacier (land ice) field that is fixed throughout the year and a sea ice field that varies on a monthly basis with both datasets giving a fractional coverage of ice in each model grid box. The ice data is read in at 1 by 1 degree resolution and is then regridded to TOMCAT's horizontal model resolution as with the land cover data. This provides a new sea ice field that varies from month to month and provides a more accurate representation of the polar ice cap retreat and growth between summer and winter in the Arctic (Figure 3.3) and the Antarctic (Figure 3.4).

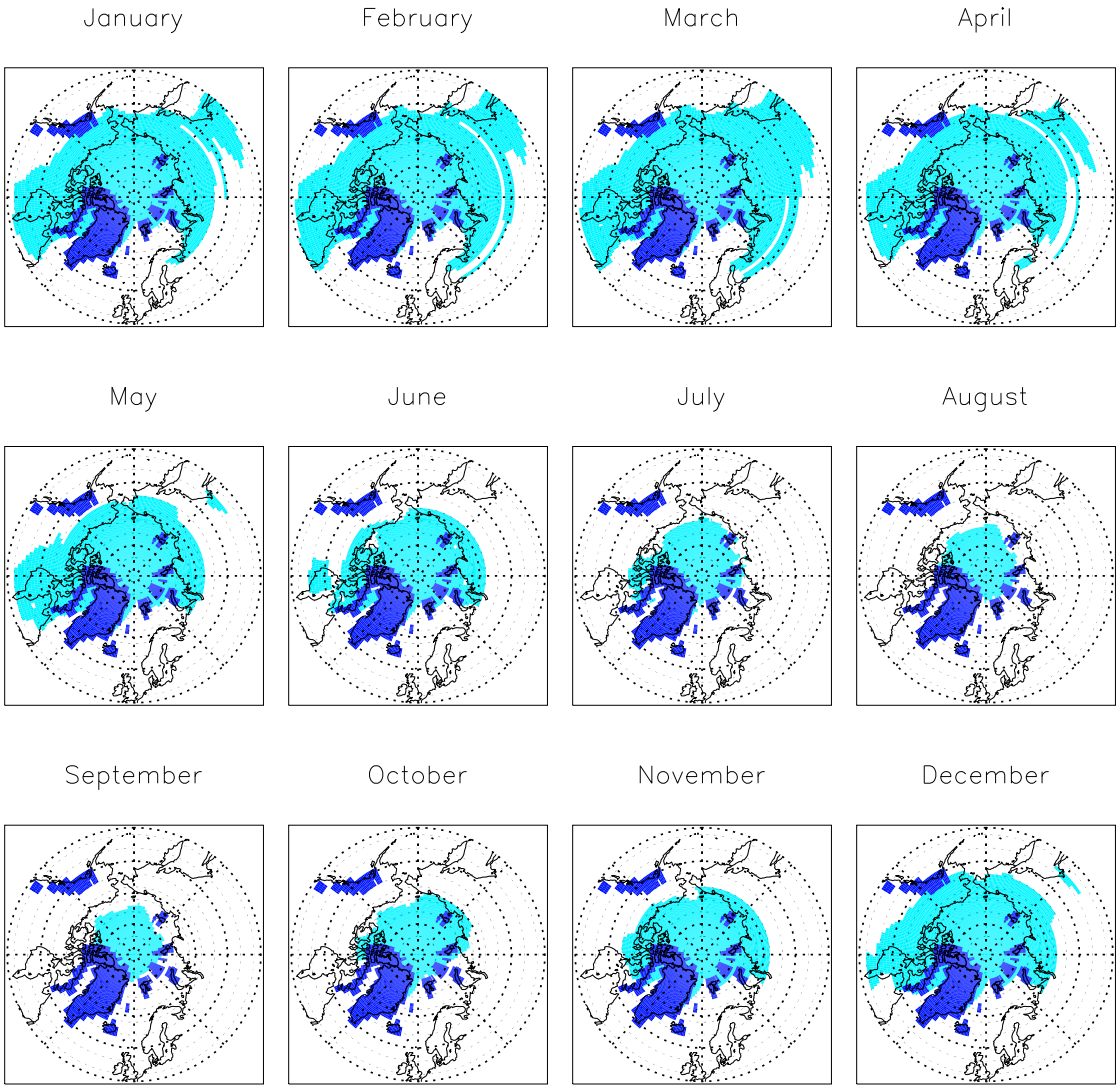

FIGURE 3.3: Updated TOMCAT monthly land/sea ice fields for the Northern Hemisphere. Dark blue indicates fixed land ice (glacier) field and light blue indicates seasonal sea ice fields and snow.

3.5 Model evaluation

This section describes the evaluation of the performance of both the TOMCAT CTM and HadGEM2 models against observational data. As described in Section 3.4.1 the chemical and physical properties of the land surface in both CTM and GCM atmospheric models plays an important role in the dry deposition of ozone and its precursor species which in itself is an integral part of the atmospheric ozone budget. Therefore it is important to represent the land surface as accurately as possible in computer models along with the exchange processes between the atmosphere and the biosphere which at present are often

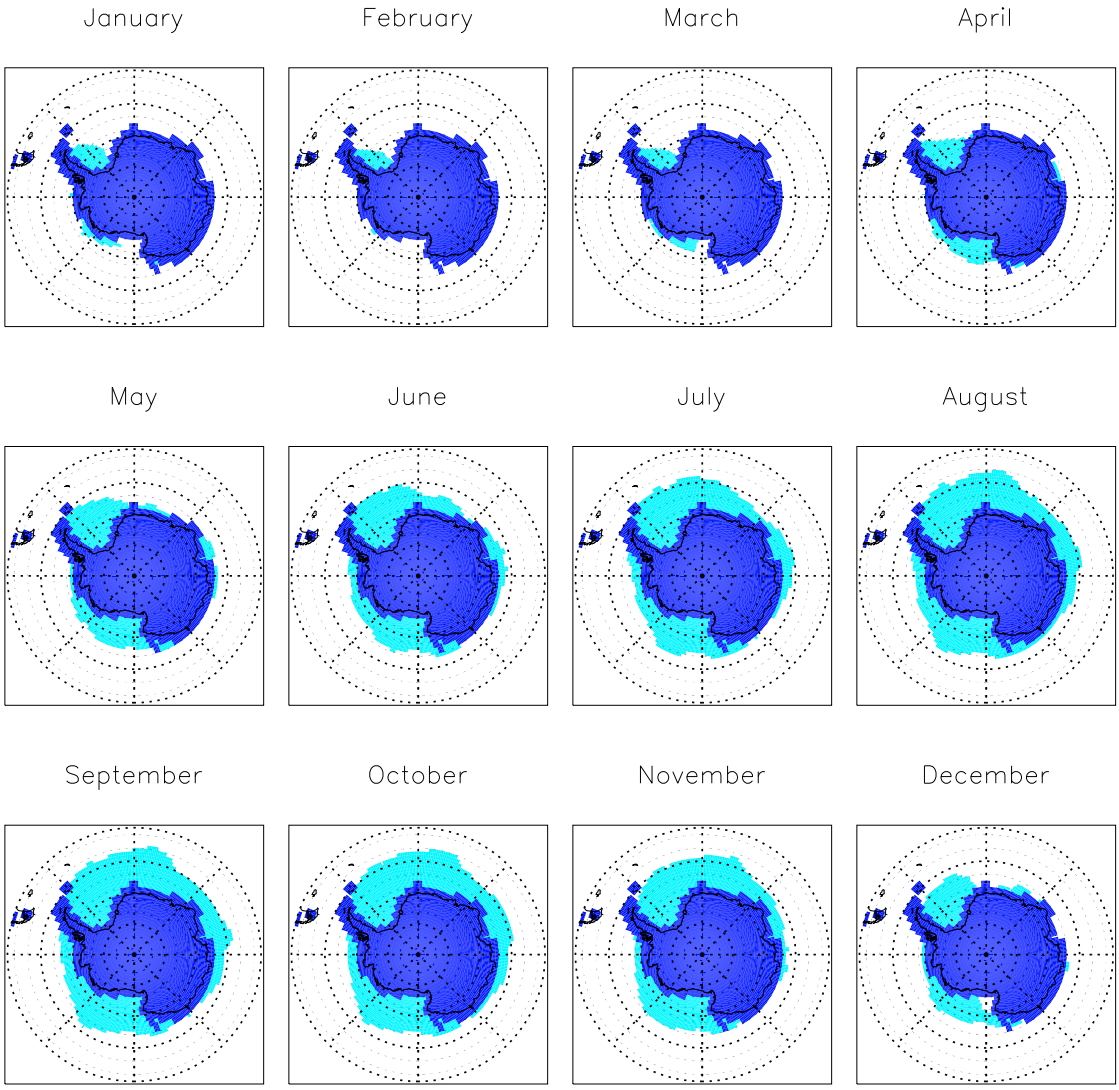

FIGURE 3.4: As Figure 3.3 except for Southern Hemisphere.

highly parametrised with high levels of uncertainty. This section will evaluate the standard versions of both TOMCAT and HadGEM2 against observational data and will then assess the subsequent impact of the model development on model performance.

3.5.1 Observational data

Modelled surface ozone is evaluated using observations from both surface monitoring networks and data composites from observations obtained on various aircraft campaigns. The surface observations are mainly taken from continuous ground based UV absorption based measurements. For this data, sites are chosen from a variety of location types including

TABLE 3.10: Summary of regions used and data sources for model evaluation.

Region	lon, lat (min)	lon, lat (max)	# of stations	References
South-West USA	−125, 30	−110, 40	7	CASTNET[1]
South-East USA	−90, 25	−80, 35	6	CASTNET[1]
Great-Lakes USA	−95, 40	−75, 50	16	CASTNET[1]
Mediterranean	5, 35	30, 45	11	EMEP[2]
Central Europe	7, 48	17, 54	38	EMEP[2]
South-East Asia	110, 20	125, 35	5	WDCGG[3]
South America	−80, −60	−35, 15	2	WDCGG[3]
Africa	−20, −35	50, 35	2	WDCGG[3]

[1] CASTNET: http://java.epa.gov/castnet/epa_jsp/prepackageddata.jsp#ozone
[2] EMEP: http://tarantula.nilu.no/projects/ccc/emepdata.html
[3] WDCGG: http://gaw.kishou.go.jp/cgi-bin/wdcgg/catalogue.cgi

both urban and rural locations, as well as coastal and inland locations, to provide coverage across polluted and relatively clean air locations. Data is obtained from the European Monitoring and Evaluation Programme (EMEP) for locations over Europe, the Clean Air Status and Trends Network (CASTNET) for locations over the United States and the World Data Centre for Greenhouse Gases (WDCGG) for locations over Asia, Africa and South America. Where available hourly observational data is used for the model versus observations comparison. Model ozone output is taken from the grid boxes containing each surface monitoring site, before being averaged across all sites within each comparison region (shown in Table 3.10).

The aircraft data used to validate the model is described by Emmons et al. (2000) and are tropospheric data from a number of aircraft campaigns that have been gridded onto global maps. These form data composites of chemical species that are important in the photochemistry of ozone. The species measured include ozone, NO, NO_2, CO and PAN. The data is provided at a resolution of 5 degrees longitude by 5 degrees latitude from a number of locations around the globe and provides vertical profiles of the measured species at a resolution of 1km.

3.5.2 Model test experiments

In order to evaluate the TOMCAT CTM and the updates to the dry deposition scheme, two scenarios were run. The first with the dry deposition scheme set to operate as in the standard model (TOM_STD) and the second with the new updated dry deposition scheme

(TOM_UPD). After a spin-up period of 4 months the model was run for one year for each scenario with meteorology representative of the year 2004.

For the evaluation of HadGEM2-ES the model was setup to run in atmosphere only configuration with all couplings to the ocean model turned off. The model was spun up for a period of 11 months and was then set to run for 2 years with the analysis performed on the second year of the simulation.

3.5.3 TOMCAT CTM evaluation

3.5.3.1 TOM_STD vs TOM_UPD: Impact on surface ozone

Figure 3.5 shows monthly mean absolute differences (in ppbv) in surface ozone between the TOM_UPD and TOM_STD model runs. The introduction of the new land-sea ice parametrization is clearly evident in the northern hemisphere winter months where ozone under the TOM_UPD scenario is on average lower throughout the months of November to April with maximum differences of up to 25 ppbv seen over parts of Canada, Northern Europe and Russia. Under the TOM_STD scenario throughout these months the land category is classified as ice/snow rather than the underlying forest or grass/crop/shrub land type under the TOM_UPD scenario. As shown in Table 3.8, the winter deposition velocity to ice/snow for ozone (0.05 cms^{-1} day (0.05 cms^{-1} night)) is significantly lower than that to forest (0.65 cms^{-1} day (0.25 cms^{-1} night)) and grass/crop/shrub (0.65 cms^{-1} day (0.25 cms^{-1} night)). Therefore under the updated land scheme, deposition of ozone to the surface will be greater and resultant surface ozone concentrations will be lower.

It is also evident in Figure 3.5 that ozone concentrations over the world's major desert regions (the Sahara, the Arabian and the Gobi desert regions) are higher under the new updated land map highlighting the introduction of the desert category in the updated land. Over theses regions, ozone differences tend to be greatest between the months of May and August where ozone concentrations under the TOM_UPD scenario tend to be greater than those under the TOM_STD scenario by approximately 10 to 15 ppbv.

Finally, the improved resolution around the coastal regions is evident where the land category is now classed as either forest or grass/crop/shrub under the updated land scheme where previously it was classified as water. Around many coastal grid boxes, the surface

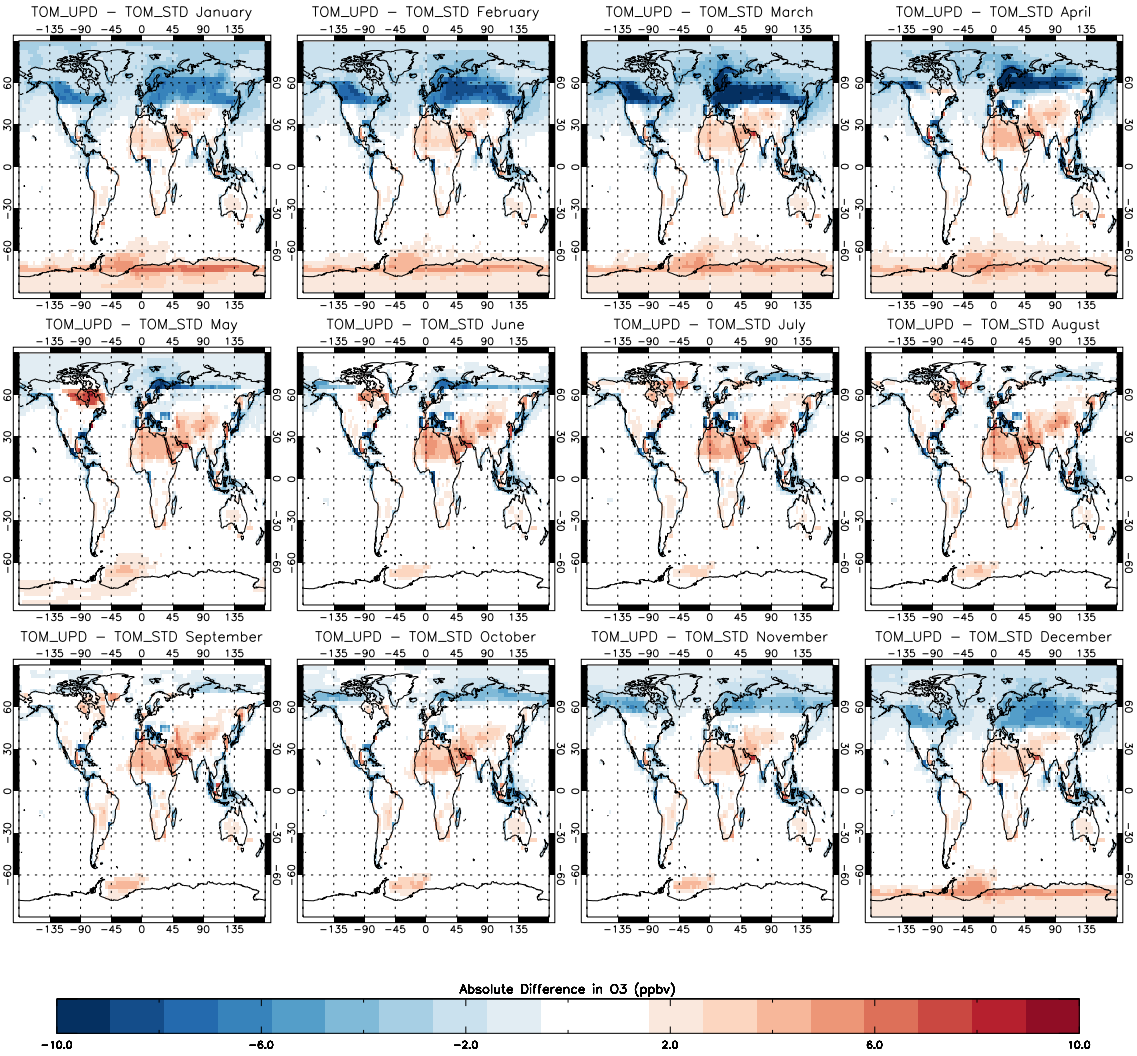

FIGURE 3.5: Absolute differences in TOMCAT monthly surface ozone between the TOM_UPD and TOM_STD model scenarios.

ozone is seen to be lower under the TOM_UPD scenario by up 20 ppbv around the coasts of eastern USA, southern parts of Europe and Indonesia highlighting the higher deposition rates of ozone to land surfaces than those to water (Table 3.8).

This therefore shows that modelled surface ozone in the TOMCAT CTM is highly sensitive to the underlying land category and furthermore indicates the importance of accurately representing the land surface in global atmospheric models.

TABLE 3.11: Regional Normalised Model Mean Biases (NMMB) for modelled versus observed surface ozone for the TOM_STD and TOM_UPD model scenarios.

		Scenario	
		TOM_STD	TOM_UPD
Region	SW USA	−21.2 %	−25.1 %
	SE USA	57.8 %	27.3 %
	USA, Great Lakes	17.3 %	10.7 %
	Mediterranean	14.2 %	0.6 %
	Central Europe	20.9 %	−2.2 %
	SE Asia	27.2 %	11.2 %
	S America	25.5 %	18.9 %
	Africa	−12.6 %	−0.9 %

3.5.3.2 TOM_STD vs TOM_UPD: Comparison with surface ozone data

Figure 3.6 shows observed and modelled monthly-mean ozone from both the TOM_UPD and TOM_STD model scenarios for the year 2004 over the regions indicated in Table 3.10. For these comparisons, the model ozone at 30 m (height of the mid-point of the lowest model layer) was scaled using the approach of the LRTAP Convention (2004) to a height of 10 m, the height at which most of the observations are made. This was done to account for the drop off in concentrations in the surface layer due to ozone dry deposition. The concentrations were scaled based on the local meteorology in each model grid box and the underlying surface characteristics. Table 3.11 shows the normalised model mean bias for each region under each scenario. The normalised model mean bias was determined for each region using Equation 3.22.

$$NMMB = \frac{\sum X_{MOD} - X_{OBS}}{\sum X_{OBS}} \times 100 \tag{3.22}$$

In Equation 3.22, X_{MOD} is the model concentration and X_{OBS} is the observational value from surface monitoring sites.

Under the TOM_STD scenario, the model performs well over the Mediterranean, Central Europe, and Africa with normalised model mean biases of −12.6 % to 20.9 %. There is less good agreement over SE USA (57.8 % bias), the Great lakes (17.3 % bias) and SE

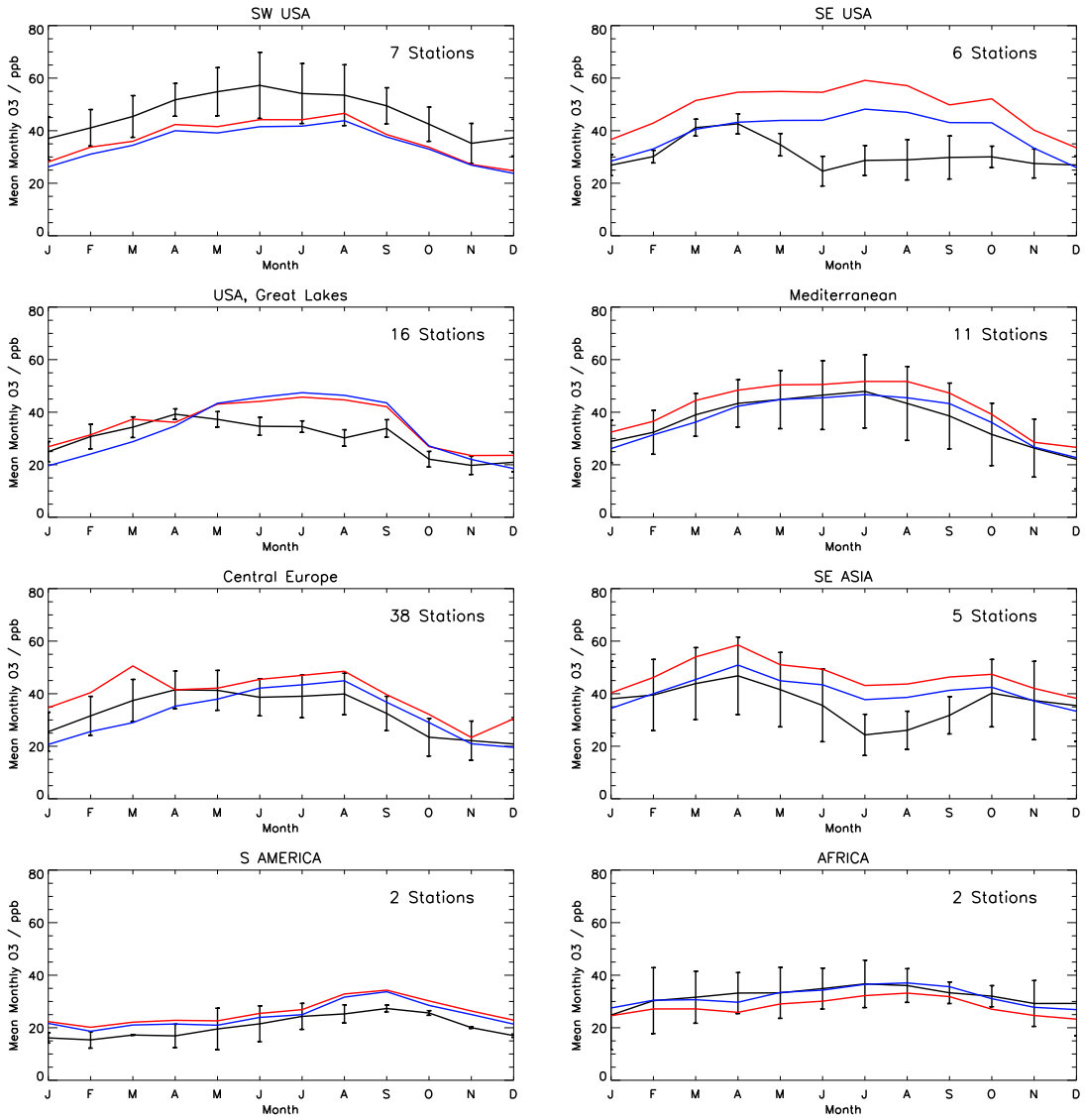

FIGURE 3.6: Regionally-averaged monthly mean surface ozone concentrations from monitoring stations (black line) and the TOMCAT model under the TOM_STD (red line) and the TOM_UPD (blue line) scenarios for the year 2004. Error bars indicate 1 standard deviation on the monthly mean observations.

Asia (27.2 % bias), where the model overestimates observed surface ozone throughout the summer months over SE Asia and the Great lakes and throughout the duration of the calendar year over the SE USA, where peak overestimates of ozone approach nearly 40 ppbv during the summer months of June, July and August. Finally, over S America the model tends to perform better with a model bias of 25.5 % however the model consistently overestimates observed surface ozone throughout the year by about 4 to 5 ppbv.

With the exception of the SW USA region, the inclusion of the updated land scheme sees a marked improvement in the model performance over all regions. The Mediterranean and

Africa show the greatest improvement where the model mean bias improves from 14.2 % to 0.6 % and from −12.6 % to −0.9 % respectively. As shown in Figure 3.6 and Table 3.11, under the TOM_UPD model scenario, the model mean biases tend to be lower than under the TOM_STD model scenario indicating that the inclusion of the updated land scheme results in improved agreement between the modelled and observed surface ozone. However, over the SW USA region, the model bias becomes greater in magnitude from −21.2 % to −25.1 % indicating lesser agreement with the observed data.

Over the SE USA regions and SE Asia, the greatest improvement is seen throughout the winter months where the model shows fairly good agreement with the surface observations. However, over both regions there is still overestimation of surface ozone by the model during the summer months. The SE USA region again shows the worst over prediction during the months of May, June and July where under the updated land scheme, modelled surface ozone is still just over 20 ppbv greater than the observed data. This indicates that during the summer months the model could potentially be underestimating the deposition of ozone to the surface and thus leading to large model biases.

This type of model bias over the United States is consistent with results shown in a previous studies (Avnery et al., 2011a; Reidmiller et al., 2009) which showed that global models tend to on average over predict observed surface ozone concentrations over eastern parts of the US by approximately 10-20 ppbv during the summer months. These studies indicate that the reasons for this bias remain unclear and could be attributed to a number of causes such as the coarse resolution of global CTM models, along with other potential issues related to heterogeneous chemistry, isoprene emissions and oxidation and the release of elevated emissions sources into the surface model layer.

As shown by the test experiments performed in this chapter, the resolution of the land surface scheme used by the model along with how accurately the underlying land surface is represented plays an important role in the model performance when compared to observational data. The inclusion of the updated land use scheme (that provides a more accurate representation of current land use types) leads to a smaller magnitude model bias over the majority of regions when comparing with surface observational data.

3.5.3.3 TOM_STD vs TOM_UPD: Comparison with surface CO data

Figure 3.7 shows observed and modelled monthly-mean CO data for the TOM_STD and TOM_UPD simulations during the year 2004. For these comparisons the observations are obtained from the WDCGG (see Table 3.10 for reference) for a variety of surface stations within the WDCGG network. This included both urban and rural locations, as well as coastal and inland locations to provide coverage across polluted and relatively clean air locations. Table 3.12 shows the normalised model mean bias for each site under each scenario.

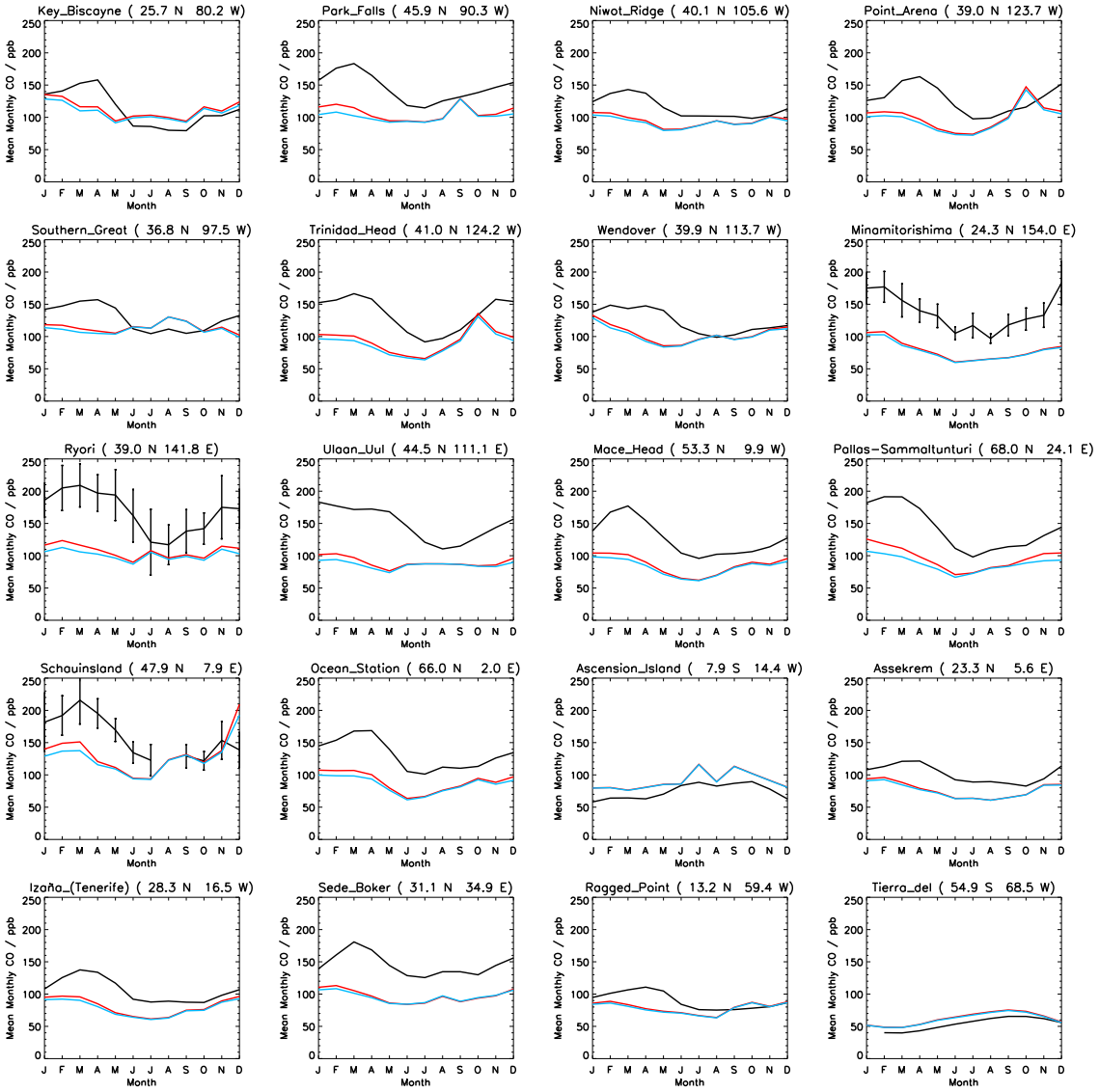

FIGURE 3.7: Monthly mean surface CO concentrations (**ppbv**) from monitoring stations (black line) and the TOMCAT model under the TOM_STD (red line) and the TOM_UPD (blue line) scenarios for the year 2004. Error bars indicate 1 standard deviation on the monthly mean observations where available.

Under the TOM_STD scenario, the model performs best at Key Biscayne, Southern Great and Ragged point with normalised model mean biases of −1.0 %, −11.4 % and −12.0 % respectively. There is less good agreement over the remaining sites where biases lie in the range −15.7 % to −42.7 % with the best agreement with observations at Wendover and the least at Minamitorishima. With the exception of the 2 southern hemisphere sites (Ascension Island and Tierra del), the model tends to underestimate CO through the winter and spring months with better agreement shown during the summer, particularly over sites located within the N American and S American domains (Table 3.10). As N America, Asia and Europe represent the more industrialised regions and are dominated by anthropogenic sources of CO, particularly during the winter months, this underestimation of winter CO could indicate an underestimation of CO emissions in the TOMCAT model. At the more remote, clean air locations such as Minamitorishima, the model underestimates CO throughout the year with a bias of −42.7 %. This is linked to the location of the station downwind from Asia with a strong influence on the site from Asian emissions. Therefore this underestimation of CO could be due to the underestimation of anthropogenic CO over Asia in the TOMCAT. Finally, at the 2 southern hemisphere stations (Ascension Island and Tierra del) the model tends to overestimate CO throughout the year. For all sites the model tends to capture the seasonal trends well.

The inclusion of the updated land scheme (TOM_UPD) sees a reduction in CO concentrations at all sites. With the exception of the 2 southern hemisphere stations this results in an increase in the magnitude of model biases. The greatest increase in bias is at Pallas-Sammaltunturi (−32.4 % to −38.2 %) and the smallest increase is seen at Sede Boker (−33.3 % to −34.1 %). The effects of including the updated land scheme are more pronounced in the winter and spring months, particularly over stations in N America, Asia and Europe (Figure 3.7) with drops in CO concentrations of up to 20 ppbv seen at Park Falls and Pallas-Sammaltunturi during the months of January, February and March. This is because for the TOM_UPD scenario, the updated land scheme has a more accurate representation of the seasonality of sea-ice coverage. Therefore where the underlying land category was previously ice for the TOM_STD scenario it is either forest or grass/crop/shrub under the TOM_UPD which increases the rate of CO deposition (Table 3.8) and hence lowers concentrations in the surface layer. At all sites the model is still shown to capture the seasonal trends of the observations with the best agreement shown during the summer months.

TABLE 3.12: Normalised Model Mean Biases (NMMB) for modelled versus observed surface CO for the TOM_STD and TOM_UPD model scenarios.

		Scenario	
		TOM_STD	TOM_UPD
Site	Key Biscayne	−1.0 %	−4.7 %
	Park Falls	−26.7 %	−30.1 %
	Niwot Ridge	−17.8 %	−19.6 %
	Point Arena	−21.9 %	−24.8 %
	Southern Great	−11.4 %	−13.3 %
	Trinidad Head	−30.4 %	−33.7 %
	Wendover	−15.7 %	−17.4 %
	Minamitorishima	−42.7 %	−44.0 %
	Ryori	−36.4 %	−39.8 %
	Ulaan Uul	−39.9 %	−42.4 %
	Mace Head	−32.4 %	−35.1 %
	Pallas-Sammaltunturi	−32.4 %	−38.2 %
	Schauinsland	−16.9 %	−20.7 %
	Ocean Station	−32.2 %	−35.3 %
	Ascension Island	21.5 %	21.0 %
	Assekrem	−24.3 %	−25.6 %
	Izaa (Tenerife)	−23.5 %	−26.0 %
	Sede Boker	−33.3 %	−34.1 %
	Ragged Point	−12.0 %	−13.3 %
	Tierra del	15.9 %	14.3 %

In contrast, for the 2 southern hemisphere stations there is a decrease in model bias with the bias dropping from 15.9 % to 14.3 % at Tierra del and from 21.5 % to 21.0 % at Ascension Island. This is again linked to reduced CO concentrations as a result of increases in the rate of CO deposition under the TOM_UPD scenario.

3.5.3.4 TOM_STD vs TOM_UPD: Comparison with surface NO_x data

Figure 3.8 shows observed and modelled monthly-mean NO_x data for the TOM_STD and TOM_UPD simulations during the year 2004. For these comparisons the observations are obtained from the WDCGG (see Table 3.10 for reference) for 4 surface sites throughout Europe with available data for 2004. Table 3.13 shows the normalised model mean bias for each site under each scenario.

For two of the sites, (Hohenpeissenberg and Rigi) the model performs well under the standard land scheme (TOM_STD) with biases of −4.4 % and 5.9 % respectively. At both of

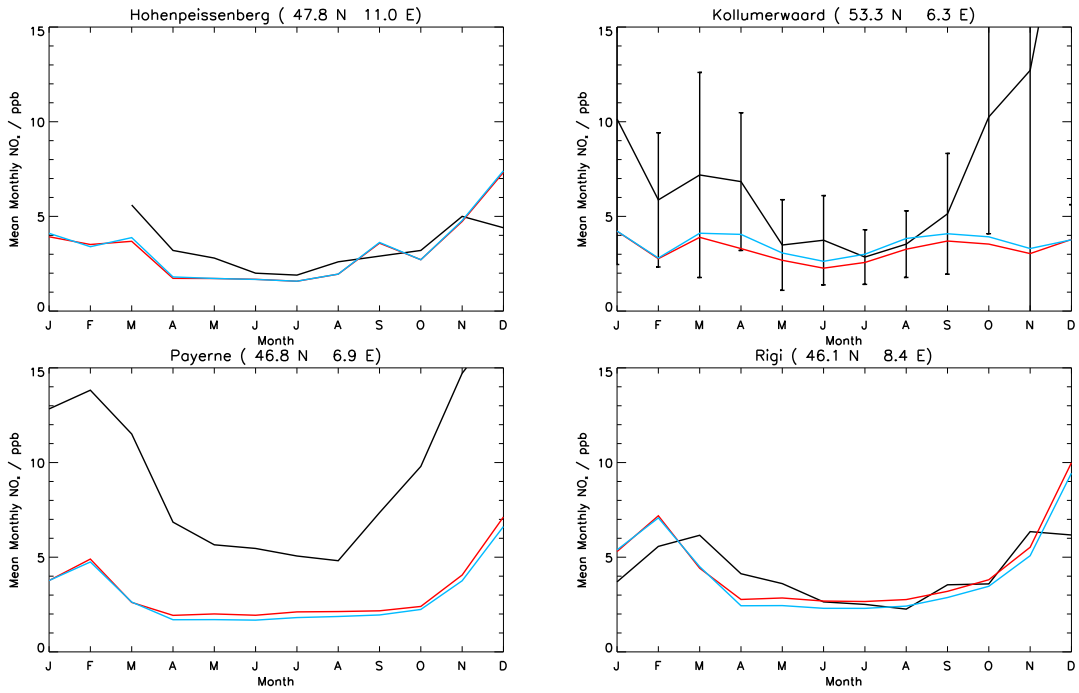

FIGURE 3.8: Comparison of monthly mean surface NO_x concentrations (**ppbv**) from monitoring stations (black line) with the TOMCAT model for the TOM_STD (red line) and the TOM_UPD (blue line) simulations for the year 2004. Error bars indicate 1 standard deviation on the monthly mean observations where available.

these locations the model also captures the seasonal variability of the observations well, particularly during the summer months. Over Payerne, the model also captures the seasonal variability of surface NO_x concentrations however greatly underestimates surface concentrations at this site. Typically models have difficulty in capturing these seasonal changes in short lived species such as NO_x over land due the relatively large model gridbox size with this evident at Kollumerwaard. At this site, under the TOM_STD scenario the model simulates summertime NO_x well, however provides a large underestimate of concentrations again during the winter months leading to an overall bias at the site of $-59.3\,\%$. This indicates that the model potentially underestimates NO_x emissions sources during the winter months. For all months at Kollumerwaard the model produces concentrations within one standard deviation of the observations.

The inclusion of the updated land scheme (TOM_UPD) sees an improvement in model performance at all sites with the exception of Payerne. At Rigi the model shows the greatest improvement in bias dropping from an overestimate of $5.9\,\%$ to a slight underestimate

Table 3.13: Normalised Model Mean Biases (NMMB) for modelled versus observed surface NO_x for the TOM_STD and TOM_UPD model scenarios.

		Scenario	
		TOM_STD	TOM_UPD
Site	Hohenpeissenberg, Germany	−4.4 %	−2.7 %
	Kollumerwaard, Netherlands	−59.3 %	−55.3 %
	Payerne, Switzerland	−67.8 %	−70.1 %
	Rigi, Switzerland	5.9 %	−1.0 %

of 1.0 %. The smallest change in bias is at Hohenpeissenberg which shows an improvement from −4.4 % to −2.7 %. However, over Payerne the bias becomes greater in magnitude from −67.8 % to −70.1 % indicating lesser agreement with the observed data. Overall at 3 of the four sites, the model captures the seasonal variability of the observations well under the updated land scheme. The variation in responses of surface NO_x concentrations to the updated land scheme is due to a combination of changing rates of dry deposition and the resultant impacts on the concentrations of NO_x itself and other tracer species that play an important role in NO_x chemistry (e.g. PAN and VOCs).

3.5.3.5 TOM_STD vs TOM_UPD: Comparison of model ozone and NO_x with aircraft campaign data

The impact of changing the model land use scheme not only affects atmospheric composition through changes to surface tracer species concentrations as a result of changing dry deposition. Depending on the lifetime of the species in the atmosphere, changes in composition can also be seen at higher altitudes. Therefore it is important to evaluate the impact of the updated land scheme at higher altitudes in the atmosphere using aircraft observations. The TOM_STD and the TOM_UPD vertical ozone profiles were also compared to aircraft data from various flight campaigns from around the globe (Emmons et al., 2000) in order to assess the model performance in the vertical domain.

TOMCAT ozone and NO_x concentrations were averaged over 5 regions at 4 different height intervals. This gave the estimated regional and vertical average background distributions of these species. The 5 regions were N America (125°–75°W, 25°– 60°N), Asia (110°– 125°E, 20°– 50°N), Europe (15°W – 45°E, 36°– 75°N), Africa (20°W –50°E, 35°S – 35°N) and S America (80°– 35°W, 60°S – 15°N). Table 3.14 shows the corresponding regional averages

TABLE 3.14: Regional comparisons of mean ozone (**ppbv**) and NO_x (**pptv**) from the TOMCAT model (for simulations TOM_STD and TOM_UPD) with aircraft campaign data (Emmons et al., 2000). Averages are for all flights for multiple campaigns in each region.

		Height Range							
		Surface–3 km		3–5 km		5–10 km		10–15 km	
		O_3	**NO_x**	**O_3**	**NO_x**	**O_3**	**NO_x**	**O_3**	**NO_x**
N AM	**TOM_STD**	53.5	403.9	62.5	53.1	95.2	81.0	292.4	505.7
	TOM_UPD	51.9	419.9	62.2	54.2	95.1	82.0	291.7	507.4
	Obs.	48.9	242.2	53.5	81.9	64.3	59.8	91.8	353.6
ASIA	**TOM_STD**	53.9	290.8	57.7	55.6	59.3	49.9	80.7	123.5
	TOM_UPD	50.2	299.6	57.4	57.3	58.9	50.6	79.7	124.5
	Obs.	45.5	297.2	48.3	57.8	53.8	69.9	66.5	113.6
EUR	**TOM_STD**	44.3	753.8	55.3	49.8	80.2	42.7	272.7	269.2
	TOM_UPD	40.9	757.4	54.3	50.5	79.7	43.2	272.0	270.6
	Obs.	43.3	N/A[a]	50.0	58.0	55.0	64.0	106.2	207.0
AFC	**TOM_STD**	56.2	156.3	60.2	45.5	56.9	47.7	60.0	95.7
	TOM_UPD	56.6	156.4	60.1	45.9	56.8	48.1	59.7	96.6
	Obs.	46.8	144.2	53.3	84.9	59.0	67.8	59.3	151.7
S AM	**TOM_STD**	40.7	256.9	47.4	36.3	56.3	43.7	125.4	104.8
	TOM_UPD	40.7	256.5	47.3	36.5	56.0	44.1	124.7	105.7
	Obs.	35.0	101.0	40.0	55.1	42.8	58.8	70.5	105.6

[a] Flights recording NO_x in the European region did not record data in the lowest height range.

for all flights from multiple campaigns in each region for comparison. For the calculation of the model averages, the ozone and NO_x concentrations from each model run were sampled both spatially and temporally to match the limited coverage of the flight campaign data in each region.

In the surface layer, the model overestimates concentrations of ozone over all regions for the TOM_STD scenario with the best agreement over Europe where modelled ozone is 44.3 ppbv and observed is 43.3 ppbv. The introduction of the updated land cover scheme lowers ozone throughout the surface layer over N America (1.6 ppbv), Asia (3.7 ppbv) and Europe (3.4ppbv) which results in simulated values closer in magnitude to the observations. Over Africa surface ozone concentrations see a small rise with the updated land scheme (0.4 ppbv) and over S America there is no change in ozone between the scenarios throughout the surface layer. In the free troposphere, the changes in ozone concentrations are much smaller (less than 1 ppbv) over all regions however the inclusion of the updated land scheme brings the model into better agreement with the aircraft data at all height ranges. However,

in the highest height range (10–15 km) model ozone still overestimates the observations by up to a factor of 3 under the updated land scheme. This is likely linked to the low vertical resolution of TOMCAT around the tropopause resulting in a potential sampling issue around this region with stratospheric air being incorrectly classified as in the troposphere. This could contribute a positive bias to upper tropospheric ozone concentrations from the ozone rich stratosphere. The low vertical resolution could also potentially lead to an overestimation of stratospheric ozone being mixed down into the troposphere.

For NO_x concentrations, with the exception of the surface layer over S America, the introduction of the updated land scheme results in an increase in concentrations. The largest increase is seen over N America in the surface layer where NO_x concentrations rise by 16 pptv from 403.9 pptv to 419.9 pptv. Overall, NO_x concentrations in the mid-troposphere layers are in better agreement with the aircraft data using the updated land scheme though over many regions the model still underestimates the observations. This underestimation is largest in the 3–5 km layer over Africa where NO_x concentrations under both scenarios are lower than the observations by around 40 pptv. This indicates that the model may underestimate NO_x sources in the free troposphere. In the 10–15 km layer, NO_x concentrations are higher than the observations over all regions with the exception of Africa. The largest overestimation is over N America where NO_x concentrations are 505.7 pptv and 507.4 pptv for the TOM_STD and TOM_UPD scenarios respectively compared to 353.6 pptv for the observations. This again could be linked to the low vertical resolution around the tropopause region.

Overall, the introduction of the updated land scheme results in improved agreement between TOMCAT and aircraft NO_x and ozone observations, particularly throughout the mid-troposphere. However, the response of the NO_x concentrations is shown to vary greatly depending on region and height in the troposphere. This could be linked to a combination of changing rates of dry deposition and the resultant impacts on the concentrations of NO_x itself and other tracer species that play an important role in NO_x chemistry (e.g. PAN and VOCs). It could also indicate that the model fails to accurately pick up the seasonal variability in NO_x concentrations in the vertical domain due to its short atmospheric lifetime.

TABLE 3.15: Mean annual global tropospheric burdens of ozone, CO and NO_x and mean mass weighted tropospheric OH concentration under the TOM_STD and TOM_UPD scenarios.

		Scenario	
		TOM_STD	TOM_UPD
Species	O_3 burden Tg(O_3)	315.6	312.2
	CO burden Tg(CO)	331.6	327.8
	NO_x burden Tg(NO_x)	0.37	0.38
	OH (10^6moleculescm^{-3})	0.957	0.960

3.5.3.6 TOM_STD vs TOM_UPD: Impact on global mean burdens

Table 3.15 shows mean annual global tropospheric burdens of ozone, CO and NO_x along with the mean mass weighted tropospheric OH concentration for both the TOM_STD and TOM_UPD scenarios. In each case the troposphere is defined as the region where the potential vorticity lies between -2 and 2 PVU and the potential temperature is less than 380 K.

The enhanced dry deposition of ozone under the updated land scheme is evident with the global ozone burden shown to drop from 315.6 Tg for the TOM_STD simulation to 312.2 Tg for the TOM_UPD simulation (a drop of 1.1 %). This falls well within the range of a recent multi-model study (307±38 Tg(O_3)) quantifying the variability of modelling the tropospheric ozone budget (Wild, 2007). The enhanced deposition rates also result in a drop in the CO burden from 331.6 Tg under the TOM_STD scenario to 327.8 Tg under the TOM_UPD scenario (a drop of 1.2 %). This drop in the CO burden can also be attributed to a rise in the mass weighted OH concentration which increases slightly from 0.957 × 10^6moleculescm^{-3} to 0.960 × 10^6moleculescm^{-3} (a rise of 0.3 %) with the introduction of the updated land scheme. As oxidation by OH is the major sink of CO this rise can act to enhance the loss of CO seen through the higher deposition.

The OH concentration under both TOMCAT scenarios (0.957 × 10^6molecules cm^{-3} for the TOM_STD simulation and 0.960 × 10^6molecules cm^{-3} for the TOM_UPD simulation) is in good agreement with previous work using TOMCAT which estimates the mass weighted OH concentration at 0.936 × 10^6molecules cm^{-3} (Arnold et al., 2005). This rise in OH could be attributed to the enhanced dry deposition of VOCs and other tracer species which lowers the concentrations of these species and hence the rate of oxidation by OH. However,

the overall reduction in surface ozone acts to counteract this increase due to ozone's role as the principal driver of OH production. Finally the NO_x burden shows an increase as a result of the updated land scheme in TOMCAT (2.7 %).

The concentration of OH in the troposphere also plays an important role in the budget of CH_4. Oxidation of CH_4 by OH is a major sink pathway in the atmosphere and the lifetime of CH_4 is governed by the concentration of OH. The annual global mean CH_4 lifetime is determined as follows:

$$\tau = \frac{\sum M_{CH_4}}{\sum k_{OH}[OH]M_{CH_4}}, \tag{3.23}$$

where M_{CH_4} is the mass of CH_4, [OH] is the concentration of OH in molecules cm^{-3} and k_{OH} is the reaction rate constant for oxidation of CH_4 by OH used in the model. The methane lifetime for the TOM_STD simulation is 8.30 years which lowers slightly to 8.28 for the TOM_UPD simulation due to the higher OH concentrations. However, under the updated land scheme the CH_4 lifetime is in good agreement with previous work falling well within the ranges quoted by the IPCC 2007 AR4 (8.7±1.3 years) and Lawrence et al. (2001) (7.79 – 10.25 years) which estimated the impact of different OH fields on CH_4 lifetime.

3.5.4 HadGEM2-ES evaluation

The various components of the HadGEM2-ES model including the chemistry component have previously been evaluated against observational data by Collins et al. (2011). In this section, HadGEM2 is evaluated against climatological observations from both surface monitoring stations and from ozone sondes from various locations around the globe (Logan, 1999). For this evaluation HadGEM2 is run with both the ozone damage and iBVOC parametrisations included.

TABLE 3.16: Regional Normalised Model Mean Biases (NMMB) for modelled versus observed surface ozone for HadGEM2-ES.

		NMMB
Region	SW USA	−7.3 %
	SE USA	23.0 %
	USA, Great Lakes	−2.4 %
	Mediterranean	39.0 %
	Central Europe	−2.1 %
	SE Asia	59.6 %
	S America	10.2 %
	Africa	13.2 %

3.5.4.1 HadGEM2-ES: Comparison with surface ozone data

For the evaluation of HadGEM2-ES against surface station ozone observations, the data is obtained from the same monitoring networks (EMEP, CASTNET and WDCGG) used to evaluate surface ozone in the TOMCAT model over the same geographical regions (Table 3.10). The regional monthly means were calculated as described in Section 3.5.1 for each individual year within the time period 1991-2000 with these used to determine climatological monthly means for each region for the decade. Climatological monthly means representative of the same decade were calculated from HadGEM2-ES with the model output spatially and temporally sampled over the same regions.

Figure 3.9 shows observed versus modelled climatological monthly means from HadGEM2-ES for 1991-2000 over the regions indicated in Table 3.10. The corresponding normalised model mean biases for each region are shown in Table 3.16.

The model performs well over SW USA, Great Lakes and Central Europe with normalised model mean biases of −7.3 % to −2.1 %. There is less good agreement over SE USA (23.0 % bias), the Mediterranean (39.0 % bias) and SE Asia (59.6 % bias) where the model tends to overestimate observed surface ozone throughout the majority of the year with the exception of during January, February and March over the SE USA where the model provides a good representation of the observed ozone profile. Peak overestimates of ozone approach 25 ppbv with this seen over SE Asia during the months of June, July and August. This bias over SE Asia during the summer months could be linked to the model inaccurately representing the Monsoon period over the region which typically runs from July to October. The monsoon

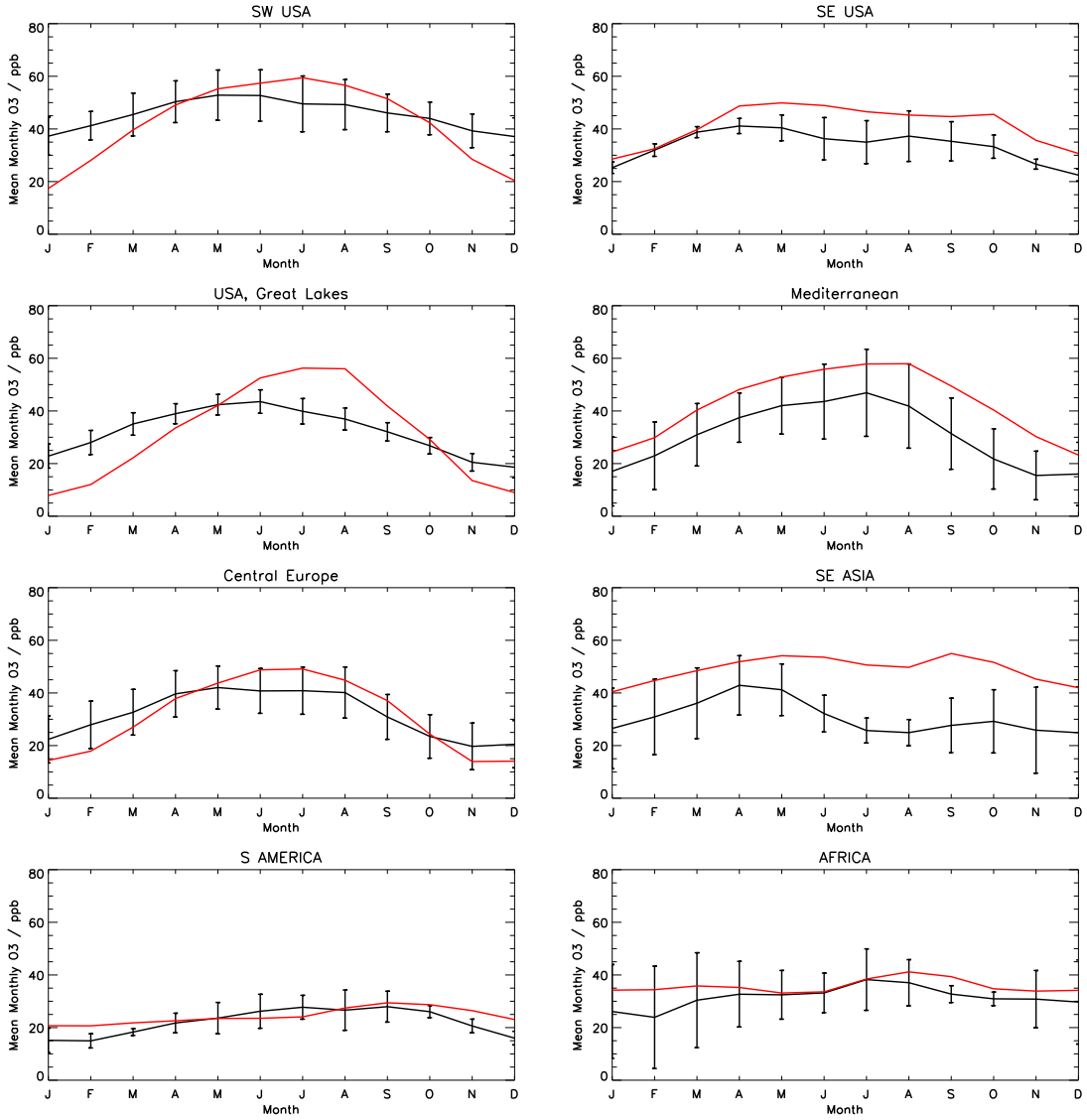

FIGURE 3.9: Regionally-averaged climatological monthly mean surface ozone concentrations from monitoring stations (black line) and the HadGEM2-ES (red line) for the time period 1991-2000. Error bars indicate 1 standard deviation on the monthly mean observations. All values are in ppbv.

brings the transport of marine air masses and weak photochemical activity, which can result in lower ozone concentrations than those during the pre-monsoon period (Zhao et al., 2010).

Finally over the African and S America regions, the model tends to perform better with mean biases of 13.2 % and 10.2 % respectively. The best agreement tends to occur from April to September with the model tending to overestimate observed surface ozone by between 5-10 ppbv over both regions between October and March. Overall, over all regions the model tends to pick out the monthly variation in ozone well.

3.5.4.2 HadGEM2-ES: Comparison with ozone sonde data

In order to evaluate the vertical profiles of ozone in HadGEM2-ES, comparisons were made with climatological observations compiled from ozone sonde launches at various locations around the globe (Logan, 1999). Figure 3.10 shows comparisons of annual average vertical profiles from both the model and observational data.

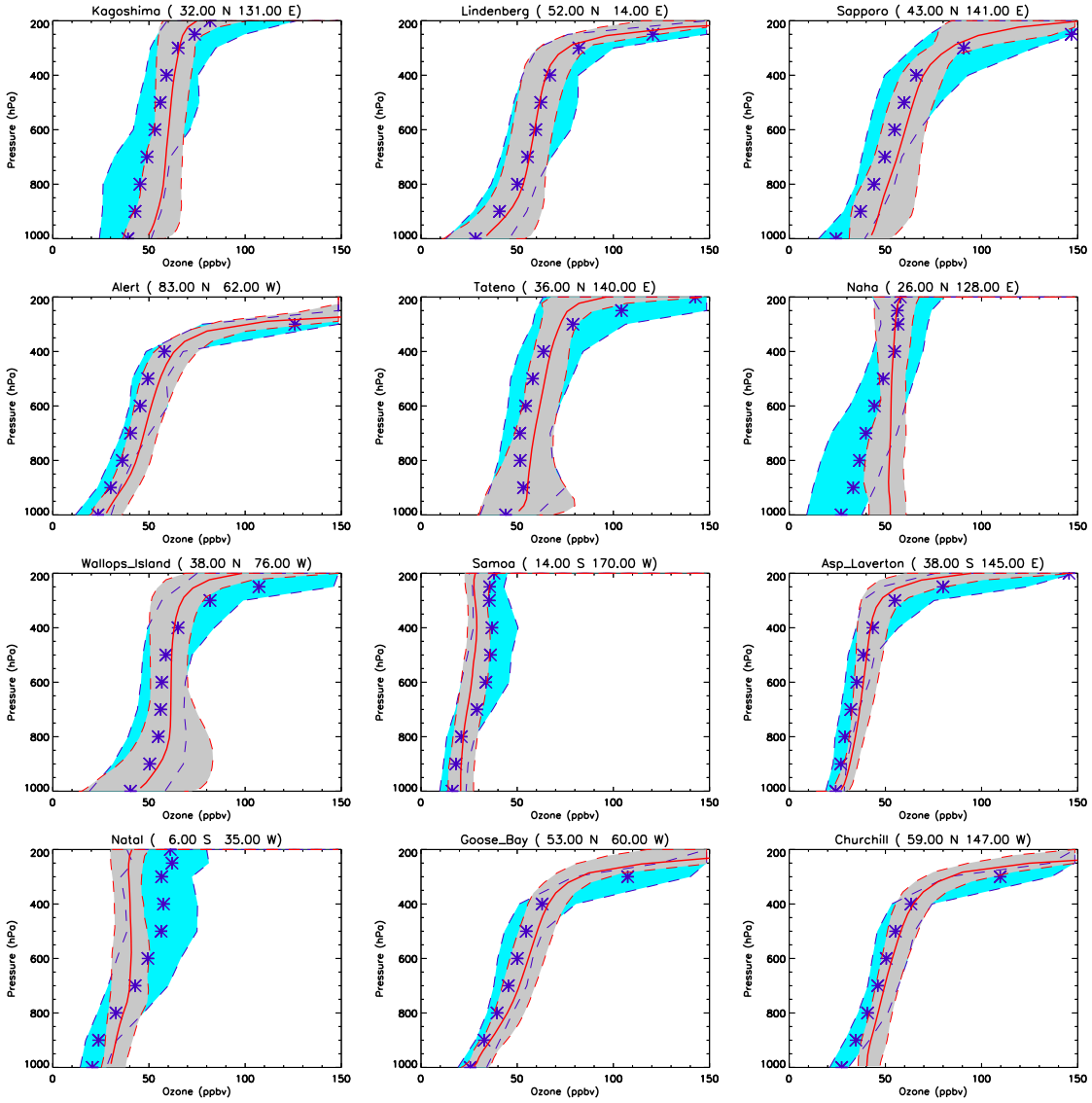

FIGURE 3.10: Annual average vertical profiles of ozone mixing ratio for time period 1991-2000 for HadGEM2-ES (Red line) and observations (Blue asterisks) from ozone sondes (Logan, 1999). The shaded areas (grey for model and blue for observations) indicate the range (minimum to maximum) of monthly values. All ozone concentrations are in ppbv.

The comparison indicates that the model compares well with the observations at the majority of sites capturing the vertical trends well throughout the atmosphere. The model

does however tend to have a positive bias at the surface level with the greatest biases seen at Sapporo, Naha and Churchill where root-mean-square annual errors are 16.3 ppbv, 26.6 ppbv and 14.0 ppbv respectively. Overall, when average across all of the sites the model has a bias of 9.6 ppbv at the surface (1000 hPa) indicating good agreement with observations. In the upper troposphere, towards the tropopause level, the model tends to underestimate the observed ozone concentrations with this most pronounced at Natal. Here ozone concentrations are up to 20 ppbv lower in the model above the 600 hPa pressure level.

At the model tropopause, a key region in the atmosphere for the calculation of the radiative effects of greenhouse gases such as ozone, the average root-mean-square annual error across all sonde stations was calculated as 52.8 ppbv (ranging between 25.9 ppbv and 83.6 ppbv). This indicates that the model provides a reasonable match for the observations around this region. Finally, as shown in Figure 3.10, the model tends to have a reduced annual cycle (defined by the shaded regions in the figure) compared to the observations indicating lower variability in ozone concentrations throughout the year. The comparisons with climatological observations show that overall, HadGEM2-ES produces good agreement with observations in the vertical domain.

3.5.4.3 HadGEM2-ES: Comparison with surface CO data

Figure 3.11 shows observed versus modelled climatological monthly mean CO for HadGEM2-ES during the period 1991-2000. For these comparisons the observations are obtained from the WDCGG (see Table 3.10 for reference) for a subset of the stations used for the evaluation of the TOMCAT CTM in Section 3.5.3.3. This subset of stations was chosen as these stations provided the best coverage of CO data during the 1991-2000 period for calculation of climatological means. Table 3.17 shows the normalised model mean bias for each site.

HadGEM2-ES performs best at Assekrem, Mace Head and Ragged Point where normalised model mean biases are 1.3 %, 1.1 % and 5.8 % respectively. There is less good agreement over the remaining sites where biases lie in the range −8.8 % to 29.9 %. In contrast to the TOMCAT model (Table 3.12), HadGEM2-ES tends to have a positive bias towards the observations though overall tends to have biases that are lower in magnitude (−8.8 % to 29.9 %) than those for TOMCAT at the same stations (−39.8 % to 21 %). As shown for

TABLE 3.17: Normalised Model Mean Biases (NMMB) for modelled versus observed surface CO for HadGEM2-ES.

		NMMB
Site	Ascension Island	18.8 %
	Assekrem	1.3 %
	Izaa (Tenerife)	11.8 %
	Key Biscayne	26.1 %
	Mace Head	1.1 %
	Ragged Point	5.8 %
	Ryori	-8.8 %
	Tierra del	29.9 %
	Sede Boker	29.5 %

TOMCAT, at locations where there is a strong influence of anthropogenic emissions on CO concentrations (e.g. Ryori) the HadGEM2-ES tends to underestimate observed CO at the surface during the winter months with better agreement shown during the summer months. This underestimation of winter CO is also seen at locations such as Mace Head and Ragged point which could be influenced by long range transport of polluted air masses from industrialised regions over N America. This suggests, that anthropogenic emissions of CO may be underestimated in HadGEM2-ES. Finally, at most locations HadGEM2-ES tends to provide a good estimation of the seasonal trend in CO throughout the year.

3.5.4.4 HadGEM2-ES global mean burdens.

Table 3.18 shows the mean annual global burdens of ozone, CO and NO_x along with the mean mass weighted tropospheric OH concentration for HadGEM2-ES under present day conditions.

The mean annual tropospheric ozone burden is calculated at 292.9 Tg which is approximately 20 Tg lower than that calculated for the TOMCAT CTM (312.2 Tg). The burden for HadGEM2-ES falls towards the lower end of the range of quoted by Wild (2007) (307±38 Tg(O_3)). This indicates that HadGEM-ES provides a simulation of tropospheric ozone in agreement with the present generation of CTM and GCM models.

For both CO and NO_x HadGEM2-ES produces mean global annual tropospheric burdens of 413 Tg(CO) and 0.70 Tg(NO_x) respectively. For comparison these are higher than the respective burdens calculated for TOMCAT (under the updated deposition scheme) which

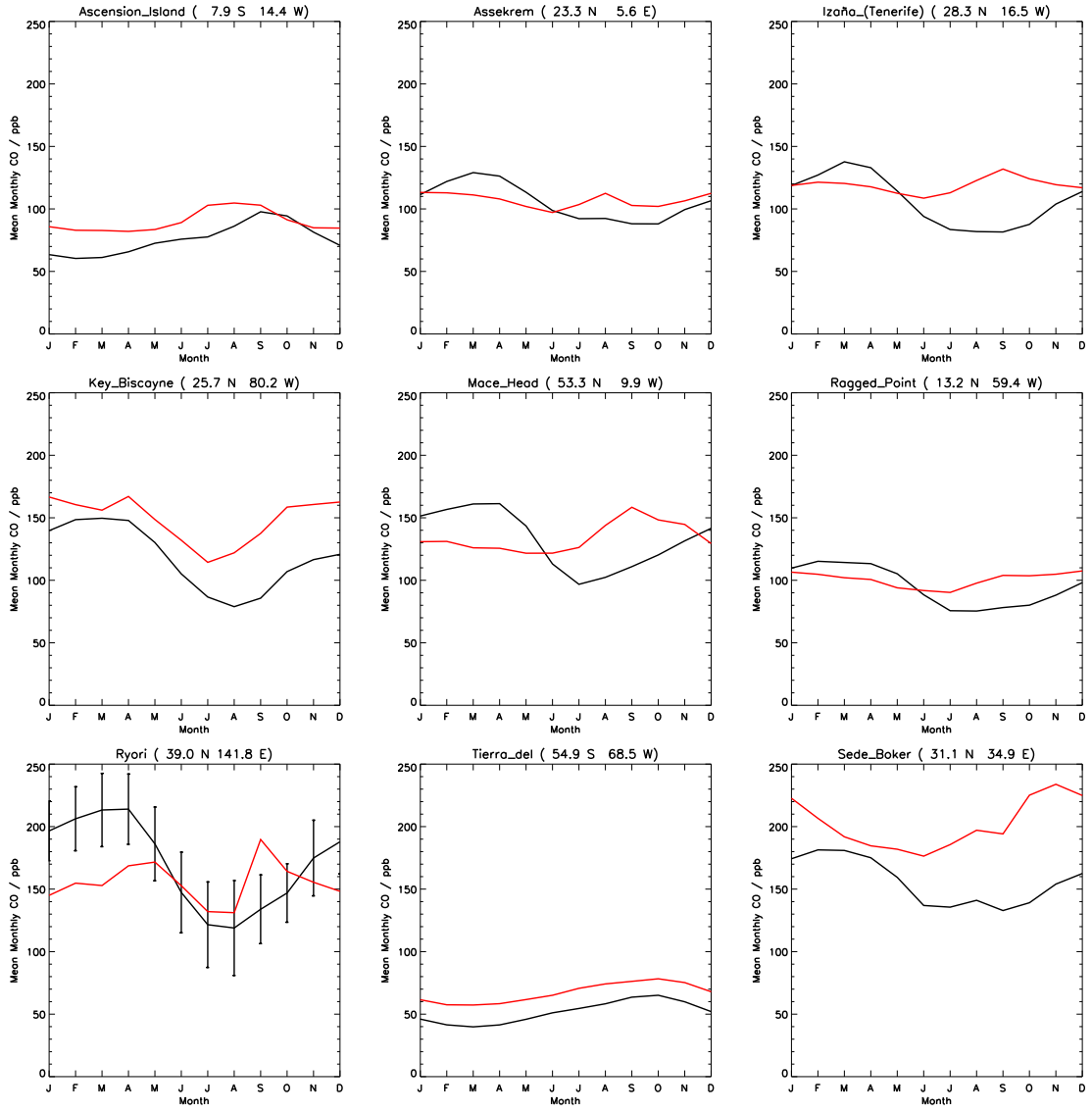

FIGURE 3.11: Climatological monthly mean surface CO concentrations from monitoring stations (black line) and the HadGEM2-ES (red line) for the time period 1991-2000. Error bars indicate 1 standard deviation on the monthly mean observations. All values are in ppbv.

determines a burden of 327.8 Tg(CO) for CO and 0.38 for NO_x Tg(NO_x). These differences could be linked to a number of factors including the different emissions and biomass burning fields prescribed to the model as well as the different chemical schemes each model utilises. The OH concentration for HadGEM2-ES (0.743×10^6moleculescm^{-3}) is of a similar order of magnitude to that for TOMCAT (0.960×10^6moleculescm^{-3} under the updated deposition scheme) though is slightly lower. This is likely linked to different concentrations of VOCs (e.g. isoprene) and other trace species (including CO) in the

respective models which are oxidised by OH. This lower OH concentration in HadGEM2-ES could also be one of the likely causes of the higher CO burden than in TOMCAT due to the principal role oxidation by OH plays as a CO sink in the atmosphere. This indicates that HadGEM2-ES produces reasonable estimates of the burdens of a number of key tracer species in the troposphere that are in agreement with those produced from a CTM model run for similar climate conditions.

TABLE 3.18: Mean annual global tropospheric burdens of ozone, CO and NO_x and mean mass weighted tropospheric OH concentration for HadGEM2 under present day climate conditions.

		Burden
Species	O_3 burden Tg(O_3)	292.9
	CO burden Tg(CO)	413.0
	NO_x burden Tg(NO_x)	0.70
	OH (10^6moleculescm^{-3})	0.743

3.6 Summary

In this Chapter, the TOMCAT CTM and HadGEM-ES models have been described in full and how they will be used to perform the model runs in this Thesis. A new updated dry deposition and land classification scheme has been added to the TOMCAT model with the impacts of this update on atmospheric composition discussed. The updated version of TOMCAT has then been evaluated against surface site and aircraft campaign observational data.

The impact of updating the dry deposition scheme in TOMCAT sees an increase in the rate of dry deposition of a number of trace species due to the improved resolution of land PFT classification and the improvement in the parametrisation of the seasonality of sea-ice. TOMCAT simulated ozone was compared to surface site and aircraft campaign observations with the standard model tending to overestimate ozone concentrations at the surface and throughout the free troposphere over the majority of regions. The inclusion of the updated dry deposition scheme results in a reduction in ozone concentrations throughout the troposphere leading to better agreement with the observations. The drop in ozone concentrations is more pronounced in the northern hemisphere due to the updated sea-ice

parametrisation which results in higher deposition rates over land masses leading to lower ozone concentrations.

Concentrations of CO are shown to be lowered in the troposphere in response to the higher deposition rates and a rise in the mean mass weighted OH concentration due to the enhanced deposition of VOCs and other tracer species that react with OH. Model biases to observations were shown to increase slightly in response to the updated land use scheme however the model captured the seasonal variation of CO concentrations well with best agreement shown in the summer months. Over the more industrialised northern hemisphere regions in the winter TOMCAT was shown to underestimate CO with both the standard model and the updated land scheme. This indicates that TOMCAT potentially under estimates anthropogenic CO emissions sources in these regions. NO_x concentrations show varying responses to the updated land scheme depending on location and height within the troposphere. This variation is due to a combination of changing rates of dry deposition and the resultant impacts on the concentrations of NO_x itself and other tracer species that play an important role in NO_x chemistry (e.g. PAN and VOCs). Overall however the inclusion of the updated land scheme leads to better agreement between the model and observational data.

Finally, the inclusion of the updated dry deposition scheme led to a reduction in the burdens of ozone and CO of 1.1 % and 1.2 % respectively and a rise in the burden of NO_x of 2.7 %. The mean global mass weighted OH concentration was shown to rise slightly by 0.3 %. This had the effect of lowering the CH_4 lifetime slightly by 0.02 years.

The evaluation of HadGEM2-ES ozone and CO output showed good agreement with climatological observations from both surface monitoring stations and ozone sonde data and was shown to calculate an ozone burden in good agreement with previous estimates of present day atmospheric conditions. The tropospheric burdens of CO, NO_x and OH were also shown to provide a good representation of present day atmospheric conditions. In this Chapter, the HadGEM2-ES model was run with the ozone damage parametrisation included. The impacts of including ozone damage in the model and the subsequent feedbacks on atmospheric chemistry will be discussed in further detail in Chapter 6 of this Thesis.

Chapter 4

Intercontinental trans-boundary contributions to ozone-induced crop yield losses in the Northern Hemisphere

4.1 Introduction

This chapter presents the first estimate of the impact of ozone precursor emissions from each of the Northern Hemisphere's major industrialized regions on crop yields. The TOMCAT CTM is used to estimate four metrics (AOT40, M7, M12 and W126) to assess the impacts of 100 % reductions in anthropogenic NO_x emissions from North (N) America, South East (SE) Asia and Europe on global and regional exposure of 6 major agricultural crop types to surface ozone, and resultant crop production losses during the year 2000 growing season. This Chapter presents the first estimates of the impact of intercontinental trans-boundary pollution on crop yields using a range of available metrics in a standardized manner.

4.2 Present understanding of the impact of ozone exposure on crop yields.

Ozone-induced crop yield reductions have been suggested to lead to economic loss and to threaten food security. This is of increasing concern, especially where the expanding economy has resulted in increased emissions of ozone precursors (Adams et al., 1982; Aunan et al., 2000; Holland et al., 2002; Li et al., 1999; Wang and Mauzerall, 2004).

Overall, emissions reductions in response to monitoring of exceedences of air quality standards (AQSs) set in health and vegetation exposure guidelines, have in part resulted in the decrease in the frequency of peak ozone levels since the 1990s (Lin et al., 2001; Soldberg and Lindskog, 2005). However as many economies are still growing rapidly (in particular those in southern and eastern Asia), the emission of ozone precursor trace gases in the Northern Hemisphere (NH) is expected to continue to rise (Zhang et al., 2009). Many observational and modelling studies have quantified contributions to regional surface ozone concentrations from import of ozone and its precursors from continental regions upwind (Dentener et al., 2010; Derwent et al., 2004; Hudman et al., 2004; Parrish et al., 2010). These studies have inferred contributions of between 2 and 10 ppbv to surface ozone in western Europe and western North (N) America from ozone precursor emissions in N America and Asia, respectively. European emissions also impact surface ozone in South East (SE) Asia by 0.2 to 3.5 ppbv (Duncan and Bey, 2004; Fiore et al., 2009; Wild et al., 2004). However, due to a paucity of strong cyclogenisis and frontal activity over Central and Eastern Europe, export of European emissions eastwards is somewhat less efficient compared with N American and Asian pollution export (Stohl, 2001). These inter-continental transport contributions to surface ozone can lead to exceedences of regional AQSs, and may become significant in the context of threshold limits for safe human health and vegetation exposure. As European and N American ozone precursor emissions continue to decline, rising East Asian emissions may play an increasing role in controlling NH background ozone (Cooper et al., 2010; Jacob et al., 1999), which has seen increases over the past 30 yr (Cooper et al., 2010; Derwent et al., 2004). Intercontinental contributions to crop ozone exposure and yield reductions have not yet been quantified, but are important to understand in the context of expected future changes in ozone precursor emissions in the Northern Hemisphere and other environmental threats to food security.

Recent studies (Avnery et al., 2011a,b; Roy et al., 2009; Tong et al., 2009b; Van Dingenen et al., 2009) have assessed the exposure of crops to ozone over various regions of the world using atmospheric models to provide the necessary regional or global ozone concentration fields for the analysis. Van Dingenen et al. (2009) estimate the global impact of surface ozone on four major agricultural crops (wheat, rice, soy and maize) under current and future emission scenarios, focusing in particular on the impact of relative yield losses on production losses in terms of the reduced yield due to ozone exposure and the associated economic losses. They estimated that present day yield losses (the reduction in yield compared to a theoretical case of no exposure of the crops to ozone) lie in the range of 7 % and 12 % for wheat, between 6 % and 16 % for soybean, between 3 % and 4 % for rice and between 3 % and 5 % for maize. Avnery et al. (2011a) estimate similar yield losses for the year 2000 showing wheat relative yield losses of 3.9 to 15.4 %, soybean relative yield losses of 8.5 to 13.9 % and maize yield losses of 2.2 to 5.5 %. Van Dingenen et al. (2009) also show that by 2030 (under a current legislation scenario) the global situation is expected to deteriorate mainly for wheat (additional 2–6 % loss globally) and rice (additional 1–2 % loss globally). They also estimated that using 2000 world market prices, the total global economic cost would be in the range of $14 to $26 billion. Avnery et al. (2011b) also estimated the damage due to ozone exposure, showing that the projected global economic loss by 2030 would fall in the range of $12 to $35 billion (depending on emissions scenario used).

These studies aim to provide quantification of ozone damage to crops on a global, regional and national scale. However, no previous study has attempted to estimate the impact of ozone precursor emissions from each of the Northern Hemisphere's major industrialized regions on crop yields globally, locally and in continents downwind. In this chapter, a global chemical transport model was used to quantify the intercontinental contributions to ozone-induced crop production losses, due to anthropogenic NO_x emissions from N America, SE Asia, and Europe. A control simulation for 2000 was compared against 3 different emissions scenarios where a 100 % reduction is applied to anthropogenic NO_x emissions in each of the 3 regions separately. These scenarios were used to quantify contributions to regional crop production losses of six major crop types, from emission reductions in each region, using a range of ozone exposure metrics (AOT40, Mx and W126). The impact of how the use of these different metrics affects the conclusions regarding tranboundary crop production loss contributions is also determined. Section 4.3 reviews the metrics

TABLE 4.1: Definitions of the ozone exposure indices. n is the number of hours in the growing season, C is the hourly ozone concentration and i is the hour index.

Index	Definition	Unit
AOT40	AOT40 $= \sum_{i=1}^{n}$ [C-40]$_i$ for C $\geq$40 ppbv	ppm h
M7	M7 $= \frac{1}{n}\sum_{i=1}^{n}$ [C]$_i$ for 09:00–15:59 h C	ppbv
M12	M12 $= \frac{1}{n}\sum_{i=1}^{n}$ [C]$_i$ for 08:00–19:59 h C	ppbv
W126	W126 $= \sum_{i=1}^{n}\left[\frac{C}{1+4403exp(-0.126\times C)}\right]_i$ for C $\geq$0 ppmv	ppm h

used to assess the ozone exposure risk of vegetation. Section 4.4 describes the TOMCAT chemical transport model, the exposure response relationships used to quantify the impact of ozone exposure on crop relative yield loss and production and the crop data sets used in this Chapter. Section 4.5 presents a model versus observations comparison of surface ozone concentrations and the different metrics along with the projected impact of the emissions reductions on crop production loss and the different impact on crop production figures. Section 4.6 discusses the estimated transboundary effects of the emissions cuts. A summary of the findings of this Chapter are presented in Section 4.7.

4.3 Metrics used to assess ozone exposure risk of vegetation

There have been a large number of field studies carried out to assess the response of crops to ozone exposure, especially in N America and Europe, and to a lesser extent in South and East Asia (Emberson et al., 2009). Mills et al. (2007) review two major studies: the US National Crop Loss Assessment Network (NCLAN) studies conducted in the 1980s (Heagle, 1989) and the European Open Top Chamber Programme (EOTCP) conducted in the late 1980s and early 1990s (Jager et al., 1992). These studies aimed to establish the response of crops to exposure to ozone and the resultant losses in yield. Mills et al. (2007) review a large set of crops to exposure to ozone data from a number of sources in the existing literature (including data from the above coordinated field experiments) in order to derive exposure-response functions for a set of 19 European agricultural and horticultural crops.

In addition to AQSs adopted to protect human health, AQSs for the protection of vegetation have been adopted in Europe (Fowler et al., 2008). Compared to those for vegetation, human exposure AQSs tend to focus on acute ozone pollution episodes rather than longer-term chronic exposure. As such, it is questionable whether human health AQSs will protect ecosystems. The AOT40 (accumulated exposure over a threshold of 40 ppbv) metric has been adopted in Europe (EEA, 1999) to assess risk to vegetation from ozone exposure, and has been used to estimate changes in crop yield losses due to ozone exposure in different global regions (Van Dingenen et al., 2009; Wang and Mauzerall, 2004). The United Nations Economic Commission for Europe (UNECE), and the World Meteorological Organization (WMO) set a critical threshold value of AOT40 at 3 ppm h daylight hour accumulated ozone exposure, which should not be exceeded during the plant growing season (WHO, 2000). In the United States, as of 2007, the USEPA has set equal primary and secondary standards for the protection of human health and human welfare (including damage to crops) respectively, with a peak 8 h mean ozone concentration not to exceed 75 ppbv more than three times a year (USEPA, 2010b). The USEPA is currently in the process of revising these AQSs (USEPA, 2010a).

The USEPA also proposed the W126 metric as a secondary standard to assess potential vegetation damage from ozone exposure (FederalRegister, 2008). This is used by several Federal agencies in the United States as well as by researchers (Wang and Mauzerall, 2004). The W126 metric is defined as the sum of hourly ozone concentrations (weighted by a sigmoidal weighting function) during daylight hours through the period of a crop growing season. W126 does not have a threshold value but the weighting function places more emphasis on higher ozone concentrations, hence like AOT40, W126 acts to emphasize both the peak and duration of ozone concentrations to which vegetation is exposed (Tong et al., 2009a).

A third set of standards developed to assess ozone impacts on vegetation are M7 and M12 (collectively referred to as Mx), as described in (Tong et al., 2009a). These indices are calculated over 3 consecutive months of a plant growing season, and defined as the mean daytime 7 h (M7) and 12 h (M12) surface ozone concentrations. These indices differ from AOT40 and W126 in that they apply equal weighting to all ozone concentrations to which the plant is exposed. As the Mx indices are calculated during daylight hours, all ozone

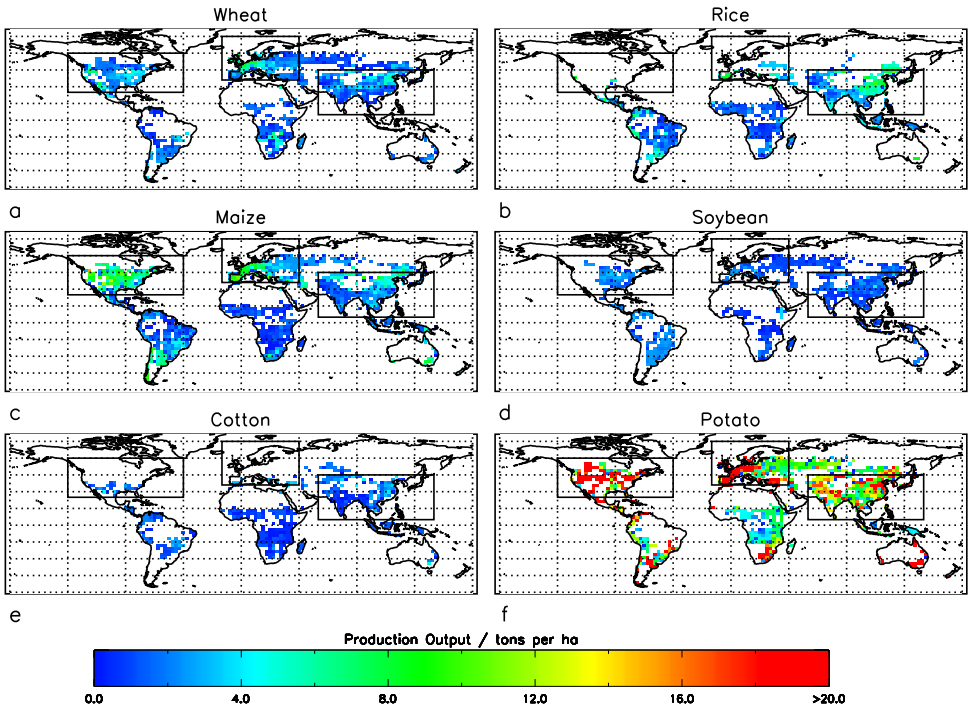

FIGURE 4.1: SAGE group (Sacks et al., 2010) derived crop locations and production output for the six crop types considered, with emissions reduction regions (N America, Europe and SE Asia) overlaid.

concentrations during this period contribute equally. Table 4.1 shows the definitions of each of the indices.

The Mx indices have been criticised for their inability to characterize different types of exposure regimes, partly as they have the potential to put more emphasis on the more numerous but less biologically significant lower ozone concentrations. However, concentrations that are less important in terms of plant damage are still able to cause some reduction in crop yields (Heck and Colwing, 1997). Using Mx can therefore account for any yield losses resulting from ozone concentrations of less than 40 ppbv, and the defined Mx Weibull relationship (see Table 4.2) used to relate ozone exposure to damage, results in less predicted damage at these lower ozone concentrations. This Weibull relationship can lead to a less severe, but similar threshold behaviour to that of the other metrics. These nuances are important to understand, especially since it has been demonstrated that damage to crops can still occur below 40 ppbv ozone exposure (Ashmore, 2005; Mills et al., 2011a; Sitch et al., 2007).

M7 and M12 have been used in a number of modelling studies to assess the impact of ozone on crop damage. Tong et al. (2009a) used a number of exposure and concentration based indices (including Mx, AOT40 and W126) to assess vegetation exposure to ozone over the United States using an air quality forecast model. M7 and M12 were also used in the USEPA's National Crop Loss Assessment Network (NCLAN) (Heck et al., 1984). Van Dingenen et al. (2009) concluded that AOT40's high sensitivity to small changes in ozone concentration close to the 40 ppbv threshold and to uncertainties in ozone concentration, made it less suitable as an indicator for crop losses in modelling-based studies. They also concluded that M7 can be more satisfactorily modelled, but is considered a less suitable indicator for crop exposure. Tong et al. (2009a) showed that W126, despite not having a threshold value, performed less satisfactorily from a modelling point of view, due to its weighting function putting more emphasis on higher ozone concentrations for which biases between the modelled and observed concentrations are larger.

An important aspect to consider is that the AOT40 index was designed to capture the most harmful effects from episodic ozone pollution. However now that background levels of ozone are increasing (Cooper et al., 2010; Derwent et al., 2004) these threshold indices are starting to become less useful. It has also been highlighted in previous modelling studies that large uncertainties can arise in using these exposure based indices to estimate yield loss from model ozone fields (Tong et al., 2009a; Van Dingenen et al., 2009). A more accurate approach is to develop plant response relationships that are based on the flux of ozone into the plant. However, at present flux-response relationships are only available for wheat and potato (Pleijel et al., 2004), and more recently tomato (Mills et al., 2011b). Not all of these have been parameterised for global application. As there is a much more comprehensive set of exposure-response relationships available to predict crop yield losses from the exposure based metrics, these were employed to include a range of major crops, and compare the results across ozone-tolerant and ozone-sensitive crops. However, it should be noted that it is difficult to assess the suitability of these concentration based indices for application in regions different from those in which they were developed (Emberson et al., 2009). Future work is needed to develop and implement flux-based metrics for predicting yield losses on the global scale.

TABLE 4.2: Ozone exposure/dose response functions to determine relative yield (RY) for wheat, rice, maize, soybean, cotton and potato based on the AOT40, M7, M12 and W126 indices. The AOT40 relationships are described in Mills et al. (2007). The M7, M12, and W126 relationships are described in Wang and Mauzerall (2004).

Crop	Metric	Exposure/dose response function: RY
Wheat	AOT40	$RY = -0.0161\,AOT40 + 0.99$
	M7	$RY = \exp[-(M7/137)^{2.34}]/\exp[-(25/137)^{2.34}]$
	W126	$RY = \exp[-(W126/51.2)^{1.747}]$
Rice	AOT40	$RY = -0.0039\,AOT40 + 0.94$
	M7	$RY = \exp[-(M7/202)^{2.47}]/\exp[-(25/202)^{2.47}]$
Maize	AOT40	$RY = -0.0036\,AOT40 + 1.02$
	M12	$RY = \exp[-(M12/124)^{2.83}]/\exp[-(20/124)^{2.83}]$
	W126	$RY = \exp[-(W126/93.7)^{3.392}]$
Soybean	AOT40	$RY = -0.0116\,AOT40 + 1.02$
	M12	$RY = \exp[-(M12/107)^{1.58}]/\exp[-(20/107)^{1.58}]$
	W126	$RY = \exp[-(W126/109.75)^{1.2315}]$
Cotton	AOT40	$RY = -0.016\,AOT40 + 1.07$
Potato	AOT40	$RY = -0.0057\,AOT40 + 0.99$

4.4 Methodology

4.4.1 TOMCAT chemical transport model and emissions scenarios

The global 3-D TOMCAT chemical transport model (CTM) (Arnold et al., 2005; Chipperfield, 2006) is used to simulate hourly global tropospheric ozone for the year 2000 under the control and each of the 3 emissions reduction scenarios. TOMCAT is forced using offline ERA-interim meteorological data from the European Centre for Medium Range Weather Forecasts (ECMWF), at a horizontal resolution of approximately $2.8° \times 2.8°$ with 31 hybrid sigma pressure levels from the surface to 10 hPa. Sub-grid transport from convection (Stockwell and Chipperfield, 1999) and boundary layer turbulence (Holstag and Boville, 1993) is parameterised. The model tropospheric chemistry includes methane, NO_x, C2-C3 VOCs, isoprene photochemistry, wet and dry deposition (Giannakopoulos et al., 1999), and NO_x emissions from lightning (Stockwell et al., 1999). Anthropogenic emissions were prescribed using the IPCC AR5 2000 emissions set (Lamarque et al., 2010) along with biomass burning emissions climatology from the Global Fire Emissions Database version 2 (GFED2) described in (van der Werf et al., 2006). In addition biogenic emissions were prescribed from the POET (Precursors of Ozone and their Effects in the Troposphere) database, used as described in Emmons et al. (2010). In order to assess the contribution

from anthropogenic NO_x emissions from N America, SE Asia, and Europe to ozone-induced crop damage, simulations for the year 2000 are repeated, applying a 100 % reduction to anthropogenic NO_x emissions over each of the source regions shown in Fig. 4.1.

The overall goal of this Chapter is to quantify the extent to which anthropogenic NO_x emissions from the major industrialised regions in the northern hemisphere contribute to ozone-induced crop yield losses, with an emphasis on quantifying trans-boundary impacts. To achieve this it was necessary to apply 100 % reductions to anthropogenic NO_x sources. Production of ozone in the troposphere varies non-linearly with changes to NO_x emissions. Hence, scaling from a more attainable emissions reduction of e.g. 20 % to total attribution is not trivial. Wild et al. (2012) and references therein show that scaling a 20 % emissions reduction by a factor of 5 can underestimate the response to a 100 % reduction. In the case of NO_x emissions, this non-scalable behaviour shows a strong seasonal dependence. In addition, the threshold nature of the AOT40 index means that its response to ozone precursor emission changes are not scalable.

In each of the simulations, emission cuts are applied only to anthropogenic surface emissions of NO_x. Biomass burning and natural NO_x emissions remain unchanged between the different scenarios. Aircraft emissions of NO_x also remain unchanged between simulations, since it is difficult to regionalize these emissions in terms of their attribution. Figure 4.2 shows NO_x emissions under the control and each of the emissions reduction scenarios. Hourly ozone concentrations were output from the midpoint of the lowest model layer, which is ∼30 m above the surface. To account for the concentration gradient of ozone in the lowest model layer (produced by deposition to the surface), model ozone was scaled to crop canopy height (assumed to be 1 m), using the approach of the Long-range Transboundary Air Pollution (LRTAP) Convention 2004, as described by Tuovinen et al. (2007).

4.4.2 Calculation of ozone exposure metrics and relative yield loss

The Mx, AOT40 and W126 exposure indices are calculated using modelled hourly ozone (scaled to crop canopy height). Using model AOT40, the relative yield loss (RYL) for 6 major crops is calculated: wheat, rice, maize, soybean, cotton and potato (Fig. 4.1). Mx is used to calculate RYL for 4 of the crops (wheat, rice, maize and soybean). The

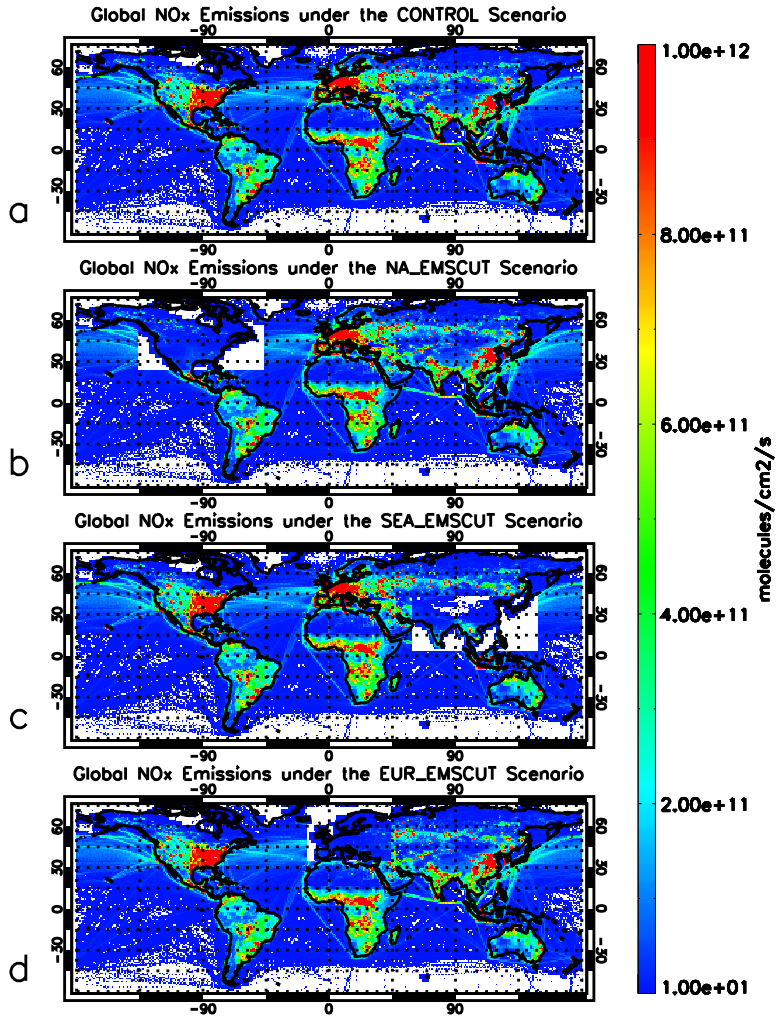

FIGURE 4.2: Global surface NO_x emission distributions under **(a)** the control and **(b–d)** each of the emissions cut scenarios.

W126 index is used to calculate RYL for 3 of the crops (wheat, maize and soybean). The choice of crops for each index is limited by the availability of exposure-response functions. Values are accumulated over a crop-specific growing season which is defined as the period between the planting date and the harvesting date for each of the crops considered (see Section 4.4.3). The use of crop-specific growing seasons allows a more realistic estimation of the exposure of crops to ozone damage, each of which grow for different periods of time in different locations. For Mx 7 h and 12 h daytime mean ozone are calculated over the duration of the same growing season used for AOT40. The approach of previous studies (Roy et al., 2009; Van Dingenen et al., 2009) is followed with daylight hours defined as a fixed 12-h period running from 08:00 to 19:59 local time (LT) for the calculation of AOT40, M12 and W126. For M7 a 7-h time period of 09:00 to 15:59 LT is used.

Firstly the relative yield (RY) for each crop is calculated based on the exposure-response

relationships compiled by Mills et al. (2007), which give linear exposure-response relationships as a function of AOT40 for the crops considered (Table 4.2). Using AOT40, allows consistent quantification of the impact of ozone exposure on both ozone sensitive (wheat, soybean and cotton) and moderately ozone tolerant (rice, maize and potato) crop types.

The AOT40 exposure-response relationships tend to have an intercept that is not equal to 1. In the case of some crops this can produce an offset that is high compared to the slope of the exposure-response relationship. Therefore a similar approach to that used in Van Dingenen et al. (2009) is adopted with the exposure response functions scaled to their value at AOT40 = 0 such that the relative yield is equal to 1 at zero exposure. Table 4.2 also summarises the exposure response relationships for the calculation of RY for wheat, rice, maize and soybean using Mx and wheat, maize and soybean using W126 from Wang and Mauzerall (2004). Finally in order to quantify the loss in crop yield as a result of ozone exposure, the RY values are converted to relative yield losses (RYL):

$$\mathrm{RYL} = 1 - \mathrm{RY} \tag{4.1}$$

Where RY is the value determined from the exposure-response functions in Table 4.2.

4.4.3 Crop data and calculation of crop production loss

The distributions and growing seasons for each crop are obtained from crop datasets from the Center for Sustainability and the Global Environment (SAGE) group at the University of Wisconsin (Sacks et al., 2010). These provide global-scale crop planting and harvesting dates for 19 widely-grown crops, covering 71 % of the world's crop growing areas, and harvested area and production output for 175 distinct crops of the world (Monfreda et al., 2008). The data are provided on a ~ 10 km by 10 km (5 min resolution) latitude-longitude grid and are produced by combining national, state and county level census statistics from 206 countries, and planting and harvesting dates from national and sub-national levels. Global maps of the crop locations are shown in Fig. 4.1.

The filled version of the crop calendar datasets are utilized, which provide a location-specific planting and harvesting date for every land point on the globe for each of the six major crop types considered. The crop location and harvest data are regridded to the 2.8°

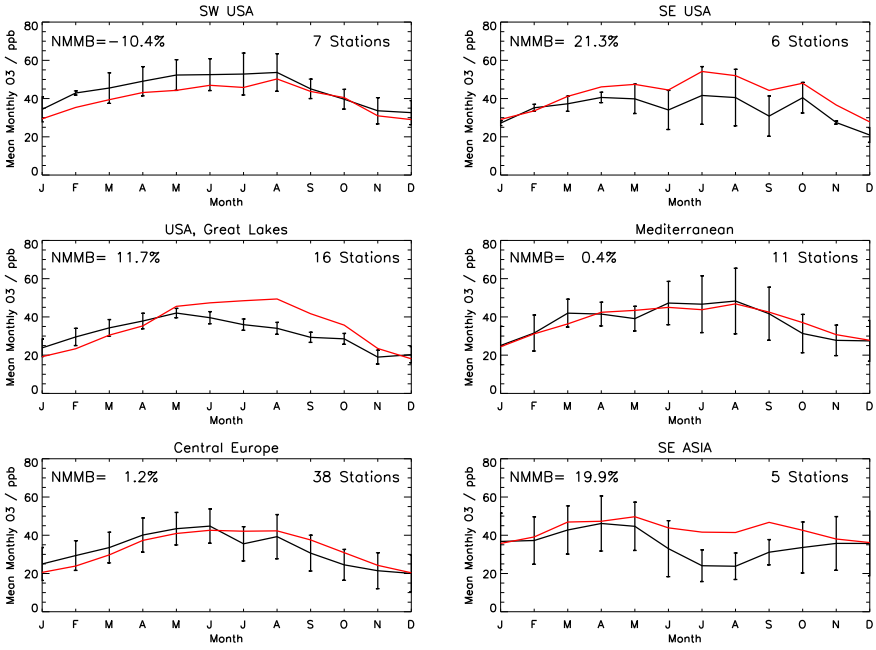

FIGURE 4.3: Regionally-averaged monthly-mean surface ozone concentrations from monitoring stations (black line) and the TOMCAT model under the control scenario (red line) for the year 2000. The model results are the means for the model gridboxes where the stations are located with the model ozone concentration scaled from 30 m (centre of surface gridbox) to 10 m (measurement sample height). Error bars indicate 1 standard deviation on the monthly mean observations. The normalised model mean bias (NMMB) is indicated for each region.

× 2.8° TOMCAT horizontal resolution. The crop-specific growing season is defined as the time in days between the planting and harvesting date for each land model gridbox.

AOT40, Mx and W126 are calculated for each crop on a global scale over the crop-specific growing seasons and then the the crop data is used to quantify regionally-aggregated relative yield losses (mean yield loss weighted according to area harvested and crop production output within each region) for each of the six major crops.

Crop production loss (CPL) is calculated based upon the relative yield loss, and the production output data:

$$\mathrm{CPL} = \frac{\mathrm{RYL}}{1 - \mathrm{RYL}} \times \mathrm{CP} \tag{4.2}$$

Where CP is the annual yield produced for each crop in the year 2000 given by Monfreda et al. (2008). CPL is calculated for each of the six crops on a global scale and over each of the 3 NH regions considered.

TABLE 4.3: Summary of regions used and data sources for model evaluation.

Region	lon, lat (min)	lon, lat (max)	# of stations	References
South-West USA	−125, 30	−110, 40	7	CASTNET[1]
South-East USA	−90, 25	−80, 35	6	CASTNET[1]
Great-Lakes USA	−95, 40	−75, 50	16	CASTNET[1]
Mediterranean	5, 35	30, 45	11	EMEP[2]
Central Europe	7, 48	17, 54	38	EMEP[2]
South-East Asia	110, 20	125, 35	5	WDCGG[3]

[1] CASTNET: http://java.epa.gov/castnet/epa_jsp/prepackageddata.jsp#ozone

[2] EMEP: http://tarantula.nilu.no/projects/ccc/emepdata.html

[3] WDCGG: http://gaw.kishou.go.jp/cgi-bin/wdcgg/catalogue.cgi

4.4.4 Model evaluation

Modelled surface ozone is evaluated using hourly ozone observations from the year 2000 averaged over several sites within each region, which is mainly taken from continuous ground based UV absorption based measurements. The data is obtained from the European Monitoring and Evaluation Programme (EMEP), the USEPA Clean Air Status and Trends Network (CASTNET) and the World Data Centre for Greenhouse Gases (WDCGG). Sites from varied location types, including both urban and rural locations, as well as coastal and inland locations are used, to provide coverage across polluted and relatively clean air locations. Sites from Japan, Malaysia, Nepal and China are used for the monthly-mean comparison over Asia, as these sites provided the best continuous surface level ozone on a monthly basis. Outside of Europe and N America, observations from the year 2000 are utilized where possible, but generally the ozone data used falls within the range 1995–2010 according to data availability. Hourly model output is taken from grid boxes containing each observation site position, before being averaged across sites within each region. Table 4.3, provides a summary of the regions compared as well as information on the sources of the observations. Modelled and observed monthly-mean ozone are compared, as well as the AOT40, Mx and W126 metrics where hourly observations allow.

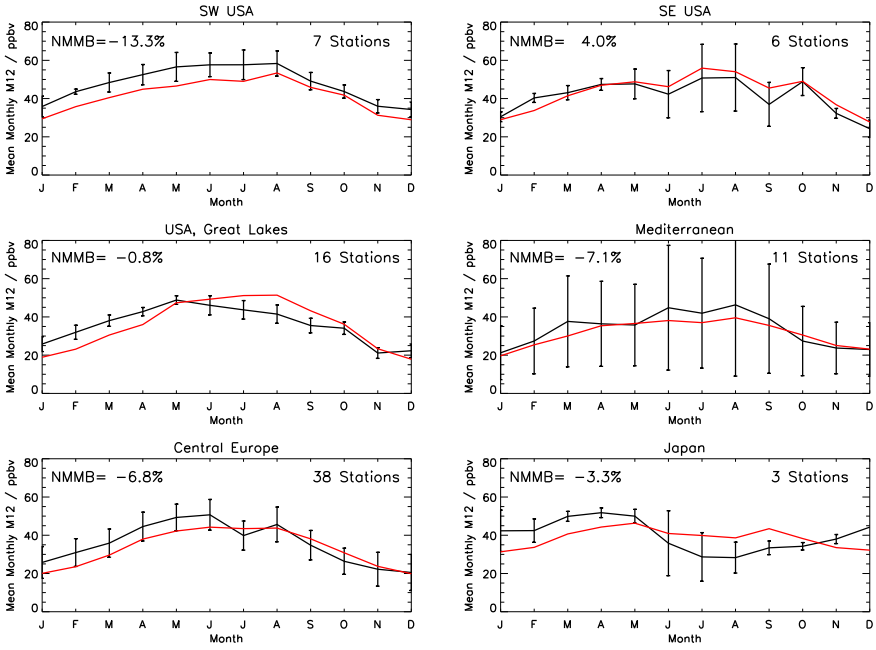

FIGURE 4.4: As Figure 4.3, but for the monthly-average M12 metric (see main text for definition).

4.5 Results

4.5.1 Comparison of model ozone concentrations and metrics with observations

Figure 4.3 shows observed and modelled monthly-mean ozone concentrations from the year 2000 control simulation for regions considered in the Chapter. For these comparisons, the model ozone at 30 m (the mid-point of the lowest model layer) was scaled using the approach of the LRTAPConvention (2004) to a height of 10 m, the height at which most of the observations are made.

The model performs well over Mediterranean, Central Europe and SW USA with normalized model mean biases of −10.4 % to 1.2 %. There is less good agreement over SE USA (21.3 % bias) and SE Asia (19.9 % bias), where the model overestimates observed ozone throughout the summer months. Over the Great Lakes, the model tends to perform better with a model mean bias of 11.7 % however summer ozone is also overestimated. Mean model surface ozone peaks above the 40 ppbv threshold limit of AOT40, over SW USA, and Central Europe during the summer months and over the Great Lakes and SE

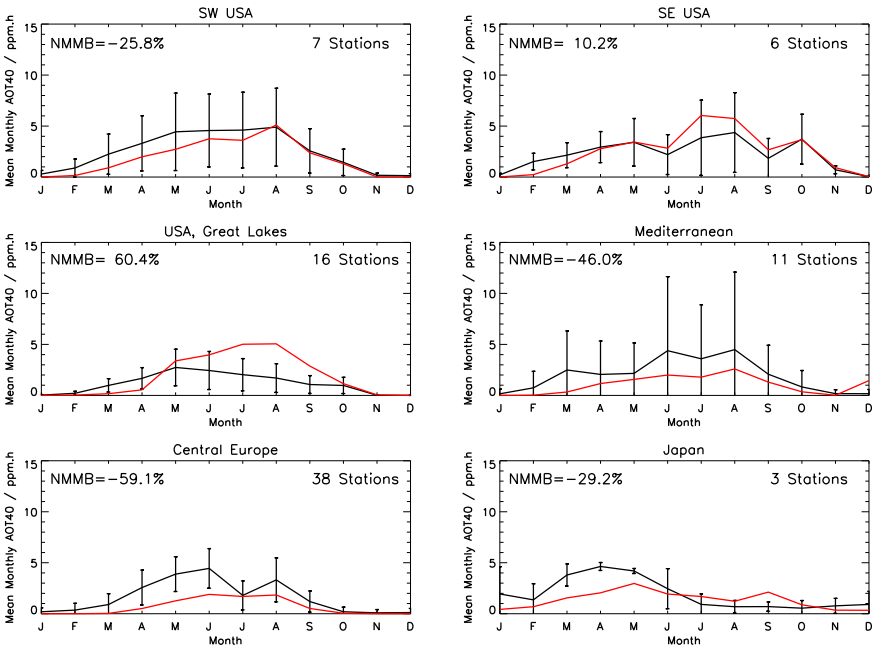

FIGURE 4.5: As Figure 4.3, but for the monthly-accumulated AOT40 metric (see main text for definition).

USA during the spring, which coincides with the growing season for many crops in the NH. Over SE Asia, a less distinct seasonal surface ozone cycle is seen due to the majority of the region lying within the tropical latitudes, where seasonality in insolation and its impacts on photochemistry are less pronounced. The positive model bias over SE Asia during the summer months could also be linked to the model inaccurately representing the monsoon period over SE Asia which typically runs from July to October. The monsoon brings the transport of marine air masses and weak photochemical activity, resulting in lower ozone concentrations than those during the pre-monsoon period (Zhao et al., 2010).

Figures 4.4, 4.5 and 4.6 compare model and observed M12, AOT40 and W126 indices respectively. The same regions are considered as in Fig. 4.3, except that SE Asia considers only Japan, since this is the only location in the region with continuous hourly surface ozone observations.

The M12 index shows good agreement over SE USA, the Mediterranean and Central Europe with the model mean biases falling between $-7.1\,\%$ and $4\,\%$. One particular region to note is SE USA, which sees a large improvement in agreement between the model and observed M12 compared to the comparison of monthly-mean ozone concentration. This indicates that the model over-predicts nighttime ozone. This may be linked to the surface

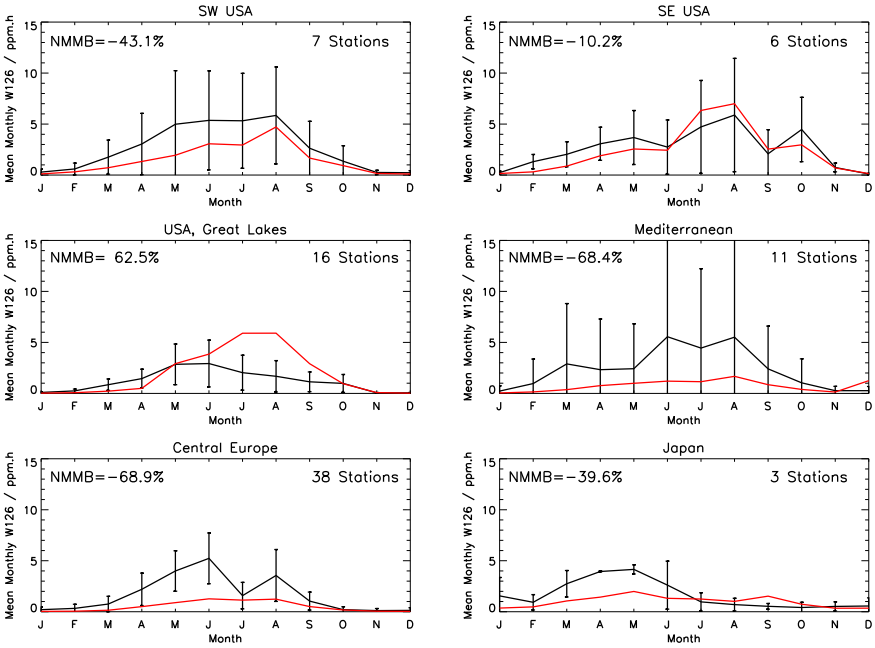

FIGURE 4.6: As Figure 4.3, but for the monthly-average W126 metric (see main text for definition).

model ozone having a potential positive bias in regions where model vertical mixing may be suppressed, as suggested by Avnery et al. (2011a) who also showed positive model biases over eastern parts of the United States. Over SW USA the model tends to underestimate observed M12, particularly during spring, where modelled M12 is about 5–10 ppbv less than observed. Over Great lakes and Japan, model M12 falls within one standard deviation of the observations during the months of May, June and July (a typical growing season in the NH) with the exception of throughout July over Great lakes. For these regions, model M12 generally has a low bias (−0.8 % and −3.3 % respectively). Overall, the model tends to overestimate summer M12 and underestimate spring M12.

The comparison of AOT40 shows similar model-observation differences as M12 (Fig. 4.5). However, these differences are amplified due to the combination of the cumulative nature of the metric along with that of a non-zero threshold, as also shown by Tong et al. (2009a). The differences are greatest over Central Europe (model mean bias of −59.1 %) and the Great Lakes (model mean bias of 60.4 %) with the best agreement over SW USA, SE USA and the Mediterranean.

For W126, the best agreement is also seen over the SW USA, SE USA and Mediterranean, where the modelled metric falls within one standard deviation of the observed W126

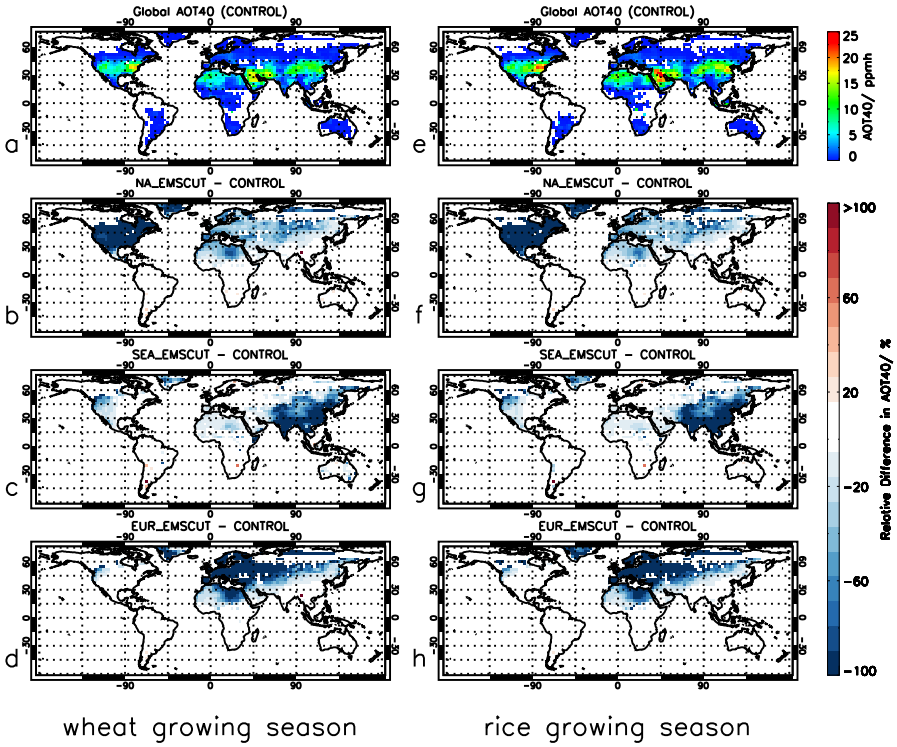

FIGURE 4.7: **(a)** Global AOT40 under the control model scenario for the wheat growing season; and relative difference in AOT40 between the control model and 100 % cut in anthropogenic NO_x emissions from **(b)** N America, **(c)** SE Asia, and **(d)** Europe for the same period. Panels **(e–h)** show the same but for the rice growing season.

(Fig. 4.6). The greatest differences are over Central Europe (model mean bias of −68.9 %) and the Great Lakes (model mean bias of 62.5 %). These large model biases reflect the cumulative nature of the W126 metric.

While larger than the biases for M12, those for AOT40 are comparable to model biases found in the recent global ozone crop exposure study of Van Dingenen et al. (2009). These biases may indicate that from a modelling perspective, AOT40 and W126 are less robust for assessing crop exposure to ozone than the concentration average Mx indices. This has also been suggested by Tuovinen et al. (2007). To account for the impacts of these model biases on the results, the simulated exposure metrics (Mx, AOT40 and W126) that are used to estimate crop production losses under each emissions scenario are bias corrected. The bias corrections and their impacts are discussed further in Sect. 4.5.3.

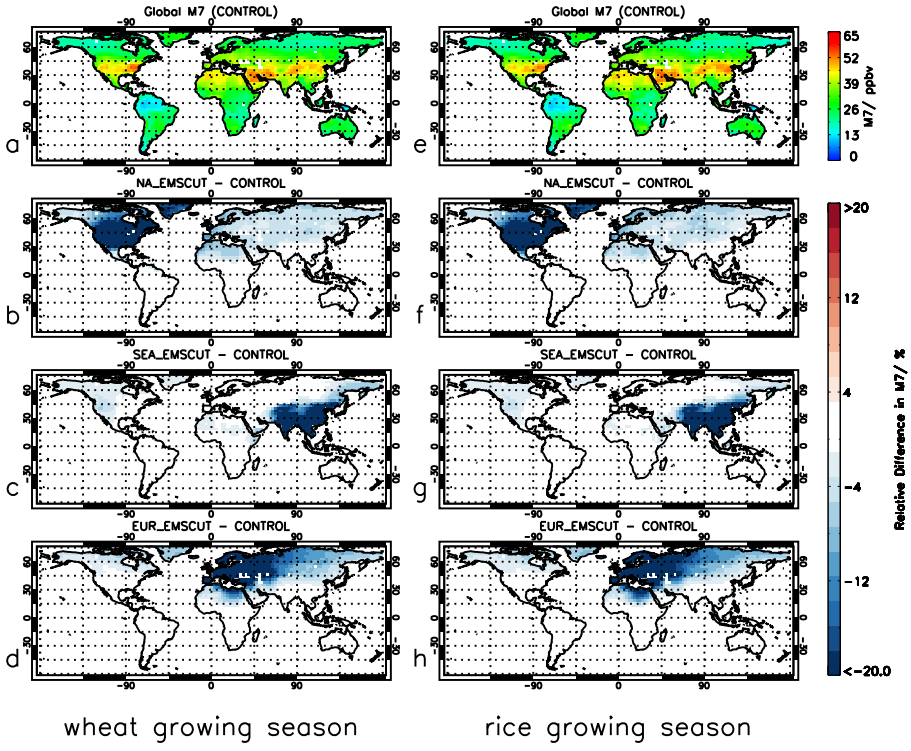

FIGURE 4.8: As Figure 4.7 but for the M7 metric.

4.5.2 Changes to exposure metrics under emissions reductions scenarios

Global relative differences in AOT40 between the control and each of the emissions reduction scenarios are shown in Fig. 4.7, along with global AOT40 calculated for control NO_x emissions over the growing seasons of two crops. Changes in AOT40 are shown for wheat (an ozone sensitive crop) and rice (an ozone tolerant crop). For both growing seasons the AOT40 index is particularly large over the major industrialized regions with peak AOT40 values approaching 20 ppm h over the eastern seaboard of the United States as well as over eastern China and the Middle East. The overall pattern is similar for both crop growing seasons, and the remaining 4 crops' growing seasons (maize, soybean, cotton and potato) exhibit similar changes in AOT40 under each emissions reduction scenario (see Appendix A). Local anthropogenic NO_x emission cuts result in a near 100 % relative decrease in AOT40 over each of the regions, although reductions over SE Asia are smaller (84.9 % for wheat growing season and 87.6 % for rice). The effect of anthropogenic NO_x emissions from each of the regions on AOT40 in downstream receptor locations is also evident. A 100 % reduction in N American anthropogenic NO_x emissions results in mean relative decreases in AOT40 over the European region of 51.8 % for the wheat growing

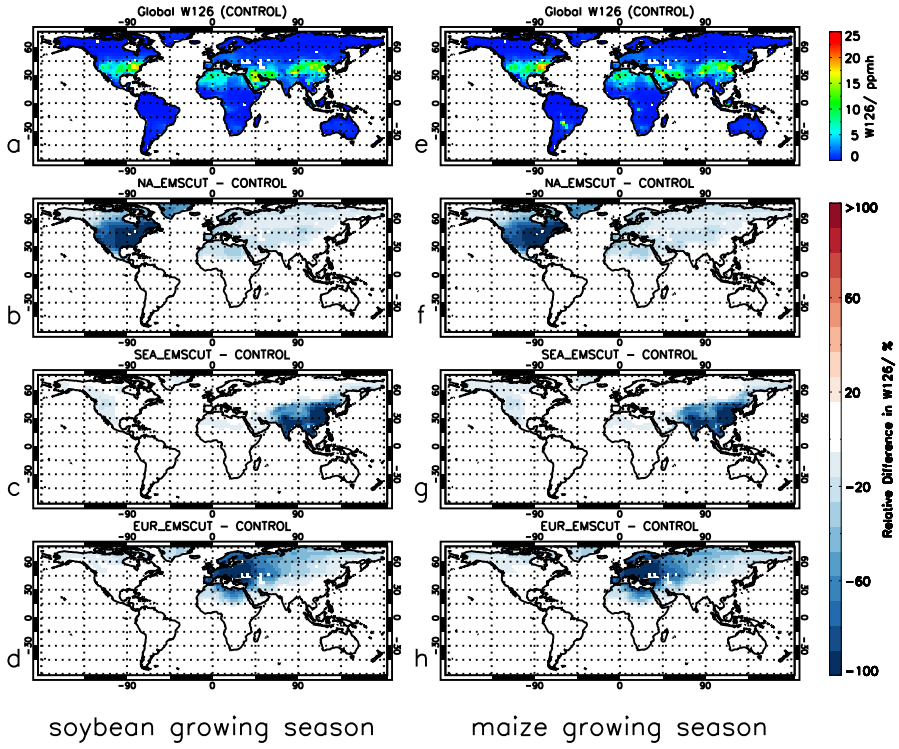

FIGURE 4.9: As Figure 4.7 but for the W126 index, and the soybean **(a-d)** and maize **(e-h)** growing seasons.

season and 49.2 % for rice, with decreases approaching 60 % over parts of north and western Europe. This transboundary effect extends into SE Asia with mean relative decreases in AOT40 of ∼16 % (over both crop growing seasons) and greatest reductions in AOT40 over western and northern parts of the region. A 100 % reduction in SE Asian anthropogenic NO_x emissions results 19.9 % to 21.0 % (range for changes in AOT40 for both growing seasons) reduction in AOT40 over N America with greatest decreases in AOT40 over the western seaboard of the US and parts of Canada and Greenland where reductions in AOT40 approach 60 %. A smaller impact is seen over the European region, where mean reductions in AOT40 range from 3.2 % to 4.2 %. The impact of a 100 % reduction in European anthropogenic NO_x emissions on AOT40 is slightly greater over SE Asia than over N America. Over SE Asia, mean regional relative decreases in AOT40 are ∼15 % with greatest reductions seen over parts of north western China and western Mongolia. The impact on N American AOT40 is ∼11 %, with reductions in AOT40 approaching 40 % over the west coast of the continental United States. Overall, reductions in anthropogenic NO_x emissions over N America produce the largest global impact on AOT40, with N American NO_x also producing the largest transboundary effect, shown by a mean reduction of 49.2 %

to 51.8 % in AOT40 over Europe. Additional calculations (not shown) suggest that the relative importance of NO_x emission reductions from each of the regions in reducing AOT exposure is invariant when the threshold of the AOT index is varied from 30 to 60 ppbv.

Figure 4.8 shows M7 mean ozone concentrations under the control scenario calculated over the same crops and growing seasons as for AOT40 (wheat and rice), and differences resulting from the three emission reduction scenarios. Anthropogenic NO_x emission reductions result in local reductions of M7 of 20 % or greater. Overall, the transboundary impacts of anthropogenic NO_x emission reductions on M7 are less pronounced than those on AOT40. A 100 % reduction in N American anthropogenic NO_x emissions reduces M7 by 5.9 % to 6.4 % over Europe, with greatest reductions over north and western parts. The impact on SE Asia is much less, with reductions in M7 for the region of 2.0 % to 2.4 %. A 100 % reduction in SE Asian anthropogenic NO_x emissions, results in decreases of 2.3 % to 2.4 % in M7 over the N American region, the largest reductions over western continental United States and Canada. The impact of the SE Asian emissions cuts on Europe is less than 1 %. Similar to AOT40, anthropogenic NO_x emissions reductions over Europe tend to produce approximately similar reductions in M7 over the N American and SE Asian regions, with mean regional relative decreases in M7 slightly larger over SE Asia (2.7 % for wheat growing season and 2.2 % for rice) than over N America (1.8 % for wheat growing season and 1.9 % for rice). Changes in the M12 metric over the maize and soybean growing season under each emissions scenario exhibit the same transboundary effects as those shown by M7 (see Appendix A).

Results using the W126 metric are shown in Fig. 4.9 for maize and soybean. The transboundary impacts show the same pattern as those for AOT40, with N America producing the largest transboundary impact on W126 over Europe, where a 100 % cut in anthropogenic NO_x over N America results in a 25.1 % decrease in European W126 during the soybean growing season and a 24.0 % decrease during the maize growing season.

Overall, reductions in anthropogenic NO_x emissions produce a similar pattern in the global AOT40, Mx and W126 fields with N American NO_x producing the largest global scale impact. N American emission reductions exhibit the largest transboundary effect, shown by the response of a range of metrics over Europe to a 100 % cut in anthropogenic NO_x over N America.

TABLE 4.4: Regionally-aggregated relative yield loss for the six crops under the model control scenario. M7 and M12 exposure response relationships are not available for potato and cotton. For these crops only yield losses based on AOT40 are presented. For W126 yield losses are shown for wheat, maize and soybean only. Values in brackets show bias-corrected results (see text for details).

CONTROL	WORLD	N AMERICA	SE ASIA	EUROPE
Wheat				
AOT40	5.8 (6.2) %	6.7 (7.1) %	10.5 (10.4) %	2.0 (2.9) %
M7	3.2 (3.5) %	3.3 (3.8) %	4.5 (4.4) %	2.6 (3.2) %
W126	1.2 (1.5) %	1.4 (1.7) %	2.4 (2.7) %	0.2 (0.7) %
Rice				
AOT40	1.4 (1.4) %	3.2 (3.4) %	1.6 (1.6) %	0.7 (1.0) %
M7	0.9 (0.9) %	1.6 (1.8) %	1.1 (1.1) %	0.9 (1.2) %
Maize				
AOT40	2.5 (2.6) %	3.5 (3.7) %	3.1 (3.1) %	0.7 (1.0) %
M12	3.4 (3.7) %	3.9 (4.4) %	4.5 (4.5) %	2.6 (3.1) %
W126	0.04 (0.06) %	0.05 (0.08) %	0.07 (0.08) %	0.0004 (0.004) %
Soybean				
AOT40	7.1 (7.5) %	11.8 (12.5) %	8.6 (8.4) %	2.6 (3.8) %
M12	10.5 (11.4) %	15.1 (16.3) %	13.7 (13.5) %	10.3 (11.9) %
W126	2.6 (2.9) %	4.3 (4.9) %	3.0 (3.3) %	0.9 (1.9) %
Cotton				
AOT40	11.2 (12.0) %	16.1 (17.1) %	13.4 (13.2) %	7.9 (11.6) %
Potato				
AOT40	1.9 (2.0) %	2.5 (2.6) %	4.5 (4.4) %	0.4 (0.7) %

4.5.3 Ozone-induced relative yield losses for 2000 under the model control scenario

Table 4.4 shows regionally-aggregated ozone-induced relative yield losses for the control model scenario based on the different metrics derived from standard model ozone, and bias-corrected metrics. Bias-corrected values are calculated by normalising simulated values of the metrics in each source/receptor region by the regional modelled:observed ratios for each metric. For locations where the model bias is not calculated explicitly, the global mean modelled:observed ratio is applied.

Globally, wheat, soybean and cotton are the most sensitive of the crops to ozone damage. Relative yield loss values for wheat range from 1.2 (1.5) (standard model ozone metric (bias corrected metric)) to 5.8 (6.2) %, AOT40 producing the largest. Relative yield losses for soybean range from 2.6 (2.9) to 10.5 (11.4) % with M12 giving the largest. For cotton only yield losses based on AOT40 are presented, which show a global value of 11.2 (12.0) %.

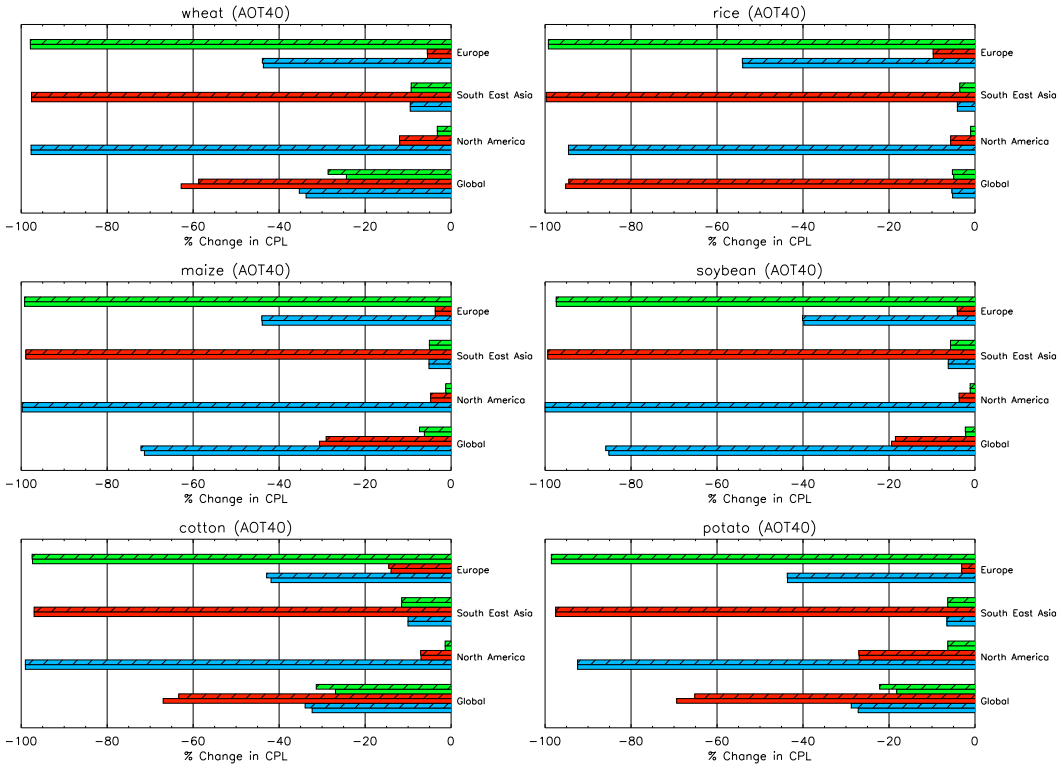

FIGURE 4.10: Percentage reductions in ozone-induced crop production loss for the 6 crops considered (based upon the AOT40 exposure index) resulting from 100 % regional cuts in anthropogenic NO_x emissions. The y-axis shows the receptor regions, and coloured bars indicate the impacts from emission cuts applied in each region compared to the control model (Green = European emission cut, Red = SE Asia emission cut and Blue = N America emission cut). Solid colour bars show results based on the standard model metric and hatched bars show results based on the bias-corrected model metric (see main text for details).

Rice and maize demonstrate higher tolerance to ozone exposure, with yield losses of around 0.9 (0.9) to 1.4 (1.4) % for rice and 0.04 (0.06) to 3.4 (3.7) % for maize. Potato yield losses are 1.9 (2.0) % globally, based upon AOT40.

A comparison with previous studies (Avnery et al., 2011a; Van Dingenen et al., 2009) shows the results presented in this Chapter produce a similar pattern of global relative yield losses for wheat, rice, maize and soybean (cotton and potato are not considered in Van Dingenen et al. (2009)) with wheat and soybean being the most sensitive crops to ozone exposure. Van Dingenen et al. (2009) also demonstrate largest relative yield losses produced from AOT40 values for wheat, and M12 producing the largest relative yield losses for soybean. The yield loss values calculated here for wheat (1.2 (1.5) to 5.8 (6.2) %) and soybean (2.6 (2.9) to 10.5 (11.4) %) are smaller than those shown in Van Dingenen et al.

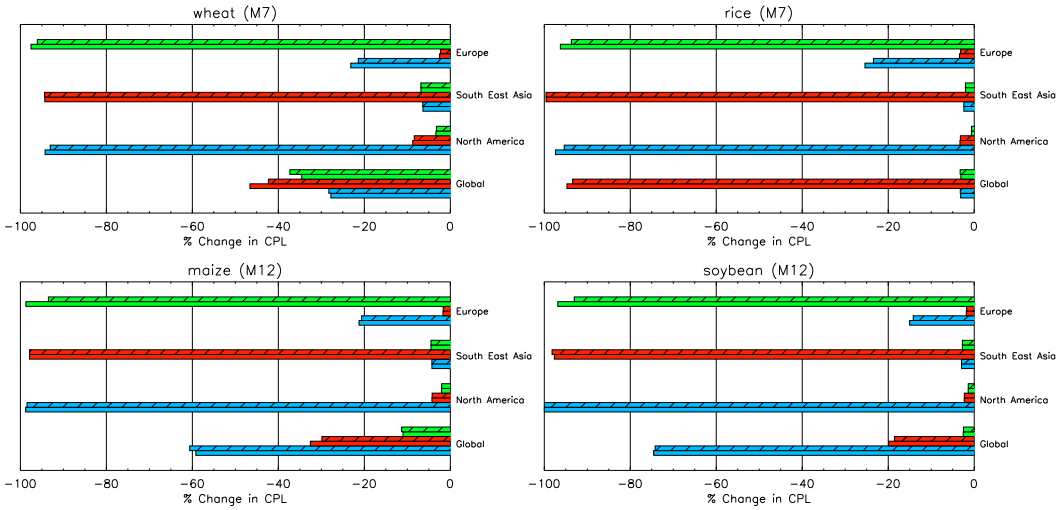

FIGURE 4.11: As Figure 4.10, but using the M7 and M12 metrics for 4 of the crops.

(2009) which were 7.3 to 12.3 % for wheat and 5.4 to 15.6 % for soybean. Yield losses are also shown to be smaller when compared to the findings of Avnery et al. (2011a) which show wheat relative yield losses of 3.9 to 15.4 % and soybean relative yield losses of 8.5 to 13.9 %. The relative yield losses for rice and maize (0.9 (0.9) % to 1.4 (1.4) % and 0.04 (0.06) % to 3.4 (3.7) %, respectively) are also smaller here than those of Van Dingenen et al. (2009) (2.8 to 3.7 % for rice and 2.4 to 4.1 % for maize) and Avnery et al. (2011a) (2.2 to 5.5 % for maize with rice not investigated). Van Dingenen et al. (2009) and Avnery et al. (2011a) both use data from the United States Department of Agriculture (USDA) to define the growing seasons. In addition, the surface ozone distributions produced from the different CTMs used are likely somewhat different. Nevertheless, the control scenario produces comparable magnitudes of yield losses to those described previously, including those presented using similar bias-correction.

Table 4.4 also shows the regionally-aggregated relative yield losses for the three individual regions. For rice and soybean, relative losses tend to be highest over N America (up to 15.1 (16.3) % for soybean and 3.2 (3.4) % for rice). For wheat and potato the relative losses are largest over SE Asia with losses of up to 10.5 (10.4) % for wheat and 4.5 (4.4) % for potato. For maize, relative yield losses based on M12 and W126 are highest over SE Asia (0.07 (0.08) % to 4.5(4.5) %) with relative yield losses based on AOT40 highest over N America (3.5 (3.7) %). Finally for cotton, highest yield losses are seen over N America with relative yield loss values of 16.1 (17.1) %. These regional relative yield losses are a

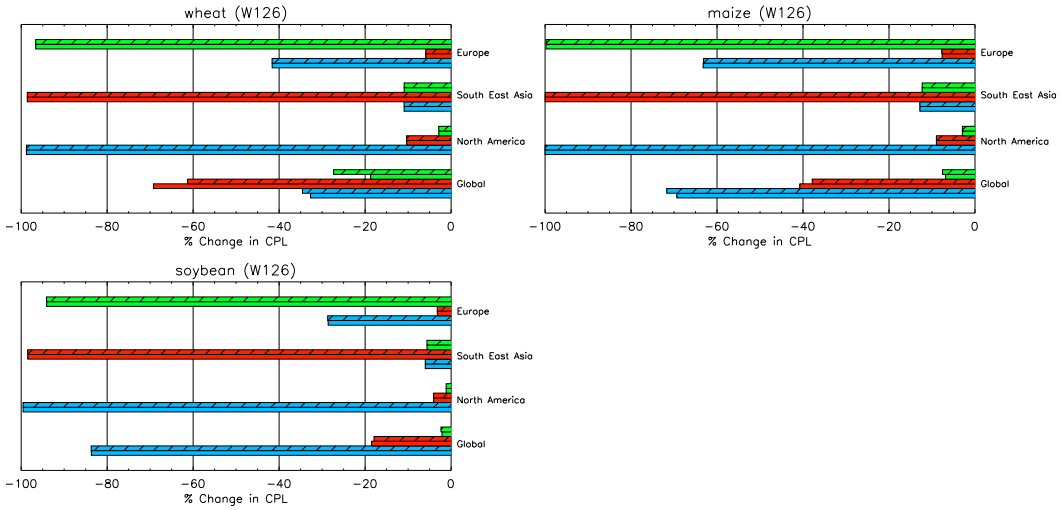

FIGURE 4.12: As Figure 4.10, but using the W126 metric for 3 of the crops.

function of the geographical locations of the crops, the amount of yield produced for each crop over each region, and the geographical pattern of elevated ozone.

4.5.4 Impact of regional cuts in NO_x emissions on ozone induced CPL

The impact of regional reductions in NO_x emissions on regionally-aggregated ozone-induced CPL calculated from AOT40 exposure is shown in Fig. 4.10 for six crop types for both standard model and bias-corrected ozone metrics. Figure 4.11 shows the impact on CPL for 4 of the 6 crop types based on Mx (using the M7 index for wheat and rice and the M12 index for maize and soybean) and Fig. 4.12 shows the impact on CPL for 3 of the crops (wheat, maize and soybean) based on W126. Globally, N American NO_x emission reductions result in largest changes to CPL for soybean and maize (59.2–85.1 % (60.6–85.9 % bias corrected)). SE Asian NO_x emission reductions result in largest changes to wheat, rice, cotton and potato CPL (46.6–95.2 % (42.3–94.4 % bias corrected)). This primarily reflects the geographical distributions of these six crops and their yield distributions. Local reductions in NO_x emissions result in near 100 % reduction in ozone-induced CPL over each of the regions, demonstrating that local emission controls and air pollution strategies could effectively mitigate ozone-induced production losses. However, ozone-related CPL for rice and potato grown in N America cannot be completely eliminated through local emissions reductions. This is shown for both the original and bias corrected model results.

In the European region, production losses are reduced by 15.0–63.2 % (14.2–63.1 % bias corrected) when cutting N American NO_x emissions. Maize CPL (based on W126) shows the most sensitivity to N American emissions (63.2 % (63.1 % bias corrected)) with cotton CPL (when based on AOT40) showing the greatest sensitivity to SE Asian NO_x sources (14.0 % (14.5 % bias corrected)). Soybean (based on M12) shows the lowest sensitivity to N American (15.0 % (14.2 % bias corrected)) emissions with maize (based on M12) showing the lowest sensitivity to SE Asian (1.71 % (1.67 % bias corrected)) emissions. When diagnosing the impact of emissions reductions it is shown for each individual metric that the impact of N American emissions on European CPL exhibits the largest intercontinental transboundary effect. Figures 4.10, 4.11 and 4.12 show that the minimum reduction in European CPL from N American emission cuts is larger than both the maximum European emissions impact on SE Asia and the SE Asian emission impact on N America. Over N America, the largest non-local impact on CPL results from SE Asian NO_x, with CPL reductions ranging from 27.0 % (based on AOT40) for potato (27.0 % bias corrected) to 2.3 % (based on M12) for soybean (2.3 % bias corrected). N American CPL reductions of 0.7–6.3 % (0.6–6.3 % bias corrected) result from reductions in European NO_x, with potato and wheat showing the largest sensitivities. On the whole, CPL of all six crops over SE Asia are reduced by approximately equal amounts as a result of N American and European emissions reductions. Cotton CPL show the greatest difference, with European emissions cuts producing a reduction in CPL of 11.5 % (11.4 % bias corrected) compared with a reduction of 10.0 % (10.0 % bias corrected) produced by N American emissions cuts.

Overall, the results exhibit that the inclusion of model bias correction does not have a significant effect on the transboundary effects deduced. When the bias corrected results are considered N American NO_x emissions still produce the largest non-local impact resulting in CPL reductions over Europe of 14.2–63.2 % (range over all crops and metrics accounting for bias correction).

4.5.5 Impact of regional cuts in NO_x emissions on crop production

Figure 4.13 shows the estimated changes in crop production under each of the emissions reduction scenarios for the standard and bias-corrected model metrics. These are the mean changes in production from all metrics considered for each of the crops (AOT40, MX and

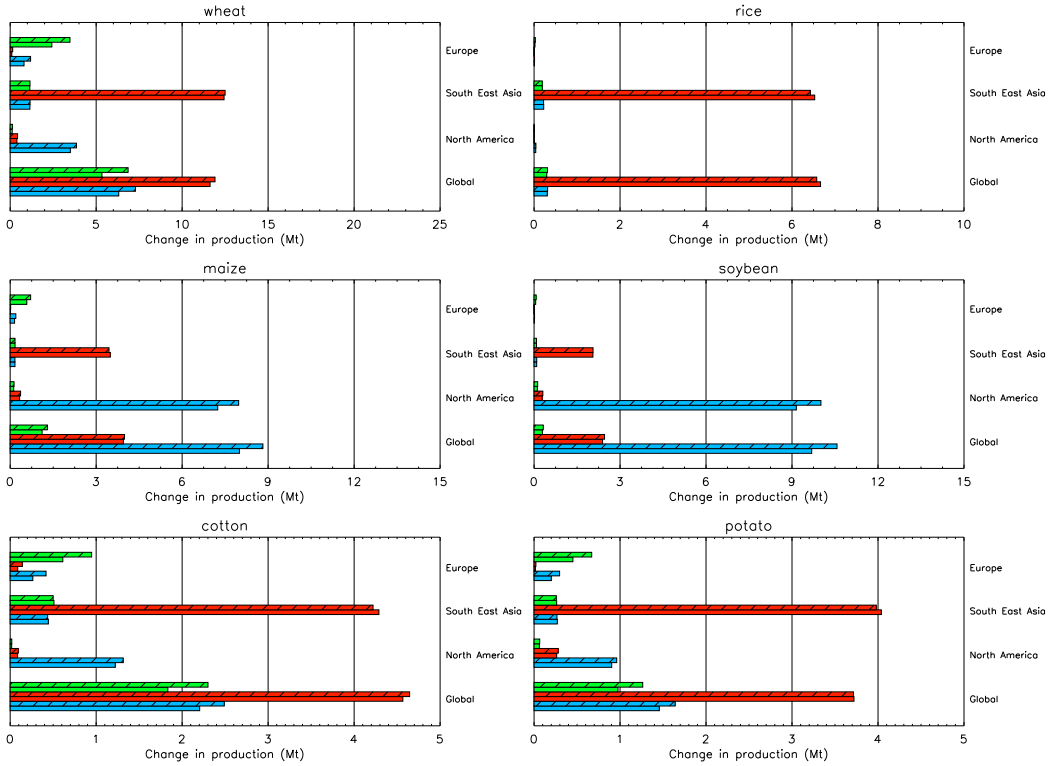

FIGURE 4.13: Projected increase in crop production (in million metric tons(Mt)) for the 6 crops resulting from 100 % regional cuts in anthropogenic NO_x emissions. The y-axis shows the receptor regions, and coloured bars indicate the average impacts based on AOT40, Mx and W126 metrics from emission cuts applied in each region compared to the control model (Green = European emission cut, Red = SE Asia emission cut and Blue = N America emission cut). Solid colour bars show results based on the standard model metric and hatched bars show results based on the bias-corrected model metric (see main text for details).

W126 for wheat, maize and soybean; AOT40 and MX for rice; and AOT40 only for cotton and potato).

N American anthropogenic NO_x emission reductions lead to the greatest increase in global production for both maize and soybean with increases of 8.0 Mt and 9.7 Mt shown respectively (8.8 Mt and 10.6 Mt bias corrected). Reductions to SE Asian emissions result in the greatest increase in production for wheat, rice, cotton and potato. Under SE Asian emissions cuts wheat and rice show the largest sensitivities, with increases in production of 6.7 Mt and 11.6 Mt respectively (6.6 Mt and 11.9 Mt bias corrected).

When shown in terms of increases in crop production, the impact of N American NO_x emissions on Europe are still shown to produce the largest transboundary effect. Over Europe, local emissions cuts result in increases in production which range from 0.02 Mt

(0.03 Mt bias corrected) for rice to 2.4 Mt (3.5 Mt bias corrected) for wheat. N American emissions reductions result in increases in production over Europe of 0.008–0.8 Mt (0.01–1.2 Mt bias corrected) with rice showing the smallest sensitivity and wheat showing the greatest. This represents 33.3–40.0 % (33.3–35.3 % bias corrected) of the increase in production attainable from local emissions cuts. Over N America, local NO_x reductions result in an increase in production of 0.04–9.15 Mt (0.04–10.0 Mt bias corrected), with rice showing the smallest sensitivity and soybean showing the largest. The largest non-local contribution to production increases is the cut in SE Asian emissions, resulting in increases in production of 0.002–0.39 Mt (0.002–0.43 Mt bias corrected). This represents 4.3–5.0 % (4.3–5.0 % bias corrected) the increase in production from local emissions cuts. Over SE Asia, N American emissions reductions result in an increase in production of 0.09–1.1 Mt (0.09–1.2 Mt bias corrected) with European emissions cuts also producing increases in production that fall within a similar range of 0.08–1.1 Mt (0.08–1.2 Mt bias corrected). These represent 4.2–8.9 % (4.2–9.6 % bias corrected) and 3.8–8.9 % (3.8–9.6 % bias corrected) respectively of the impact of a reduction in local emissions (2.1–12.4 Mt (2.1–12.5 Mt bias corrected)).

Overall, on both a regional and global scale, increases in production are greatest for wheat, maize and soybean which are 3 of the most widely grown crops in the world (Fig. 4.1), with wheat production benefitting greatly from reductions in SE Asian NO_x emission reductions and maize and soybean tending to benefit from reductions in N American emissions. The results also show that the inclusion of model bias correction introduces a range of −1.8–60.2 % difference to the increases in production estimated under each emissions scenario. However, even within this uncertainty, the reduction in N American emissions still produces the largest non-local increase in crop production over Europe when compared to the estimated impacts of local European emission reductions.

4.6 Discussion and comparisons with previous work

Using the 4 metrics (AOT40,M7,M12,W126), model calculations show that for 4 of the major crops considered (wheat, rice, cotton and potato) reductions in SE Asian NO_x emissions tend to produce the greatest reduction in crop production losses on a global scale. These correspond to an estimated increase in crop production of 3.7 to 11.6 Mt

(3.7 to 11.9 Mt bias corrected). Cuts to N American emissions result in the greatest global impact on crop production losses for maize and soybean, producing an estimated increase in crop production of 8.0 to 9.7 Mt (8.8 to 10.6 Mt bias corrected). The changes in CPL based on Mx show a similar pattern to those calculated using the AOT40 and W126 indices, however they are much smaller. Figure 4.3 shows that under control emissions, modelled mean monthly surface ozone is slightly above the 40 ppbv threshold of AOT40, particularly over Europe, SW USA and SE Asia. Under emission reduction scenarios, small reductions in ozone resulting in concentrations falling below 40 ppbv can produce a relatively large decrease in AOT40. Due to the linear relationship of yield loss with AOT40, this produces a comparable relative change in yield. The change in Mx however, is directly related to the fractional change in mean background ozone, which may be smaller than the respective change in AOT40 where ozone is near to 40 ppbv. Due to the Weibull relationship between Mx and relative yield loss (Table 4.2), a given change in Mx also produces smaller changes in relative yield loss. N American NO_x emissions produce the largest intercontinental ozone impact in this Chapter. This is consistent with previous studies that have shown trans-Atlantic transport of ozone and its precursors to be more efficient compared with trans-Pacific and trans-Siberian transport (Stohl, 2001).

The results demonstrate that local air quality and emissions control strategies over each of the regions have the potential to effectively mitigate ozone-induced production losses for six major crop types. A 100 % reduction in local anthropogenic NO_x emissions results in near 100 % reductions in AOT40 derived crop production losses for wheat, rice, maize, soybean, cotton and potato in each of the regions. In N America, a 100 % reduction in local anthropogenic NO_x produces a 94.5 % (94.6 % bias corrected) reduction in local rice production losses and a 92.4 % (92.4 % bias corrected) reduction in potato production losses. This indicates a smaller sensitivity of 40 ppbv exeedences over potato and rice growing regions to local anthropogenic emissions compared to Europe and SE Asia. Figure 4.1 shows that the majority of N American potato growing regions are in north and western USA. The greatest potato production output is over the north west of the N American region. Rice growing is located over the south east of the region and a small area along the west coast. The production data shows higher output of rice to the west. Jaffe (2011) recently showed that for the period 1995–2009, biomass burning emissions through the summer are significantly correlated with the number of days where surface ozone exceeds AQS guideline levels in the western United States. This indicates that biomass burning

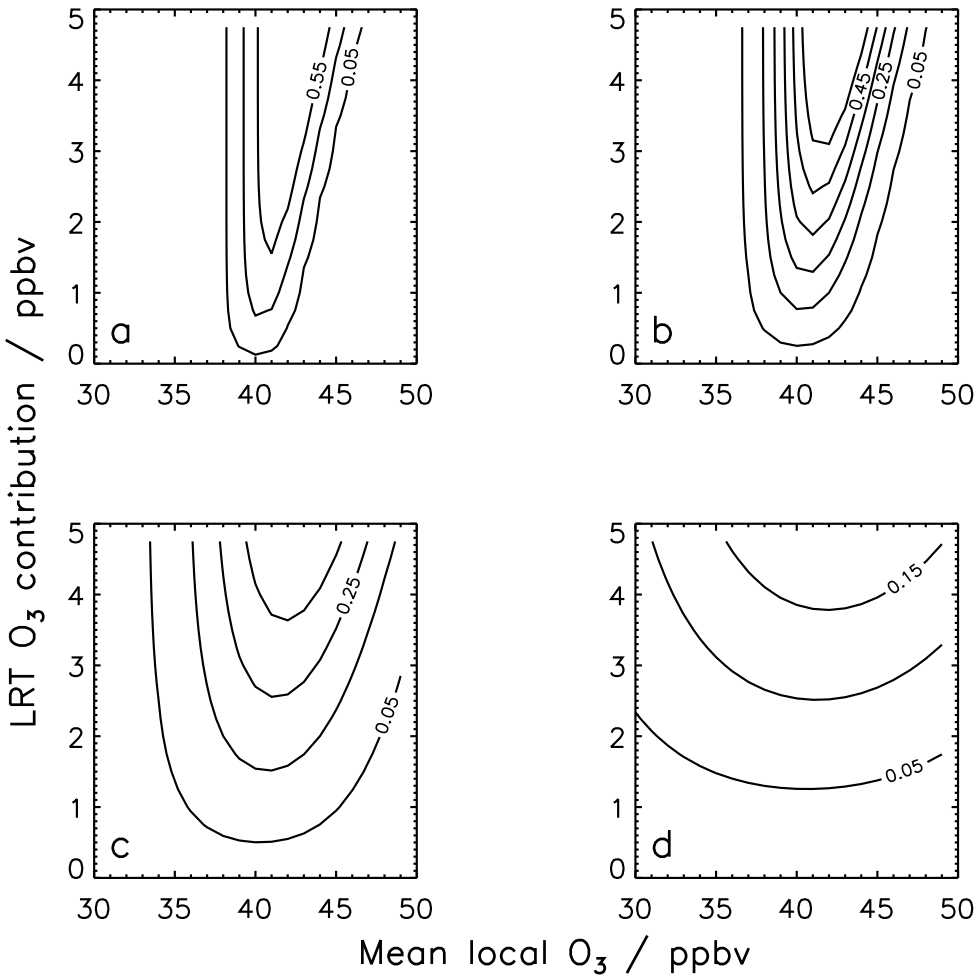

FIGURE 4.14: Fractional change in AOT40 due to long-range transport (LRT) as a function of mean local ozone and LRT ozone contribution. Panels **(a–d)** are based on normally-distributed local ozone distributions, with standard deviations of **(a)** 1 ppbv, **(b)** 2 ppbv, **(c)** 4 ppbv and **(d)** 10 ppbv. The LRT contribution is assumed to uniformly translate the local ozone distribution across all concentrations. AOT40 is assumed proportional to the fraction of distribution concentrations exceeding 40 ppbv. Plot generated by S. Arnold (Pers. Comms 2012)

emissions are likely playing a role in controlling the exposure of crops to ozone in this region. It can be seen in Fig. 4.2 that under N American emissions reductions, there are still parts of the N American domain (over western Canada) where biomass burning NO_x emissions of reasonable magnitude remain. These remaining emissions could still lead to exceedances of the 40 ppbv threshold of AOT40.

As discussed above, the threshold nature of the AOT40 index means that it is sensitive to small ozone concentration changes around 40 ppbv. Contributions of a few ppbv to surface ozone from non-local emissions therefore have the potential to significantly alter the AOT40 exposure of crops. This also results in a large sensitivity to errors in the model

surface ozone distribution, and consequent uncertainty in the AOT40-derived production losses (Tuovinen et al., 2007). The inclusion of bias-corrected calculations allows the impact of such uncertainty on the results to be accounted for. The present-day sensitivities of AOT40-derived yield loss to non-local emissions are a function of not only the non-local ozone precursor emissions themselves, but also the local ozone abundance. In more general terms, the threshold nature of the AOT40 metric results in long-range transport contributions to yield loss being strongly dependent on local ozone concentrations. Figure 4.14 shows calculations of the change in AOT40 as a function of mean local ozone concentration and the ozone contribution from long-range transport, assuming a normal distribution of local ozone concentrations. Maximum sensitivity of AOT40 to non-local ozone is seen where the mean local ozone is close to 40 ppbv. In addition, a relatively small variability in local ozone around 40 ppbv increases this sensitivity. This highlights the problem of using a threshold metric to assess contributions of different ozone sources to local yield loss. Under future emission and climate scenarios, where surface ozone concentrations may be larger in many regions, the AOT40-derived yield-loss response to non-local emission reductions may be reduced, if such reductions are not sufficient to bring ozone concentrations below the 40 ppbv threshold. Alternatively, under a scenario where local emissions in Europe and N America are reduced, but an increase in background ozone concentrations is driven by increasing Asian emissions (e.g. Jacob et al., 1999), the sensitivity of European and N American AOT40 yield-loss to Asian emission reductions may increase.

Since relative yield loss is linearly related to AOT40 (Mills et al., 2007), the reduction in yield loss under the emissions cut scenarios changes proportionally with the magnitude of a change in AOT40. Assuming that under each of the emission scenarios, ozone remains greater than 40 ppbv, this leads to a linear relationship between ozone reduction and yield loss reduction, which is independent of the absolute ozone concentration. For the concentration based indices Mx, yield loss reductions depend on the magnitude of the absolute ozone concentration, in addition to the ozone change. This is due to the non-linear Weibull relationship between yield loss and Mx (shown in Fig. 4.15), which is also dependent on the sensitivity of each crop to ozone exposure. With the exception of soybean, at larger background ozone concentrations (and hence higher Mx), a given change in the mean background ozone concentration would result in a greater response of yield reduction for each crop, than at smaller background ozone concentrations. This behaviour means that the Mx indices can mimic a threshold response, similar to that of

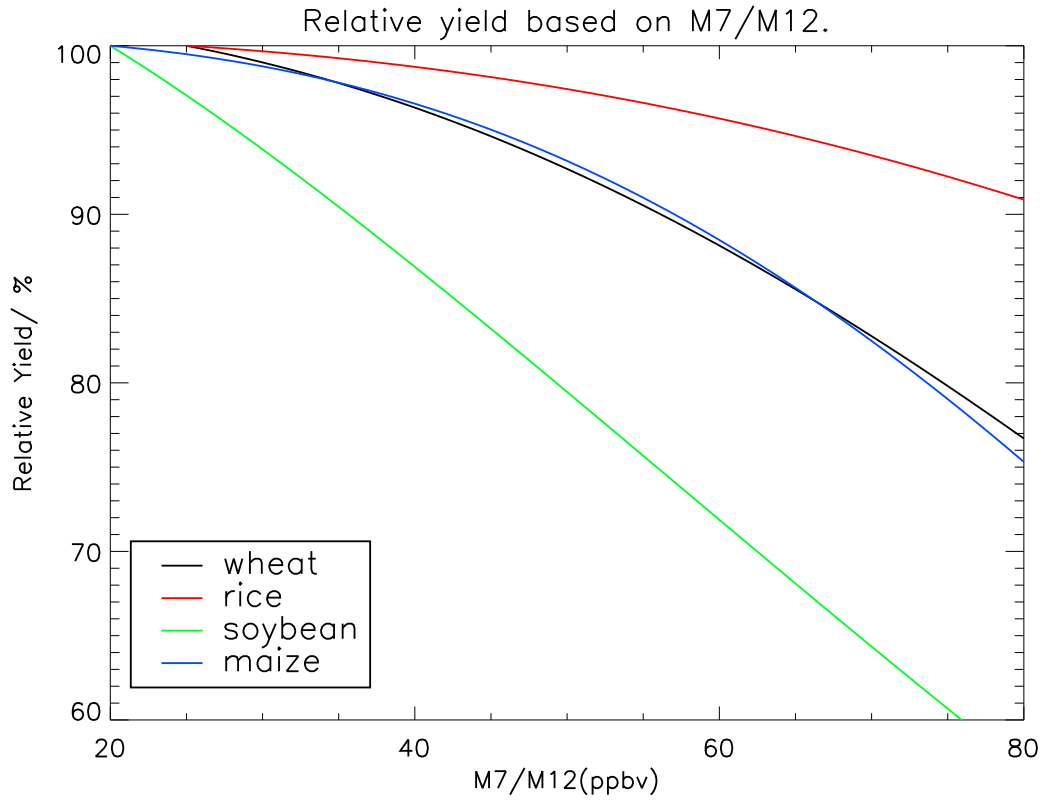

FIGURE 4.15: Relative yield as a function of M7/M12 for wheat, rice, maize and soybean. The equations for these functions are shown in Table 4.2.

AOT40. This behaviour also means that under increased background ozone, the relative yield loss changes produced under the respective emissions cut scenarios would be more pronounced, and thus the impact on crop production would be more pronounced.

The results of this Chapter only consider crop production losses that are related to ozone exposure. In reality, there are many other drivers that can cause a reduction in crop yields. These factors include exposure to higher temperatures under a warmer climate, drought stress, and whether the crops are properly irrigated. It is shown by Liu et al. (2010), that for a winter wheat-summer maize cropping system in the Huang-Huai-Hai Plain of China, a 5°C increase in temperature results in an overall yield reduction of 18.5±22.8 %. They also present an overall yield reduction of 2.3±13.2 % for temperature rise of 2°C. By comparison, the results presented here show that for the SE Asia region (which contains China), for wheat, regionally-aggregated relative yield losses due to ozone exposure are 2.4 to 10.5 % (2.7 to 10.4 % bias corrected) (Table 4.4), showing that ozone-induced crop damage under control emissions for 2000 is similar in magnitude to that caused by 2°C temperature rise and up to roughly half of that of a 5°C temperature rise. For maize, the

effect of ozone damage over SE Asia is less, with relative yield losses of 0.07 to 4.5 % (0.08 to 4.5 % bias corrected).

An additional factor to consider is the possible benefits to crop yields under future climate due to fertilization from enhanced CO_2, which can act to increase the biomass of crops (Franzaring et al., 2008). This could offset yield losses through rising ozone or temperatures. The location of crop cultivation, the extent of crop irrigation and the management of the crops are also important factors. It has also been shown in a recent study that ozone damage to plants can feed back on yield loss through the effect on evapotranspiration. Bernacchi et al. (2011) showed that ozone exposure of soybean can reduce water use by as much as 15 %, resulting in increased sensible heat flux which is indicative of a day-time increase in canopy temperature of up to 0.7°C, with warmer temperatures leading to further reduction in crop yields (Liu et al., 2010). With a rise in surface ozone coupled with a warmer climate, the impact on crop yields due to ozone-induced production loss may act to enhance the yield loss observed for crops due to the warmer temperatures. However, it should be noted that these yield-limiting factors interact in non-linear ways depending on whether warmer temperatures limit ozone uptake and hence the damage caused. The transboundary impact of ozone and its precursor emissions on yields highlight that even non-local emission reduction strategies could at least partially offset a reduction in crop yields under a warmer future climate. These interactions all play important roles in determining how climate change and emission changes may affect crop yields.

Bias correction of the results to account for model error, introduces a range of uncertainty into the crop production response under each emissions cut scenario. For example, the impact of N American emission cuts on global soybean production produces a difference of up to 0.9 Mt between the control model results (a 9.7 Mt increase in production) and the bias-corrected results (a 10.6 Mt increase in production). Bias correction of results for the impact of European emissions cuts on global wheat production also produces a difference of about 1.5 Mt. This demonstrates that model error can produce up to 1.5 Mt difference in the estimated impacts on crop production from regional anthropogenic NO_x emission cuts. However, it is also shown that the estimated transboundary effects are much more robust to model error, with little difference when accounting for model bias correction compared to the control model metrics. The impact of N American NO_x on European crop production produces the largest transboundary effect for both the bias-corrected and

standard model results. Therefore there is high confidence in the relative importance of the transboundary effects shown in this Chapter. It is however acknowledged that each individual metric produces different absolute changes in crop yield losses due to ozone exposure.

An additional source of uncertainty is that the indices used (AOT40,Mx,W126) have not been designed with the specific purposes of estimating yield losses due to the intercontinental transport of ozone. The exposure response functions used are based on data collected from cultivars of crops grown in N America and Europe. They therefore may not adequately represent the sensitivities of crops grown over Asia to ozone exposure, which may differ in ozone sensitivity to those grown over Europe and N America. These indices were also developed in regions where, at the time, concern was placed on peak ozone concentrations (Heck and Colwing, 1997). Since their development, regional ozone distributions have changed, due to declining ozone precursor emissions over N America and Europe, and rising emissions over East Asia, changing contributions to background NH ozone (Cooper et al., 2010; Jacob et al., 1999). This shift has resulted in less episodic high ozone events, but an increase in background ozone concentrations over Europe and N America. This may result in different exposure regimes of crops to ozone and hence the resultant impact on crop production.

4.7 Summary

The findings presented in this Chapter are the first to estimate the impact of ozone precursor emissions from each of the Northern Hemisphere's major industrialized regions (N America, SE Asia, and Europe) on crop yields globally and in continents downwind of each region. The results have made the first estimates of the impact of intercontinental transboundary pollution on crop yields, using a range of available metrics applied in a standardized manner.

It is shown that for 4 of the crops considered (wheat, rice, cotton and potato), reductions in SE Asian anthropogenic NO_x emissions are predicted to produce the greatest reduction in global crop production losses (46.6 to 95.2 % (42.3 to 94.4 % bias corrected)), based on AOT40, Mx and W126 metrics. This corresponds to an estimated increase in crop

production of 3.7 to 11.6 Mt (3.7 to 11.9 Mt bias corrected). Cuts to N American emissions result in the greatest global impact on crop yield reductions for maize and soybean (59.2 to 85.1 % (60.6 to 85.9 %) bias corrected). This results in an estimated increase in crop production of 8.0 to 9.7 Mt (8.8 to 10.6 Mt bias corrected). Model calculations suggest that reductions in anthropogenic NO_x emissions from N America give the largest non-local effect, resulting in European production loss reductions of between 15.0 % and 63.2 % (14.2–63.1 % bias corrected), for a 100 % emissions cut. The impact on absolute crop production also shows that a reduction in N American NO_x emissions results in the greatest non-local contribution to production increases, enhancing production over Europe by approximately one third of the production increase produced by the local European emission cut for wheat. These results demonstrate that local air quality and emission control strategies have the potential to partly alleviate ozone-induced crop production loss in continents downstream, in addition to effectively mitigating local ozone-induced yield losses. It also indicates that for three of the world's most widely grown crops (wheat, maize and soybean) local air quality strategies can significantly benefit crop production output.

Finally, it is shown that quantification of the transboundary effects on crop yield loses due to long-range transport of ozone and precursors differs depending on the ozone damage metric used, and for threshold-based indices such as AOT40, the inferred long-range transport contribution shows a strong dependence on the local ozone concentration distribution. Nevertheless, the conclusions regarding the relative importance of the different regions in controlling crop production losses downstream are robust across the range of metrics used. The work presented in this Chapter could be extended to incorporate flux-response relationships to assess the effect of long range transport of ozone and its precursors on crops. Flux based methods consider the flux of ozone into the plant, mainly through the stomata, and can begin to account for modifying environmental conditions and hence could be more applicable in different global regions and future climates (Harmens et al., 2007). However, at present flux-response relationships are only available for wheat, potato and tomato (Mills et al., 2011a; Pleijel et al., 2004), and these have not been parameterised for global application.

Chapter 5

Impacts of pre-industrial to present day land cover change on tropospheric ozone and its radiative forcing

5.1 Introduction

This chapter investigates the impacts of pre-industrial to present day land cover change on tropospheric ozone and its estimated radiative forcing. The HadGEM2-ES model was used to simulate pre-industrial atmospheric composition using present day and pre-industrial land cover with online interactive isoprene emissions determined using an interactive BVOC (iBVOC) emissions scheme. HadGEM2-ES was used to quantify the sensitivity of tropospheric ozone and its precursor species to land cover change, through its impacts on dry deposition and isoprene emissions. The final part of this chapter performed the same experiments using the TOMCAT CTM, using offline isoprene emissions from the Community Land Model (CLM) to simulate the response of isoprene to the land use changes. This was done in order to test the robustness of the results by quantifying the impact of land cover change on ozone whilst removing the effects of land surface changes on the climate through the effect on model dynamics.

5.2 Present understanding on modelling pre-industrial ozone.

Since the industrial revolution, anthropogenic emissions of ozone precursor gases (NO_x, CO, CH_4 and VOCs) have likely led to increased ambient ozone over many regions with model calculations estimating the resultant radiative forcing to lie between 0.25-0.65 Wm^{-2} (Forster et al., 2007). This range indicates the uncertainty in the modelled ozone concentrations in the pre-industrial period (in this Chapter defined as the mid-nineteenth century), along with the processes which govern these concentrations. These include the prescribed anthropogenic and natural trace gas emissions in the model, the underlying land use classification and the representation of interactions between the atmosphere and the biosphere such as dry deposition and the emission of precursor species such as isoprene. Uncertainty in the estimate can also arise from differences in model climate and hence meteorology and transport which can have important implications for the tropospheric ozone distribution (Chapter 2).

A limited data set of late nineteenth and early twentieth century ozone observations are available for a range of surface air and mountain sites (Marenco et al., 1994; Pavelin et al., 1999; Volz and Kley, 1988) and though models are in relatively good agreement with one another and calculate changes in the global tropospheric ozone burden since pre-industrial times of 7-13 Dobson units (DU, 1 DU = 2.7×10^{16} molecules cm^{-2}), they have been shown to systematically overestimate these observations (Wang and Jacob, 1998). The most reliable of these pre-industrial observations are considered to be those at Montsouris in Paris, which show 7-10 ppbv of surface ozone throughout the year, with little seasonal variation. In comparison to this, previous studies have shown that the best global model estimates over Europe for the pre-industrial period are typically double this at 15-20 ppbv (Brasseur et al., 1998; Kiehl et al., 1999; Mickley et al., 1999; Roelofs et al., 1997; Wang and Jacob, 1998).

Previous studies (Kley et al., 1988; Pavelin et al., 1999) have suggested that these differences between the models and observations could be due to calibration problems in the observational data, though it has been acknowledged that deficiencies in the ability of models to simulate the pre-industrial atmosphere must also be considered (Mickley et al., 2001). Mickley et al. (2001) showed that reducing NO_x emissions from lightning and soils

and increasing the emission of biogenic hydrocarbons can produce ozone in better agreement with the available pre-industrial observations and present a revised radiative forcing due to ozone since pre-industrial times of 0.72-0.80 Wm^{-2}. This range is higher than the estimates shown by Forster et al. (2007) and indicates the sensitivity of the radiative forcing to changes in pre-industrial model conditions. Large uncertainties currently exist in present day emissions of isoprene and other biogenic VOC (BVOC) compounds (Abbot et al., 2003; Gedney et al., 2004; Guenther et al., 1995, 2006; Lathiere et al., 2005; Levis et al., 2003; Naik et al., 2004; Sanderson et al., 2003; Shindell et al., 2004; Wang and Shallcross, 2000) with much greater uncertainty expected in the emissions of these compounds in the pre-industrial period (Mickley et al., 2001; Shindell et al., 2003). Additional factors that could account for this overestimation of pre-industrial ozone include uncertainties associated with the representation of inorganic bromine (Br_y) chemistry in the models (Parrella et al., 2012) and the magnitude of biomass burning in the pre-industrial period (Lamarque et al., 2005; Shindell et al., 2003; Wang and Jacob, 1998).

The emission of BVOCs, isoprene in particular, is highly dependant on the type of vegetation cover (Guenther et al., 2006; Niinemets et al., 2010a,b) though environmental controls such as light (Monson and Fall, 1989), temperature (Guenther et al., 1993), atmospheric CO_2 (Monson et al., 2007) and soil moisture (Monson et al., 2007; Pegoraro et al., 2004) also play a major role. The rate of isoprene emission increases with temperature until an optimum of about 40°C (Niinemets et al., 1999). Conversely, measurements have shown high levels of CO_2 inhibit isoprene emission, with the potential of different response patterns to short and long term changes in the CO_2 burden (Pacifico et al., 2009; Young et al., 2009). Changes in both the magnitude and spatial distribution of isoprene emissions can have important effects on tropospheric ozone as depending on the local NO_x burden, isoprene can act as an ozone source or sink (Arneth et al., 2007).

As shown in Chapter 2, isoprene and its oxidation products play an important role in the cycling of NO_x and HO_x, with the products of these chain reactions having important implications for the tropospheric concentrations of ozone, CO and CH_4. In addition to this, isoprene oxidation in the presence of NO_x can also result in the formation of peroxyacetylnitrate (PAN) (Chapter 2) which can act as reservoir species for NO_x enabling long range transport to remote regions and resulting in ozone formation. This effect can be particularly important in the tropics where isoprene sources are high (Guenther et al.,

2006; Lelieveld et al., 2008) and coincide with regions of deep convection resulting in PAN being transported to the free troposphere. Here, temperatures are sufficiently low for PAN to remain relatively stable and be transported over long distances (Moxim et al., 1996).

As well as affecting BVOC emissions the underlying vegetation surface can also influence the rate of dry deposition of ozone and its precursor species (including NO_x, PAN, MPAN and other reactive nitrogen species) to the land surface (Ganzeveld and Lelieveld, 1995; Giannakopoulos et al., 1999) which can also result in changes in atmospheric composition. As the major pathway for ozone uptake is through the plant stomata (Smith et al., 2000), the background CO_2 concentration can influence the rate of dry deposition due to higher CO_2 concentrations inducing stomatal closure and hence reducing the rate of trace gas exchange between the biosphere and the atmosphere (Gedney et al., 2006).

In this chapter, the impacts of 1865 to present day (here defined as the year 2000) land cover changes on tropospheric ozone were investigated using a coupled global Earth System (ES) model with interactive biogenic VOC emissions, to separately assess the impacts of changes in land surface cover, climate and atmospheric CO_2 on the dry deposition of ozone and its precursors, and on biogenic isoprene emissions and the resultant impact on the estimated pre-industrial tropospheric ozone distribution. Additional experiments were run using a global CTM to quantify the impact of land cover change on ozone whilst removing the effects of the change in land surface on the climate through the effect on model dynamics. Finally, the resultant impact of these land cover driven changes are used to quantify the sensitivity of the pre-industrial to present day tropospheric ozone radiative forcing to the representation of biosphere-atmosphere interactions in the model.

5.3 Overview of pre-industrial observations

In this Chapter, observational data is presented from 12 sites which recorded ozone concentrations during the later half of the 19th Century. The data for all sites (Lamarque et al., 2005; Linvill et al., 1980; Sandroni and Anfossi, 1994; Sandroni et al., 1992) with the exception of Montsouris (Volz and Kley, 1988) are reconstructed based on measurements collected using the Schönbein method. The Schönbein index is related to the ozone concentration and relative humidity (Linvill et al., 1980) through a very non-linear function. The Schönbein indices (usually on a scale of 0-10) are converted to ozone concentrations

TABLE 5.1: Site location data for the 12 sites providing pre-industrial surface ozone observations. The final column provides the years the observations provided coverage for.

		Site Location		
		LON	LAT	Years covered
Site	Lansing	43N	85W	1876 – 1880
	Cordoba	30S	64W	1886 – 1892
	Montevideo	35S	56W	1883 – 1885
	Manilla	14N	121E	1878 – 1882
	Rio de Janeiro	23S	43W	1882 – 1885
	Oaxaca	17N	97W	1892 – 1899
	Montsouris	50N	2E	1876 – 1883
	Pic du midi	43N	0E	1881 – 1909
	Vienna	48N	16E	1891 – 1895
	Tokyo	35N	139E	1895 – 1901
	Luanda	9S	14E	1890 – 1895
	Adelaide	35S	138E	1883 – 1907

using the Linvill et al. (1980) relationship and are then normalized to the Montsouris data where both direct and Schönbein measurements were recorded concurrently (Volz and Kley, 1988). This was carried out by Anfossi et al. (1991) and utilizes the following regression (Equation 5.1) to correct the ozone concentration obtained from the Linvill et al. (1980) conversion.

$$O_3 = 2.9 + 0.088X, \tag{5.1}$$

where X is the ppbv value obtained from Linvill et al. (1980)'s conversion. It should be noted however, that there is large uncertainty associated with these pre-industrial observations (Marenco et al., 1994) and large errors of around 25% should be assumed for the mean monthly values. Table 5.1 provides a summary of the location of each of the 12 sites.

5.4 Sensitivity of modelled pre-industrial tropospheric ozone to 1865 to 2000 land cover changes

This section presents the results of the HadGEM2-ES simulations to assess the sensitivity of the modelled pre-industrial tropospheric ozone distribution to changing dry deposition and biogenic isoprene emissions as a result of changing the prescribed model land classification map from 1865 to 2000. This section also presents a comparison with the typical model setup used in previous pre-industrial model simulations (Hauglustaine and Brasseur, 2001; Lamarque et al., 2005; Mickley et al., 2001) along with a comparison of the modelled ozone in HadGEM2-ES with the limited available observations from the turn of the 19th Century.

5.4.1 Model setup and scenarios

The global 3-D HadGEM2-ES model (Chapter 3) was used to simulate atmospheric conditions for the pre-industrial period, here termed as 1865. The model was run at a horizontal resolution of 1.9° × 1.3°, with 38 hybrid height levels which extend from the surface up to an altitude of approximately 39 km (termed N96L38). The model was run in its atmosphere only configuration with the full Earth system couplings not applied such that changes in concentrations of ozone and associated trace gases (including BVOCs) did not feedback to the climate system through the model radiation scheme or carbon cycle through primary productivity.

The model chemistry scheme used was the extended chemistry version of the UK Community Chemistry and Aerosol (UKCA) scheme which features approximately 300 chemical reactions and accounts for 83 species. The scheme includes tropospheric CH_4-NO_x-CO-O_3 chemistry (O'Connor et al., 2011) which is representative of the tropospheric background with the addition of simplified isoprene reactions (Folberth et al., 2006) based around the Mainz Isoprene Mechanism (Poschl et al., 2000). For the treatment of dry deposition of tracer species, the UKCA scheme used an adaptation of the Wesely (1989) scheme as described by Sanderson et al. (2006). Dry deposition fluxes for gas phase species and aerosols were calculated using a 'big leaf' model approach (Smith et al., 2000) which utilises a resistance analogy to quantify the 3 main phases of the dry deposition process. These are the aerodynamic resistance (r_a), the quasi-laminar boundary layer resistance (r_b), and

the surface resistance (r_c) with the latter term strongly dependant on the chemical and physical properties of the underlying surface. For vegetated surfaces, r_c is a combination of resistances to uptake through the plant stomata, the uptake through the leaf surface or cuticles and uptake through the soil.

The emissions of BVOC species were calculated on-line using the iBVOC emissions scheme which calculates interactive surface emissions of isoprene, a lumped monoterpene species, acetone and methanol. The isoprene emissions scheme, as described by Pacifico et al. (2011) is based upon the scheme adopted by Arneth et al. (2007) and calculates the rate of isoprene synthase and emission based upon vegetation type and the rate of photosynthesis and dark respiration. The iBVOC scheme includes empirical factors to account for the effects of atmospheric CO_2 and temperature on isoprene emissions. This scheme calculates global total isoprene emissions of 431.6 $TgCyr^{-1}$ for the present day and 580.0 $TgCyr^{-1}$ for the pre-industrial period. Finally, for monoterpenes, acetone and methanol, the emissions were calculated interactively based upon the model leaf area index (LAI), a proxy for photosynthetic primary production and vegetation growth, with the effect of temperature on BVOC emission again accounted for through a lumped terpene empirical factor (Arneth et al., 2007; Niinemets et al., 1999).

For the pre-industrial control run (PI_CTRL) the model was set up to calculate a pre-industrial climate from climatological monthly mean sea surface temperatures (SSTs) and sea-ice fields. Anthropogenic surface emissions representative of the 1860s were taken from the historical (1850 to 2000) gridded emissions dataset used for the Climate Model Intercomparison Program#5 (CMIP5) simulations (Lamarque et al., 2010). Greenhouse gases and land cover were set to pre-industrial levels. The model was run with fixed vegetation (Section 5.4.2) with the TRIFFID dynamic vegetation model set to update leaf phenology on a daily basis which determined the evolution of leaf LAI. The rate of photosynthesis and the resultant emissions of BVOCs through the interactive emissions scheme were determined through HadGEM2-ES's land surface scheme, MOSES II (Essery et al., 2003).

Two model experiments were performed in addition to the PI_CTRL simulation to assess the impacts of present day to pre-industrial land use changes on tropospheric ozone levels and its radiative forcing. For all scenarios the model was spun up for a period of nine months and then run for 10 years with the analysis performed on climatological averages

over the last 8 years of each model run. This was done because the changes in land surface between the scenarios not only affect dry deposition and iBVOC but can also affect model meteorology through impacts on dynamics through roughness length and the model radiation balance through impacts on surface albedo. A summary of the model scenarios can be found in Table 5.2.

TABLE 5.2: Summary of HadGEM2-ES pre-industrial model scenarios to assess sensitivity of pre-industrial ozone to 1865 to 2000 land cover change.

Model Scenario	Land cover (LC)	Isoprene Emissions	Atmospheric CO_2[a]	SST + Sea-ice	Tracer Emissions
PI_CTRL	1865	iBVOC 1865 LC	286 ppmv	1860s clim	1860s clim
LC_2000	2000	iBVOC 2000 LC	286 ppmv	1860s clim	1860s clim
EMS_1860	2000	iBVOC 2000 LC	368 ppmv	2000s clim	1860s clim

[a] In each model scenario the other active greenhouse gases CH_4 and N_2O are fixed at 1865 values (0.8 ppmv for CH_4 and 276 ppbv for N_2O)

5.4.2 1865 to 2000 vegetation land cover change.

For all of the runs performed in this chapter, the model land cover was prescribed from a dataset representative of historical changes in land use as processed for the CMIP5 (Hurtt et al., 2011). This data was derived from the present-day climatology IGBP dataset (Loveland et al., 2000) and reconstructions of anthropogenic land-use from the HYDE3 dataset (Klein Goldewijk et al., 2010). For the PI_CTRL scenario the land cover was representative of the year 1865 and held fixed for the duration of the run and for the LC_2000 and EMS_1860 runs the land field was fixed at values representative of the year 2000.

Figure 5.1 shows the global coverage of the five vegetation plant functional types (PFTs) used in HadGEM2-ES for the year 1865 along with the change in the coverage of these PFTs between 1865 and 2000 with a regional summary of the changes shown in Table 5.3. Between 1865 and 2000, the broadleaf tree, needleleaf tree and shrub categories show a decline in global coverage with shrubs showing the largest decline (-1404.1 Mha) and needleaf trees showing the smallest (-218.5 Mha). Both C3 and C4 grasses show increases in global coverage of 1736.9 Mha and 933.0 Mha respectively. This reflects the general change in land patterns since the pre-industrial period due to anthropogenic activity resulting in

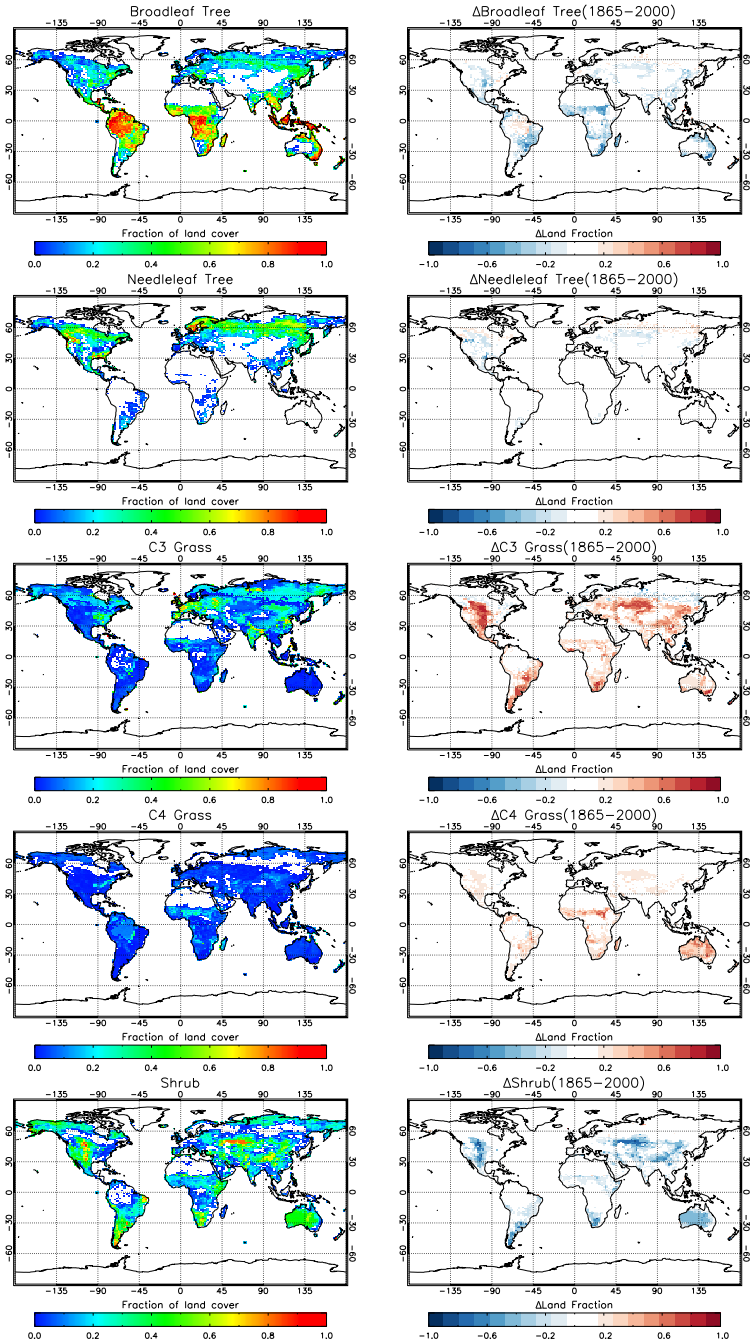

FIGURE 5.1: 1865 PFT coverage (left column) and change in PFT coverage from 1865 to 2000 (right column). Dataset representative of historical changes in land use as processed for the CMIP5 (Hurtt et al., 2011).

the replacement of forested regions by agricultural crops since the 1850s (Ramankutty and Foley, 1999; Richards, 1990; Turner et al., 1993).

On a regional scale, changes in coverage of needleleaf tree, C3 grass and shrubs are largest over the northern hemisphere mid-latitudes and changes in the coverage of broadleaf trees and C4 grasses are largest over the tropics. This change in broadleaf tree coverage over the

tropics between 1865 and 2000 (-721.6 Mha) is particularly important as it has important impacts on isoprene emissions. This is because broadleaf trees in the tropics are known high emitters of isoprene (Guenther et al., 2006). Finally, for all land categories the changes in coverage are more pronounced in the northern hemisphere than in the southern due to the larger proportion of land lying within the northern hemisphere.

TABLE 5.3: Global and regional differences in HadGEM2-ES PFT coverage in Mha between 1865 and 2000.

		Region			
		Globe	Tropics	NH mid-lats	SH mid-lats
PFT	Broadleaf Tree	-1092.4 Mha	-721.9 Mha	-230.2 Mha	-140.9 Mha
	Needleaf Tree	-218.5 Mha	-46.4 Mha	-150.7 Mha	-24.0 Mha
	C3 Grass	1736.9 Mha	636.9 Mha	847.3 Mha	257.7 Mha
	C4 Grass	933.0 Mha	548.4 Mha	228.5 Mha	156.8 Mha
	Shrubs	-1404.1 Mha	-428.3 Mha	-726.1 Mha	-252.2 Mha

5.4.3 Impact of land cover change on modelled pre-industrial tropospheric ozone

Figure 5.2 shows the changes in surface ozone concentrations between the PI_CTRL and LC_2000 simulations. As a result of the change in model land cover, surface ozone concentrations under the LC_2000 simulation are up to 3 ppbv greater over parts of S America and Africa in January and up to 5 ppbv greater over parts of N America, Asia and Europe during July. The regions of maximum increase in ozone correspond with the greatest transitions of tree to grass land type shown in Figure 5.1. This impact on surface ozone can be attributed to two major pathways as a result of the changing land cover. Firstly, as shown in Figure 5.1, the decline in the coverage of the broadleaf and needleleaf tree PFT types and the increase in the coverage of C3 and C4 grass PFT types will impact the rate of dry deposition of ozone and associated precursor species (NO_2 and PAN) to the land surface. As ozone deposits more readily to forest and tree land categories due to greater leaf area and higher stomata uptake (Ganzeveld and Lelieveld, 1995), this 1865 to 2000 land cover change results in lower rates of uptake by vegetation and hence an increase in surface ozone levels. This is evident in Figure 5.3 which show overall lower stomatal conductances under the LC_2000 scenario than for the PI_CTRL scenario. The largest differences are seen over the regions where the decline in broadleaf and needleleaf tree PFT coverage is

greatest (Figure 5.1) where stomatal conductances under the LC_2000 are up to 3.0x10^{-3} ms^{-1} lower than under the PI_CTRL scenario.

Secondly, the change in land category also impacts the amount of isoprene emitted to the atmosphere. Broadleaf tree species (particularly in the tropics) are known strong emitters of isoprene (Guenther et al., 2006). Therefore the replacement of these with grasses under the LC_2000 scenario (1865 to 2000 land cover change) leads to a reduction in isoprene emissions which can have important feedbacks on surface ozone concentrations. Overall, under the LC_2000 scenario global annual isoprene emissions are 470.9 TgCyr^{-1} a drop of 109 TgCyr^{-1} from global emissions under the PI_CTRL scenario (579.9 TgCyr^{-1}). In the pre-industrial atmosphere, where global emissions of NO_x are generally lower than under present day conditions (NO_x emissions are 34.3 TgNO_xyr^{-1} for the pre-industrial compared to 138.1 TgNO_xyr^{-1} for the present day), isoprene reacts directly with ozone and acts as an ozone sink rather than being oxidised by OH and cycling NO to NO_2 which causes ozone production. Therefore the lower isoprene emissions under the LC_2000 scenario (Figure 5.3) results in greater surface ozone concentrations. The seasonality of isoprene emissions is evident with greater changes seen in the northern hemisphere during July and in the southern hemisphere in January corresponding to the regions where ozone concentrations increase by the largest amount under the LC_2000 scenario from the PI_CTRL.

In contrast, Figure 5.2 shows over the regions away from the major isoprene and NO_x sources, ozone concentrations under the LC_2000 scenario are lower than the PI_CTRL scenario by up to 3 ppbv over parts of Africa in January and by up to 4 ppbv over parts of central Asia in July. Lower concentrations are also observed over the oceans by up to 2 ppbv over tropical oceanic regions in both months. Overall, this results in a lower tropospheric burden of ozone under the LC_2000 scenario (200.4 Tg) than under the PI_CTRL simulation (203.7 Tg), reduction of 3.3 Tg (1.6 %).

Figure 5.2 shows the changes in surface NO_x and PAN concentrations between the PI_CTRL and LC_2000 scenarios for the months of January and July. NO_x concentrations are shown to be greater under the LC_2000 scenario due to the reduced dry deposition to the surface vegetation. The greatest changes are seen over parts of Argentina and Central Africa in January (up to 300 pptv) and over large areas of N America, Europe and Russia during

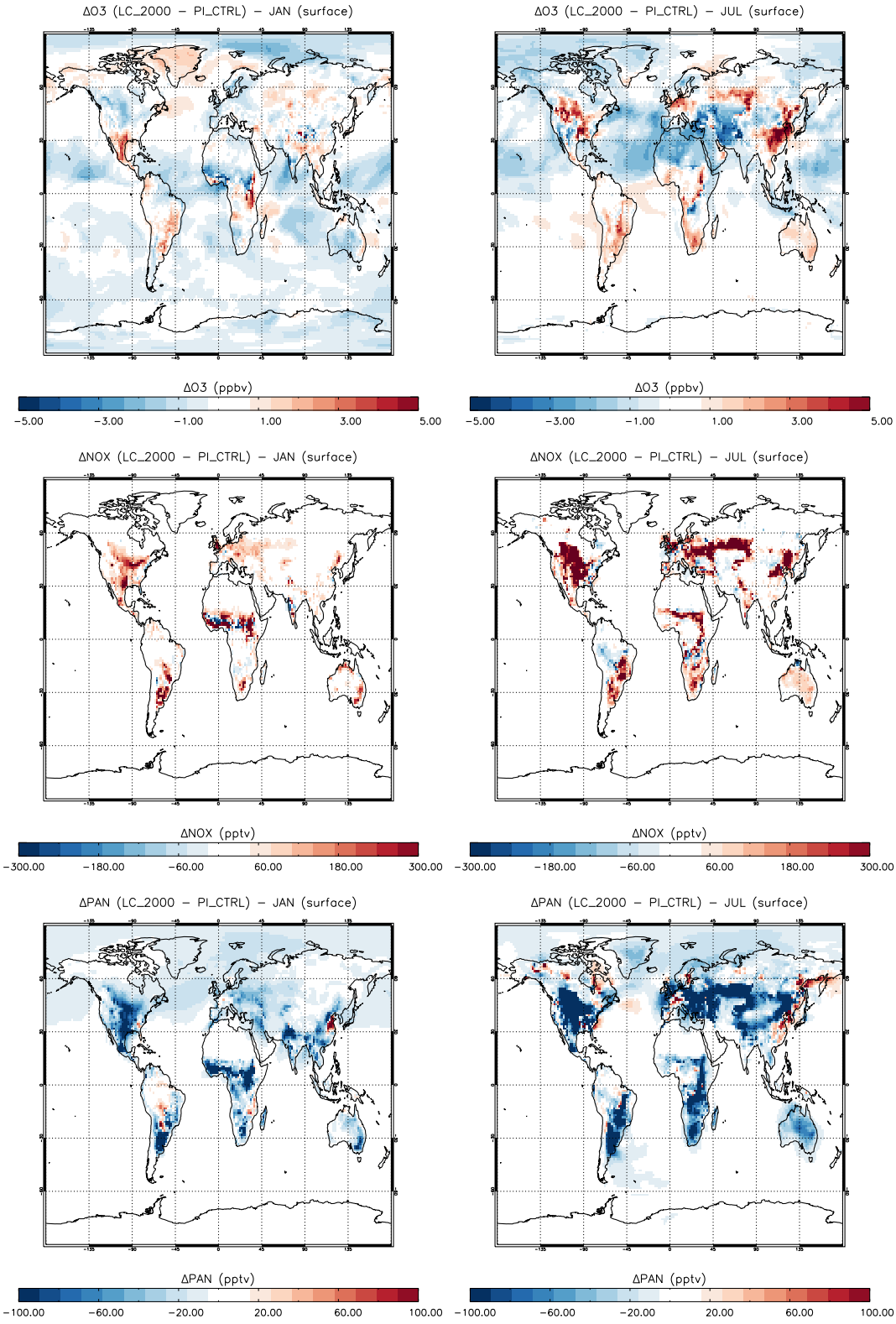

FIGURE 5.2: Changes in surface ozone, NO_x and PAN concentrations between PI_CTRL and LC_2000 scenarios for January (left) and July (right). Ozone changes are shown in ppbv, NO_x and PAN changes are shown in pptv.

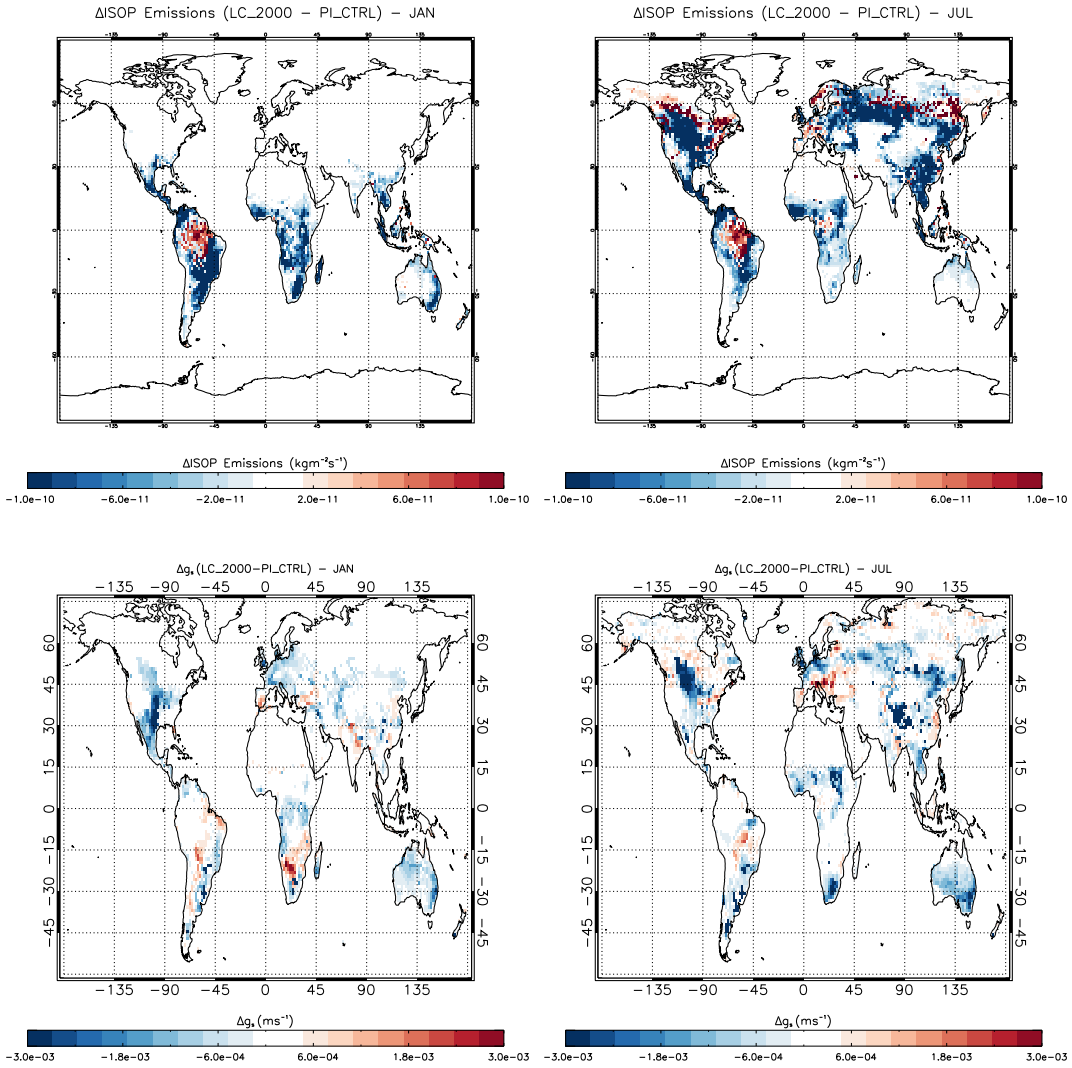

FIGURE 5.3: Changes in isoprene emissions (top row) and stomatal conductance (bottom row) from vegetation between PI_CTRL and LC_2000 scenarios for January (left) and July (right). Isoprene emissions are in $\mathrm{kgCm^{-2}s^{-1}}$ and stomatal conductances are in $\mathrm{ms^{-1}}$.

July (around 200 to 300 pptv). This reflects the seasonality of the NO_x emissions (Figure 5.4). In contrast, as a result of the greater isoprene emissions and resultant PAN formation under the PI_CTRL scenario, there are higher surface NO_x mixing ratios over more remote regions such as the tropical oceans and coastal areas in the vicinity of areas of peak NO_x emissions where mixing ratios are around 10 to 30 pptv higher than under the LC_2000 scenario.

Figures 5.3 and 5.4 show that the greater isoprene emissions under the PI_CTRL scenario coincide in both January and July with the regions where surface NO_x emissions are greatest. Therefore during the isoprene oxidation process (Chapter 2), the greater amounts

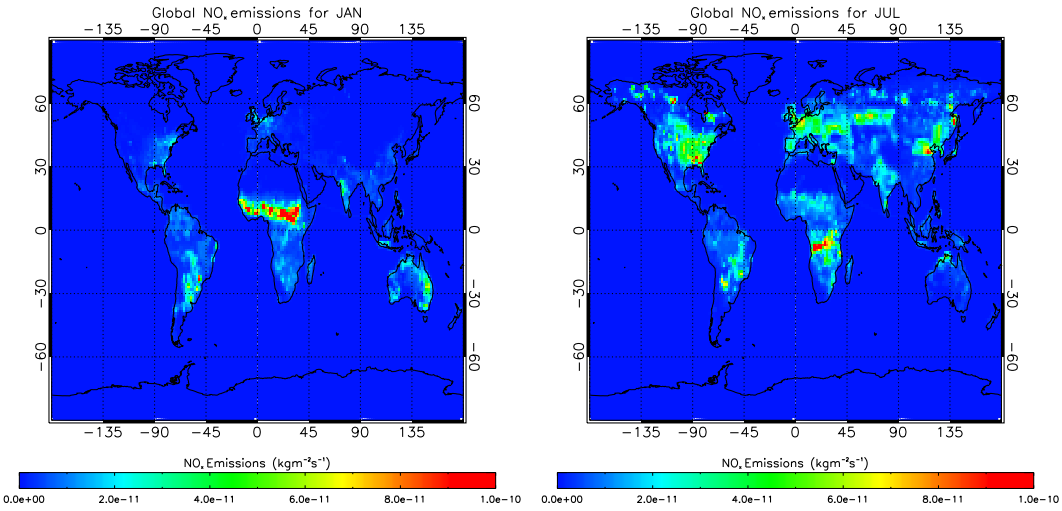

FIGURE 5.4: Surface NO_x emissions for January and July representative of the 1860s. Emissions are in $kgm^{-2}s^{-1}$

of isoprene present over these regions result in greater rates of conversion of NO_x into PAN and analogue compounds such as MPAN. These species are longer lived than NO_x in the atmosphere and act as a reservoir species allowing the transport of NO_x to more remote regions (Moxim et al., 1996). This effect is evident in the bottom panels of Figure 5.2 where surface PAN mixing ratios are shown to be greater under the PI_CTRL scenario over the majority of locations. In January, PAN mixing ratios are homogeneously greater over the entire northern hemisphere mid latitude and polar regions with differences of 20 to 50 pptv seen over the more remote regions and differences of 60 to 100 pptv seen over regions closer to the enhanced isoprene emissions over parts of the USA and Mexico. These greater PAN mixing ratios in the northern hemisphere winter are due to longer PAN lifetimes during the winter months when its thermal breakdown is less effective due to cooler temperatures. In the southern hemisphere, the enhanced isoprene emissions under the PI_CTRL scenario results in larger PAN mixing ratios of 100 pptv or greater close to the primary isoprene emissions regions of the Amazon, Central Africa and SE Asia.

In July, the seasonality of the isoprene source is evident with the greatest differences in PAN concentrations between the PI_CTRL and LC_2000 scenarios now seen over the northern hemisphere mid-latitudes with greater concentrations seen over much of the USA, Europe, Siberia and extra-tropical Asia, where there are widespread differences of 100 pptv or greater. This effect is important as the lifetime of PAN is significantly shorter in the northern hemisphere summer indicating the strong role isoprene emissions play

in controlling the surface PAN mixing ratios. During the southern hemisphere winter, homogeneous increases in surface PAN mixing ratios are seen due to the greater isoprene under the PI_CTRL scenario, though these are much less pronounced than in January due to generally lower NO_x emissions in the southern hemisphere compared to the north (Figure 5.4). However PAN mixing ratios of 100 pptv or greater are seen over the Amazon and much of southern Africa close to regions of isoprene sources.

These enhanced levels of PAN over the oceans and more remote regions can result in higher NO_x concentrations and results in the higher background ozone levels seen over these regions under the PI_CTRL scenario when compared to the LC_2000.

Figure 5.5 shows the impact of changing the land surface map from 1865 to 2000 on the ozone, isoprene (C_5H_8), formaldehyde (HCHO), PAN, OH and HO_x distribution and magnitude. The impact of the higher isoprene emissions under the PI_CTRL scenario is clearly evident with modelled ozone concentrations shown to be on the whole greater throughout the troposphere by around 0.4 ppbv to 0.8 ppbv with larger differences of around 1 ppbv seen in northern hemisphere tropics and 2 ppbv or higher in the upper troposphere lower stratosphere (UTLS) region over the tropics of both hemispheres.

Overall, isoprene concentrations are shown to be greater under the PI_CTRL scenario. Due to the short lifetime of isoprene in the atmosphere (around 1.7 hours (Pacifico et al., 2009)) the greatest differences are as expected close to the major isoprene sources with concentrations under the PI_CTRL scenario shown to be 30 pptv or larger than for the LC_2000 scenario between 30S and 60N. In the free troposphere, these differences are smaller at around 6 to 18 pptv with the larger concentrations seen under the PI_CTRL scenario and the greatest differences seen in the upper troposphere over the tropics. This is due to deep convection in the boundary layer coinciding with the higher isoprene emissions under the PI_CTRL scenario resulting in rapid transport of isoprene to higher altitudes despite its short lifetime. Here it can be oxidised by reaction with OH and in the presence of NO_x result in ozone formation.

As a result of the higher isoprene emissions under the PI_CTRL scenario, PAN formation is enhanced and once formed is transported throughout the entire troposphere by convective mixing. PAN concentrations are homogeneously greater throughout the entire troposphere by 10 pptv to 50 pptv with the largest differences seen in the northern hemisphere free

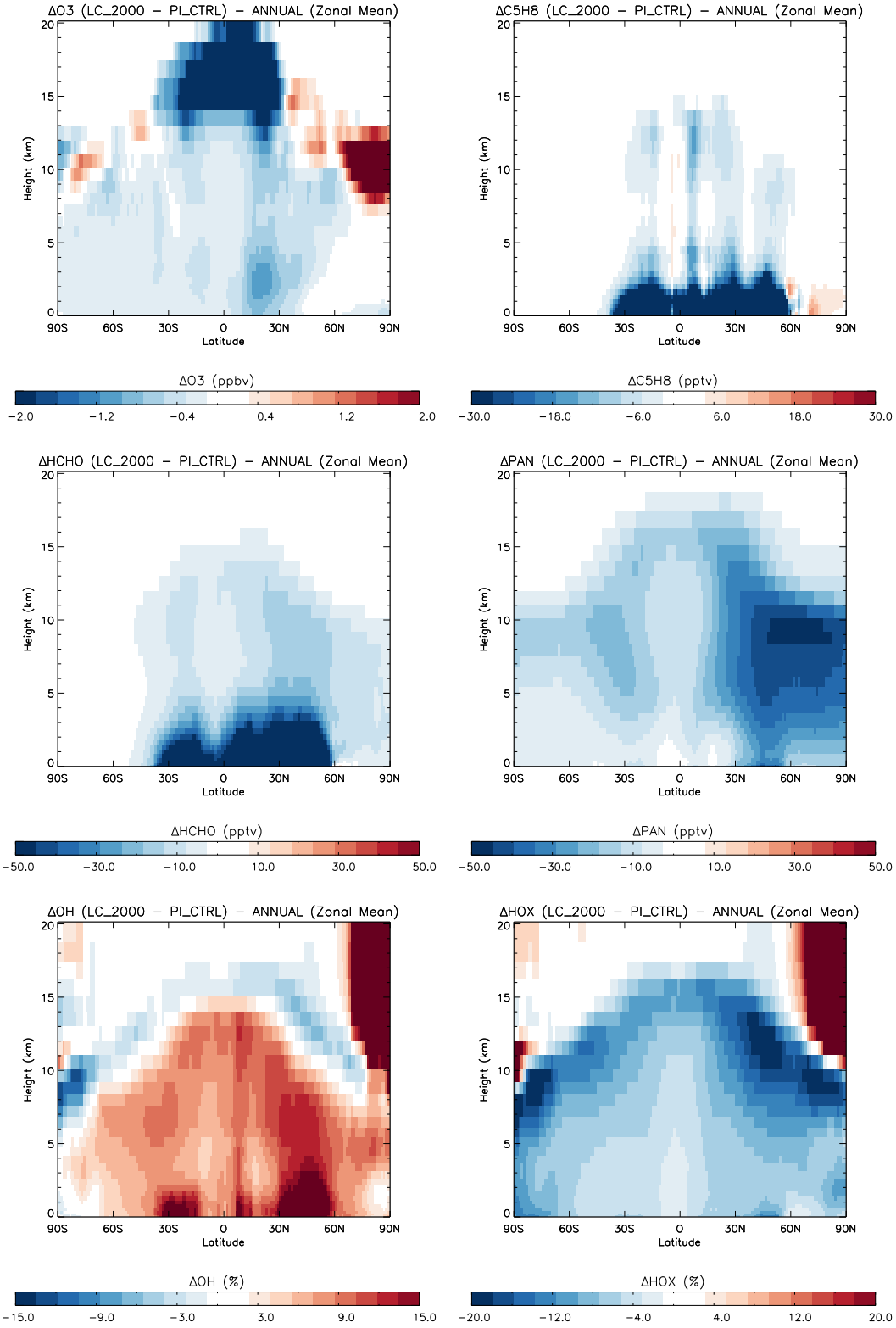

FIGURE 5.5: Annually and zonally averaged changes in ozone (ppbv), isoprene (pptv), HCHO (pptv), PAN (pptv), OH(%) and HO_x between the PI_CTRL and LC_2000 scenarios.

troposphere. Ultimately this PAN will break down, releasing NO_2 and resulting in ozone formation. In the UTLS region in the tropics, the higher PAN mixing ratios of around 10 pptv to 20 pptv coincide with the larger isoprene concentrations which acts to increase ozone production in this region. This contributes to the larger ozone mixing ratios in this region under the PI_CTRL scenario (2 ppbv to 6 ppbv).

OH concentrations under the PI_CTRL scenario are lower than those under the LC_2000 scenario with greatest differences seen at the surface over the tropics and the northern hemisphere mid-latitudes where mixing ratios are up to 15% lower, close to the regions where the changes in isoprene emissions are greatest. In the free troposphere, OH concentrations are greater under the LC_2000 scenario by approximately 3 % to 9 % with the largest changes over the northern hemisphere tropics and mid-latitudes However around the tropopause region OH concentrations are shown to be greater under the PI_CTRL scenario by around 3 to 6 %. The tropospheric global mean OH concentration under the PI_CTRL scenario is 6.4×10^5 molecules cm^{-3} which is 0.4×10^5 molecules cm^{-3} lower than under the LC_2000 scenario (6.8×10^5 molecules cm^{-3}) with the higher isoprene emissions under the PI_CTRL accounting for this drop. This is due to the larger isoprene emissions resulting in a greater sink of OH through higher rates of isoprene oxidation.

HCHO does not a have a sufficiently long enough lifetime in the atmosphere to be mixed homogeneously throughout the troposphere however under the PI_CTRL scenario the higher isoprene emissions result in larger HCHO (50 pptv or greater) over the tropics and the northern hemisphere mid-latitudes (Figure 5.5). This results in the transportation of HCHO to the upper troposphere through the deep convection in the tropics. This is shown in Figure 5.5 where formaldehyde mixing ratios are greater by at least 10 pptv throughout the entire northern hemisphere and are around 20 to 30 pptv greater in the free troposphere above the major isoprene source regions. Upon reaching the upper troposphere, HCHO can undergo photochemical decomposition which constitutes an important HO_x source in the UTLS region. This is consistent with the findings of Folberth et al. (2006) which also showed an increase in HO_x in the UTLS region as a result of increased isoprene emissions.

Figure 5.5 shows that despite the reduced OH concentrations due to larger isoprene emissions under the PI_CTRL scenario, the photochemical decomposition of isoprene and its oxidation products in fact adds to the HO_x burden of the troposphere with concentrations

under the PI_CTRL scenario shown to be at least 4 % greater throughout the troposphere. The differences are most pronounced in the UTLS region where concentrations are greater by up to 20 %, particularly over the tropics and northern hemisphere mid-latitudes where HCHO concentrations are greater. A contribution to this higher HO_x in the UTLS region could also be from the elevated ozone levels under the PI_CTRL scenario through the formation of OH. Overall, the higher HO_x mixing ratios under the PI_CTRL scenario play an important role in ozone formation as they act as intermediate species in photochemical ozone production by driving the conversion of NO to NO_2 (Sommariva et al., 2011). The response of the ozone production rate to changing NO_x concentrations has also been shown to have a strong dependence on the production rate of HO_x (Thornton et al., 2002).

5.4.4 Comparison of PI_CTRL and EMS_1860 PI scenarios

Figure 5.6 shows a comparison of mean annual surface and zonal ozone mixing ratios between the PI_CTRL scenario used in this Chapter and a typical model setup (here termed the EMS_1860 scenario (Table 5.2)) used to estimate the pre-industrial tropospheric ozone distribution in previous model studies (Hauglustaine and Brasseur, 2001; Lamarque et al., 2005; Mickley et al., 2001). The model setup for the EMS_1860 scenario differs from the PI_CTRL simulation in that it is run with a climate representative of the present day including prescribed greenhouse gas concentrations, sea-surface temperatures and sea-ice (Table 5.2). The EMS_1860 scenario is also run with fixed land cover representative of the year 2000.

Surface ozone mixing ratios are greater under the EMS_1860 scenario throughout the northern hemisphere by at least 1 ppbv, with differences approaching 5 ppbv over parts of the United states and Greenland. In the southern hemisphere the greatest differences are mainly confined to the land masses with ozone concentrations being greater under the EMS_1860 scenario by around 3 to 5 ppbv over parts of S America and Africa, though Central regions of Africa see greater ozone mixing ratios under the PI_CTRL scenario by around 1 ppbv. Over the southern hemisphere marine regions, changes in surface ozone are much smaller. Concentrations are greater under the EMS_1860 by up to 2 ppbv off of the coast of S America and within the coastal regions of Indonesia. Elsewhere, differences are less than 1 ppbv. The changes in the zonal ozone distribution between the scenarios shows that ozone mixing ratios are greater under the EMS_1860 scenario by at least 2 ppbv

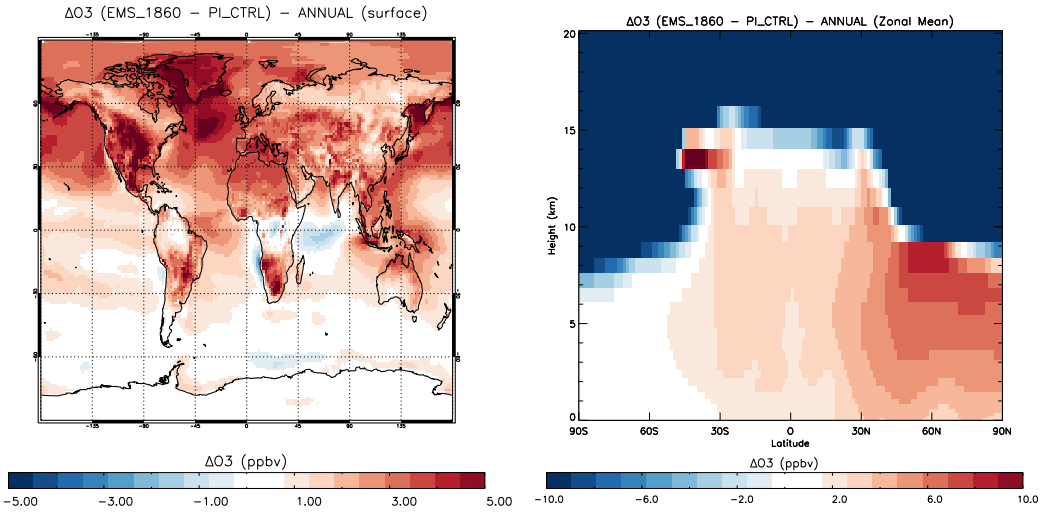

FIGURE 5.6: Mean annual differences in surface (left) and zonal ozone (right) concentrations between PI_CTRL and EMS_1860 scenarios. All values are in ppbv.

throughout the entire northern hemisphere troposphere and southern hemisphere tropical troposphere with differences increasing to around 6 to 8 ppbv in the free troposphere around the mid-latitude and polar regions in the north. The model yields differences between the 2 scenarios of 10 ppbv or greater throughout the stratosphere though this is linked to differences in the climate setup of the model and the prescribed model ozone for the stratosphere. As the model for the EMS_1860 scenario has a present day climate setup, stratospheric ozone in this scenario is representative of the year 2000 and hence is lower than that for a pre-industrial climate setup (the PI_CTRL scenario).

As the anthropogenic emissions of ozone precursors are held constant between model runs, this change in tropospheric ozone mixing ratios can be linked back to the different land maps between the two scenarios (1865 land classification map under the PI_CTRL scenario and 2000 land classification map under the EMS_1860 scenario) which results in lower deposition rates and smaller isoprene emissions under the EMS_1860 scenario. The lower deposition rates can affect the deposition of NO_2 and PAN (not shown) which can be transported to more remote environments and enhance ozone production contributing to the rise in ozone concentrations. The higher CO_2 mixing ratios under the EMS_1860 scenario result in suppression of stomatal uptake by vegetation and inhibition of isoprene emissions (discussed in further detail in Section 5.5.2). This acts to further reduce the rate of ozone uptake and its precursor species. The lower isoprene emissions also see the removal of the isoprene ozone sink in the major source regions which contributes to higher

ozone concentrations over land for the EMS_1860 simulation. The combined impacts of the land cover change and higher CO_2 concentrations under the EMS_1860 scenario lead to overall higher ozone concentrations with the effects more pronounced in the northern hemisphere as there is greater land mass than in the southern hemisphere, hence the sensitivity to changing surface characteristics is much greater.

Finally, for the EMS_1860 simulation the model is setup with a present day climate including SSTs, sea-ice and greenhouse gases (CO_2,CH_4 and N_2O) which leads to an overall warmer climate than under the PI_CTRL scenario. This can impact the rate of CH_4 oxidation and also leads to changes in atmospheric H_2O which affects the production of OH the resultant oxidation rates of tracer species such as isoprene. Both of these processes can impact ozone formation.

5.4.5 Comparison with pre-industrial observations

Figure 5.7 shows modelled monthly-mean ozone from the PI_CTRL, LC_2000 and EMS_1860 model simulations compared with available monthly mean ozone observations from the end of the 19th Century (Section 5.3) and Table 5.4 shows the annual model mean bias for each site under each scenario.

The model has a positive mean annual bias of 5.5 to 17.9 ppbv, 5.7 to 17.6 ppbv and 9.2 to 18.0 ppbv under the PI_CTRL, LC_2000 and EMS_1860 scenarios respectively. This overall positive bias is consistent with those found in previous studies which aim to provide the best model estimate of the pre-industrial troposphere (Lamarque et al., 2005; Mickley et al., 2001; Shindell et al., 2003; Wang and Jacob, 1998). For 8 of the 12 sites, the PI_CTRL scenario has the lowest bias towards the observations with the lowest bias of 5.5 ppbv over Tokyo. For 3 of the sites (Manilla, Montsouris and Pic du Midi) the LC_2000 scenario provides the lowest bias with a value of 11.2 ppbv over Pic du Midi showing the best match to the observations. Finally, over the Luanda site model biases are high under all scenarios with the EMS_1860 scenario providing the best match to the observations with a bias of 16.8 ppbv. This high bias over Luanda is consistent with the findings of Lamarque et al. (2005) which showed a model bias over Luanda of 21.4 ppbv.

When comparing the PI_CTRL and EMS_1860 scenarios, the greatest reduction in model bias is seen at Lansing (3.9 ppbv drop in bias) with Montevideo seeing the least (reduction

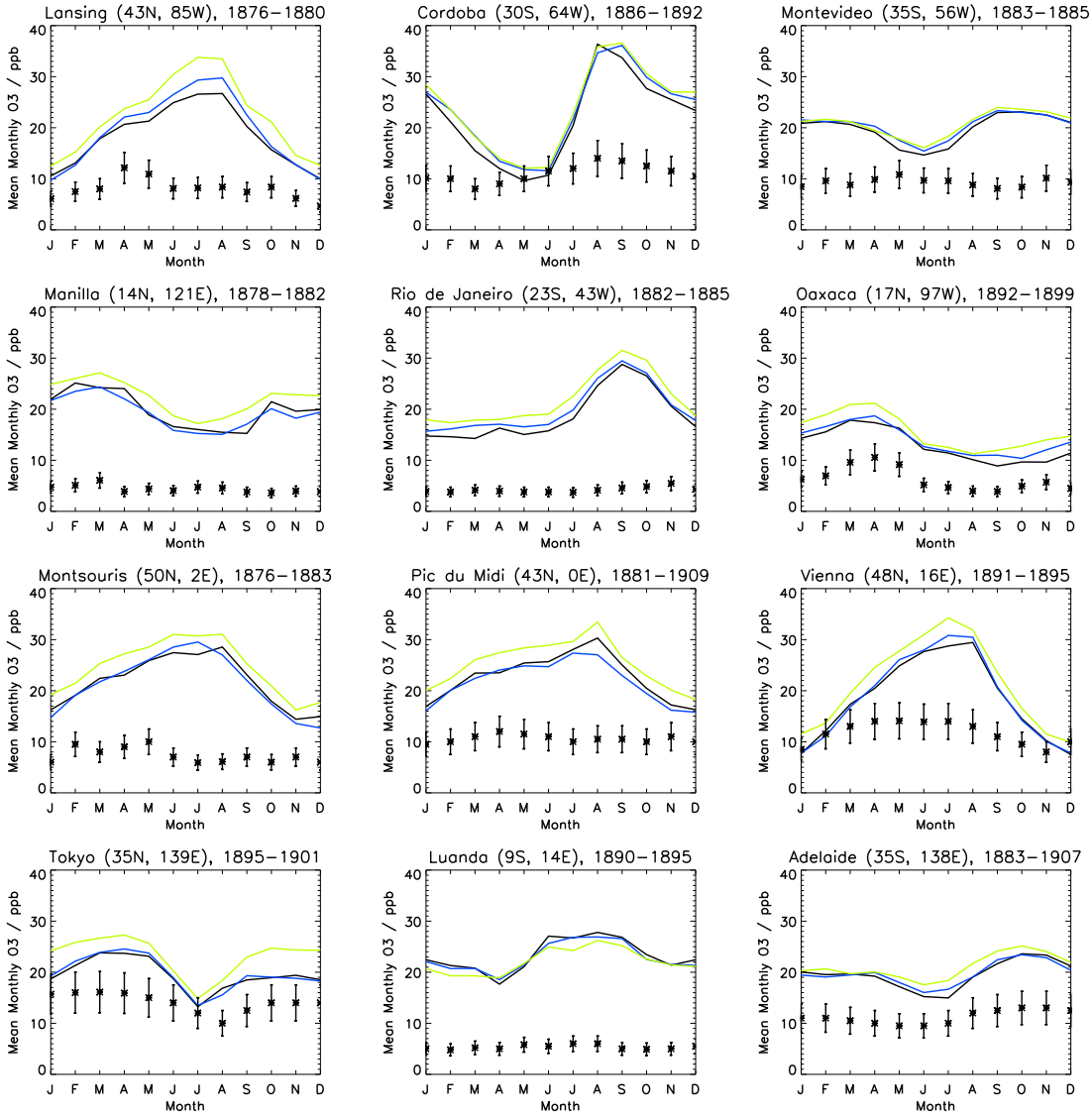

FIGURE 5.7: Comparison of monthly mean ozone from the PI_CTRL **(Black line)**, LC_2000 **(Blue line)** and EMS_1860 **(Green line)** model simulations with available pre-industrial monthly mean observations (See Section 5.3 for details) from the end of the 19th Century **(∗)**. Error bars indicate 25% uncertainty associated with observations (Marenco et al., 1994). All values are in ppbv.

in bias of 0.9 ppbv). When comparing the PI_CTRL and LC_2000 scenarios Cordoba sees the greatest bias reduction (1.5 ppbv) compared to Adelaide which shows the least (bias reduction of 0.1 ppbv). Overall, this shows the importance of representing the model land classification scheme as accurately as possible when simulating pre-industrial conditions as using a land map representative of the present day can introduce annual mean model biases of up to 1.5 ppbv. When the model is setup to run with a present day climate as well as a present day land map, these biases can potentially increase to 3.9 ppbv. It should however be noted here that high levels of uncertainty exist in the pre-industrial ozone observations

TABLE 5.4: Annual mean model bias in ppbv for modelled versus observed pre-industrial ozone for the PI_CTRL, LC_2000 and EMS_1860 model scenarios. The values highlighted in bold indicate the lowest bias for each respective site.

		Scenario		
		PI_CTRL	LC_2000	EMS_1860
Site	Lansing	**10.4**	11.4	14.3
	Cordoba	**10.8**	12.3	13.0
	Montevideo	**10.5**	11.2	11.6
	Manilla	15.5	**14.9**	18.0
	Rio de Janeiro	**14.6**	15.8	17.7
	Oaxaca	**6.6**	7.6	9.3
	Montsouris	14.4	**14.1**	17.3
	Pic du midi	12.1	**11.2**	14.8
	Vienna	**6.7**	7.0	9.6
	Tokyo	**5.5**	5.7	9.2
	Luanda	17.9	17.6	**16.8**
	Adelaide	**8.4**	8.5	9.9

(up to 25% (Marenco et al., 1994)). An additional factor to consider here however is that although there are changes in the model biases under different representations of biosphere-atmosphere interactions the overall bias to the pre-industrial observations remains large (mean bias of 11.1 ppbv under the PI_CTRL scenario). This points towards further investigation into other processes that could result in model overestimation of pre-industrial ozone concentrations.

5.5 Sensitivity of modelled pre-industrial tropospheric ozone to vegetation CO_2 exposure

This section presents the results of the HadGEM2-ES simulations to assess the sensitivity of the modelled pre-industrial tropospheric ozone distribution to the prescribed CO_2 concentration that the vegetation was exposed to through the response of stomatal conductance and biogenic isoprene emissions.

5.5.1 Model setup and scenarios

For the model simulations performed in this section the PI_CTRL run was setup as previously (Section 5.4.1) with land cover representative of 1865, greenhouse gases fixed at 1865 concentrations and sea-ice and SSTs representative of the 1860s (Table 5.5). Anthropogenic surface emissions were once again representative of the pre-industrial period (1860s). Two model experiments were performed in addition to the PI_CTRL simulation to assess the sensitivity of tropospheric ozone to the prescribed CO_2 mixing ratio that the vegetation was exposed to. For all scenarios the model was spun up for a period of nine months and then run for 3 years with the analysis performed on the final year of each run. It was not necessary to run the model for 10 years for these cases because the changes in dry deposition and biogenic emissions in response to the CO_2 only impact the chemical composition of the atmosphere and do not feedback to the model dynamics or radiation scheme as these couplings are not activated (Section 5.4.1). As the model initialisation fields are taken from the CMIP5 transient run for the pre-industrial climate the model is thus very close to a spun up state at the start of the run and is therefore representative of the pre-industrial period. This holds the model climate fixed under each scenario allowing analysis to be performed on a single year of each run. A summary of the model scenarios can be found in Table 5.5.

TABLE 5.5: Summary of HadGEM2-ES pre-industrial model scenarios to assess sensitivity of ozone to vegetation CO_2 exposure.

Model[a] Scenario	Atmospheric CO_2[b]	SST + Sea-ice	Tracer Emissions
PI_CTRL	286 ppmv	1860s clim	1860s clim
CO2_DD	368 ppmv (dry dep only)[c]	1860s clim	1860s clim
CO2_DDBVOC	368 ppmv (iBVOC + dry dep only)[d]	1860s clim	1860s clim

[a] All scenarios are setup with a fixed land cover representative of 1865.

[b] In each model scenario the other active greenhouse gases CH_4 and N_2O are fixed at 1865 values (0.8 ppmv for CH_4 and 276 ppbv for N_2O)

[c] Dry deposition scheme sees 368 ppmv CO_2, rest of model sees 286 ppmv CO_2.

[d] Dry deposition and iBVOC schemes sees 368 ppmv CO_2, rest of model sees 286 ppmv CO_2.

5.5.2 Impact of vegetation CO_2 exposure on modelled pre-industrial tropospheric ozone

Under the CO2_DD scenario, the surface vegetation is exposed to a fixed present day CO_2 mixing ratio of 368 ppmv rather than pre-industrial levels of CO_2 (286 ppmv) under the PI_CTRL scenario. Figure 5.8 shows the differences in stomatal conductances between the 2 scenarios. As expected, higher CO_2 values (CO2_DD scenario) induce stomatal closure (Gedney et al., 2006) with greatest decreases seen over the tropical rainforest regions of the southern hemisphere in January (-1.8x10^{-3} ms^{-1} to -2.0x10^{-3} ms^{-1}) and over widespread areas of N America, Europe, Siberia and SE Asia during July (up to -2.0x10^{-3} ms^{-1}). This therefore indicates an overall drop in the rate of uptake of trace gases by vegetation under the CO2_DD scenario.

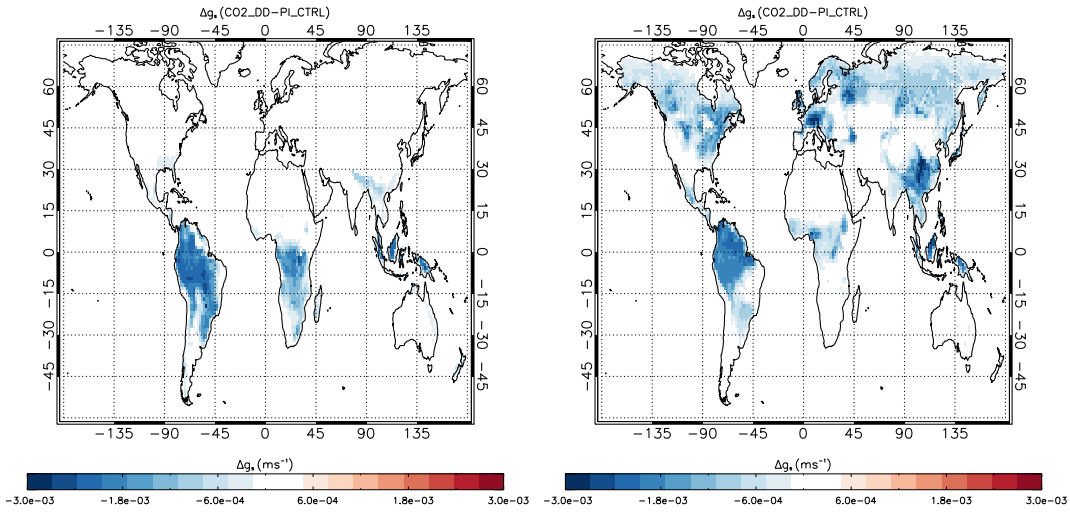

FIGURE 5.8: Changes in vegetation stomatal conductance between PI_CTRL and CO2_DD scenarios for January (left) and July (right). Values are in ms^{-1} and are averaged over all model PFT types.

The resultant impact of this change is shown in Figure 5.9 which shows the differences in surface mixing ratios of ozone, NO_x and PAN between the PI_CTRL and CO2_DD scenarios. Ozone mixing ratios are shown to overall be greater under the CO2_DD scenario with the largest differences seen over the Amazon and central parts of Africa in January (ozone concentrations are up to 1 ppbv greater than under the PI_CTRL scenario). In July much of the northern hemisphere is shown to have larger surface ozone concentrations by at least 0.4 ppbv over much of N America, Europe and Asia though these differences approach 1 ppbv over eastern parts of the United states and central Europe. Ozone is also

greater in the marine atmosphere with mixing ratios of at least 0.2 ppbv greater under the CO2_DD scenario. A contributing factor to this increase in ozone is the impact of reduced stomatal conductances on the uptake of NO_x and PAN.

PAN mixing ratios are greater under the CO2_DD scenario as a result of the lower rate of uptake through the plants' stomata with the greatest differences once again seen over the Amazon and Central Africa in January (12 to 20 pptv) and over large parts of the northern hemisphere during July with widespread regions of N America, Europe and eastern Siberia seeing PAN mixing ratios that are in excess of 20 pptv greater under the CO2_DD scenario. As shown in Section 5.4.3 these enhanced PAN concentrations can be responsible for the higher ozone levels observed over the more remote marine regions. Despite the reduction in the rate of uptake of NO_2 through dry deposition, NO_x mixing ratios are overall lower under the CO2_DD scenario than under the PI_CTRL, by up to 10 pptv over parts of the Amazon and Central Africa during both January and July. However, these regions correspond to the areas of greatest differences in PAN mixing ratios indicating that greater proportions of NO_x are locked up in the PAN reservoir hence resulting in lower surface NO_x. Over the marine regions NO_x mixing ratios are marginally higher under the CO2_DD scenario by up to 1 pptv, due to the long range transport of PAN which enhances ozone production over theses regions.

These changes in the PAN and NO_x surface concentrations are driven by the reduced stomatal uptake induced by the higher CO_2 under the CO2_DD scenario. However the rise in NO_x mixing ratios due to reduced dry deposition acts to increase the rate of PAN formation close to the major isoprene sources. This dominates over the dry deposition impact on NO_x leading to a net reduction in concentrations. Concurrently to this the chemical production of PAN is increased acting to enhance the reduced uptake of NO_y species. Overall, these NO_x and PAN effects are largely controlled by the reduction in dry deposition.

Under the CO2_DDBVOC scenario, both the model vegetation and the iBVOC scheme are exposed to the 368 ppmv present day CO_2 value. As shown under the CO2_DD scenario, the response of the vegetation is a reduction in the rate of dry deposition to vegetated surfaces due to closure of the plants' stomata as a result of the higher CO_2 concentration (Figure 5.8). As discussed previously (Heald et al., 2009; Pacifico et al., 2009; Young et al., 2009), higher CO_2 levels can result in the inhibition of isoprene emissions with this effect

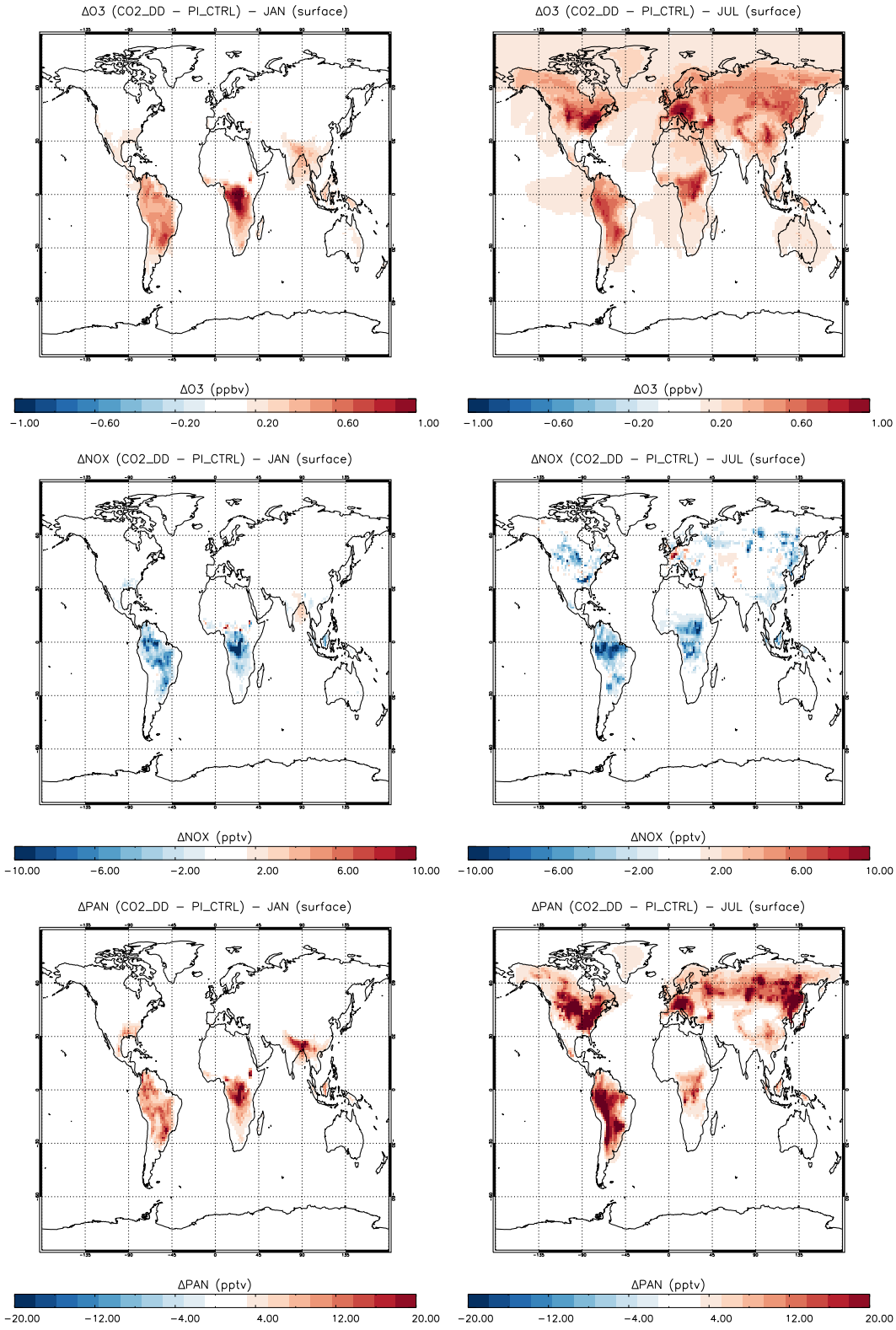

FIGURE 5.9: Changes in surface ozone, NO_x and PAN concentrations between PI_CTRL and CO2_DD scenarios for January (left) and July (right). Ozone changes are shown in ppbv, NO_x and PAN changes are shown in pptv.

shown in Figure 5.10. In January, isoprene emissions are lower under the CO2_DDBVOC scenario by up to 1.0x10^{-10} kgCm^{-2}s^{-1} over large parts of the Amazon and Central Africa. In July, the differences in isoprene emissions are largely seen in the northern hemisphere with emissions rates shown to be lower under the CO2_DDBVOC scenario by 1.0x10^{-10} kgCm^{-2}s^{-1} or greater over large parts of N America, Europe, Siberia and SE Asia. However, large differences are still seen over the major isoprene sources over the Amazon and Central Africa during July. As a result of this global annual total isoprene emissions under the CO2_DDBVOC scenario are 456 TgCyr^{-1} compared to 580 TgCyr^{-1} under the PI_CTRL scenario.

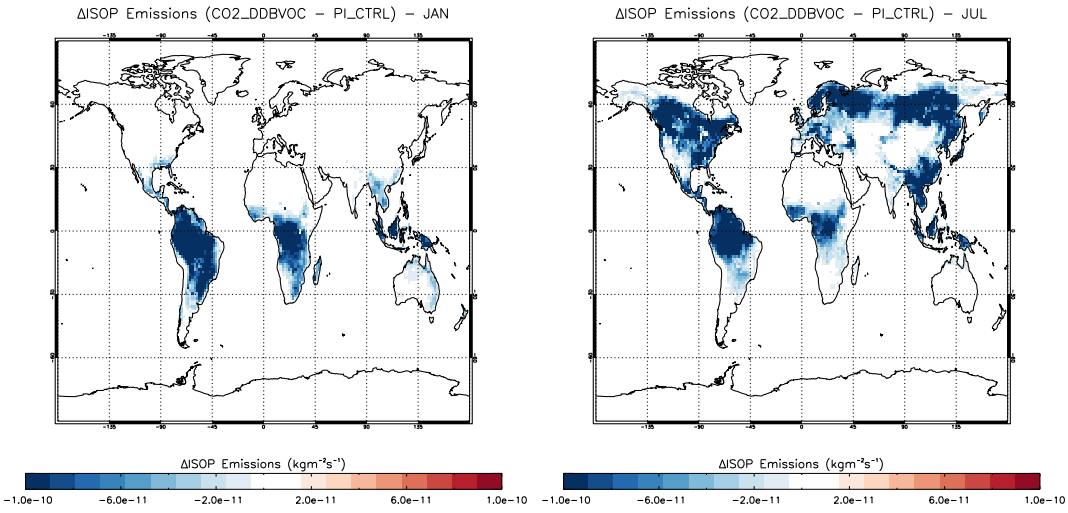

FIGURE 5.10: Changes in isoprene emissions from vegetation between PI_CTRL and CO2_DDBVOC scenarios for January (left) and July (right). All values are in kgCm^{-2}s^{-1}

Figure 5.11 shows differences in surface ozone, NO_x and PAN between the CO2_DDBVOC and PI_CTRL scenarios. The response of surface ozone mixing ratios to the reduced dry deposition and isoprene emissions under the CO2_DDBVOC scenario is similar to that seen between the comparison of the PI_CTRL and LC_2000 scenarios. In both months, ozone mixing ratios are shown to be greater under the PI_CTRL scenario over the marine regions by up to 1 ppbv around the tropical Atlantic. This is linked to enhanced PAN formation due to greater isoprene emissions under the PI_CTRL scenario and transport of NO_x to the cleaner marine regions resulting in ozone formation. Over land, ozone mixing ratios are higher under the CO2_DDBVOC scenario by up to 2 ppbv due to reduced stomatal uptake of ozone and its precursors and CO_2 inhibition effect on isoprene emissions due to the higher CO_2 mixing ratio the vegetation is exposed to.

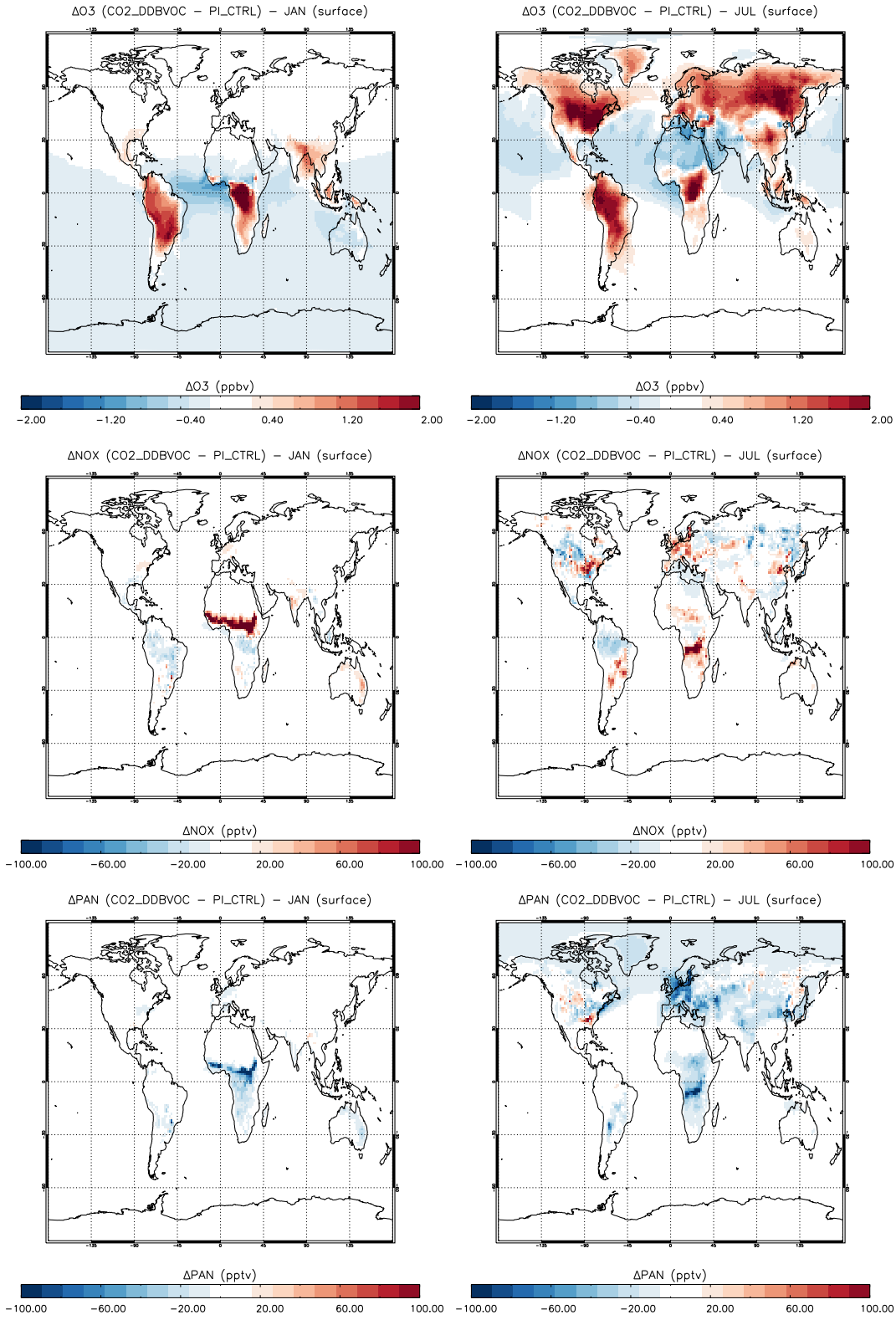

FIGURE 5.11: Changes in surface ozone, NO_x and PAN concentrations between PI_CTRL and CO2_DDBVOC scenarios for January (left) and July (right). Ozone changes are shown in ppbv, NO_x and PAN changes are shown in pptv.

Figure 5.12 shows the zonal mean differences in ozone, HCHO, OH and HO_x between the CO2_DDBVOC and PI_CTRL scenarios. The ozone distribution shows contrasting responses in each hemisphere. In the southern hemisphere, mixing ratios are shown to be greater under the PI_CTRL scenario by 0.1 to 0.2 ppbv due to the greater formation of ozone over the more remote marine regions. In the northern hemisphere, mixing ratios are shown to be greater under the CO2_DDBVOC throughout the entire free troposphere by at least 0.1 ppbv though they are greater by 0.5 ppbv or more in the mid-latitudes and polar free troposphere. At the surface mixing ratios are greater under the CO2_DDBVOC scenario by 0.5 ppbv or greater throughout the northern hemisphere mid latitudes and polar regions. This is due to the greater land mass in the northern hemisphere and the increase in surface ozone due to reduced stomatal conductance over vegetated regions (Figure 5.8). In contrast at the surface in the tropics, ozone mixing ratios are shown to be greater under the PI_CTRL scenario by 0.1 to 0.3 pptv, with this linked to the enhance PAN formation under the PI_CTRL scenario due to larger isoprene emissions throughout this region (Figure 5.10). This results in a slight increase in the tropospheric ozone burden from 203.7 Tg under the PI_CTRL scenario to 204.1 Tg under the CO2_DDBVOC scenario.

In the UTLS region over the tropics differences in ozone mixing ratios are shown to exceed 0.5 ppbv with the larger values seen for the PI_CTRL scenario. This can be explained by the change in PAN and isoprene distributions. For both species, concentrations are shown to be greater throughout the troposphere under the PI_CTRL scenario, particularly at the tropical tropopause where the higher isoprene and PAN mixing ratios coincide. This increases the free radical and NO_x concentrations in this region leading to ozone formation and the higher ozone mixing ratios. This is largely due to the greater isoprene emissions under the PI_CTRL and deep convection in the tropics transporting isoprene and PAN to higher altitudes. This convection is evident from a plume of higher isoprene (of 30 pptv or greater) concentrations for the PI_CTRL which extends from the surface up to a height of approximately 15 km, just below the tropical tropopause.

HO_x mixing ratios are greater under the PI_CTRL scenario with differences approaching 12 to 16 % in the tropical UTLS region. A contribution to this increase in HO_x at the tropical tropopause is from the larger ozone mixing ratios through the formation of OH. Alternatively, larger HCHO mixing ratios of up to 50 pptv for the PI_CTRL scenario as a result of the higher isoprene emissions also provide a contribution to the higher HO_x

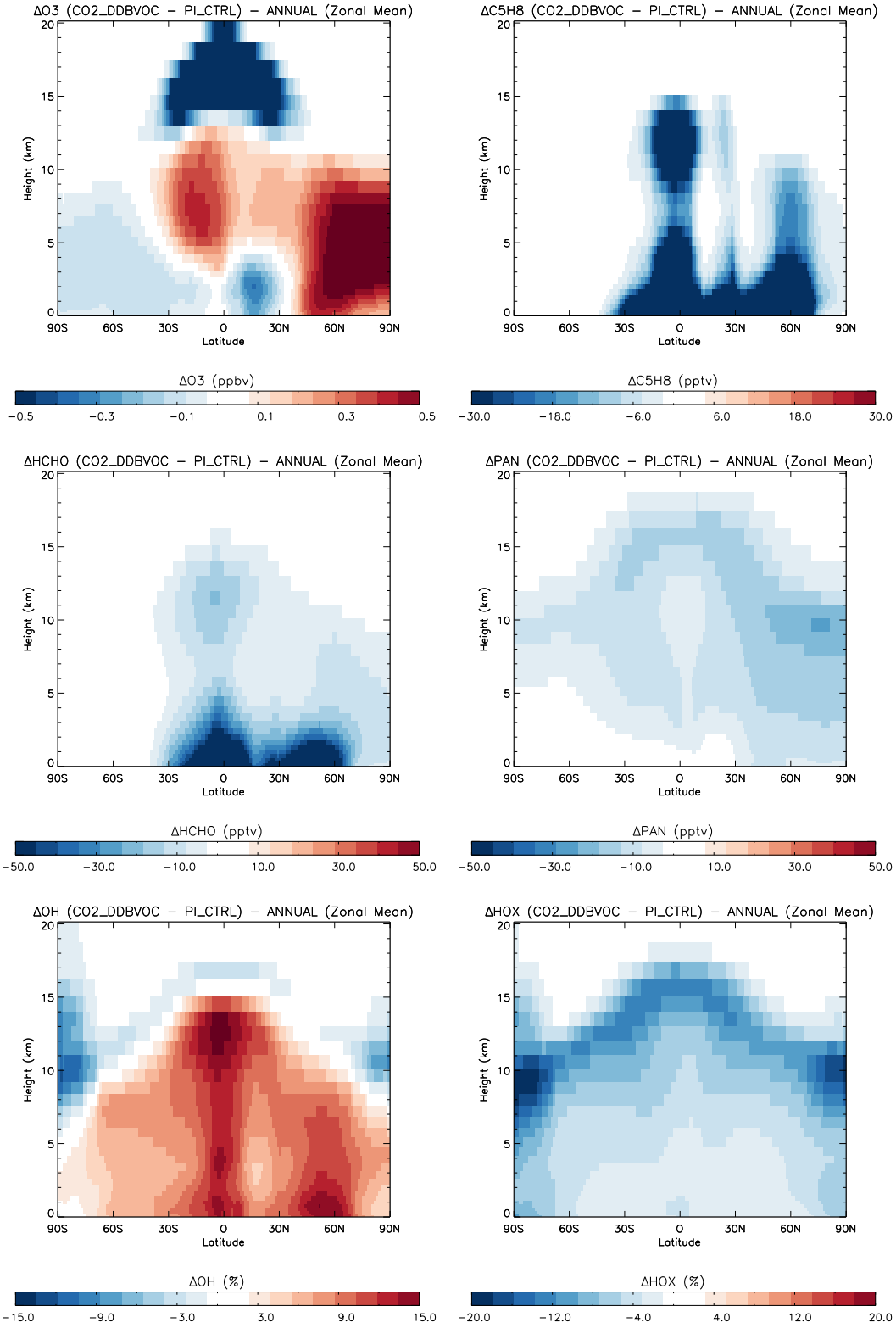

FIGURE 5.12: Annually and zonally averaged changes in ozone (ppbv), isoprene (pptv), HCHO (pptv), PAN (pptv), OH(%) and HO_x between the PI_CTRL and CO2_DDBVOC scenarios.

concentrations. Finally, tropospheric OH values under the CO2_DDBVOC are shown to be larger than under the PI_CTRL scenario by 3 to 15% with the greatest differences tending to be shown in the northern hemisphere. This results in an OH burden of 6.9 $\times$ 10^5 molecules cm^{-3} under the CO2_DDBVOC scenario which is 0.4 $\times$ 10^5 molecules cm^{-3} greater than under the PI_CTRL (6.5 $\times$ 10^5 molecules cm^{-3}). This is important, as changes in the abundance and production rate of HO_x can impact the rate of ozone formation (Sommariva et al., 2011; Thornton et al., 2002).

Finally, in order to isolate the effect of changing isoprene emissions as a result of exposing the iBVOC scheme to present day CO_2, surface ozone concentrations the CO2_DD and CO2_DDBVOC scenarios are compared (shown in Figure 5.13).

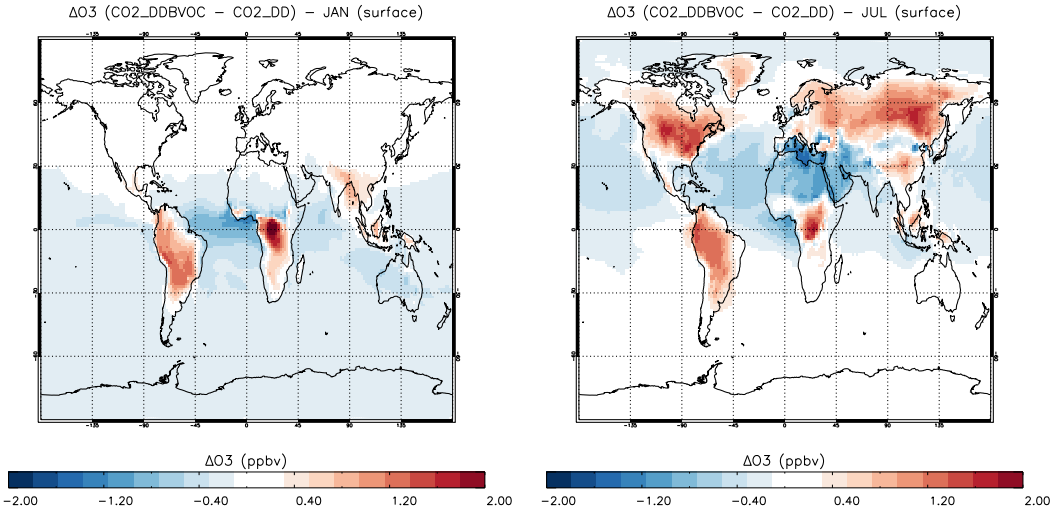

FIGURE 5.13: Changes in surface ozone concentrations between CO2_DD and CO2_DDBVOC scenarios for January (left) and July (right). Values are shown in ppbv.

The pattern of surface ozone concentration differences between the CO2_DDBVOC and CO2_DD scenarios show a similar pattern to those for the comparison of the PI_CTRL and CO2_DDBVOC scenarios. However, they are less pronounced over the major vegetated regions in the summer of each respective hemisphere with maximum differences of up to 1.2 ppbv over the Amazon in January and over parts of N America, Europe, Russia and China in July with the CO2_DDBVOC simulation showing larger concentrations than the CO_DD simulation. For the PI_CTRL and CO2_DDBVOC comparison, these differences are larger at up to 2 ppbv with the PI_CTRL showing the higher concentrations.

Overall, tropospheric ozone concentrations are shown to be sensitive to the CO_2 mixing ratio that the model vegetation is exposed to. When vegetation is exposed to higher levels of CO_2 there is a reduction in dry deposition of ozone and its precursor species due to stomatal closure induced by the higher CO_2 levels. In addition to this, isoprene emissions are also inhibited under higher CO_2. The impacts on ozone concentrations are shown to be stronger for the changes in isoprene emissions than for the reduction in dry deposition. This is in agreement with the findings of Lamarque et al. (2005) which showed a greater sensitivity of simulated pre-industrial ozone to changes in precursor emissions rather than dry deposition changes.

5.5.3 Comparison with pre-industrial observations

Figure 5.14 shows monthly-mean ozone from the PI_CTRL, CO2_DD and CO2_DDBVOC model scenarios compared with available monthly mean observations from the pre-industrial period (Section 5.3) and Table 5.6 shows the annual model mean bias for each site under each scenario.

For 9 of the 12 sites the model has the smallest bias to the observations under the PI_CTRL scenario, with the smallest bias over Tokyo (5.6 ppbv). For the other 3 sites (Manilla, Luanda and Adelaide) the CO2_DDBVOC scenario provides the smallest bias with a value of 8.2 ppbv over Adelaide showing the best match to the observations. Once again, the largest model bias is seen over the Luanda site which shows a ranges at 17.7 to 18.1 ppbv over the 3 scenarios with the CO2_DD scenario yielding the highest value.

When comparing the PI_CTRL and the CO2_DD scenarios, Lansing shows the greatest improvement in model bias with a reduction of 0.4 ppbv, with Montsouris showing the least improvement (0.1 ppbv). For the comparison between the PI_CTRL and CO2_DDBVOC scenarios Vienna shows the greatest improvement in bias (0.9 ppbv) compared to Oaxaca which shows least (bias reduction of 0.2 ppbv).

Overall, this indicates that the ability of the model to reproduce pre-industrial ozone observations, is sensitive to the CO_2 mixing ratio that is prescribed to the surface vegetation field and iBVOC scheme, producing an increase in model bias of up to 0.9 ppbv when both are exposed to a fixed present day value of CO_2. The biases produced in these comparisons are however smaller in magnitude than those shown where the land classification

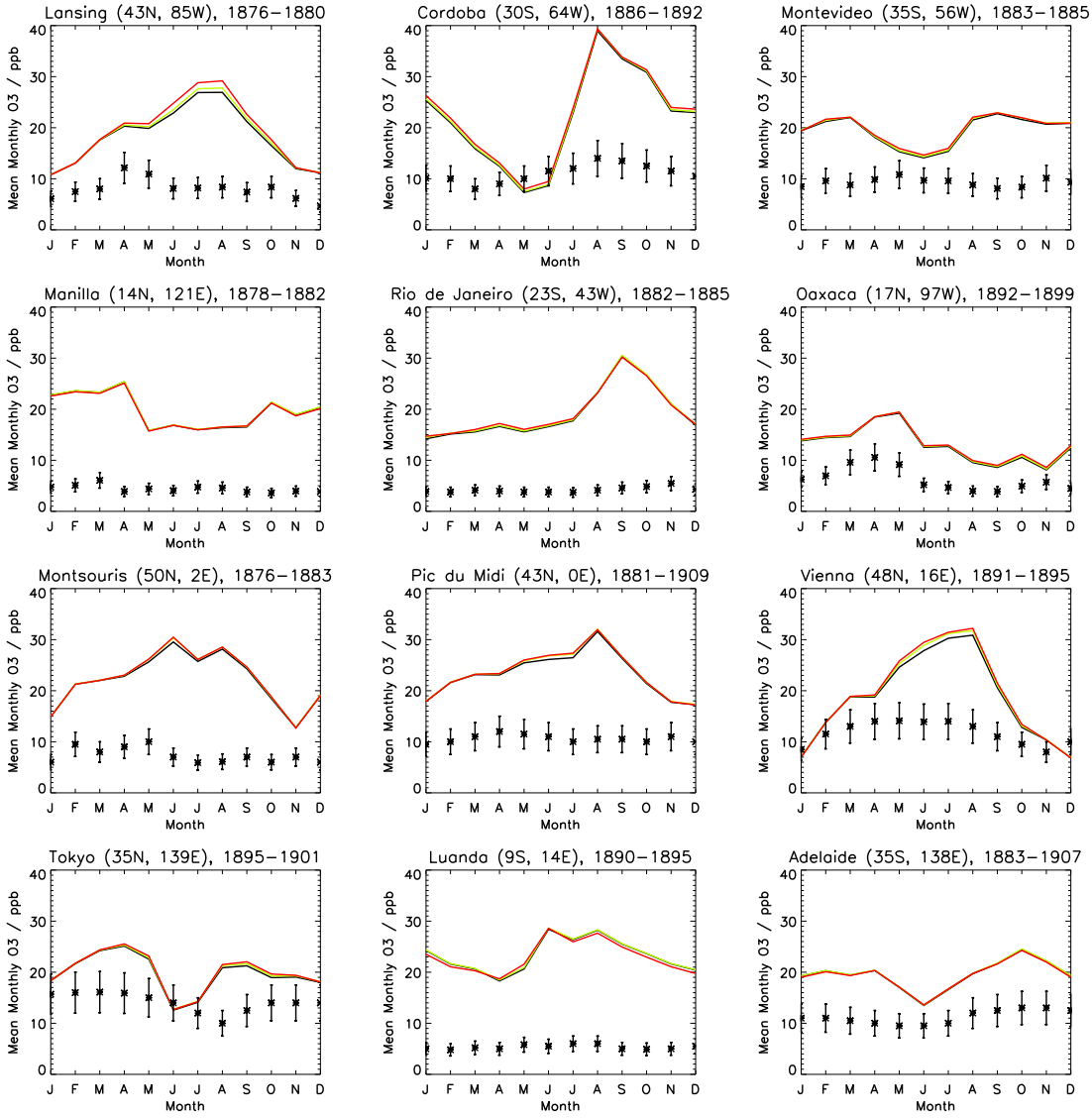

FIGURE 5.14: Comparison of monthly mean ozone from the PI_CTRL **(Black line)**, CO2_DD **(Green line)** and CO2_DDBVOC **(Red line)** model simulations with available pre-industrial monthly mean observations (See Section 5.3 for details) from the end of the 19th Century **(∗)**. Error bars indicate 25% uncertainty associated with observations (Marenco et al., 1994). All values are in ppbv.

map and model climate are varied, which show an improvement in model bias up to 3.9 ppbv (Section 5.4.5). It should also be noted here that the change in model biases in response to changing CO_2 are not significant by comparison to the overall bias to the pre-industrial observations. Therefore further investigation is required into the processes that could account for the model overestimation of pre-industrial ozone concentrations.

TABLE 5.6: Annual mean model bias in ppbv for modelled versus observed pre-industrial ozone for the PI_CTRL, CO2_DD and CO2_DDBVOC model scenarios. The values highlighted in bold indicate the lowest bias for each respective site.

		Scenario		
		PI_CTRL	CO2_DD	CO2_DDBVOC
Site	Lansing	**10.3** ppbv	10.6 ppbv	11.2 ppbv
	Cordoba	**10.9** ppbv	11.1 ppbv	11.6 ppbv
	Montevideo	**10.1** ppbv	10.3 ppbv	10.5 ppbv
	Manilla	15.4 ppbv	15.5 ppbv	**15.3** ppbv
	Rio de Janeiro	**14.9** ppbv	15.1 ppbv	15.2 ppbv
	Oaxaca	**6.7** ppbv	6.8 ppbv	7.0 ppbv
	Montsouris	**14.8** ppbv	15.0 ppbv	15.0 ppbv
	Pic du midi	**12.6** ppbv	12.9 ppbv	12.9 ppbv
	Vienna	**6.9** ppbv	7.3 ppbv	7.5 ppbv
	Tokyo	**5.6** ppbv	5.8 ppbv	6.0 ppbv
	Luanda	18.0 ppbv	18.1 ppbv	**17.7** ppbv
	Adelaide	8.3 ppbv	8.4 ppbv	**8.2** ppbv

5.6 Pre-industrial to present day radiative forcing

In Sections 5.4 and 5.5 it was shown that the modelled pre-industrial tropospheric ozone distribution is sensitive to the prescribed land classification map and the CO_2 mixing ratio that the vegetation is exposed to. One particular feature highlighted was the change in ozone at the tropical tropopause due to the effect on modelled isoprene emissions. Changing the model land classification map from 1865 to 2000, caused a reduction of 2 to 6 ppbv around this region driven by the changes in isoprene emissions as a result of the land use change. When the surface vegetation was exposed to a present day concentration of CO_2 the resultant inhibition of isoprene emissions caused a reduction in excess of 0.5 ppbv around the tropical tropopause. Changes in ozone concentrations around the tropopause can have important implications on the estimated pre-industrial to present day radiative forcing.

The latest Intergovernmental Panel on Climate Change (IPCC) 4th Assessment Report defines the radiative forcing as the change in net irradiance (incoming shortwave solar radiation plus outgoing longwave radiation in Wm^{-2}) at the tropopause after allowing for stratospheric temperatures to readjust to radiative equilibrium, but with surface and tropospheric temperatures held fixed at unperturbed values (Forster et al., 2007). This allows the effect of changing tropospheric ozone and other species (E.g. CO_2) due to

anthropogenic activities to be assessed and compared. Therefore under this definition, changes in the magnitude and distribution of ozone around the tropopause can potentially have important impacts on the net radiative forcing.

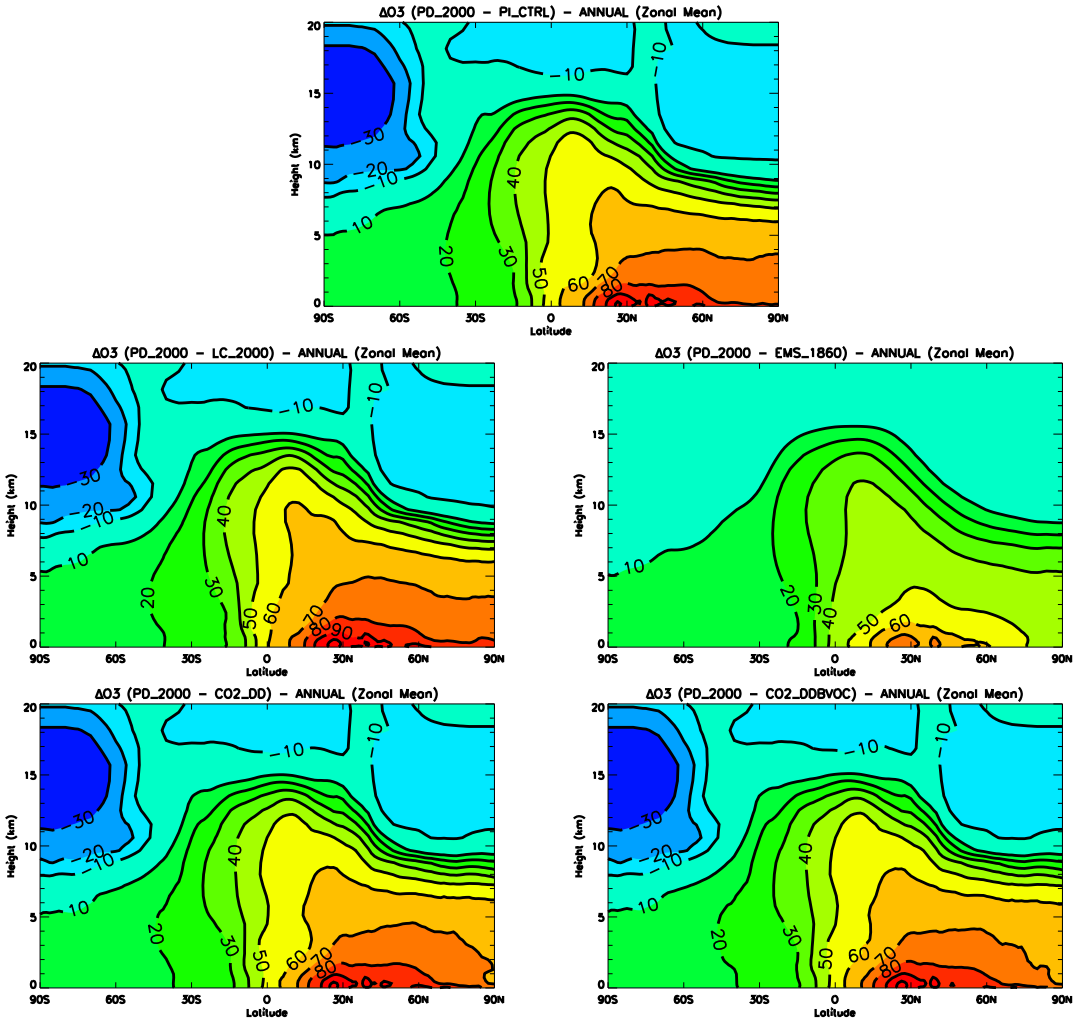

FIGURE 5.15: Percentage change of zonally averaged annual mean ozone from the each of the pre-industrial simulations to the present day.

Figure 5.15 shows the annually and zonally averaged changes in ozone between each of the pre-industrial simulations and the present day atmosphere (PD_2000). With the exception of the EMS_1860 to PD_2000 comparison all scenarios show ozone concentrations to increase by at least 50% from the pre-industrial to the present throughout the northern hemisphere troposphere. These increases approach 80% to 90% in the lower to mid northern hemisphere troposphere with an approximate doubling of ozone shown at the surface

TABLE 5.7: Summary of calculated radiative forcing since the pre-industrial period due to tropospheric ozone under each of the model simulations.

	Scenario				
	PI_CTRL	LC_2000	EMS_1860	CO2_DD	CO2_DDBVOC
Ozone Burden[a], Tg O_3	203.7	200.4	220.9	204.5	204.1
ΔBurden[b], Tg O_3	89.2	92.5	71.9	88.3	88.8
Total forcing, Wm^{-2}	0.233	0.244	0.227	0.231	0.231

[a] All values are global annual averages. [b] Change in ozone burden with respect to present day simulation (292.9 Tg O_3)

between 30N and 60N. For the EMS_1860 scenario, the changes in ozone to the present day are much lower with increases of at least 40% shown throughout the northern hemisphere troposphere with these increases approaching 60% to 70% at the surface around the mid-latitude regions. For all scenarios, southern hemisphere ozone concentrations are shown to increase from the pre-industrial to the present day by 10% to 40% with the greatest changes seen around the tropical regions.

In the upper troposphere, all scenarios show an increase in ozone of at least 10%, with the greatest changes shown around the tropical tropopause. These changes are as low as 40% for the EMS_1860 scenario and peak at 60% under the LC_2000 scenario at around 20N to 30N. Overall, these changes fall within the range of a recent multi-model study (Gauss et al., 2006) which show pre-industrial to present day increases in tropospheric ozone of 40% to 130% in the lower troposphere in the northern hemisphere, 30% to 150% in the upper tropical troposphere and 10% to 70% throughout the southern hemisphere troposphere. However, this wide range highlights the large uncertainty associated with simulating the pre-industrial atmosphere.

Table 5.7 shows the pre-industrial to present day change in ozone burden for each scenario and the radiative forcing associated with this change in ozone. Figure 5.16 shows the geographical and zonal changes in radiative forcing between each pre-industrial scenario and the present day atmosphere.

The simulations indicate a pre-industrial ozone burden which ranges from 200.4 Tg under the LC_2000 scenario up to 220.9 Tg under the EMS_1860 scenario. The simulated present day burden is 292.9 Tg which results in a modelled change in ozone burden ranging from

71.9 Tg to 92.5 Tg. These results are consistent with previous studies (Lamarque et al., 2005; Mickley et al., 2001; Shindell et al., 2003; Wang and Jacob, 1998) which estimated the pre-industrial to present day change in ozone burden at 71 to 130 Tg.

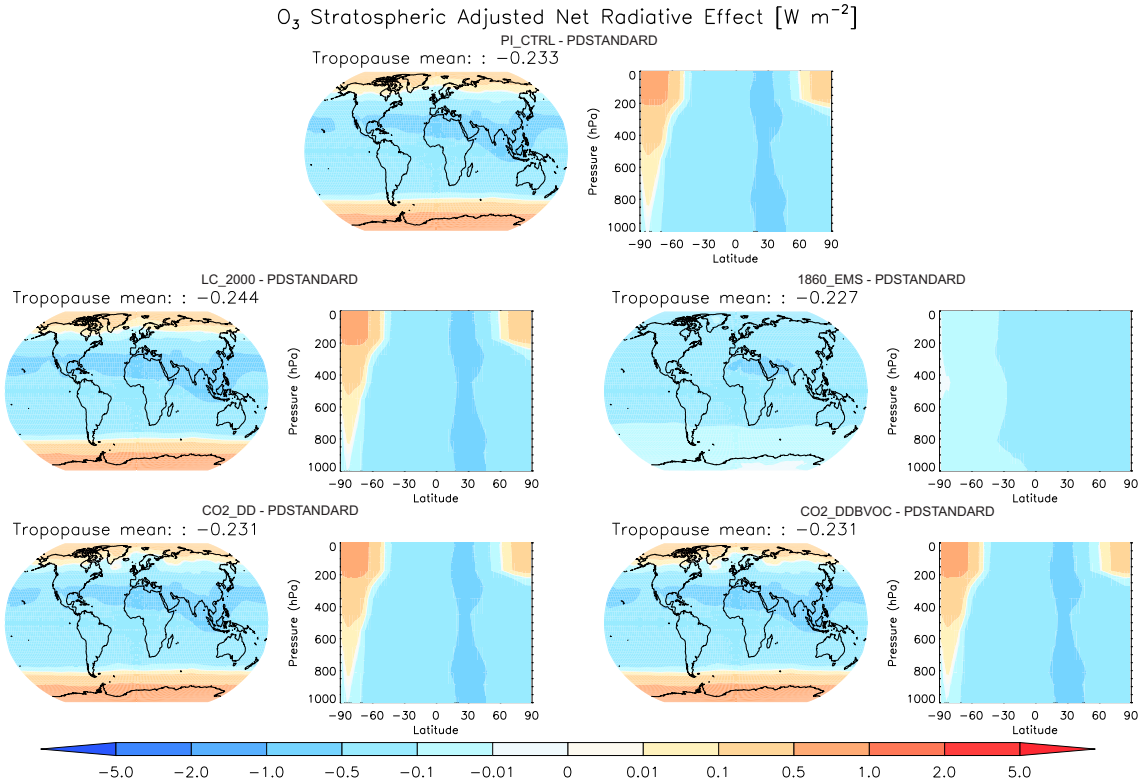

FIGURE 5.16: Net stratospheric adjusted pre-industrial to present day radiative forcing due to tropospheric ozone under each model scenario. All values are in Wm^{-2}. Plot generated by A. Rap (Pers. Comms. 2012) from ozone fields simulated under each model scenario.

These changes in the tropospheric ozone distributions under each scenario are used to calculate the associated pre-industrial to present day radiative forcing. The offline version of the Edwards and Slingo (1996) radiative transfer model is used with 6 bands in the shortwave, 9 bands in the longwave and a delta-Eddington 2 stream scattering solver at all wavelengths (Radiative transfer code runs provided by A. Rap (Pers. Comms. 2012)). The code uses monthly averaged climatology of temperature, water vapour and trace gases based upon the ECMWF reanalysis data. The resolution is 2.5° × 2.5° in the horizontal with 23 pressure levels in the vertical from the surface up to 1 hPa (Rap et al., 2010). Cloud and surface albedo data are compiled from the International Satellite Cloud Climatology Project (ISCCP) archive (Rossow and Schiffer, 1999) and averaged over the time period 1983 to 2005. The ozone fields from the HadGEM2-ES simulations were regridded to the

resolution of the radiation code in order to calculate the pre-industrial to present day radiative forcing under each model scenario.

The estimated radiative forcing over all scenarios falls in the range of 0.227 Wm^{-2} to 0.244 Wm^{-2} with the EMS_1860 scenario producing the lowest and the LC_2000 scenario producing the highest. Geographically, the net radiative forcings are shown to be largest in the northern hemisphere between 0N and 30N where they fall between 0.5 and 1.0 Wm^{-2}. With the exception of the EMS_1860 scenario which has the same climate setup as the present day, all scenarios show greater radiative forcings in the polar regions for the pre-industrial case (0.01 Wm^{-2} to 1.0 Wm^{-2} in the Antarctic and 0.01 Wm^{-2} to 0.5 Wm^{-2} in the Arctic) though this can be attributed to the higher pre-industrial ozone seen in the polar stratosphere under the pre-industrial model scenarios (10% to 30% greater in the south and 10% greater in the north (Figure 5.15)). This observed pattern is consistent with that shown by Shindell et al. (2003) who observed a simulated larger radiative forcing for the pre-industrial period around the polar regions particularly in the southern hemisphere where forcings were shown to be greater by 0.1 Wm^{-2}.

The impact of running a pre-industrial simulation with a land classification map representative of the present day (LC_2000 scenario) is shown to produce an increase in the radiative forcing of 0.011 Wm^{-2} from 0.233 Wm^{-2} (under the PI_CTRL scenario) to 0.244 Wm^{-2}. This can be attributed to the lower pre-industrial to present day ozone difference in the northern hemisphere upper troposphere under the PI_CTRL scenario. Under the PI_CTRL simulation there is greater ozone in the UTLS region due to larger isoprene emissions resulting in an increase in PAN formation which enhances NO_x concentrations. This coincides with higher isoprene concentrations in the the UTLS region which acts to enhance ozone formation resulting in greater concentrations (2 pptv to 6 pptv). The enhanced PAN formation under the PI_CTRL scenario also increases the transport of NO_x to more remote regions which results in higher ozone concentrations throughout the troposphere. This is reflected in the higher ozone burden under the PI_CTRL scenario (203.7 Tg) compared to 200.4 Tg under the LC_2000 scenario.

The sensitivity of the radiative forcing to the CO_2 mixing ratio that the vegetation and iBVOC scheme is exposed to is much less than under the change in land use map. Under both the CO2_DD and CO2_DDBVOC scenarios the global mean net raditive forcing is 0.231 Wm^{-2}, a decrease of 0.002 Wm^{-2} compared to the PI_CTRL scenario. Both

scenarios show higher ozone burdens (204.5 Tg and 204.1 Tg) respectively than under the PI_CTRL scenario (203.7 Tg) with this increase driven by the CO_2 inhibition of stomatal conductance and hence the reduction of ozone dry deposition. Under the CO2_DDBVOC scenario the increase in ozone burden is slightly less due to the effect of lower isoprene emissions resulting in lower PAN formation and hence lesser ozone levels over more remote regions, similar to the impact of the LC_2000 scenario.

Finally, the EMS_1860 scenario shows the lowest radiative forcing (0.227 Wm^{-2}) which corresponds to a much higher ozone burden (220.9 Tg) than under the other 4 pre-industrial scenarios (200.4 Tg to 204.5 Tg). This is due to greater ozone concentrations throughout the troposphere under this scenario as a result of a different prescribed model climate and land use map which impacts ozone dry deposition and isoprene emissions (discussed in detail in Section 5.4.4). This greater burden of ozone results in a lower pre-industrial to present day change in ozone (71.9 Tg) than under the PI_CTRL scenario (89.2 Tg) and hence a smaller radiative forcing.

The range of radiative forcings presented in this Chapter (0.227 Wm^{-2} to 0.244 Wm^{-2}), falls at the lower end of the range quoted in the IPCC AR4 (0.25-0.65 Wm^{-2} (Forster et al., 2007)) though considering the uncertainty associated with modelling pre-industrial atmospheres indicate a significant contribution of tropospheric ozone to the total estimated radiative forcing since the pre-industrial period. In comparison to previous studies (Gauss et al., 2006; Mickley et al., 2001; Shindell et al., 2003) the radiative forcings calculated here once again fall towards the lower range of estimates with Shindell et al. (2003) calculating a radiative forcing of 0.30 Wm^{-2} and Gauss et al. (2006) reporting a range of 0.25 Wm^{-2} to 0.45 Wm^{-2} from a multi-model study. Mickley et al. (2001) present the radiative forcing as an instantaneous forcing (without accounting for stratospheric adjustment) and determine a value using the standard model setup of 0.44 Wm^{-2}. If instantaneous radiative forcings are considered the simulations presented in this Chapter show a range of 0.276 Wm^{-2} to 0.418 Wm^{-2} with the EMS_1860 scenario showing the lowest and the LC_2000 showing the highest. The PI_CTRL scenario which is the best estimate of a pre-industrial atmosphere in this work yields a value of 0.409 Wm^{-2}. This falls slightly below the estimate of Mickley et al. (2001) though indicates that the values presented here lie within a sensible range and are in agreement with previous findings.

Overall, it is shown that the radiative forcing due to tropospheric ozone is sensitive to the representation of biosphere atmosphere interactions in the model with the changes in dry deposition and isoprene attributed to land use change having a larger effect (a difference of +0.011 Wm^{-2} from the PI_CTRL scenario) than those associated with the CO_2 concentration that the model vegetation is exposed to (a difference of -0.002 Wm^{-2} from the PI_CTRL scenario). When both of these effects are combined with a present day climate setup as used in some model studies the difference is slightly greater (a difference of -0.006 Wm^{-2} from the PI_CTRL scenario). This highlights the importance of representing these processes as accurately as possible in model simulations to represent pre-industrial to present day changes in the tropospheric ozone burden.

5.7 Uncertainties in simulating the pre-industrial atmosphere

As identified by previous studies (Lamarque et al., 2005; Mickley et al., 2001; Shindell et al., 2003) a large number of uncertainties exist in using atmospheric models to calculate pre-industrial to present day radiative forcings. As highlighted by Mickley et al. (2001) and Shindell et al. (2003) these uncertainties largely lie with poor constraints on the emissions of ozone precursors in the pre-industrial period. Mickley et al. (2001) found that by changing the emissions of BVOCs from vegetation and NO_x emissions from soil and lightning, an instantaneous radiative forcing of 0.72 Wm^{-2} to 0.80 Wm^{-2} was calculated, approximately double the value in the standard simulation (0.44 Wm^{-2}). In contrast, Shindell et al. (2003) suggested that the radiative forcing was not greatly sensitive to changes in biomass burning NO_x emissions.

In comparison to this, the sensitivity of the radiative forcings presented in this Chapter is much smaller (0.227 Wm^{-2} to 0.244 Wm^{-2}). In the simulations performed by Mickley et al. (2001) all BVOC emissions (isoprene, acetone with the addition of monoterpenes) were increased globally by 50% which resulted in an increase of 275 Tg of isoprene from the standard simulation (550 Tg to 825 Tg). The simulations run by Mickley et al. (2001) also represent no changes in the surface land map. In the simulations performed here, the change in isoprene is much lower (e.g. 580 Tg under the PI_CTRL scenario dropping to 471 Tg under the LC_2000 scenario) as a result of changing the land use map from 1865 to 2000. The simulations run in this Chapter however calculate the isoprene emissions

interactively using the iBVOC emissions scheme based upon the underlying land map. The effect of this isoprene change combined with the impact of changing the land use map on dry deposition results in smaller changes in the tropospheric ozone burden and hence the impact on radiative forcing. The findings presented in this Chapter also further highlight another area of uncertainty associated with representing atmosphere biosphere interactions in the pre-industrial period.

One final uncertainty to consider is the effect that changing the model land map has on surface roughness length, surface albedo and consequently simulated temperatures and model dynamics and to what extent the changes in the ozone distribution observed in the land cover change simulations is a result of this effect rather than chemistry changes. In order to test this, the TOMCAT CTM was utilised to perform the same land cover experiments with meteorology held constant in order to remove the effects of land cover change on climate through model dynamics. The results of these experiments are shown in Section 5.8.

5.8 TOMCAT pre-industrial model simulations

This section presents the results of model runs performed using the TOMCAT CTM to test the robustness of the results presented in this chapter by quantifying the impacts of land cover change on modelled pre-industrial ozone whilst removing the effects of the land cover change on the climate through model dynamics. This section also presents results using the TOMCAT CTM to isolate the dry deposition impacts of changing land cover on pre-industrial tropospheric ozone.

5.8.1 Model description and scenarios

The 3D global TOMCAT CTM (Chapter 3) was set up to run at T42 resolution with approximately 2.8 degrees spacing between the centres of each model grid box. In the vertical the model has 31 vertical levels covering the entire troposphere and the lower stratosphere. For the standard pre-industrial (PI_STNDRD) simulation, all anthropogenic emissions of carbon monoxide, methane, NO_x, formaldehyde and hydrocarbons, were excluded. Biomass burning emissions were kept at present day values and were obtained

from the GFED2 database (van der Werf et al., 2006) as climatological monthly means. Biogenic emissions of CO, non-methane hydrocarbons and NO_x were kept at present day values and were obtained from the POET (Precursors of Ozone and their effects in the Troposphere) database, used as described by Emmons et al. (2010) and methane was specified at 0.7 ppm. The model was provided with offline CLM (Chapter 3) isoprene emissions (CLM model runs provided by S. Arnold, (Pers. Comms. 2012)) representative of the 1850s. Finally, land cover was prescribed as representative of the pre-industrial period (1850) using output from the CLM. Table 5.8 shows the mean annual emissions of the tracer species used by TOMCAT for the PI_STNDRD run. The model was forced using present day meteorological fields from the ECMWF representative of the year 2004.

TABLE 5.8: Annual mean emissions fluxes for the TOMCAT pre-industrial control run.

Species	Emissions ($Tgyr^{-1}$)
CO	595.7
CH_4	25.6
NO_x	36.0
CH_3CHO	4.86
CH_3COCH_3	29.2
HCHO	5.86
CH_3OH	31
C_2H_2	1.50
C_2H_4	9.90
C_2H_6	3.88
C_3H_8	3.38
C_5H_8	744.2

Two model experiments were performed in addition to the PI_STNDRD run in order to assess the sensitivity of tropospheric ozone levels to changes in the model land classification map. The first scenario assessed the impact of changing land cover on surface ozone through the effect on dry deposition processes only. In this scenario (1850_DD) the 1850 CLM land cover was replaced with a land map representative of the year 2000 (also from the CLM), with the offline isoprene emissions held constant at 1850 levels . The final model scenario followed the 1850 to 2000 CLM land use change but in addition to the effect on dry deposition processes, the model was prescribed with offline 2000 CLM isoprene emissions (CLM model runs provided by S. Arnold) in order to reflect the change in BVOC emissions that would accompany the changing land use (Niinemets et al., 2010a,b) and the higher CO_2 concentrations in the 2000s. For all model scenarios ozone was output on a monthly

basis for the period of one year after a one year spin up. A summary of the model scenarios can be found in Table 5.9 along with the emissions totals of isoprene from vegetation under each scenario.

5.8.2 Impact of changing land cover on TOMCAT modelled pre-industrial ozone

Figure 5.17 shows the annual zonal mean changes in ozone from the standard model setup (PI_STNDRD) for the 1850_DDISOP TOMCAT scenario and the 1850_DD TOMCAT scenario. In these runs the meteorology is held constant from the PI_STNDRD setup hence allowing the removal of the effects that the land use change has on climate through changes in dynamics.

Table 5.9: Summary of TOMCAT pre-industrial model scenarios.

Scenario	Land cover	Isoprene Emissions	Total isoprene emissions ($Tgyr^{-1}$)
PI_STNDRD	1850 LC	1850 CLM[a]	918.2
1850_DD	2000 LC	1850 CLM[b]	918.2
1850_DDISOP	2000 LC	2000 CLM[b]	744.2

[a] 2000 CLM with MEGAN, 1850 LC, 280 ppm CO_2 [b] 2000 CLM with MEGAN, 2000 LC, 360 ppm CO_2

In the TOMCAT CTM runs, the setup for the 1850_DDISOP run represents the same change in biosphere-atmosphere interactions as the setup for the LC_2000 scenario run using HadGEM2-ES. However, the change in isoprene emissions from the standard pre-industrial setup is greater (a drop of 174 Tg) compared to that in the HadGEM2-ES simulations (a drop of 109 Tg from the PI_CTRL to the LC_2000 scenario). In general, the response of the zonal distribution of ozone in the troposphere for the TOMCAT simulations are similar to that produced by HadGEM2-ES (Figure 5.17). In both models, ozone concentrations are shown to be greater when the land classification map is representative of the 1850s by around 1% to 3% throughout the troposphere, though the TOMCAT runs indicate slightly higher concentrations towards the northern hemisphere polar regions. More importantly in both sets of simulations, the models capture a 3% to 5% change in ozone mixing ratios around the tropical tropopause region as a result of the larger isoprene emissions under each models respective standard pre-industrial setup. The TOMCAT comparisons also pick up 3% to 5% changes in ozone concentrations at surface level due to

the larger isoprene emissions under the PI_STNDRD setup. This translates into a change in the global tropospheric ozone burden from 199.1 Tg under the PI_STNDRD scenario to 194.5 Tg under the 1850_DDISOP simulation, a decline of 2.3 %. This is slightly larger than the change for the same scenarios in HadGEM2-ES which show a drop in the ozone burden of 1.6 % (Table 5.7). Due to the fixed model dynamics in TOMCAT this therefore provides confidence that the patterns observed under the HadGEM2-ES land use change scenarios (Section 5.4) are due to changes in atmospheric composition due to changing biosphere-atmosphere interactions under different land classification maps.

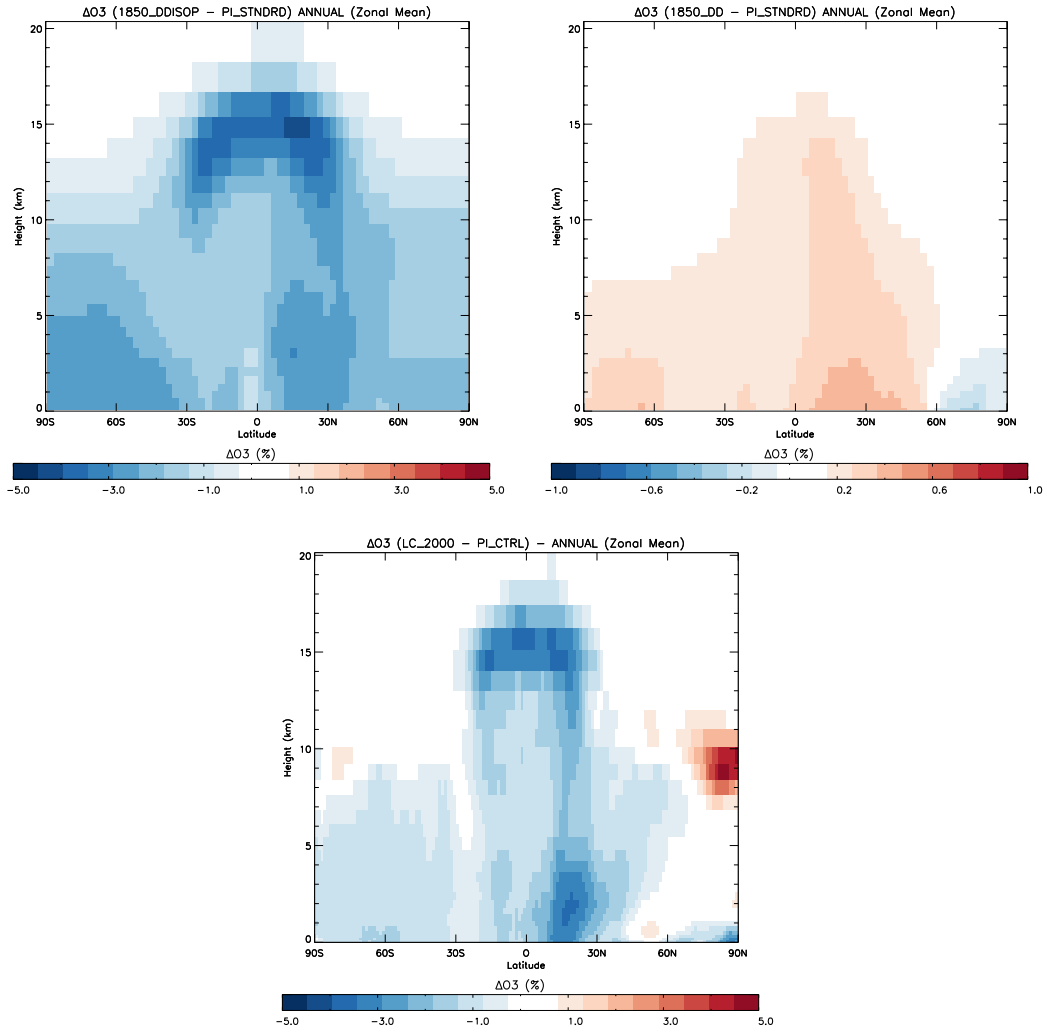

FIGURE 5.17: Annually and zonally averaged changes in ozone (%) between the TOMCAT 1850_DDBVOC and PI_STNDRD scenarios (top left) the TOMCAT 1850_DD and PI_STNDRD scenarios (top right) with the PI_CTRL versus LC_2000 HadGEM2 results (bottom middle) for comparison. Note the different values on the colourbars between panels.

As the TOMCAT CTM is run without interactive isoprene emissions, it enabled simulations to be run to isolate the dry deposition effects of the land use change whilst holding the isoprene emissions constant (1850_DD scenario). Figure 5.17 shows the differences between tropospheric ozone concentrations under this scenario and under the standard TOMCAT pre-industrial model setup. When the land classification map is changed from 1850 to 2000, the coverage of the forest land category decreases to be replaced by the grass/crop/shrub land type in order to represent pre-industrial to present day deforestation and increase in agricultural activity (Ramankutty and Foley, 1999; Richards, 1990; Turner et al., 1993). This has the effect of reducing the rate of deposition of ozone resulting in larger concentrations (Ganzeveld and Lelieveld, 1995). This is reflected in Figure 5.17 which shows an increase in ozone concentrations under the 1850_DD scenario throughout the southern hemisphere troposphere of between 0.2% and 0.3%. In the northern hemisphere slightly larger changes are shown between 0N and 60N with increases of 0.2% to 0.4% throughout the free troposphere with these approaching 0.6% near to the surface. In contrast surface ozone concentrations are shown to be smaller in the northern hemisphere polar regions by around 0.2% to 0.3%. This can be attributed to lower amounts of sea-ice under the 2000 CLM land map which acts to increase the rate of dry deposition to the surface and lower surface ozone levels (Ganzeveld and Lelieveld, 1995). These changes in tropospheric ozone concentrations translate into a change in the global tropospheric burden from 199.1 Tg under the PI_STNDRD scenario to 199.4 Tg under the 1850_DD simulation, a slight rise of 0.2 %.

Overall, the TOMCAT simulations show that the sensitivity of tropospheric ozone to changes in dry deposition processes is small (less than 1%) and provides a small contribution to the overall differences seen when the land map is changed from 1850 to 2000 (1% to 5%). This indicates that changes to isoprene emissions as a result of the land use change play a more important role in the observed ozone changes. This agrees with the findings of Lamarque et al. (2005) which showed that simulated pre-industrial ozone was more sensitive to changes in the emissions of precursor species such as isoprene than to changes in dry deposition velocities. Though the work presented in Lamarque et al. (2005) does concede that dry deposition plays a role and should be considered in pre-industrial simulations.

5.9 Summary

The findings presented in this Chapter indicate that the estimated pre-industrial tropospheric ozone distribution and pre-industrial to present day radiative forcing are sensitive to land cover change through the resultant impacts on dry deposition and isoprene emissions. Simulations run using the HadGEM2-ES model indicate a pre-industrial ozone burden which ranges from 200.4 Tg to 220.9 Tg with the variation resulting from differences in the model land PFT distribution, the CO_2 mixing ratio the vegetation was exposed to and the model climate setup. The pre-industrial to present day change in ozone burden (present day burden of 292.9 Tg) ranged from 71.9 Tg to 92.5 Tg which translates into a radiative forcing range of 0.227 Wm^{-2} to 0.244 Wm^{-2}.

Changes in dry deposition and isoprene emissions attributed to land cover change (1865 to 2000) were shown to have a larger effect on the ozone burden (a 1.6 % drop from a control simulation) than those associated with the CO_2 concentration that the model vegetation was exposed to (a 0.4 % rise from a control simulation). It was also shown that the response of ozone concentrations to land cover changes is dominated by the impacts of the changing isoprene emissions rather than changing dry deposition, agreeing with the findings of previous work (Lamarque et al., 2005). Finally, simulations with the TOMCAT CTM model confirm that the changes in surface ozone in response to the land cover change is due changes in atmospheric composition and chemical processes rather than impacts through model dynamics.

Comparisons with available pre-industrial ozone observations showed that the ozone concentrations for the control simulation best matched the observations over 8 of the 12 surface and mountain sites. The control scenario provides the best model estimate of the pre-industrial atmosphere with the best representation of biosphere-atmosphere processes. However, the control scenario indicated higher surface ozone concentrations in more remote marine regions due to the larger isoprene emissions enhancing PAN formation and resulting in the transport of NO_x to these regions leading to higher ozone concentrations. The overestimation of available nineteenth Century ozone readings by standard pre-industrial models could be explained by uncertainties in the calibration of the measured data (Marenco et al., 1994). However, as presented in this Chapter, uncertainties associated with the representation of biosphere-atmosphere processes and the prescribed

land coverage could account for part of the discrepancy between modelled and observed data.

Overall, the radiative forcings presented in this Chapter ($0.227\,\mathrm{Wm}^{-2}$ to $0.244\,\mathrm{Wm}^{-2}$) fall at the lower end of the IPCC AR4 estimate (0.25-0.65 Wm^{-2} (Forster et al., 2007)) though considering the uncertainty associated with modelling pre-industrial atmospheres indicate a significant contribution of tropospheric ozone to the estimated total radiative forcing since the pre-industrial period. This sensitivity of the radiative forcing indicates that there is a need to better understand the representation of interactions between the biosphere and the atmosphere with these processes often highly parametrised or neglected in the current generation of climate models.

Chapter 6

Ozone vegetation damage and impacts on atmospheric chemistry

6.1 Introduction

The effect of ozone damage on vegetation has become of increasing concern over the past decade (Ashmore, 2005; Sitch et al., 2007; Van Dingenen et al., 2009; Wang and Mauzerall, 2004) particularly in relation to the impact of ozone damage on crop yields (Roy et al., 2009; Van Dingenen et al., 2009; Wang and Mauzerall, 2004). The impact on stomatal conductances can potentially affect the uptake of atmospheric CO_2 resulting in a possible indirect radiative forcing from the resultant rise in atmospheric CO_2 levels which could act to enhance the direct radiative forcing associated with ozone's role as a greenhouse gas (Sitch et al., 2007). As shown by Forster et al. (2007), ozone is an important greenhouse gas and has also been shown to have adverse effects on human health as well as having significant air quality implications (Fowler et al., 2008). Additionally, the reduction in stomatal closure can also limit evapotranspiration which can have important implications for the hydrological cycle through impacting surface runoff and soil moisture content resulting in potential climate impacts (Bonan, 2008).

The dry deposition of ozone and its precursor species to the land surface has been shown to play an important role in the tropospheric ozone budget (Wild, 2007), with the rate of uptake by vegetated surfaces shown to be more significant than the rate of deposition

to water, bare ground and ice surfaces (Ganzeveld and Lelieveld, 1995; Giannakopoulos et al., 1999). The controlling factor in the uptake of ozone and its precursor species by vegetation is typically the stomatal conductance which essentially defines the amount of opening of the apertures in the surfaces of leaves, which control the flow of CO_2, water and other trace gas species into or out of the plant's leaf structure. It has been shown there is some uptake of trace species including ozone and NO_2 through the waxy cuticle surface of a plant's leaf, however resistances to this uptake (known as the cuticle resistance ($r_{\text{leafsurface}}$)) tend to be higher than those through the stomata (Smith et al., 2000).

Previous field experiments (Krupa et al., 1998) have shown that ozone can not only cause visible damage to leaf surfaces, it can also lead to the death (necrosis) of cells within the leaf. This can result in the reallocation of a plant's resources from photosynthesis to repairing the damage caused by ozone rather than being used for growth. One such important impact of ozone damage that is included in few global modelling studies (Felzer et al., 2005; Sitch et al., 2007) is the resultant impact of the cellular damage on the stomatal conductance and the subsequent impact on the dry deposition of ozone and associated precursor species to plant surfaces. Another limiting factor on the stomatal conductance of a plant is the effect of enhanced atmospheric CO_2 (Field et al., 1995), which itself can lead to stomatal closure. Finally, stomatal closure can also be induced by drought conditions (Flexas et al., 2008) which in turn can inhibit the rate of photosynthesis in the plant leaf (Chaves et al., 2003).

Finally, the process of isoprene synthesis and emission from vegetation is itself dependant upon the rate of photosynthesis and net primary production within a plant (Arneth et al., 2007; Niinemets et al., 1999; Pacifico et al., 2011) along with environmental controls such as ambient air temperature and CO_2 concentrations. The emission of isoprene is also heavily reliant upon the vegetation type with broadleaf trees in the tropical regions shown to be strong emitters of isoprene (Guenther et al., 2006). Isoprene comprises the largest proportion of the emissions of VOCs from the biosphere with an estimated flux of approximately 400-600 TgCyr^{-1} (Arneth et al., 2008), approximately equivalent in terms of carbon to the size of the CH_4 source from the biosphere (220-510 TgCyr^{-1}) (Denman et al., 2007).

Isoprene is highly reactive (Chapter 2) with typical reaction lifetimes in the atmosphere of 0.8 h, 1.7 h and 1.3 days when it reacts with nitrate (NO_3), OH and ozone respectively

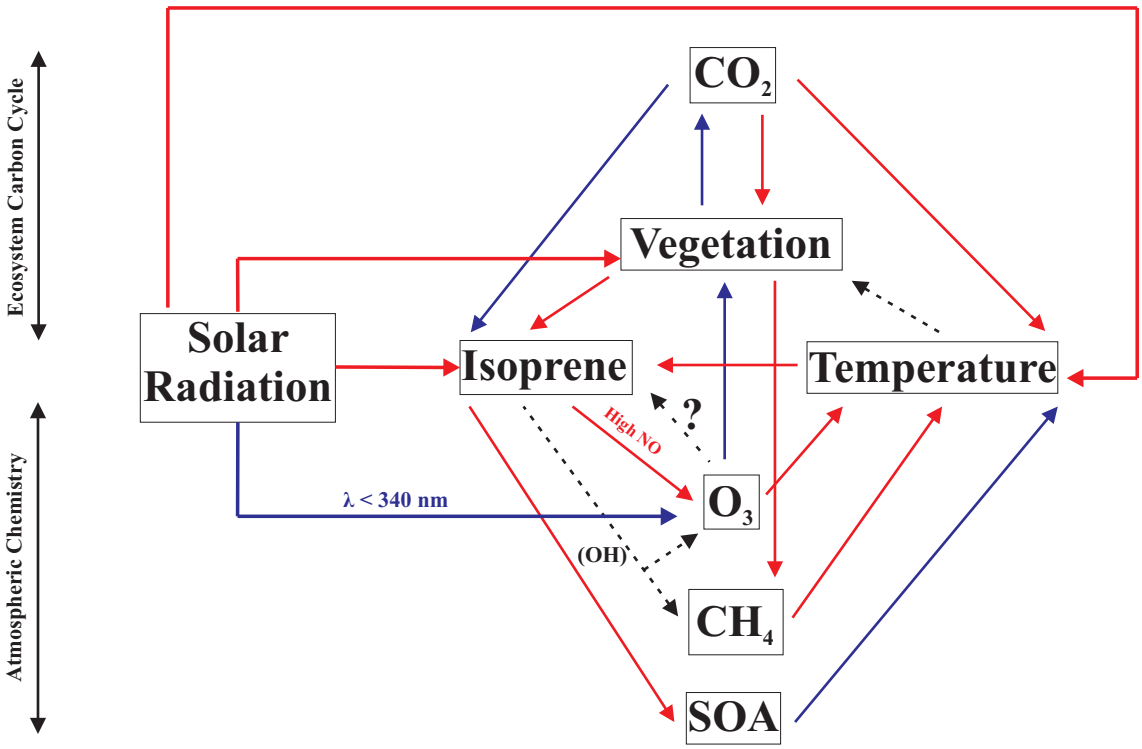

FIGURE 6.1: Summary of feedbacks between ozone, isoprene emissions, environmental controls and atmospheric chemistry processes. Red arrows indicate a positive effect, blue arrows indicate a negative effect and black dashed arrows indicate effects where the impact of the effect is uncertain. Adapted from Pacifico et al. (2009)

(Seinfeld and Pandis, 1998). This high reactivity of isoprene and its oxidation products (Atkinson and Arey, 2003) indicates that any potential change in isoprene emissions fluxes could have important implications for atmospheric composition, particularly ozone, CH_4 and secondary organic aerosol (SOA) concentrations in the troposphere (Figure 6.1), which can ultimately have resultant impacts on the climate system.

Present understanding of the impact of elevated atmospheric ozone concentrations on isoprene emissions is highly uncertain (Figure 6.1) with recent studies only quantifying the effect on a limited number of plant species with contrasting results (Calfapietra et al., 2008; Pinelli and Tricoli, 2004; Tiiva et al., 2007; Velikova et al., 2005). During ozone fumigation experiments isoprene emissions were observed to decrease for *P. tremuloides* (Aspen) (Calfapietra et al., 2008) and *Q. pubescens* (Downy Oak) (Velikova et al., 2005) under high atmospheric ozone concentrations. However Pinelli and Tricoli (2004) showed that emissions from *Q. pubescens* were in fact stimulated under intermediate ozone exposure (190 ppbv as opposed to 300 ppbv under high ozone concentrations) and Tiiva et al. (2007) showed that elevated ozone concentrations had zero statistically significant effects

on isoprene emissions from a boreal peatland. It should be noted however that in these studies the ozone concentrations the plants were exposed to were much higher than standard ambient concentrations at surface level typically found in the atmosphere. These studies are also only based upon certain plant species on local to regional scales. No study has attempted to quantify the impact of ozone damage on isoprene emissions on a global and continental scale and the subsequent feedback on tropospheric ozone concentrations.

Isoprene has also been shown to prevent visible damage to vegetation caused by exposure to ozone (Loreto et al., 2001; Loreto and Velikova, 2001) and therefore the emission of isoprene by a plant could indicate resistance to ozone damage (Sharkey et al., 2007). Isoprene can also prevent measurable losses in photosynthetic capacity by ozone and other reactive oxygen species (Affek and Yakir, 2002; Penuelas and Llusia, 2002; Penuelas et al., 2005; Velikova et al., 2004) and therefore it has been indicated that isoprene emissions may be stimulated by enhanced ozone concentrations due to this potential defence mechanism.

In this Chapter, the HadGEM2-ES model was used to quantify for the first time the impact of ozone vegetation damage on reactive trace gas deposition and the subsequent feedback on atmospheric ozone concentrations. The Chapter also utilised the iBVOC emissions scheme to provide the first estimate of the feedback on isoprene emissions of ozone damage through the plant photosynthesis response to ozone exposure. This Chapter also compared this impact with other environmental controls on isoprene emissions such as CO_2 inhibition, temperature controls and land use change to highlight the importance of accounting for the effects of ozone exposure in global climate models when estimating the response of atmospheric composition to future emissions scenarios.

Section 6.2 describes the set up of the model for the scenarios simulated in this Chapter, Section 6.3 provides an overview of the impact of ozone damage on stomatal conductances of vegetation, Section 6.4 quantifies the sensitivity of the stomatal dry deposition sink of ozone and its precursors to ozone exposure. Section 6.4 highlights the effects of ozone damage on the total stomatal uptake rate of ozone by the terrestrial biosphere. The impacts of ozone vegetation damage on the surface ozone distribution and the potential feedbacks of this on local air quality are discussed in Sections 6.6 and 6.7 respectively. Section 6.8, provides the first estimate of the global scale impact of ozone damage on isoprene emissions. Section 6.8 also quantifies the effects on atmospheric composition of including both the dry deposition and isoprene emissions impacts of including ozone

damage in model simulations. Section 6.9 compares the effects of ozone damage on isoprene emissions with those of previous studies including the impacts of other environmental controls on isoprene emissions such as those of CO_2 and land use change. Uncertainties are discussed in Section 6.10 and finally Section 6.11 provides a summary of the main findings of this Chapter.

6.2 Model setup and experiments

6.2.1 HadGEM2-ES model setup

The HadGEM2-ES model was used to perform the runs in this chapter, and was run at a 1.25° by 1.875° horizontal resolution (Chapter 3). The model was run in atmosphere only configuration with the full Earth system couplings not applied such that changes in atmospheric composition (namely ozone and aerosols) did not feedback to the climate system through the model radiation scheme. This removes the feedbacks of any changes in the model chemical fields on the dynamics scheme and thus isolates the chemical impact of including the effects of ozone damage on vegetation within the model.

The UKCA extended tropospheric chemistry scheme (Chapter 3) was used with the iBVOC scheme to determine interactive surface emissions of isoprene, a lumped monoterpene species, acetone and methanol. Dry deposition fluxes were calculated using the 'big leaf' approach of Smith et al. (2000), with the stomatal conductance (g_l) modified to account for vegetation ozone damage as calculated using the parametrisation developed by Sitch et al. (2007) (Chapter 3).

The model was set up to calculate a present-day climate derived from annual average sea surface temperatures and sea-ice fields representative of the decade 1990-2000 taken from the CMIP5 simulations (Jones et al., 2011). Anthropogenic surface emissions for 2000 were taken from the historical (1850 to 2000) gridded emissions dataset used for the Climate Model Intercomparison Program#5 (CMIP5) simulations (Lamarque et al., 2010). Greenhouse gas concentrations were prescribed and fixed at levels representative of the decade 1990-2000. The model was run with annually-varying vegetation for 1990-2000 with the TRIFFID dynamic vegetation model set to update leaf phenology on a daily basis which determined the evolution of leaf LAI. The model distribution of PFTs were

prescribed from a dataset used by the CMIP5 (Hurtt et al., 2011). This data was derived from the present-day climatology IGBP dataset (Loveland et al., 2000) and reconstructions of anthropogenic land-use from the HYDE3 dataset (Klein Goldewijk et al., 2010). Land surface exchange processes including photosynthesis and canopy stomatal conductance were modelled using MOSES II.

6.2.2 Experiments to assess impact of ozone damage on stomatal uptake

The impact of ozone damage on stomatal conductance was parametrised using the approach of Sitch et al. (2007) (described in Chapter 3) with leaf stomatal conductance modified according to an ozone exposure factor (F) which was calculated based upon the extent to which the stomatal flux of ozone into a leaf exceeded a critical PFT-specific threshold (Equations 3.7 to 3.12). For the model control (CTRL) run the modified stomatal conductance was used to calculate the rate of dry deposition of ozone, and reactive nitrogen species (NO_y: NO_2, PAN, PPAN, MPAN and OnitU) to vegetated surfaces. In the CTRL run all PFT types were assumed to have low sensitivity to ozone damage.

In addition to the CTRL simulation 4 additional experiments were performed in order to quantify the impact of ozone damage on reactive trace gas deposition and the subsequent impacts on atmospheric composition and air quality. In these experiments, only stomatal resistances with respect to ozone, NO_2 and reactive nitrogen were modified to reflect the change in dry deposition associated with ozone damage, with all other model settings left unchanged from the CTRL simulation. In order to separately test the sensitivity of ozone and NO_y dry deposition to ozone damage one simulation was run where ozone damage only affected ozone uptake (O3_DD) and one simulation was run where ozone damage impacted NO_y uptake only (NOY_DD). To test the overall sensitivity of atmospheric composition to ozone damage, a simulation was run without the effects of ozone damage included (OFF). A final simulation was run where plants had high sensitivity to ozone damage (HIGHSENS) in order to provide a range of sensitivities of trace gas concentrations to the inclusion of the ozone damage parametrisations. The low and high sensitivities of each PFT type represent the tolerance of each vegetation category to ozone exposure (Table 3.6, Chapter 3). In the model these are represented by the fractional reduction in photosynthesis with ozone uptake by the leaves and are calibrated using data from field studies (Sitch et al., 2007). As described in Chapter 3, the dry deposition scheme in HadGEM2-ES also accounts for

the dry deposition of SO_2 and NH_3 to vegetation, however in these simulations the ozone damage parametrizations do not impact the uptake of these species in order to constrain the simulated results to changes in ozone and its precursor species only. In all simulations the model was spun up for a period of nine months and then run for 2 years with the analysis performed on the final year of the simulation. Table 6.1 provides a summary of the simulations.

TABLE 6.1: Overview of simulations for investigation of ozone damage on dry deposition of trace species and isoprene emissions from the biosphere.

Model Simulation	Ozone Damage O_3 deposition effect	Ozone Damage NO_y deposition effect	Ozone Damage iBVOC effect	Plant Sensitivity
CTRL	ON	ON	OFF	Low
O3_DD	ON	OFF	OFF	Low
NOY_DD	OFF	ON	OFF	Low
OFF	OFF	OFF	OFF	N/A
HIGHSENS	ON	ON	OFF	High
ISOP	ON	ON	ON	Low
ISOP_HIGH	ON	ON	ON	High

6.2.3 Experiments to assess impact of ozone damage on isoprene emissions through the suppression of vegetation net photosynthesis

A second series of experiments were also run in order to quantify the effect of ozone vegetation damage on the emission of isoprene from the biosphere. This effect was parametrised in HadGEM2-ES using the on-line iBVOC emissions scheme with the modification of the isoprene emissions rate using the ozone exposure factor determined by the ozone damage parametrization code. As isoprene production and carbon assimilation both occur in the leaf chloroplasts and both processes share the same biogeochemical intermediates, it has been suggested that a close relationship exists between isoprene production and the process of photosynthesis (Arneth et al., 2007; Delwiche and Sharkey, 1993; Niinemets et al., 1999; Pacifico et al., 2011). In the iBVOC emissions scheme, the canopy isoprene emission rate is directly related to the net rate of photosynthesis and the scheme derived by Sitch et al. (2007) accounts for ozone damage by modifying this rate by applying the ozone uptake or exposure factor. Therefore this allows the impact of ozone damage on isoprene emissions to be estimated through modifying Equation 3.16 to give Equation 6.1.

$$I = IEF\frac{(A_{canopy} + R_{D_{canopy}})}{A_{st} + R_{D_{st}}} f_T \cdot f_{\mathrm{CO}_2} \cdot F_{\mathrm{O}_3} \tag{6.1}$$

Where, I is the canopy isoprene emissions rate, A_{canopy} and $R_{D_{canopy}}$ are the canopy level net photosynthesis and dark respiration rates respectively, A_{st} and $R_{D_{st}}$ are the rates of net photosynthesis and dark respiration at standard conditions. Standard conditions are defined as a temperature ($\mathrm{T_{st}}$) of 30°C, photosynthetically active radiation of 1000 μmolm^{-2}s^{-1} and a CO_2 atmospheric concentration of 370 ppmv (Arneth et al., 2007; Guenther et al., 1995). Finally f_{T} and f_{CO_2} are the empirical factors which represent the effect of temperature and CO_2 on isoprene emission and F_{O_3} is the ozone uptake factor Equation 3.8.

To quantify the impact of ozone damage on isoprene emissions from the biosphere, and the resultant feedback on atmospheric composition, 2 additional experiments were performed to compare with the OFF scenario (Table 6.1). In the first of these experiments (ISOP), the model setup was the same as the CTRL run with ozone damage affecting ozone and $\mathrm{NO_y}$ uptake however in addition to this isoprene emissions were modified to account for the ozone damage (Equation 6.1). Plant sensitivity to ozone damage remained low. For the second of these experiments (ISOP_HIGH), the setup was identical to the ISOP run however plants had high sensitivity to ozone damage. These additional runs were again spun up for nine months and then run for a period of two years with the first year discarded. A summary of the simulations can be found in Table 6.1.

6.3 Impacts of ozone damage on vegetation stomatal conductances

Figure 6.2 shows the global distribution of stomatal conductance estimated by the model in the absence of ozone damage effects. The figure shows the total bulk stomatal conductance per model grid box over all PFT types. The seasonality of vegetation activity is clearly evident with stomatal conductances shown to be greatest over the Amazon, southern Africa and Indonesia (locations in the tropics dominated by broadleaf tree vegetation) during the month of January where values of 0.01 ms^{-1} or greater are seen. This corresponds to

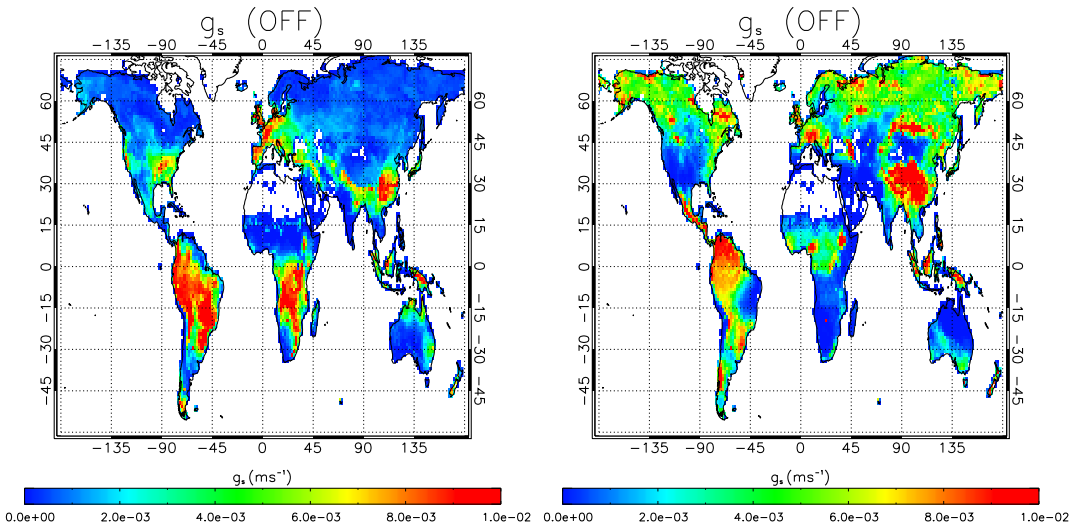

FIGURE 6.2: Global model bulk leaf stomatal conductance in the absence of ozone damage effects (OFF Scenario). The left map shows values for January and the right shows values for July. Values are bulk leaf stomatal conductance (ms^{-1}) for each model grid box weighted by fractional PFT coverage and grid box land fraction.

the summer season in the Southern Hemisphere tropical regions where temperatures are greater and the amount of incoming solar radiation is greater hence vegetation is more photosynthetically active. In contrast stomatal conductances are lower in the Northern Hemisphere in January due to the winter season where vegetation has either died back or is less photosynthetically active. A contrasting situation is shown for July where it is summer in the Northern Hemisphere and winter in the south, with stomatal conductances shown to be greater in general in the North.

Figure 6.3 shows the relative change (with respect to the OFF scenario) in bulk leaf stomatal conductance with the inclusion of ozone damage under the CTRL and HIGHSENS scenarios (Table 6.1). In general, under both scenarios, the reduction of stomatal conductance through ozone damage is more pronounced during the summer months in each respective hemisphere. This is because, as described above, vegetation is more photosynthetically active in the summer and due to higher levels of ozone throughout the summer due to the photochemical nature of ozone formation (Chapter 2). The areas that see the greatest reduction in stomatal conductance are the major industrialised regions of the Northern Hemisphere (N America, South East Asia and Europe) where ambient ozone levels tend to be highest. This is as a result of rising ozone concentrations since the pre-industrial period due to an increase in emissions of NO_x, CO, methane and other VOCs

(Prather et al., 2001).

Under the CTRL ozone damage scenario where plants have low sensitivity to ozone damage, the effects are shown to be more pronounced in the Northern Hemisphere summer with July stomatal conductances decreasing by up to 0.5 % over the major industrialised regions. In January, the major reductions are mainly shown over central Africa (0.1%) and northern parts of India (0.3% to 0.5%). When plants were set to have high sensitivity to ozone damage (HIGHSENS scenario), the impacts on stomatal conductances were shown to increase greatly with reductions of approximately 6 % or greater seen over the majority of the major industrialised regions of the Northern Hemisphere in July with Europe and eastern N America showing the most widespread decreases. More importantly, drops in stomatal conductances of 1 to 3 % were shown over the forested regions of southern Africa and the Amazon during July. In January, the largest decreases were shown once again over central Africa and northern India where reductions in stomatal conductances approached 6 % though a more pronounced impact was shown over parts of S America where decreases were shown of around 1 to 2 %.

The importance of the seasonality of ozone concentrations and stomatal conductance is highlighted in Figure 6.3 where under high plant sensitivity the variation in the impact of ozone damage on stomatal conductance between January and July is more pronounced than when plants have low sensitivity. This is shown by the more widespread reductions in stomatal conductance throughout the northern hemisphere in July when ozone concentrations are at their summertime peak.

6.4 Quantifying the effects of ozone damage on dry deposition fluxes and the subsequent feedback on surface ozone concentrations.

The decreases in stomatal conductances under ozone damage diagnosed in the previous section are used to estimate the resultant change in the stomatal flux of ozone and thus the impact of ozone damage on the dry deposition flux of ozone to the biosphere. The flux of ozone to the stomata was calculated as follows:

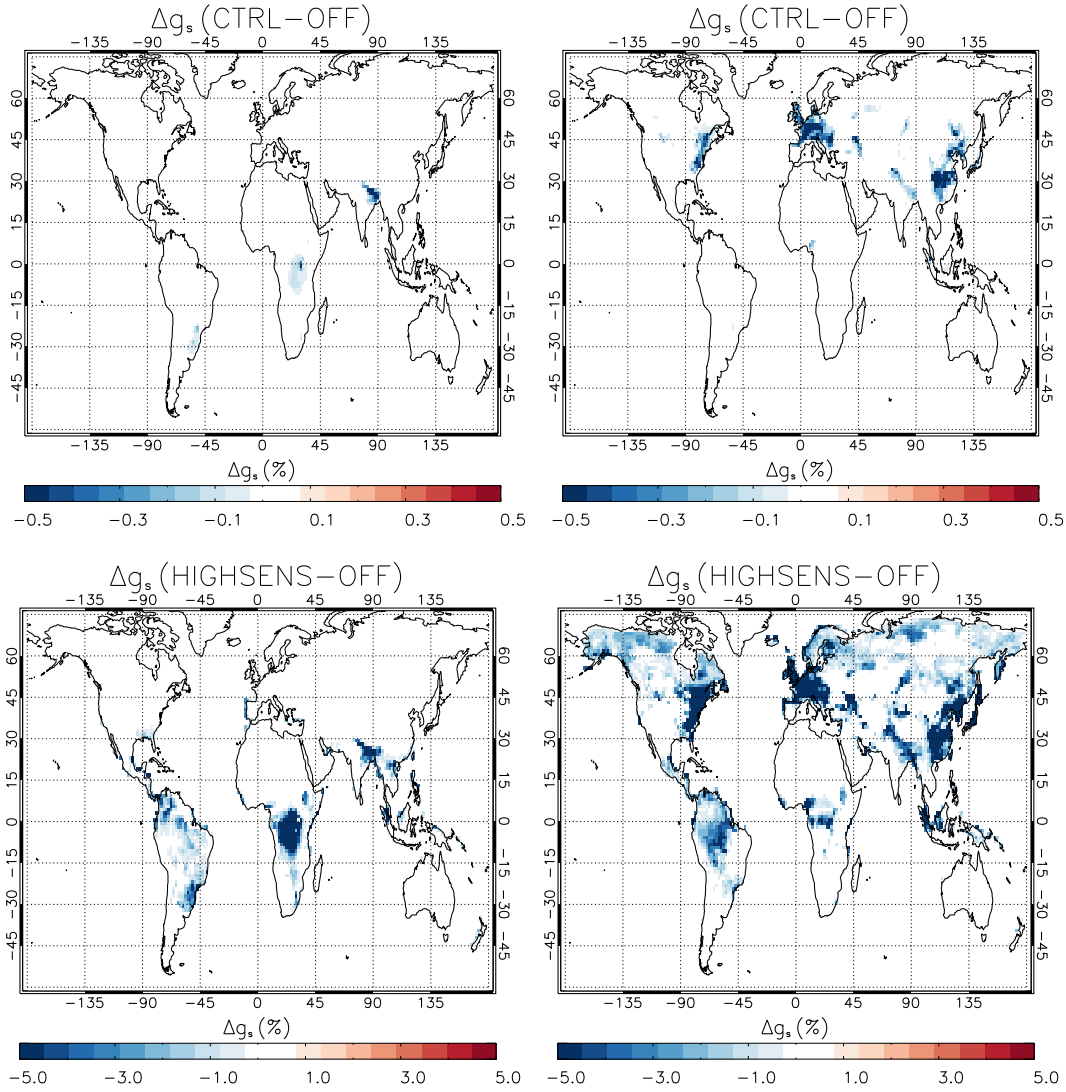

FIGURE 6.3: Changes in global monthly mean model leaf conductance when ozone damage is included. The first column shows the differences for January and the second shows the differences for July. The first row shows changes for OFF versus CTRL simulations and the second OFF versus HIGHSENS simulations.

$$F_{O3} = \frac{[O_3]}{R_a + [\frac{\kappa_{O3}}{g_l}]}, \tag{6.2}$$

where F_{O3} is the flux of ozone to the stomata (nmol O_3 m^{-2} s^{-1}), [O_3] is the molar concentration at reference level (nmol m^{-3}), R_a is the aerodynamic and boundary layer resistance between the leaf surface and the reference level (s m^{-1}), g_l is the leaf conductance for H_2O (m s^{-1}) and κ_{O_3} is the ratio of leaf resistance for ozone to the leaf resistance for

water vapour ($\kappa_{O_3} = 1.67$). The resultant change in the exchange of ozone and associated precursor species with the atmosphere is then used online by HadGEM2-ES to quantify the corresponding change in surface ozone levels.

Figure 6.4 shows the global and regional differences in monthly mean stomatal flux over all PFT types between each of the ozone damage scenarios and the OFF scenario and the corresponding changes in surface ozone concentrations. On a global scale, the greatest changes in surface ozone concentrations and stomatal fluxes are seen in the months of July to September with the largest increase in surface ozone of approximately 0.06 ppbv seen under the HIGHSENS scenario during July. This corresponds to a maximum decline in stomatal flux of 0.8 $\mathrm{nmolm^{-2}s^{-1}}$. A similar pattern is evident over the E USA, SE Asia and W Europe regions where maximum increases in surface ozone peak at 0.27 ppbv over E USA, 0.42 ppbv over SE Asia, and 0.48 ppbv over W Europe during the summer months under the HIGHSENS scenario.

Over the Amazon and Central African regions, the effects of ozone damage differ from those in the more polluted regions as these environments are remote (low $\mathrm{NO_x}$) environments where isoprene emissions tend to be very high due to location of the tropical rainforests within these regions, with the Amazon in particular shown to have very high isoprene emissions (Lelieveld et al., 2008). Over both of these regions, the response of surface ozone concentrations to the inclusion of ozone damage is largely controlled by the availability of $\mathrm{NO_x}$, which is heavily influenced by biomass burning. Over the Amazon the main burning season lasts from August to October (Stavrakou et al., 2009) and during this season $\mathrm{NO_x}$ emissions are higher than throughout the remainder of the year. This pattern is reflected in the differences in surface ozone concentrations where the greatest changes are seen throughout the burning season with the largest increases of around 0.15 ppbv shown in September under the HIGHSENS scenario.

Over Africa, a similar picture is shown with the greatest differences seen between the months of November and February which corresponds to the biomass burning season throughout this region (van der Werf et al., 2006) with peak increases from the OFF scenario of around 0.11 ppbv shown in surface ozone during the month of January. It is also shown that over both of these regions the response to ozone damage is much lower than over the more polluted Northern Hemisphere regions where mean annual ambient surface ozone concentrations tend to be higher (43.0 ppbv, 44.9 ppbv and 39.9 ppbv over E USA,

SE Asia and W Europe respectively) than over these more remote regions (26.2 ppbv over Amazon and 39.2 ppbv over Africa). Once again the greatest declines in stomatal fluxes correspond to the increases in surface ozone concentration though these again are less pronounced than over the more polluted regions (-0.08 $\mathrm{nmolm^{-2}s^{-1}}$ over Amazon and -0.07 $\mathrm{nmolm^{-2}s^{-1}}$ over Central Africa).

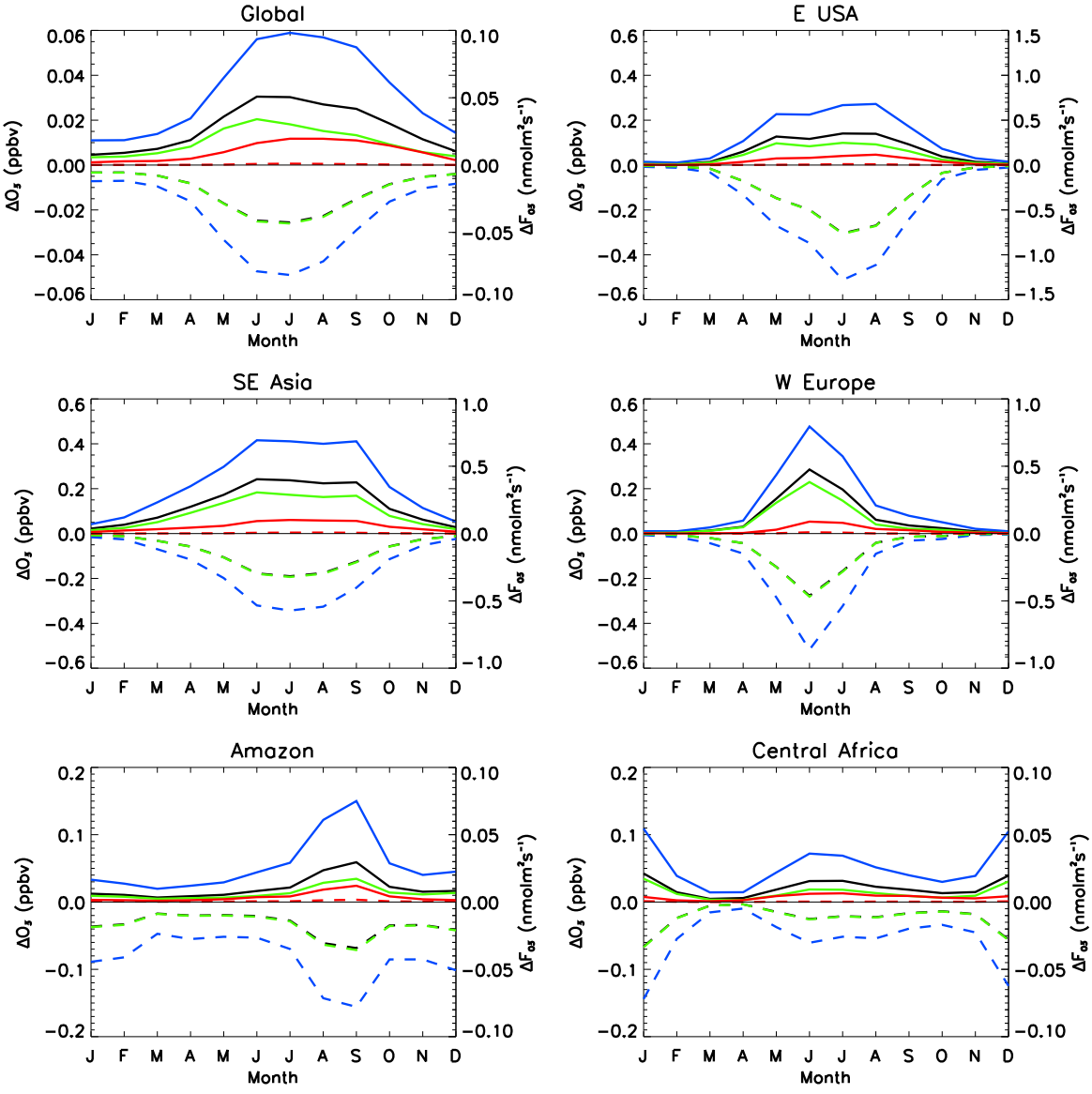

FIGURE 6.4: Global and regional yearly profiles of surface ozone concentration differences (solid lines) between the ozone damage scenarios and the OFF scenario in comparison with the corresponding changes in stomatal flux of ozone for surface vegetation (dashed lines). Differences are averages over all PFT types. The blue line shows differences for the HIGHSENS scenarios, the black line for the CTRL scenario, the green for the O3_DD scenario and the red for the NOY_DD scenario.

According to Equation 6.2 the reduction in stomatal conductance results in a corresponding decrease in stomatal ozone flux which in turn reduces the amount of ozone dry deposited to the plant, thus allowing surface ozone concentrations to increase. Under the CTRL scenario the response of ozone flux and thus concentrations is less pronounced due to lower plant sensitivity to ozone exposure and thus a less pronounced decline in stomatal conductance and hence rate of ozone stomatal uptake. This also accounts for the more pronounced decline in stomatal fluxes under the HIGHSENS scenario than the CTRL scenario.

When the sensitivity to the effects of ozone exposure impacting ozone and NO_y uptake separately (the O3_DD and NOY_DD scenarios) were taken into account, surface ozone concentrations relative to the OFF scenario are shown to still increase under both simulations though were less pronounced than under the CTRL and HIGHSENS scenarios. When vegetation is exposed to ozone the rate of stomatal uptake of NO_2 and other reactive nitrogen species is decreased resulting in a build up of these species which can enhance ozone formation. The contribution of this effect is shown under the NOY_DD scenario where the effects of ozone exposure are confined to the uptake of NO_y only with ozone uptake left unaffected. Over all regions, under this scenario, there is an increase in surface ozone due to the reduction of reactive nitrogen uptake and the associated build up of local NO_x. This affect is shown to be as strong as the affect on ozone uptake itself through the winter months, particularly on a global scale where during the months of October, November and December both the O3_DD and NOY_DD scenarios produce similar changes in ozone concentrations with respect to the OFF scenario.

Under the O3_DD scenario, the ozone stomatal flux shows a very similar response to ozone exposure under the CTRL scenario however during the months where the decrease in ozone flux is at its peak, the simulated decline is slightly greater under the O3_DD scenario with greatest differences over SE Asia, W Europe and the Amazon. Similar stomatal flux differences with respect to the OFF scenario are shown as under the CTRL scenario due to vegetation having low sensitivity to ozone damage in both scenarios (Table 6.1) and stomatal conductance under both scenarios seeing the effects of ozone damage. Under the O3_DD scenario, surface ozone concentrations are shown to be lower than under the CTRL scenario, hence using Equation 6.2 to determine the flux, results in a lower rate of stomatal uptake due to the smaller differences in stomatal conductance between the

scenarios (Section 6.3). The resultant effect is a slightly larger decline in stomatal fluxes than is shown from the CTRL scenario.

For the NOY_DD scenario, the ozone exposure effects do not impact the stomatal conductance of ozone hence the controlling factor on the stomatal flux of ozone determined by Equation 6.2 becomes the changing surface ozone concentrations due to added NO_y in the atmosphere due to the reduced stomatal uptake of these species. Therefore, as surface ozone concentrations are shown to rise under the NOY_DD scenario, the corresponding change in flux is a very slight increase in surface fluxes (Figure 6.4), though this increase is very small peaking at around 0.01 $\mathrm{nmolm^{-2}s^{-1}}$ during the summer months over E USA, SE Asia and W Europe. Therefore under the NOY_DD scenario, ozone uptake is enhanced rather than reduced. However, ozone concentrations at the surface still increase due to the enhanced concentrations of precursor species resulting in greater ozone production.

6.5 Quantifying the effects of ozone damage on the total biosphere stomatal uptake rate of ozone.

Table 6.2 shows the global and regional mean annual ozone uptake as calculated from the stomatal fluxes under each model scenario. The table also provides a break down of ozone uptake per PFT type in the HadGEM2 land classification scheme. Figure 6.5 shows global maps of the relative changes in mean annual ozone uptake under each model scenario.

On a global scale, under the OFF scenario, the mean annual ozone uptake is 5.21 $\mathrm{mmolO_3m^{-2}}$ with broadleaf trees and C3 grasses providing the greatest contribution (1.79 $\mathrm{mmolO_3m^{-2}}$ and 1.88 $\mathrm{mmolO_3m^{-2}}$ respectively). The other PFT types provide a much smaller contribution (0.43–0.63 $\mathrm{mmolO_3m^{-2}}$) with the C4 grasses providing the smallest. On a regional scale, mean ozone uptake rates are greatest over the Amazon (31.92 $\mathrm{mmolO_3m^{-2}}$) and smallest over W Europe (16.94 $\mathrm{mmolO_3m^{-2}}$). Over all regions, broadleaf trees and C3 grasses contribute the most to the the total uptake with C3 grasses dominating over the Northern Hemisphere industrialised regions (36.7 % to 57.9 %) and broadleaf trees dominating over Amazon and Central Africa (61.6 % to 63.9 %). This reflects the general land use patterns in these regions with the Amazon and African areas being largely dominated

TABLE 6.2: Global and regional mean annual O_3 uptake under each of the model scenarios per PFT type. Values are in $mmolO_3m^{-2}$.

		PFT Type					
	Scenario	BL	NL	C3	C4	Shrub	**TOTAL**
Global	OFF	1.79	0.63	1.88	0.43	0.48	**5.21**
	CTRL	1.74	0.63	1.73	0.42	0.47	**4.99**
	HIGHSENS	1.65	0.62	1.67	0.42	0.44	**4.79**
	O3_DD	1.73	0.63	1.73	0.42	0.47	**4.98**
	NOY_DD	1.79	0.63	1.89	0.43	0.48	**5.21**
E USA	OFF	5.89	3.76	7.30	1.52	1.41	**19.87**
	CTRL	5.36	3.73	6.18	1.41	1.28	**17.95**
	HIGHSENS	4.56	3.65	5.78	1.34	1.09	**16.42**
	O3_DD	5.35	3.73	6.17	1.41	1.28	**17.93**
	NOY_DD	5.90	3.76	7.30	1.52	1.41	**19.90**
SE Asia	OFF	7.26	1.78	12.58	1.34	2.51	**25.47**
	CTRL	6.82	1.77	10.92	1.27	2.35	**23.13**
	HIGHSENS	6.08	1.73	10.23	1.22	2.07	**21.33**
	O3_DD	6.81	1.77	10.90	1.27	2.34	**23.10**
	NOY_DD	7.27	1.79	12.61	1.34	2.51	**25.52**
W Europe	OFF	2.44	2.74	9.81	0.60	1.34	**16.94**
	CTRL	2.28	2.73	8.48	0.58	1.26	**15.33**
	HIGHSENS	1.99	2.69	7.95	0.56	1.13	**14.33**
	O3_DD	2.28	2.73	8.47	0.58	1.26	**15.31**
	NOY_DD	2.45	2.74	9.83	0.60	1.34	**16.96**
Amazon	OFF	20.40	0.08	6.49	3.49	1.45	**31.92**
	CTRL	20.09	0.08	6.36	3.48	1.42	**31.43**
	HIGHSENS	19.49	0.08	6.30	3.48	1.36	**30.70**
	O3_DD	20.08	0.08	6.36	3.48	1.42	**31.42**
	NOY_DD	20.42	0.08	6.49	3.49	1.45	**31.94**
Central Africa	OFF	12.74	0.02	3.68	2.68	1.58	**20.70**
	CTRL	12.50	0.02	3.58	2.66	1.54	**20.31**
	HIGHSENS	12.04	0.02	3.54	2.65	1.47	**19.72**
	O3_DD	12.50	0.02	3.58	2.66	1.54	**20.30**
	NOY_DD	12.75	0.02	3.68	2.68	1.58	**20.71**

by the tropical rainforests and the more industrialised Northern Hemisphere regions having less forest coverage and more C3 grass coverage due to anthropogenic activity resulting in the replacement of forested regions by agricultural crops since the 1850s (Ramankutty and Foley, 1999; Richards, 1990; Turner et al., 1993).

When the effects of ozone damage are included (CTRL) the global mean annual uptake of ozone dropped by approximately 0.22 $mmolO_3m^{-2}$ to 4.99 $mmolO_3m^{-2}$, a drop of 4.2 %. Broadleaf trees and C3 grasses show the greatest sensitivity to ozone exposure with declines in mean annual uptake of 0.05 $mmolO_3m^{-2}$ (1.79 $mmolO_3m^{-2}$ to 1.74 $mmolO_3m^{-2}$) and

0.15 mmolO_3m^{-2} (1.88 mmolO_3m^{-2} to 1.73 mmolO_3m^{-2}) respectively. The response of the other PFT types is much smaller with uptake by needle leaf trees showing no response of uptake to ozone damage.

When plants have high sensitivity (HIGHSENS scenario), a similar pattern is shown in declines of global mean ozone uptake with a drop of around 0.42 mmolO_3m^{-2} from 5.21 to 4.79 mmolO_3m^{-2} (8.1 %), with broadleaf trees and C3 grasses again exhibiting the greatest sensitivity to ozone damage (declines of 0.14 mmolO_3m^{-2} and 0.21 mmolO_3m^{-2} respectively). When the effects of ozone damage are limited to ozone uptake only (O3_DD) the response of surface vegetation is similar in magnitude to that of the CTRL scenario, however the overall drop in total stomatal uptake is slightly greater declining from 5.21 mmolO_3m^{-2} to 4.98 mmolO_3m^{-2}, a drop of 4.4 %. This is due to the slightly lower stomatal fluxes of ozone seen under the O3_DD scenario compared to the CTRL scenario (Section 6.4). The response over each individual PFT type is shown to be similar to that of the CTRL scenario with the drop in uptake again shown to be slightly more pronounced. Finally, when the effects of ozone damage were only set to impact the uptake of NO_y species, the total surface flux was shown to rise very slightly (approximately 0.1 %). This is because as shown in Section 6.4, when only NO_y dry deposition is affected by ozone induced stomatal closure, the resultant rising surface NO_y concentrations increase the rates of ozone formation and enhance stomatal fluxes increasing the rate of ozone uptake.

On a regional basis similar patterns are seen, however responses to ozone damage are more pronounced over the industrialised regions of the Northern Hemisphere. Over E USA mean ozone uptake drops from 19.87 mmolO_3m^{-2} to 17.95 mmolO_3m^{-2} (9.7 %) under the CTRL scenario (16.42 mmolO_3m^{-2} under the HIGHSENS scenario, a 17.4 % drop). For SE Asia a drop from 25.47 mmolO_3m^{-2} to 23.13 mmolO_3m^{-2} (9.2 %) under the CTRL scenario (21.33 mmolO_3m^{-2} HIGHSENS, a drop of 16.3 %) is seen and for W Europe a reduction from 16.94 mmolO_3m^{-2} to 15.33 mmolO_3m^{-2} (9.5 %) under the CTRL scenario (14.33 mmolO_3m^{-2} HIGHSENS, a drop of 15.4 %) is estimated. Over these regions, the greatest response is from the C3 grass PFT, again reflecting the vegetation distribution over these regions and highlighting C3 grass as the most sensitive type to ozone exposure. Over the Amazon and Central Africa regions, the reduction in mean stomatal uptake is approximately the same under both the CTRL (1.5 % over the Amazon and 1.9 % over Central Africa) and HIGHSENS (3.8 % and 4.7 %) scenarios, though less pronounced than

over the other regions. Over these more forested regions, the largest changes in ozone uptake are observed over the broadleaf tree category, though the sensitivity of C3 grasses was still shown to be evident. The patterns under the O3_DD and NOY_DD scenarios are similar when quantified on a regional basis.

The spatial distribution of changes in mean annual ozone uptake (Figure 6.5) shows the more pronounced reductions over the northern hemisphere industrialized regions with large parts of the E USA, SE Asia and W Europe region seeing drops of 10 % or greater larger under the CTRL scenario. In the southern hemisphere, the effects of ozone damage are seen though reductions in uptake are lower at around 2–4 % over Central Africa and parts of Brazil. When plants have high sensitivity, these changes are much more widespread and the effects of ozone damage are more evident in the southern hemisphere where drops in uptake are larger at 6–8 % over the forested regions of Central Africa and the Amazon. The reductions under the O3_DD scenario are similar to those under the CTRL though are slightly larger as discussed above. For the NOY_DD scenario, the small rises in fluxes are evident with maximum increases of up to 0.5 % over parts of northern India and southern and eastern China (Figure 6.5).

Overall, broadleaf trees and C3 grasses exhibit the largest sensitivity to ozone exposure. The sensitivity parameters used in the ozone damage parametrisation of Sitch et al. (2007) show C3 grasses to be the most sensitive to ozone damage followed by C4 grasses and then broadleaf trees (Table 3.6 in Chapter 3). Due to the greater coverage of the Broadleaf PFT type in HadGEM2, the response to ozone damage over these regions is estimated to be greater than that of C4 grasses despite the greater tolerance to ozone exposure. This can also have important implications for the emissions of isoprene as broadleaf tree species have been shown to be substantial emitters of isoprene particularly over the tropical regions (Guenther et al., 2006) and the general consensus is that isoprene emissions from plants tends to be confined to the C3 photosynthetic pathway (Harley et al., 1999; Pacifico et al., 2009). Therefore due to this estimated greater sensitivity to ozone exposure, the inclusion of ozone damage effects could potentially have important implications on isoprene emissions and further feedbacks on atmospheric composition. This effect is discussed further in Section 6.8.

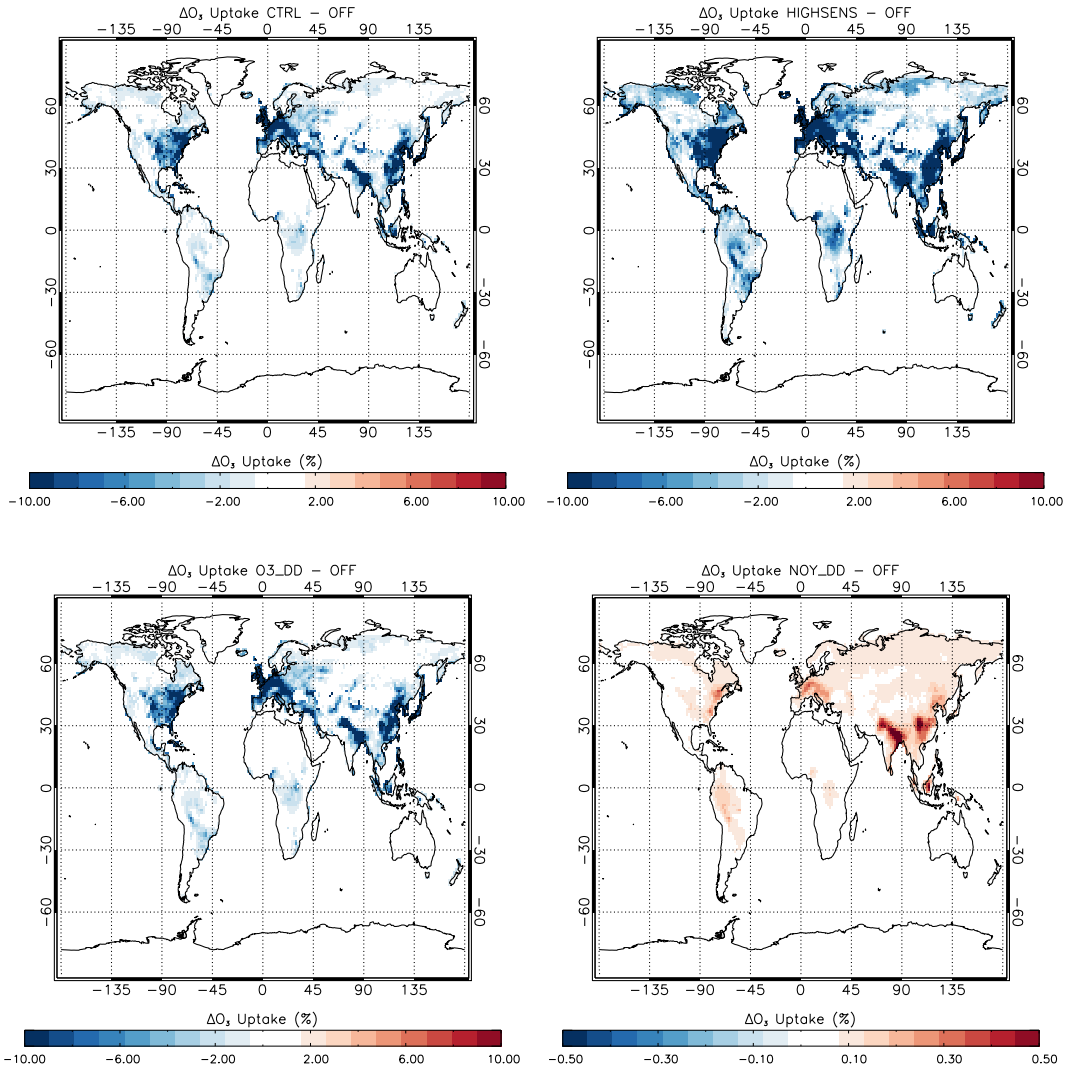

FIGURE 6.5: Percentage changes in mean annual ozone uptake between each of the ozone damage scenarios and the OFF scenario. Note the different scale in the bottom right plot.

6.6 Effects of stomatal ozone damage on surface ozone distributions and peak ozone concentrations.

Table 6.3 shows the changes in ground level ozone concentrations between the model simulation in the absence of ozone damage (OFF) and each of the other model scenarios. Overall the impact of ozone damage on global surface ozone concentrations is small under all scenarios with the greatest change shown under the HIGHSENS scenario where mean annual global concentrations increase by 0.03 ppbv or approximately 0.1 %. Under low plant sensitivity a 0.02 ppbv increase is shown with equal contribution from (approximately

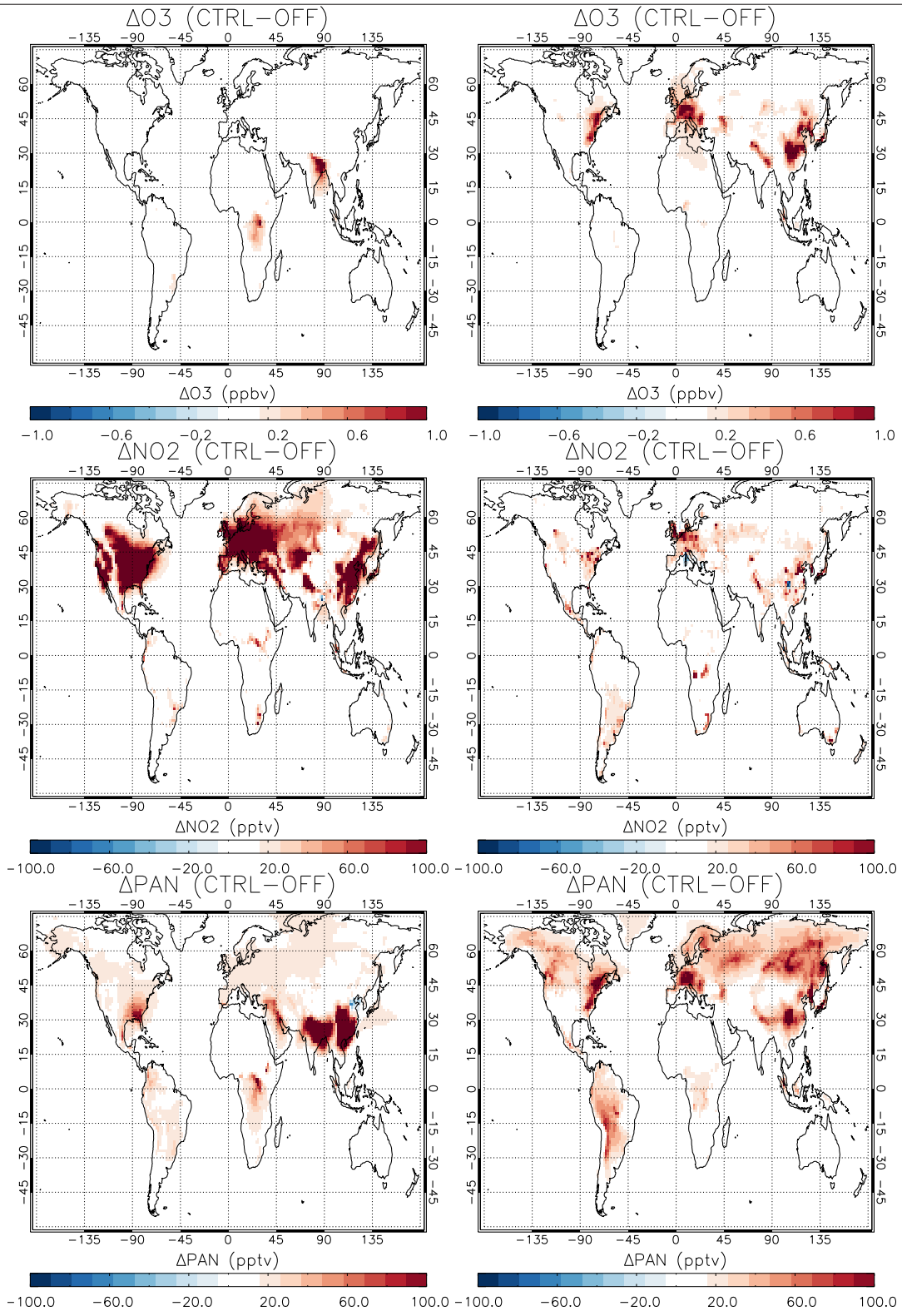

FIGURE 6.6: Differences in global monthly mean surface concentrations for OFF versus CTRL simulations. The left hand column shows differences for January and the right shows differences for July. The first row shows differences for ozone (in ppbv), the second NO_2 (in pptv) and the last row PAN (in pptv).

0.01 ppbv) the inclusion of ozone damage effects on the uptake of ozone and NO_y by vegetation respectively. These increases in surface ozone are observed due to the decrease in ozone dry deposition to vegetated surfaces through the reduction in stomatal conductance (Figure 6.3) and the resultant decline in the rate of ozone stomatal uptake (Section 6.4).

From Figure 6.4 the inclusion of ozone damage parametrisations result in relatively low monthly mean changes under all scenarios (less than 1 ppbv) when the changes are averaged across the entire domain of each region. Figures 6.6 and 6.7 however show that under both the CTRL and HIGHSENS scenarios, increases in surface ozone in excess of 1 ppbv are seen over individual model grid boxes in parts of N America, Europe and SE Asia during July and parts of the Amazon and Central Africa during the month of January.

Under both scenarios there is an increase in both NO_2 and PAN in both January and July due to the reduction in stomatal conductances causing a drop in the rate of uptake of these species by vegetation. For NO_2 the largest changes occur in January where peak increases in surface concentrations are seen to be in excess of 100 pptv over the major industrialised regions of the Northern Hemisphere. The increases are less pronounced under both scenarios in July, where the changes due to reduced dry deposition are competing with the photolysis sink of NO_2 which is greater in the summer and the reaction of NO_2 with OH whose concentrations would be affected by the local changes in surface ozone due to the ozone exposure effects. In July however, NO_2 concentrations still increase by up to 60 pptv over the industrialised regions of the Northern Hemisphere.

For PAN, increases in surface concentrations are more widespread throughout the Northern Hemisphere in July under both scenarios with peak concentration increases approaching 80 pptv or greater over N America, Europe and SE Asia. In January the increases are less widespread though peak changes are greater over parts of northern India and eastern China where increases are in excess of 100 pptv. Overall, these increases in background NO_y results in enhanced NO_x which causes enhanced formation of surface ozone. This compliments the increased surface ozone levels due to the direct impact of ozone damage on its own uptake.

The responses of peak annual, monthly and daily mean surface ozone values were also analysed under each ozone damage scenario with the results presented in Table 6.3. In this case the peak mean change was calculated as the maximum change in any individual

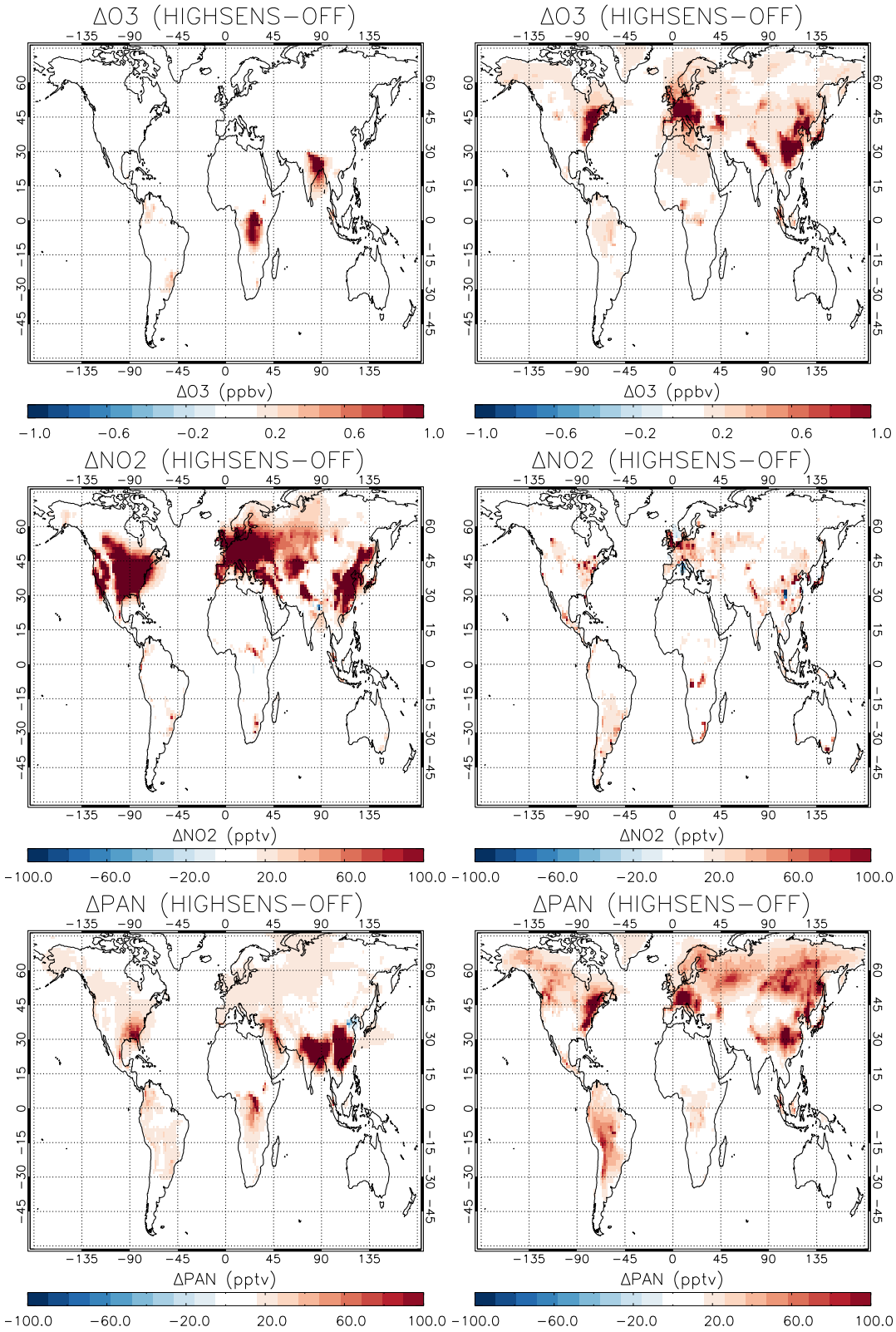

FIGURE 6.7: As Figure 6.6 except for OFF versus HIGHSENS scenario.

TABLE 6.3: Summary of changes in ground level ozone in ppbv for the experiments to quantify the effect of ozone damage on atmospheric ozone concentrations through the impact on dry deposition. The relative changes are shown in brackets. All differences are relative to the scenario with no ozone damage to vegetation (OFF)

	O3_DD	NOY_DD	CTRL	HIGHSENS
Global:				
Annual mean	0.01 [<0.1 %]	0.01 [<0.1 %]	0.02 [<0.1 %]	0.03 [0.1 %]
E USA:				
Peak annual mean[a]	0.26 [0.5%]	0.09 [0.2 %]	0.35 [0.7 %]	0.60 [1.1 %]
Peak monthly mean[a]	0.84 [1.5 %]	0.28 [0.5 %]	1.07 [1.9 %]	2.30 [4.0 %]
Peak daily mean[a]	2.08 [3.0 %]	0.90 [1.4 %]	2.55 [3.6 %]	5.44 [8.3 %]
SE Asia:				
Peak annual mean[a]	1.04 [1.7 %]	0.34 [0.6 %]	1.41 [2.3 %]	1.98 [3.7 %]
Peak monthly mean[a]	3.80 [4.8 %]	0.82 [1.3 %]	4.67 [5.9 %]	6.60 [8.3 %]
Peak daily mean[a]	8.26 [8.4 %]	2.24 [2.4 %]	10.67 [11.1 %]	13.70 [14.2 %]
W Europe:				
Peak annual mean[a]	0.33 [0.7 %]	0.06 [0.1 %]	0.40 [0.8 %]	0.66 [1.3 %]
Peak monthly mean[a]	1.61 [3.2 %]	0.31 [0.5 %]	1.86 [3.7 %]	2.89 [5.7 %]
Peak daily mean[a]	3.14 [6.6 %]	0.86 [1.2 %]	3.58 [6.7 %]	5.18 [9.1 %]
Amazon:				
Peak annual mean[a]	0.10 [0.4 %]	0.05 [0.1 %]	0.16 [0.5 %]	0.40 [1.2 %]
Peak monthly mean[a]	0.61 [1.2 %]	0.33 [0.7 %]	0.95 [1.9 %]	2.25 [4.6 %]
Peak daily mean[a]	1.33 [1.9 %]	1.06 [1.4 %]	2.44 [3.3 %]	5.65 [7.7 %]
Central Africa:				
Peak annual mean[a]	0.13 [0.4 %]	0.03 [0.1 %]	0.15 [0.5 %]	0.39 [1.3 %]
Peak monthly mean[a]	0.82 [1.5 %]	0.16 [0.3 %]	0.99 [1.8 %]	1.82 [3.3 %]
Peak daily mean[a]	1.46 [2.4 %]	0.29 [0.5 %]	1.77 [2.9 %]	3.13 [5.7 %]

[a] Values given are the maximum change in any individual gridbox in the stated domain.

gridbox within the stated domain over the timescale indicated. Peak changes were analysed because as discussed in Chapter 4, changes in these values can have important implications for the estimation of the impact of ozone damage on yield losses of crops when using threshold exposure based indices such as AOT40 and W126 which were designed to capture the most harmful effects of episodic ozone pollution. Changes in peak ozone concentrations particularly when the mean ambient ozone is around the threshold value of these indices (e.g. 40 ppbv for AOT40) can result in significant changes in the estimated AOT40 index and thus the resultant predicted yield loss.

For all regions, the inclusion of ozone damage effects produces the greatest response on peak daily mean surface ozone concentrations with SE Asia showing the greatest responses where concentrations increase by up to 10.67 ppbv under the CTRL scenario (11.1 %) and

13.7 ppbv (14.2 %) under the HIGHSENS scenario with respect to the OFF scenario. The smallest response is over Central Africa where peak daily mean concentrations increase by up to 1.77 ppbv (2.9 %) under the CTRL scenario and 3.13 ppbv (5.7 %) under the HIGHSENS scenario. Peak annual means exhibit the smallest responses to ozone damage effects with SE Asia once again showing the largest response in peak annual ozone concentrations and Central Africa showing the smallest response.

When the effects of ozone exposure on its own and NO_y deposition are considered in isolation it is shown with respect to the OFF scenario, the impact on ozone deposition only, produces the largest response with maximum increases in the range of 1.33 ppbv (2.4 %) over the Amazon to 8.26 ppbv (8.4 %) over SE Asia. When the ozone damage effects are limited to NO_y deposition only the increases are less pronounced ranging from 0.29 ppbv (0.5 %) over Central Africa to 2.24 ppbv (2.4 %) over SE Asia, though is still shown to provide a significant contribution to surface ozone changes. This is particularly evident over the Amazon where increases in daily peak mean ozone under the NOY_DD scenario are 1.06 ppbv (1.2 %), nearly as large as that observed under the O3_DD scenario.

Overall, when ozone damage effects are included in model simulations both mean and peak surface and ozone concentrations increase with maximum regional increases of up to ∼14 ppbv in daily mean surface ozone values. These changes can have important implications on atmospheric composition, air quality and climate which can result in further feedbacks on the biosphere. Examples of such impacts include the reduction in isoprene emissions from vegetation due to lower rates of photosynthesis and a reduction in vegetation yields and quality as a result of changing surface ozone concentrations.

6.7 Impacts of ozone damage stomatal uptake effect on local air quality

As discussed in Chapter 4, the AOT40 metric has been adopted in Europe as an air quality standard to assess the risk to vegetation from ozone exposure. In order to quantify the air quality impacts of changing ozone concentrations due to the dry deposition impact of ozone damage, the AOT40 metric is calculated from the surface ozone concentrations in the absence of ozone damage (OFF scenario) and under low and high plant sensitivity to

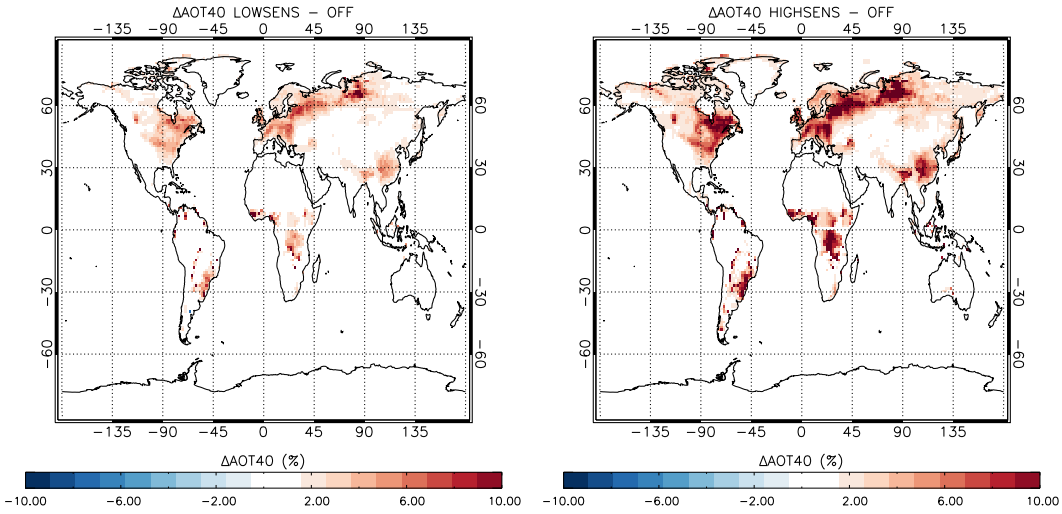

FIGURE 6.8: Percentage changes in model AOT40 with respect to the OFF scenario under low (LOWSENS) and high plant sensitivity (HIGHSENS) to ozone damage.

ozone exposure. The AOT40 under each scenario are calculated as per the method used in Chapter 4 however a standard growing season of May, June, July is adopted for the northern hemisphere, offset by six months for the southern hemisphere. Figure 6.8 shows spatial changes in AOT40 with respect to the OFF scenario under low (LOWSENS) and high plant sensitivity (HIGHSENS) and Table 6.4 shows the global and regional mean percentage changes in AOT40.

On the global scale, the effects of ozone damage lead to a mean rise in AOT40 of 1.68 % with low plant sensitivity and 3.49 % with high plant sensitivity. When plants have low sensitivity, E USA and W Europe see the largest regional increases of 2.30 % and 2.01% respectively though these rises are seen to approach 6–8 % over the east coast of the USA and parts of northern France and Germany (Figure 6.8). Central Africa shows the smallest increase in AOT40 of 0.95 % though parts of the region see rises approaching 6 %. However, when plants have high sensitivity to ozone damage, the Amazon shows the largest increases in AOT40 (4.24 %) with the E USA and W Europe showing slightly smaller rises of 4.02 % and 3.56 % respectively. Central Africa still shows the smallest increase in AOT40 under high plant sensitivity (2.33 %). The impact of higher plant sensitivity to ozone damage is clearly evident however, with increases in AOT40 approaching 10 % or greater over parts of all regions (Figure 6.8).

The large relative changes in AOT40 over the Amazon are likely to arise from the elevated

TABLE 6.4: Global and regional mean percentage changes in AOT40 with respect to the OFF scenario under low (LOWSENS) and high plant sensitivity (HIGHSENS) to ozone damage.

		Scenario	
		LOWSENS	HIGHSENS
Region	Global	1.68 %	3.49 %
	E USA	2.30 %	4.02 %
	SE Asia	1.66 %	2.99 %
	W Europe	2.01 %	3.56 %
	Amazon	1.67 %	4.24 %
	Central Africa	0.95 %	2.33 %

surface ozone concentrations pushing hourly ozone values over the 40 ppb threshold of the AOT40 metric in parts of the region which results in ozone concentrations not previously accounted for in the calculation of the metric now being included. This is reflected by locations in central Brazil seeing increases of AOT40 in excess of 60 %. Over the more industrialized regions of E USA, SE Asia and W Europe, ozone concentrations are already above the threshold of the metric with low plant sensitivity, therefore the changes in ozone concentrations as a result of the change in plant sensitivity produce a smaller increase in the relative change in AOT40 (1.72 % for E USA, 1.33 % for SE Asia and 1.55 % for W Europe) than over the Amazon (2.57 %).

As shown in Chapter 4, the change in relative yield loss (RYL) of a plant is linearly related to AOT40 (Mills et al., 2007) therefore increases in yield loss will change proportionally with the magnitude of the change in AOT40. This is shown in Table 6.5 which shows the resultant global and regional changes in RYL based on AOT40 assuming all locations grow wheat during the pre-defined growing season. This shows that the effects of ozone damage not only reduce the rate of dry deposition to vegetated surfaces but the resultant rise in surface ozone concentrations can lead to potential rises in global mean RYL of 1.78–3.72 % for wheat. On a regional scale RYL can increase by values in excess of 4 % with the Amazon and E USA showing the greatest increases.

As discussed in Chapter 4, ozone damage is not the only environmental factor which can result in yield losses on crops and plants with other drivers of yield reductions including heat stress, drought stress and whether the crops are properly irrigated. For comparison it is shown by Liu et al. (2010), that for a winter wheat-summer maize cropping system

TABLE 6.5: Global and regional mean percentage changes in RYL for wheat with respect to the OFF scenario under low (LOWSENS) and high plant sensitivity (HIGHSENS) to ozone damage.

		Scenario	
		LOWSENS	HIGHSENS
Region	Global	1.78 %	3.72 %
	E USA	2.30 %	4.02 %
	SE Asia	1.66 %	2.99 %
	W Europe	2.02 %	3.56 %
	Amazon	1.66 %	4.23 %
	Central Africa	0.96 %	2.33 %

in the Huang-Huai-Hai Plain of China, a 5°C increase in temperature results in an overall yield reduction of -18.5 ± 22.8 %. They also show the impact of a 2°C temperature rise as a reduction of -2.3 ± 13.2 % in yield. Table 6.5 shows that over the SE Asia region (which contains China) plant yields drop by 1.66 % with low plant sensitivity to ozone damage and by 2.99 % when plants have high sensitivity. This is comparable with the effects of a 2°C rise in temperature. Over the other regions, the drops in yield as a result of ozone damage are also comparable in magnitude to the impact of a temperature rise, though over the E USA and Amazon regions with high plant sensitivity the effects are nearly double at 4.02 % and 4.23 % respectively. This highlights the importance of including the effects of ozone damage in model simulations particularly when investigating the response of vegetation to ozone concentrations in future warmer climates.

Finally, it was also demonstrated in Chapter 4, that long range transport of ozone and its precursor species plays an important role in the local air quality of a given region and the resultant reduction in crop yields as quantified using the AOT40 metric. It was also highlighted that the relative contribution of long range transport to local AOT40 calculations has strong dependence on the local ozone distribution. As demonstrated in Section 6.6, the inclusion of ozone damage in model simulations can have impacts on peak daily ozone of up to 14 ppbv which can significantly alter the local ozone distribution and therefore the contribution of long range transport to local AOT40 calculations. This further highlights the importance of including ozone damage impacts in model simulations to quantify the impacts of changing air quality on vegetation.

6.8 Impacts of ozone damage on isoprene emissions

The global and regional differences in monthly mean isoprene emissions totalled over all PFT types between the ISOP and ISOP_HIGH and the OFF scenario and the resulting changes in surface ozone concentrations are shown in Figure 6.9. Figures 6.10 and 6.11 show regional annual spatial changes in isoprene emissions with respect to the OFF scenario for the ISOP and ISOP_HIGH scenarios respectively and Figure 6.12 shows global and regional changes in total isoprene emissions per PFT type for low (ISOP) and high (ISOP_HIGH) plant sensitivity to ozone damage.

When the effects of ozone damage on isoprene were included in the simulations, the patterns in surface ozone changes were largely similar to those shown when the effects of ozone damage were limited to stomatal uptake only with all regions showing a general rise in surface ozone concentrations. However, Figure 6.9 shows that these changes were less pronounced with maximum global increases in monthly mean surface ozone of approximately 0.04 ppbv under high plant sensitivity (ISOP_HIGH) as compared to 0.06 ppbv under the HIGHSENS scenario where only stomatal uptake was affected. This less pronounced increase in surface ozone is also evident when plants have low sensitivity to ozone damage (0.02 ppbv under the ISOP scenario as compared to 0.03 under the CTRL). On a regional scale the inclusion of the isoprene effect produces a similar impact with surface ozone concentrations still showing an increase, though less pronounced than the stomatal uptake only runs. The largest differences are seen over the E USA regions and the smallest over the Amazon where there is little difference between surface ozone concentrations (less than 0.01 ppbv).

Figure 6.9 also shows the corresponding changes in isoprene emissions under the ISOP and ISOP_HIGH scenarios. On a global scale isoprene emissions decrease throughout all months of the year with the greatest drops in the month of June of -2.71 μgCm^{-2}h^{-1} under the ISOP_HIGH scenario. On a regional scale, isoprene emissions show differing responses depending on the region of interest. Over the more polluted Northern Hemisphere regions of E USA, SE Asia and W Europe the greatest drop is in the late spring/early summer months (May to July) with reductions of up to 18.5 μgCm^{-2}h^{-1}, 19.5 μgCm^{-2}h^{-1} and 12.1 μgCm^{-2}h^{-1} respectively under the ISOP_HIGH scenario. Over the less polluted Amazon and Central African regions, reductions in isoprene emissions were much less (lower than

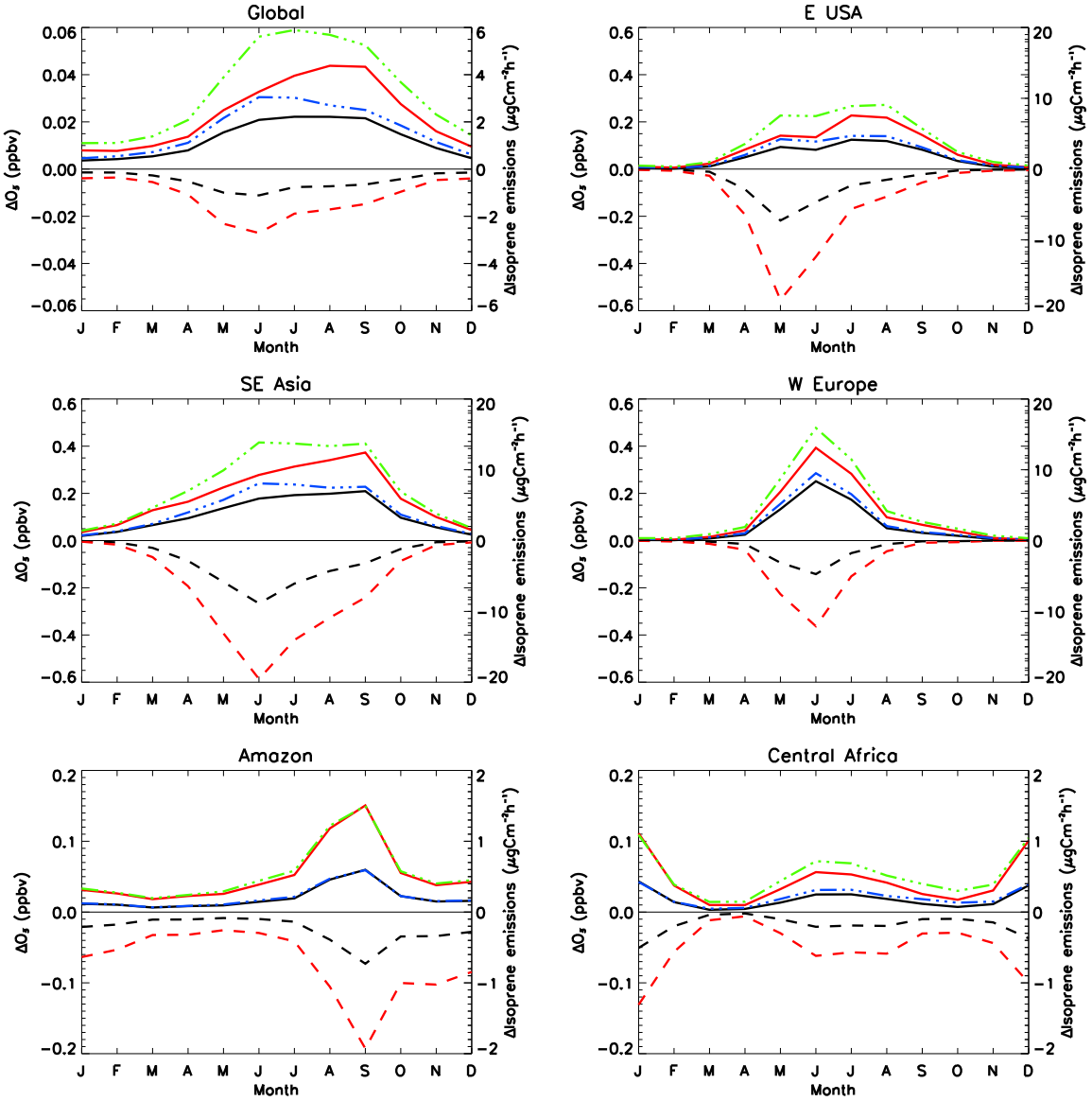

FIGURE 6.9: Global and regional yearly profiles of surface ozone concentration differences (solid lines) between the ozone damage scenarios and the OFF scenario in comparison with the corresponding changes in isoprene emissions for surface vegetation (dashed lines). Differences are averages over all PFT types. The red line shows differences for the ISOP_HIGH scenario, and the black line for the ISOP scenario. The dashed and dotted lines represent the change in surface ozone where damage affects dry deposition only with the green line showing differences for the HIGHSENS scenario and the blue line representing the CTRL scenario for comparison.

2 μgCm^{-2}h^{-1}) falling in the same months as biomass burning seasons in each respective region.

The surface maps of emissions changes (Figures 6.10 and 6.11) also highlight the seasonality of the changes in isoprene emissions from vegetation, with the E USA, SE Asia and W Europe showing widespread areas where the drop in emissions exceeded 20 μgCm^{-2}h^{-1},

particularly over eastern parts of China and the W Europe region. Under both scenarios, ozone-induced declines in emissions are much less however over southern parts of E USA and SE Asia declines approached 1 μgCm^{-2}h^{-1} or greater in places. The reverse pattern occurs over the Amazon and Central Africa where the greatest changes in emissions are in January when compared to July.

The comparison of surface ozone concentrations under the scenarios where isoprene emissions are affected (ISOP and ISOP_HIGH) and those where stomatal uptake only is affected (CTRL and HIGHSENS) show that the changes in isoprene emissions as a result of ozone damage have different impacts on ozone levels depending on the concentrations of NO_x in the region of interest (Figure 6.9). Over the more polluted high NO_x regions of the Northern Hemisphere, VOC:NO_x ratios tend to be low leading to these regions being described as VOC-sensitive (Sillman, 1999). Therefore, a reduction in isoprene emissions due to ozone damage results in a decline in ozone production due to isoprene's role as an ozone precursor upon oxidation in NO_x-rich environments (Chapter 2). This impact is evident in Figure 6.9 during the summer months where the reduction in isoprene emissions are the greatest, the ozone concentrations differences are less pronounced under the ISOP and ISOP_HIGH scenarios than under the CTRL and HIGHSENS scenarios. This effect was apparent over all of the high NO_x regions. During the winter months in these regions the increases in surface ozone concentrations are similar between all scenarios as the drop in isoprene emissions are seen to be smaller resulting in lesser declines in the amount of ozone production. In these regions the effect of ozone damage on isoprene emissions is shown to counteract the dry deposition impact, however the overall result is still an increase in surface ozone levels indicating that the dry deposition effect plays a stronger role in these regions.

Over the less polluted low NO_x regions of Central Africa and the Amazon, the isoprene effect was shown to produce a different result in surface ozone changes. In these low NO_x environments, the VOC:NO_x ratio is high resulting in ozone production to be NO_x-sensitive (Sillman, 1999). Therefore isoprene will act as a net ozone sink through reaction with ozone itself (ozonolysis of isoprene) or by enhancing ozone loss more than production (Sillman, 1999). Over Central Africa and the Amazon, it is shown that when the drop in isoprene emissions are greatest (January over Central Africa and September over the Amazon) the increases in surface ozone concentrations under the ISOP and ISOP_HIGH

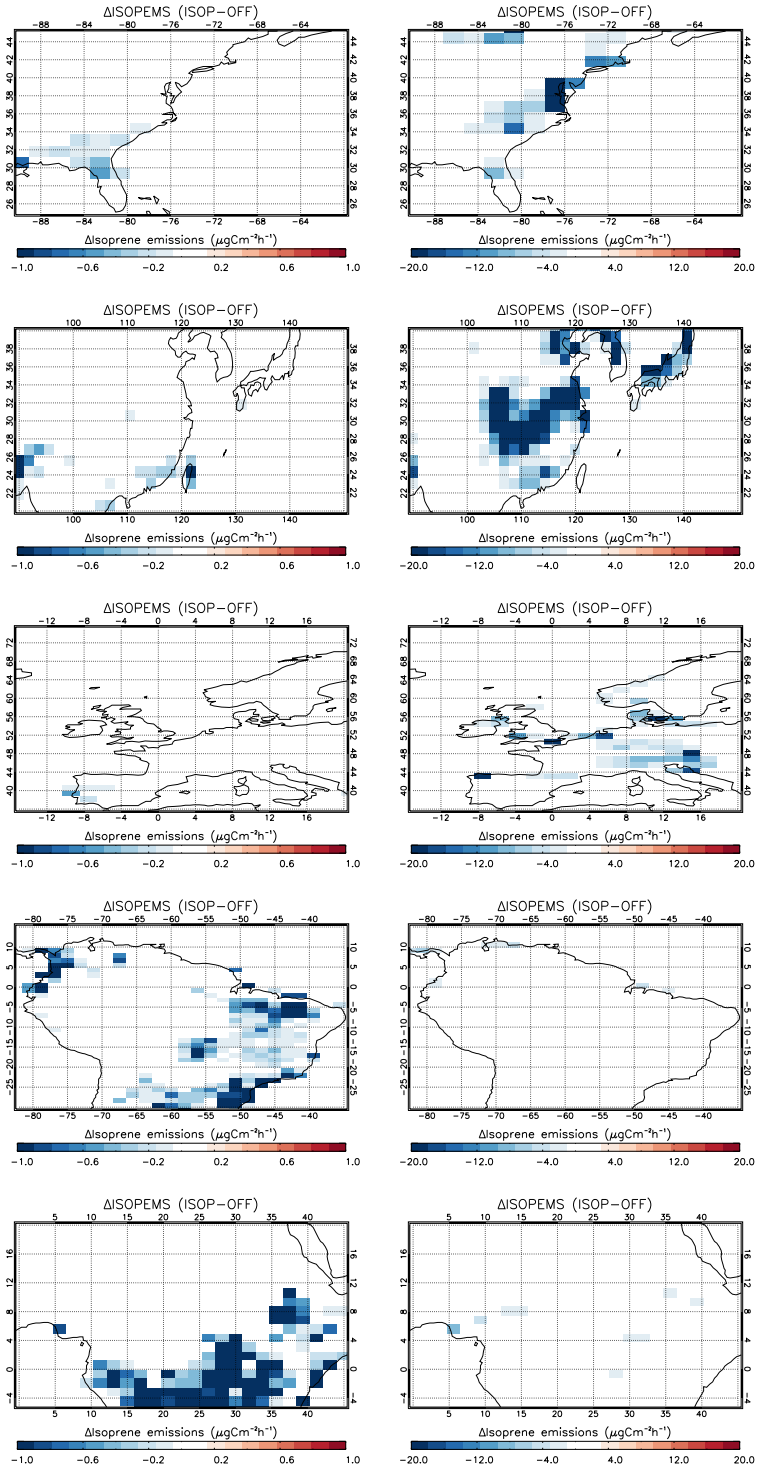

FIGURE 6.10: Changes in surface isoprene emissions between the ISOP and OFF scenarios. The first column shows differences for January and the second column shows changes for July. Note values on scales differ between months.

scenarios are slightly higher than under the CTRL and HIGHSENS scenarios respectively. Therefore the drop in isoprene emissions as a result of ozone exposure reduces the ozone

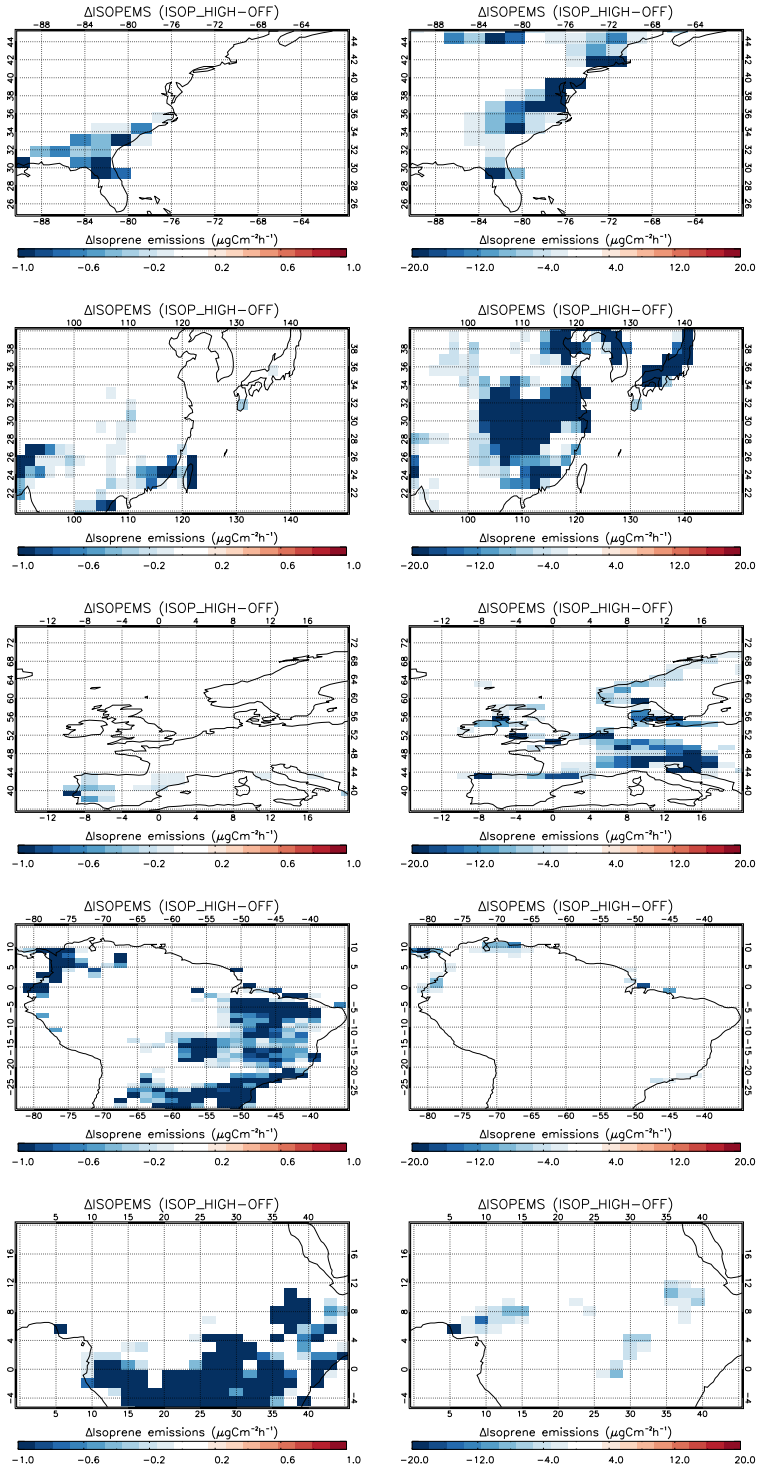

FIGURE 6.11: As Figure 6.10, except for ISOP_HIGH minus OFF scenario.

sink and causes a rise in surface ozone which enhances the increases due to the stomatal uptake effect.

As shown in Figure 6.12 isoprene emissions decline under both scenarios on a global and

regional scale. Globally, total annual isoprene emissions drop from 431.6 $TgCyr^{-1}$ under the OFF scenario to 430.8 $TgCyr^{-1}$ under the ISOP scenario where plants had low sensitivity to ozone damage, a drop 0.8 $TgCyr^{-1}$. Emissions from broadleaf trees and C3 grasses show the greatest sensitivity to the effects of ozone exposure with drops in emissions of 0.25 $TgCyr^{-1}$ and 0.26 $TgCyr^{-1}$ respectively. When plants have high sensitivity, the drop in global isoprene emissions is larger at 1.8 $TgCyr^{-1}$, with the largest drops seen for the broadleaf tree and shrubs PFT types.

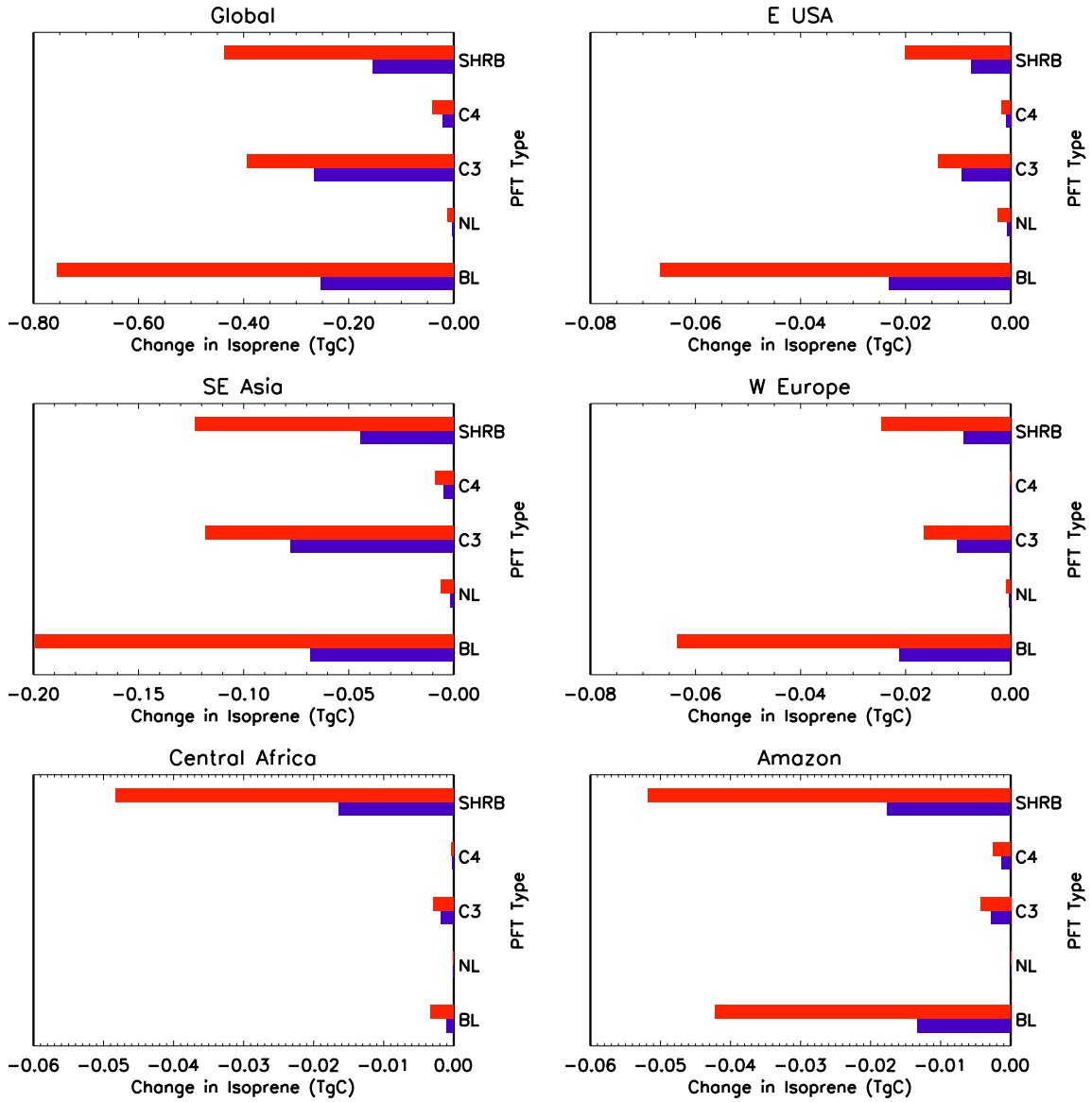

FIGURE 6.12: Global and regional changes in total annual mean isoprene emissions per PFT type between the ISOP (blue bar) and OFF scenarios and the ISOP_HIGH (red bar) and OFF scenarios. Note values on scales differ between regions.

On a regional scale, the pattern is similar over E USA, SE Asia and W Europe to that

shown on the global scale. The effects are most pronounced over SE Asia for broadleaf tree (0.068 $TgCyr^{-1}$ drop) and C3 Grasses (0.078 $TgCyr^{-1}$) under low plant sensitivity and broadleaf tree (0.199 $TgCyr^{-1}$) and shrubs (0.123 $TgCyr^{-1}$) under high sensitivity. Over Central Africa, the shrub PFT type sees the largest reduction in emissions (0.018 $TgCyr^{-1}$ low sensitivity and 0.052 $TgCyr^{-1}$ high sensitivity) and over the Amazon broadleaf tree (0.013 $TgCyr^{-1}$ low sensitivity and 0.042 $TgCyr^{-1}$ high) and shrubs (0.018 $TgCyr^{-1}$ low sensitivity and 0.052 $TgCyr^{-1}$ high) PFT types show the largest reductions.

6.9 Comparison of ozone damage impacts on isoprene emissions with previous work

Previous studies (Calfapietra et al., 2008; Pinelli and Tricoli, 2004; Tiiva et al., 2007; Velikova et al., 2005) have shown that there is great uncertainty in the response of isoprene emissions to rising ozone concentrations with some showing reduced emissions under elevated ozone (Calfapietra et al., 2008; Velikova et al., 2005) and some showing stimulated emissions with rising ozone levels (Pinelli and Tricoli, 2004). Velikova et al. (2005) showed that when plants were fumigated with 300 ppbv of ozone, isoprene emissions rates were reduced immediately by 8.0 $nmolm^{-2}s^{-1}$ (1958 $\mu gm^{-2}h^{-1}$), from the control case with no ozone exposure with emission rate shown to recover to control levels within 72 hours. Exposure to ozone at lower concentrations produced little response in isoprene emissions indicating a potential tolerance to ozone exposure. This was shown for a Mediterranean Oak species grown at an experimental station in Rome, Italy. In contrast to this a different fumigation experiment on the same species of oak (*Q. Pubescens*) by Pinelli and Tricoli (2004) showed that when the plants were exposed to intermediate levels of ozone (190 ppbv) the rate of isoprene emission dropped immediately after ozone exposure but in fact increased above control levels by approximately 5 $nmolm^{-2}s^{-1}$ (1224 $\mu gm^{-2}h^{-1}$) 288 hours after fumigation.

By comparison, the model simulations presented in this Chapter indicate reductions in isoprene emissions over the Europe domain (which includes Italy) in the range of 57.87 to 169.68 $\mu gm^{-2}h^{-1}$ depending upon plant sensitivity to vegetation. These reductions agree with the findings of Velikova et al. (2005) though they are much smaller in magnitude. This could be for a number of reasons. Firstly the experimental data from field experiments

(Calfapietra et al., 2008; Pinelli and Tricoli, 2004; Tiiva et al., 2007; Velikova et al., 2005) are collected at a specific location under controlled conditions and the plant were exposed to much higher ozone concentrations than they would be exposed to at typical atmospheric background levels. Therefore under the higher ozone concentrations, the stomatal flux of ozone will be larger (Equation 6.2) resulting in greater damage to the plant and hence a larger reduction in isoprene emissions. Secondly the data was collected for a specific tree species (Oak) whereas the parametrisations used in the model to determine plant responses to ozone exposure are derived for a generic broadleaf tree species.

However, the results presented in these field studies (Pinelli and Tricoli, 2004; Velikova et al., 2005) indicate a reduction in the rates of photosynthesis and stomatal conductance immediately after ozone exposure with these shown to also recover to control levels within 72-288 hours of exposure as with the isoprene emissions. As isoprene is mainly derived from photosynthetic intermediates (Sharkey and Yeh, 2001) it was suggested by Velikova et al. (2005) that the reduction in isoprene emissions was driven by the inhibition of photosynthesis, similar to the response modelled using the ozone damage parametrisations in HadGEM2.

As shown in Figure 6.9 during the times of year when ozone levels are at their lowest (e.g. the winter months in the Northern Hemisphere), the reduction in isoprene emissions from the OFF scenario were shown to be negligible after peaking during the summer months when ozone levels were higher. This therefore indicates a recovery of modelled isoprene emissions to approximately control levels after exposure to higher levels of ozone. This response from the model simulations again is consistent with the findings of Velikova et al. (2005). Therefore the changes in global scale isoprene emissions estimated with HadGEM2 are consistent with the responses expected from plants through the photosynthetic control on isoprene production and emission.

As mentioned previously (Pacifico et al., 2009), there are a number of other environmental controls that play a role in the magnitude of emissions of isoprene from the terrestrial biosphere. One such control is that of CO_2 with the general consensus that elevated CO_2 levels reduce the rate of isoprene emissions (Pacifico et al., 2009). However, some experiments report that isoprene emissions do rise under elevated CO_2 concentrations (Sharkey et al., 1991; Tognetti et al., 1998). In a recent CLM model study, (Heald et al., 2009), it was shown that accounting for the CO_2 effects caused a relatively small change

in present day isoprene emissions which in fact increased slightly from 508 to 523 $TgCyr^{-1}$ a 3 % rise. This was because the present day CO_2 mixing ratio of 365 ppmv was lower than the 400 ppmv critical threshold where the isoprene activity factor starts to fall below unity and results in a reduction of isoprene emissions (Possell et al., 2005; Wilkinson et al., 2009). By comparison the results presented in this Chapter show that the effect of ozone damage on global isoprene emissions is much smaller with a reduction from 431.6 $TgCyr^{-1}$ (in the absence of ozone damage) of 0.8 $TgCyr^{-1}$ (0.2 %) under low plant sensitivity and 1.8 $TgCyr^{-1}$ (0.4 %) under high plant sensitivity. This indicates that under present day conditions isoprene emissions show a greater response to the CO_2 effect than the impacts of ozone damage.

However, Heald et al. (2009) show that under a future climate change scenario with a doubling of CO_2 (to 717 ppmv) by the year 2100, projected global isoprene emissions were predicted to drop from 696 to 479 $TgCyr^{-1}$ a drop of 31 %. This is in agreement with the findings of Possell et al. (2004) which showed an approximate reduction in isoprene emissions of 50 % from English Oak species under a CO_2 increase from 360 ppmv to 660 ppmv. In both of these studies, the CO_2 levels increases beyond 400 ppmv and hence begin to inhibit isoprene emissions. Therefore if the effects of ozone exposure were accounted for in a long term run for future conditions, they could act to enhance the drop in isoprene emissions estimated by the CO_2 inhibition effect with potentially significant implications on climate and air quality.

Future land use change scenarios can also play a role in controlling isoprene emissions with Ganzeveld et al. (2010) estimating a reduction in isoprene emissions of approximately 50 $TgCyr^{-1}$ under a 2050 land use change scenario, largely controlled by the deforestation of forested areas over the Amazon and Africa which would see the removal of high isoprene emitting broadleaf trees. The effects over these regions are projected increases in surface ozone levels of up to approximately 9 ppbv. The effects of including ozone damage were again shown to be much smaller than those caused by land use change however the inclusion of ozone damage parametrisations in model simulations could act to enhance the reduction in isoprene emissions through the impact on photosynthesis and enhance rising surface ozone levels through the reduction in stomatal uptake of surface ozone. This further highlights the importance of including these effects in climate model simulations.

6.10 Uncertainties

A number of uncertainties have to be considered in the estimates of the impacts of including ozone damage on atmospheric composition and isoprene emissions using model simulations. Firstly it should be noted that the sensitivity parameters utilised by the ozone damage parametrisation in the simulations in this Chapter are typically based on the response of young trees to ozone exposure (Karlsson et al., 2004) with data mainly collected from open-top chamber experiments (Sitch et al., 2007). It has been shown previously that in some climatic conditions (high radiation and temperature), the microclimate conditions in open top chambers may differ from that of the ambient air (Nussbaum and Fuhrer, 2000). The response of young trees to ozone exposure is also assumed to be representative of trees of all ages and a constant ozone flux response is assumed of all plants throughout the growing season (Sitch et al., 2007). In reality the response of vegetation to ozone damage has been shown to differ from species to species within a certain plant type, depending upon the local conditions of where the plant is grown and the plants tolerance to ozone exposure (Mills et al., 2007).

Secondly, as discussed in Section 6.9 there is still great uncertainty in the response of isoprene emissions from vegetation to enhanced ozone levels. It has been suggested that isoprene emissions can in fact be stimulated by a rise in ozone levels due to it being able to prevent measurable losses in photosynthetic capacity by ozone and other reactive oxygen species (Affek and Yakir, 2002; Penuelas and Llusia, 2002; Penuelas et al., 2005; Velikova et al., 2004). The results presented here only consider the response of isoprene emissions to the inhibition of photosynthesis as a result of ozone damage and do not consider the potential enzymatic response of vegetation which increases isoprene emissions in order to offset the stress caused by ozone damage. Therefore the estimated global impacts of ozone exposure on isoprene emissions could differ when these other factors are considered as well as the photosynthetic impact. However, as shown in Section 6.9 the results presented in this Chapter show responses in isoprene emissions that are consistent with those seen in field experiments indicating confidence in the estimated impacts of ozone exposure.

Finally, a recent study (Lombardozzi et al., 2012) has drawn attention to the fact that the process of photosynthesis and stomatal conductance may not be as tightly correlated as previously thought particularly under chronic ozone exposure. It has been shown that

acute exposure to moderate or high ozone concentrations can cause similar instantaneous reductions in both photosynthesis and stomatal conductance (Farage et al., 1991) however chronic exposure can often lead to sluggish stomatal responses due to loss of stomatal functioning and a decoupling of conductance from photosynthesis (Paoletti and Grulke, 2005; Tjoelker et al., 1995). This could potentially result in an increase in stomatal conductance and hence enhanced rates of trace gas exchange with the atmosphere. The inclusion of these effects could potentially affect the rate of stomatal uptake by vegetation and thus the impact on surface ozone levels. The results presented by Lombardozzi et al. (2012) suggest that modifying stomatal conductance directly rather than indirectly through the impact of ozone damage on photosynthesis reduces the effect of ozone exposure on GPP and transpiration processes. This could therefore indicate higher stomatal conductances under chronic ozone exposure than predicted by the simulations in this Chapter and hence lesser impacts on surface ozone concentrations. These effects will need to be considered in future simulations where background levels of ozone are increasing (Cooper et al., 2010; Derwent et al., 2004) and there is less episodic episodes of pollution where there is acute exposure to ozone (effects of which are accounted for by the current Sitch et al. (2007) parametrisation) and more chronic exposure of vegetation to higher ozone levels.

6.11 Summary

The findings presented in this Chapter indicate that the inclusion of ozone damage effects in HadGEM2 model simulations highlights the complex nature of feedbacks and interactions between the atmosphere and the biosphere and indicated two major competing effects which control the response of surface ozone concentrations to ozone vegetation damage. When the impacts of ozone exposure were limited to the stomatal uptake only of ozone, thus affecting its dry deposition ozone was shown to have a self limiting effect on its own uptake leading to a positive feedback on ozone concentrations. Depending upon plant sensitivity to ozone exposure, the mean total global stomatal uptake was shown to decline by 0.22 to 0.42 $\mathrm{mmolO_3m^{-2}}$ which results in a rise in average surface ozone concentrations of 0.02 to 0.03 ppbv with local increases of up to 14 ppbv (over parts of SE Asia). The effects of ozone damage were shown to result in a reduction in the stomatal conductance of plants through the inhibition of the rate of photosynthesis (Sitch et al., 2007) which

also reduced the rate of uptake of NO_y species (precursor species for ozone formation). This resulted in a build up in concentrations of these species which led to enhanced ozone concentrations and further damage through ozone exposure setting up a positive feedback loop. These higher surface ozone concentrations were also shown to result in rises in the AOT40 metric of 1.68 %–3.49 % which translate into comparable increases in yield loss for wheat. On a regional scale increases in AOT40 and hence yield loss were shown to be as high as 4.24 % under high plant sensitivity. This therefore shows that the effects of ozone damage can have important implications for both regional and global air quality.

In competition with this effect, the reduction in the rate of photosynthesis due to ozone damage impacted the rate of isoprene emissions with global total isoprene emissions shown to drop by 0.8 $TgCyr^{-1}$ to 1.8 $TgCyr^{-1}$ depending upon the plant sensitivity to ozone damage. In general this reduction in isoprene was shown to reduce ozone levels due to isoprene's role as a precursor species to ozone pollution. This effect was particularly evident over the more polluted regions of the Northern Hemisphere. However, it was shown over parts of the Amazon and Central Africa that the reduction in isoprene caused a slight rise in ozone concentrations due to isoprene's role as an ozone sink in less polluted regions.

When both of these effects are included in model simulations it was shown that overall there was still a positive rise in surface ozone concentrations with these increases shown to be more pronounced when plants had high sensitivity to ozone exposure. This demonstrates that the effects of ozone damage on surface ozone concentrations through the impacts on stomatal uptake were stronger than those caused through the reduction in isoprene emissions.

The results presented in this Chapter indicate the significance of representing the effects of ozone damage in global Earth System models as the increase in surface ozone levels due to reduced stomatal uptake not only results in a positive feedback through further vegetation damage but can also have important implications for regional air quality. Although the impact on mean global and regional ozone concentrations are small in light of the uncertainties associated with the processes represented in this Chapter, the effects of including ozone damage in HadGEM2-ES produces large impacts on the peak ozone concentrations (up to 14 ppbv). Changes to peak ozone concentrations can have significant impacts on the calculation of air quality indices such as AOT40 and W126 (Chapter 4) resulting in important regional air quality impacts and reduction in crop yields. Damage to vegetation

can have indirect climate impacts through the effects on CO_2 uptake and transpiration processes (Lombardozzi et al., 2012; Sitch et al., 2007). These impacts on local air quality can also be detrimental to human health (Fowler et al., 2008). Previous studies have also shown that isoprene not only plays a role in ozone chemistry but also plays an important role in the formation of secondary organic aerosol (SOA) (Claeys et al., 2004). Therefore the responses in isoprene emissions to the effects of ozone damage are also important to consider with this respect, as aerosols are known to have a cooling effect on the climate (Forster et al., 2007).

Chapter 7

Conclusions

7.1 Summary of main results

In this thesis, the TOMCAT and the HadGEM-ES models were used to improve understanding of the complex interactions between tropospheric ozone and the global biosphere, focussing on the effects and feedbacks of changing dry deposition and BVOC emissions on atmospheric composition and air quality. This Chapter provides a summary of the major findings of this thesis with reference to the aims set out in Chapter 1. Suggestions for future work are also presented.

7.1.1 Aim 1: Quantify the intercontinental trans-boundary contributions of the emissions of ozone precursors to ozone induced crop yield losses in the northern hemisphere.

Chapter 4 presents the first estimates of the impact of ozone precursor emissions from each of the northern hemisphere's major industrialised regions (N America, SE Asia and Europe) on crop yields globally and in continents downwind of each region. A range of available exposure-response metrics were applied in a standardised manner to calculate the contributions of intercontinental trans-boundary pollution to crop yields. Six major agricultural crops were considered: wheat, rice, cotton, potato, soybean and maize.

For four of the crops considered (wheat, rice, cotton and potato), 100 % reductions in SE Asian anthropogenic NO_x emissions were predicted to produce the greatest reduction in

global crop production losses (46.6 to 95.2 % (42.3 to 94.4 % when corrected to account for model bias to observations)), based upon the AOT40, Mx and W126 metrics. Cuts to N American emissions resulted in the greatest global impact on crop yield reductions for maize and soybean (59.2 to 85.1 % (60.6 to 85.9 % bias corrected)). This results in an estimated increase in crop production of 8.0 to 9.7 Mt (8.8 to 10.6 Mt bias corrected). Model calculations suggested that reductions in anthropogenic NO_x emissions from N America provided the largest non-local effect, resulting in European production loss reductions of between 15.0 % and 63.2 % (14.2–63.1 % bias corrected), for a 100 % emissions cut. The impact on absolute crop production also showed that a reduction in N American NO_x emissions results in the greatest non-local contribution to production increases, enhancing production for wheat over Europe by approximately one third of the production increase produced by the local European emission cut. This is in agreement with previous work that has shown trans-Atlantic pollution transport to be more efficient compared with trans-Pacific and trans-Siberian transport. These results also demonstrate that local emissions control strategies have the potential to alleviate ozone-induced crop production loss in continents downstream, as well as effectively mitigating local ozone-induced yields losses. It was also estimated that for three of the world's most widely grown crops (wheat, maize and soybean) local air quality controls can significantly benefit crop production output.

Finally, the quantification of the trans-boundary effects was shown to differ depending the ozone damage metric used, and when the threshold-based indices such as AOT40 were used, the inferred long range transport contribution showed a strong dependence on the local ozone distribution. Overall however, the conclusions regarding the relative importance of the different regions in controlling crop production losses downstream were robust across the range of metrics used.

7.1.2 Aim 2: Quantify the impact of pre-industrial to present day land cover changes on the pre-industrial tropospheric ozone distribution and its radiative forcing.

The results presented in Chapter 5 indicate that the estimated pre-industrial tropospheric ozone distribution and associated radiative forcing of ozone is sensitive to the prescribed model vegetation distribution and its effects on the representation of dry deposition processes and isoprene emissions in a coupled chemistry-climate model.

Simulations using the HadGEM2-ES model indicated a pre-industrial ozone burden which ranged from 200.4 Tg to 220.9 Tg with the variation resulting from differences in the model land PFT distribution, the CO_2 mixing ratio the vegetation was exposed to and the model climate setup. The change in pre-industrial to present day ozone burden (present day burden of 292.9 Tg) ranged from 71.9 Tg to 92.5 Tg which agrees with the range presented in a recent study (Lamarque et al., 2005). This change in burden translates into a radiative forcing range of 0.227 Wm^{-2} to 0.244 Wm^{-2}. This radiative forcing range falls at the lower end of the IPCC AR4 estimate (0.25-0.65 Wm^{-2} (Forster et al., 2007)) though indicates a significant contribution of tropospheric ozone to the estimated total net radiative forcing since the pre-industrial period.

It was also shown in Chapter 5 that the responses of tropospheric ozone concentrations to land cover changes (a 1.6 % drop in mean global tropospheric ozone concentrations from a control simulation) were shown to be greater than responses to changes in the CO_2 mixing ratio that the model vegetation was exposed to (a 0.4 % rise from a control simulation). The responses of ozone concentrations were also shown to be dominated by the impacts of the changing isoprene emissions rather than changing dry deposition, agreeing with the findings of previous work.

Comparisons with available pre-industrial ozone observations indicated that the uncertainties associated with the representation of biosphere-atmosphere processes and the prescribed land coverage potentially contribute to the typical overestimation of such observations by models (Lamarque et al., 2005; Mickley et al., 2001).

Finally, simulations with HadGEM2-ES indicated that background surface ozone concentrations in more remote regions may be higher than currently estimated by previous pre-industrial model simulations which typically do not change the prescribed land use map between pre-industrial and present day model runs (Mickley et al., 2001). Using interactive isoprene emissions, when prescribed with a PFT distribution representative of 1865, the model simulates larger isoprene emissions over the tropics which enhances PAN formation. This results in greater transport of NO_y to remote regions releasing NO_x to enhance ozone formation.

7.1.3 Aim 3: Investigate the effects of ozone vegetation damage on tropospheric chemistry through its effects on dry deposition and isoprene emissions.

The findings presented in Chapter 6 indicated two major competing effects which control the response of surface ozone concentrations to ozone vegetation damage. When the impacts of ozone exposure were limited to the dry deposition of ozone and NO_y species, ozone was shown to have a self limiting effect on its own uptake leading to a positive feedback on ozone concentrations. Depending upon plant sensitivity to ozone exposure, the mean total global stomatal uptake was shown to decline by 0.22 to 0.42 $\mathrm{mmol O_3 m^{-2}}$ which results in a rise in average surface ozone concentrations of 0.02 to 0.03 ppbv with local increases of up to 14 ppbv (over parts of SE Asia). The reduced rate of uptake of NO_y species resulted in a build up of concentrations which led to enhanced ozone concentrations and further damage through ozone exposure setting up a positive feedback loop. These higher surface ozone concentrations were also shown to result in rises in the AOT40 metric of 1.68 %–3.49 % which translate into comparable increases in yield losses. On a regional scale increases in AOT40 and hence yield loss were shown to be as high as 4.24 % under high plant sensitivity. This therefore shows that the effects of ozone damage can have important implications for both regional and global air quality.

In competition with this effect, the reduction in the rate of photosynthesis due to ozone damage impacted the rate of isoprene emissions, with global total isoprene emissions shown to drop by 0.8 $\mathrm{TgC yr^{-1}}$ to 1.8 $\mathrm{TgC yr^{-1}}$ depending upon the plant sensitivity to ozone damage. In general this reduction in isoprene was shown to reduce ozone levels due to isoprene's role as a precursor species to ozone pollution. This effect was particularly evident over the more polluted regions of the Northern Hemisphere. However, it was shown over parts of the Amazon and Central Africa that the reduction in isoprene caused a slight rise in ozone concentrations due to isoprene's role as an ozone sink in less polluted regions.

The inclusion of both effects in model simulations resulted in an overall rise in surface ozone concentrations, with these increases shown to be more pronounced when plants had high sensitivity to ozone exposure. This demonstrates that the dry deposition impacts of ozone damage to plants were stronger than the effects due to the inhibition of isoprene emissions.

The results presented in Chapter 6 indicate the importance of representing the effects of ozone damage in global Earth system models as the increase in surface ozone levels due to reduced stomatal uptake not only results in a positive feedback through further vegetation damage but could also potentially feedback on the climate due to ozone's role as a greenhouse gas. Rising ozone levels can also have significant impacts on local air quality which can be detrimental to human health as well as vegetation (Fowler et al., 2008). Previous studies have also shown that isoprene not only plays a role in ozone chemistry but also plays an important role in the formation of secondary organic aerosol (SOA) (Claeys et al., 2004). Therefore the responses in isoprene emissions to the effects of ozone damage are also important to consider with this respect, as aerosols are known to have a cooling effect on the climate (Forster et al., 2007) and are also detrimental to air quality.

Finally, the reductions in stomatal flux due the effects of ozone damage are important to consider to understand how vegetation will adapt to future and warmer climates where the tropospheric ozone distribution is likely to change (Jacob et al., 1999). The effects on ozone stomatal flux are also important to understand as it is widely acknowledged that the impacts of ozone on plants are more closely related to the flux of ozone through the open stomata rather than exposure in the atmosphere (Emberson et al., 2000; Fuhrer et al., 1992; Musselman and Massman, 1999) and air quality standards are being developed with this in consideration.

7.2 Future work

The work performed in this thesis has also highlighted key areas that require further consideration in future work to investigate the interactions between tropospheric ozone and the biosphere. These include:

- In Chapter 4 it was highlighted that the effect of long range transport of ozone and its precursors on crop yields could be extended to incorporate flux-response relationships. These are important to consider as they consider the direct flux of ozone into the plant, mainly through the stomata, and can begin to account for modifying

environmental conditions and hence could be more applicable in different global regions and future climates (Harmens et al., 2007). These flux-response relationships will also be able to factor in the effects of ozone vegetation damage due to the direct modification of stomatal conductance by the effects of ozone exposure on the rates of photosynthesis. At present flux-response relationships exist for wheat, tomato and potato (Mills et al., 2011a; Pleijel et al., 2004), though these have not been parametrised for global application. However it would be useful to consider these relationships to understand the impacts of ozone damage on these crops under the present and indeed a future, warmer climate.

- In order to further the understanding of the effect changing model land cover has on pre-industrial tropospheric ozone concentrations it would be useful to investigate the sensitivity to changes in natural NO_x emissions sources associated with the land cover change. This would include the impact of land cover change on biomass burning and soil NO_x sources.

- It has been suggested that under chronic ozone exposure, the process of photosynthesis and stomatal conductance may not be as tightly correlated as previously thought (Lombardozzi et al., 2012). Chronic ozone exposure can often lead to sluggish stomatal responses due to loss of stomatal functioning and a decoupling of conductance from photosynthesis (Paoletti and Grulke, 2005; Tjoelker et al., 1995). This could therefore affect the responses of the stomatal uptake of ozone and other reactive trace gases to the effects of ozone damage. At present this mechanism has not been included online in coupled chemistry-climate models however it would be useful to investigate the effects of including this in future climate simulations. This is of particular importance because background levels of ozone are expected to continue to rise into the future (Cooper et al., 2010; Derwent et al., 2004) and there are expected to be less episodic pollution episodes where there is acute exposure to ozone and more chronic exposure of vegetation to higher ozone levels.

- A potential impact of ozone damage on isoprene emissions could be the feedback on atmospheric aerosol concentrations due to the role that isoprene plays in the formation of SOA (Claeys et al., 2004). Changes to atmospheric aerosol can impact cloud formation and subsequently impact the amount of incident shortwave radiation. As discussed by Pacifico et al. (2009) solar radiation plays an important role in

controlling the amount of emissions of isoprene from vegetation thus setting up a potential feedback loop. Changes to incident solar radiation will also have an impact on the rate of photolysis and thus the formation of ozone (Crutzen et al., 1999) which could potentially lead to impacts on ozone concentrations and further ozone damage to vegetation. Further work is required to investigate the effects of these isoprene-aerosol-photolysis interactions in order to compare these with the impacts of ozone damage on dry deposition of ozone and its precursor species.

- Finally, the inclusion of ozone damage parametrisations in HadGEM2-ES will enable the quantification of the effects of ozone damage on the hydrological cycle through the impacts on stomatal conductance and the resultant impacts on evapotranspiration and surface run-off rates. Therefore the response of the exchange of water vapour between the biosphere and atmosphere to ozone damage can allow a more accurate representation of the water cycle including atmospheric water vapour which is a key gas in regulating climate. This area requires more research to investigate the effects of ozone damage on the ability of vegetation to adapt to future warmer climates.

Appendix A

Supplementary Material

A.1 Intercontinental trans-boundary contributions to ozone-induced crop yield losses in the Northern Hemisphere

The following pages present supplementary figures for Section 4.5.2, in Chapter 4. The Figures show changes in model calculated AOT40 (for soybean, maize, cotton and potato growing seasons), M12 (for soybean and maize growing seasons) and W126 (for wheat growing season) under 100% NO_x emissions reductions over each of the Northern Hemisphere's major industrialized regions. See Chapter 4 for further information.

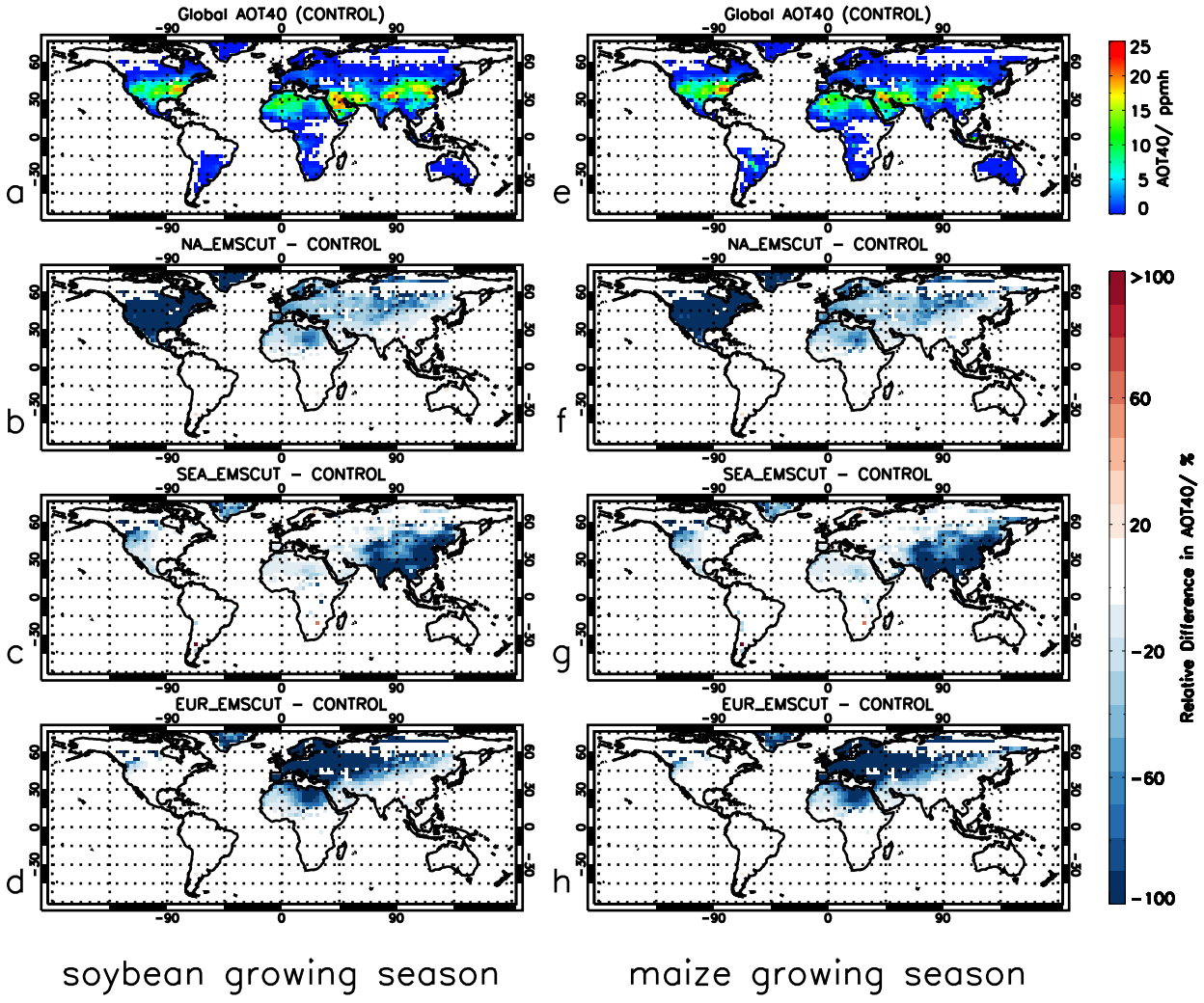

FIGURE A.1: **(a)** Global AOT40 under the control model scenario for the soybean growing season; and relative difference in AOT40 between the control model and 100 % cut in anthropogenic NO_x emissions from **(b)** N America, **(c)** SE Asia, and **(d)** Europe for the same period. Panels **(e–h)** show the same but for the maize growing season.

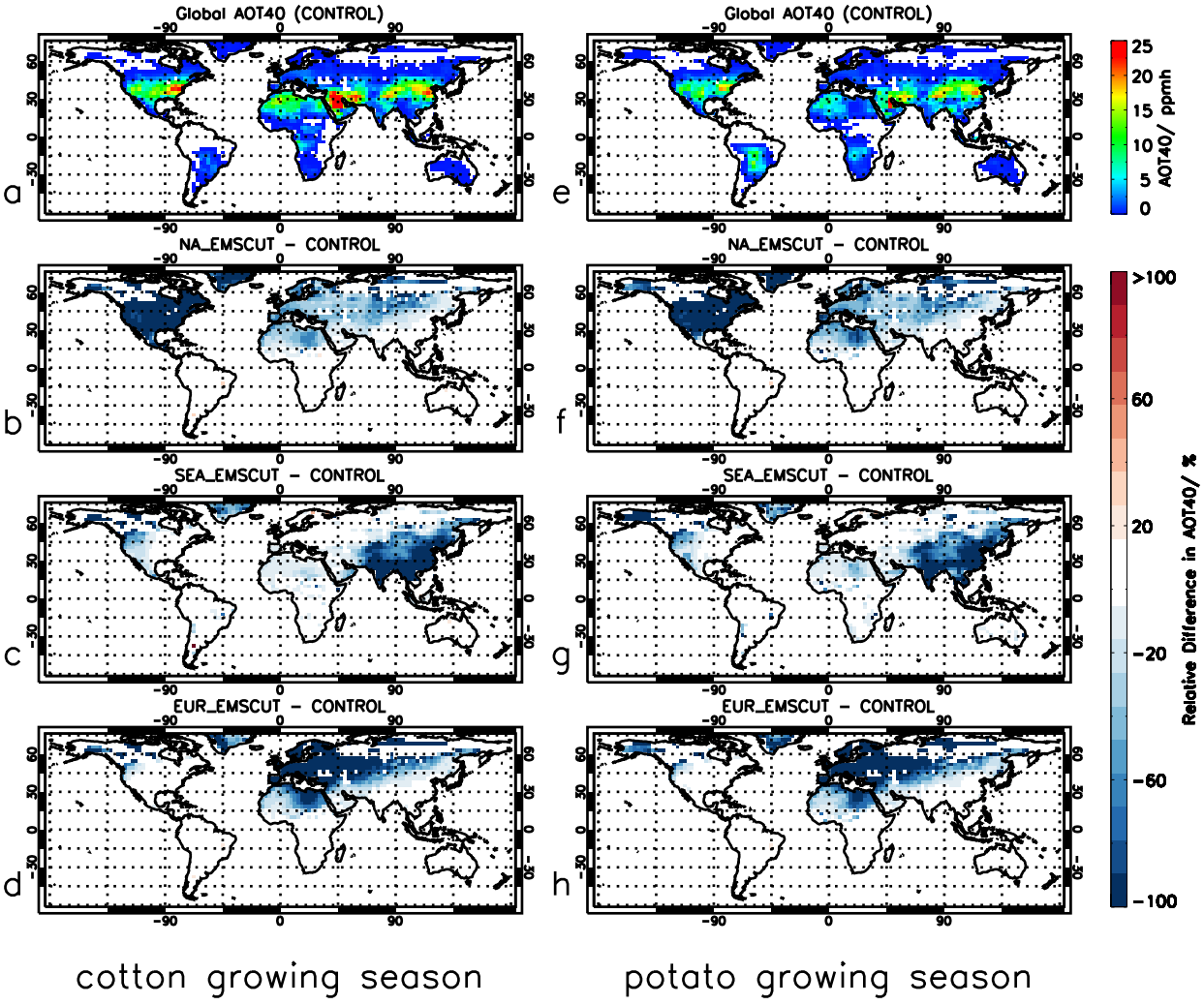

FIGURE A.2: As Figure A.1 but for cotton **(a–d)** and potato growing seasons **(e–h)**.

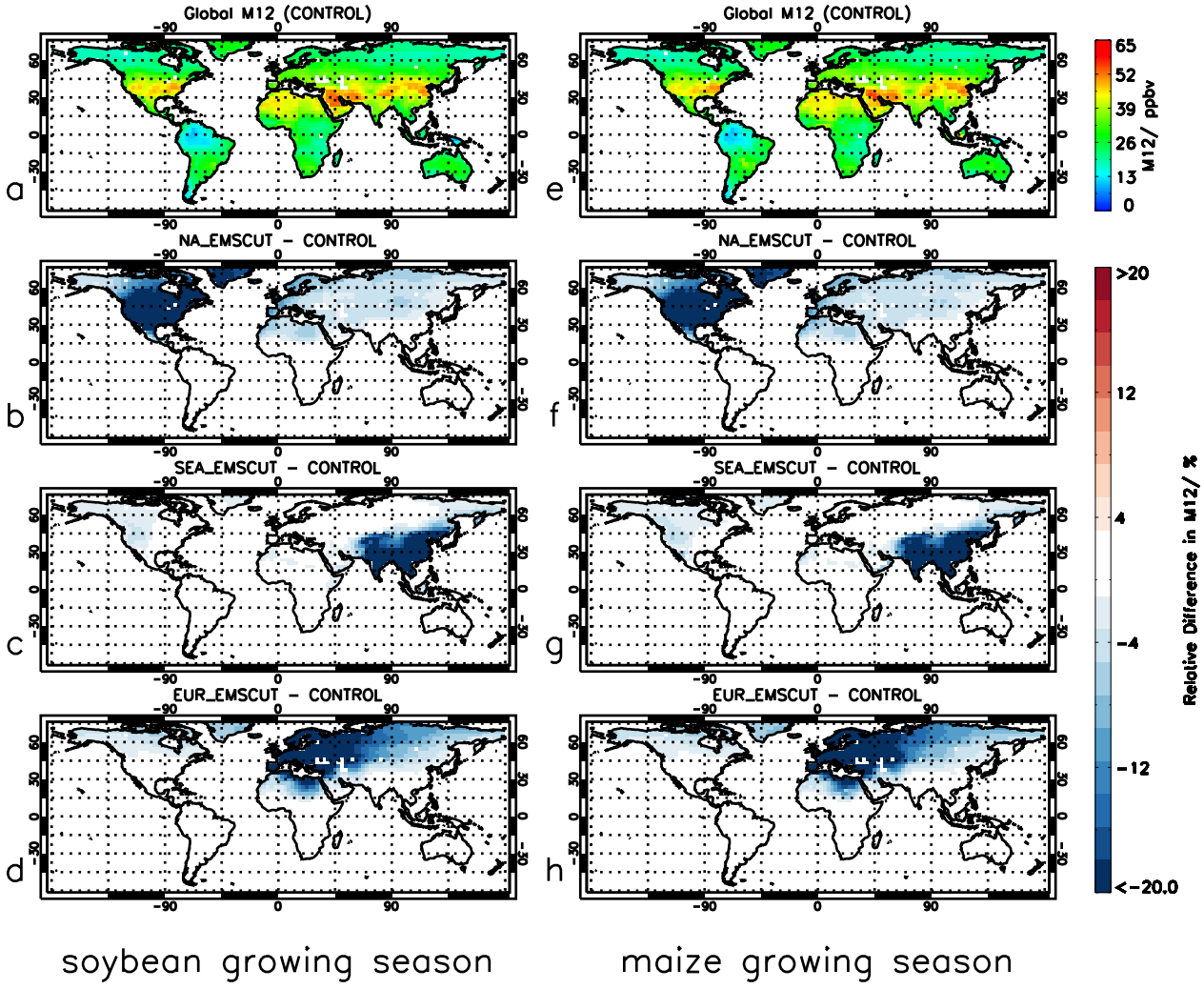

FIGURE A.3: As Figure A.1 but for M12 metric.

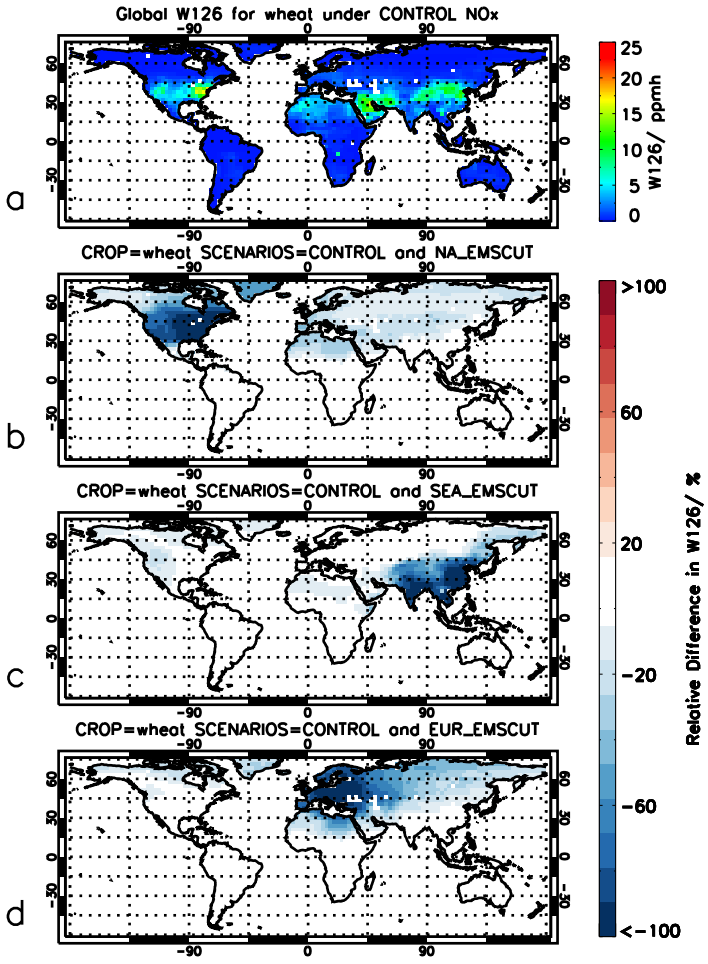

FIGURE A.4: As Figure A.1 but for W126 metric and wheat growing season **(a–d)**.

References

Abbot, D. S., P. I. Palmer, R. V. Martin, K. V. Chance, D. J. Jacob, and A. Guenther, 2003: Seasonal and interannual variability of North American isoprene emissions as determined by formaldehyde column measurements from space. *Geophysical Research Letters*, **30**, 1886.

Adams, R., T. Crocker, and N. Thanavibulchai., 1982: An economic assessment of air pollution damages to selected annual crops in southern California. *Journal of Environmental Economics and Management.*, **9**, 42–58.

Affek, H. and D. Yakir, 2002: Protection by isoprene against singlet oxygen in leaves. *Plant Physiology*, **129**, 269–277.

Andreae, M., 1991: Biomass burning - its history, use, and distribution and its impact on environmental-quality and global climate. *Global Biomass Burning: Atmospheric, Climatic, And Biospheric Implications*, J. Levine, ed., NASA; Natl. Sci. Fdn; US EPA; USDA, Forest Serv.; Int Geosphere Biosphre Programs; Int Global Atmosphere Chem Project, MIT Press, Cambridge, 3–21, chapman Conf on global Biomass Burning: Atmospheric, Climatic and Biospheric Implications, Williamsburg, VA, MAR 19–23, 1990.

Anfossi, D., S. Sandroni, and S. Viarengo, 1991: Tropospheric ozone in the 19th-century - the Moncalieri series. *Journal Of Geophysical Research-Atmospheres*, **96**, 17349–17352.

Arneth, A., R. Monson, G. Schurgers, U. Niinemets, and P. Palmer, 2008: Why are estimates of global isoprene emissions so similar (and why is this not so for monoterpenes)? *Atmospheric Chemistry And Physics*, **8**, 4605–4620.

Arneth, A., U. Niinemets, S. Pressley, J. Bäck, P. Hari, T. Karl, S. Noe, I. C. Prentice, D. Serça, T. Hickler, A. Wolf, and B. Smith, 2007: Process-based estimates of terrestrial ecosystem isoprene emissions: incorporating the effects of a direct CO_2-isoprene interaction. *Atmospheric Chemistry and Physics*, **7**, 31–53, doi:10.5194/acp-7-31-2007.

Arnold, S., M. Chipperfield, and M. Blitz, 2005: A three-dimensional model study of the effect of new temperature-dependent quantum yields for acetone photolysis. *Geophysical Research-Atmospheres*, **110**, D22305.

Ashmore, M., 2005: Assessing the future global impacts of ozone on vegetation. *Plant, Cell and Environment*, **28**, 949–964.

Atkinson, R. and J. Arey, 2003: Gas-phase tropospheric chemistry of biogenic volatile organic compounds: a review. *Atmospheric Environment*, **37**, S197–S219.

Aunan, K., T. Bernsten, and H. Seip, 2000: Surface ozone in China and its possible impact on agricultural crop yields. *Ambio*, **29**, 294–301.

Avnery, S., D. Mauzerall, J. Liu, and L. Horowitz, 2011a: Global crop yield reductions due to surface ozone exposure: 1. Year 2000 crop production losses and economic damage. *Atmospheric Environment*, **45**, 2284–2296, doi:10.1016/j.atmosenv.2011.01.045.

— 2011b: Global crop yield reductions due to surface ozone exposure: 2. Year 2030 potential cro production losses and economic damage under two scenarios of O_3 pollution. *Atmospheric Environment*, **45**, 2297–2309, doi:10.1016/j.atmosenv.2011.01.002.

Avol, E. L., W. C. Navidi, E. B. Rappaport, and J. M. Peters, 1998: Acute effects of ambient ozone on asthmatic, wheezy, and healthy children. *Research report (Health Effects Institute)*, 1–18;.

Bala, G., K. Caldeira, M. Wickett, T. J. Phillips, D. B. Lobell, C. Delire, and A. Mirin, 2007: Combined climate and carbon-cycle effects of large-scale deforestation. *Proceedings Of The National Academy Of Sciences Of The United States Of America*, **104**, 6550–6555.

Bell, M. L., F. Dominici, and J. M. Samet, 2005: A meta-analysis of time-series studies of ozone and mortality with comparison to the national morbidity, mortality, and air pollution study. *Epidemiology*, **16**, 436–445.

Bell, M. L., A. McDermott, S. L. Zeger, J. M. Samet, and F. Dominici, 2004: Ozone and short-term mortality in 95 US urban communities, 1987-2000. *Jama-Journal Of The American Medical Association*, **292**, 2372–2378.

Bellouin, N., J. Rae, A. Jones, C. Johnson, J. Haywood, and O. Boucher, 2011: Aerosol forcing in the climate model intercomparison project (CMIP5) simulations by HadGEM2-ES and the role of ammonium nitrate. *Journal Of Geophysical Research-Atmospheres*, **116**, D20206.

Bernacchi, C., A. Leakey, B. Kimball, and D. Ort, 2011: Growth of soybean at future tropospheric ozone concentrations decreases canopy evapotranspiration and soil water depletion. *Environmental Pollution*, **159**, 1464 –1472.

Bernsten, T. and I. Isaksen, 1997: A global three-dimensional chemical transport model for the troposphere 1. Model description and CO and ozone results. *Journal of Geophysical Research-Atmospheres*, **102**, 21239–21280.

Bonan, G. B., 2008: Forests and climate change: Forcings, feedbacks, and the climate benefits of forests. *Science*, **320**, 1444–1449.

Bonan, G. B., S. Levis, L. Kergoat, and K. W. Oleson, 2002: Landscapes as patches of plant functional types: An integrating concept for climate and ecosystem models. *Global Biogeochemical Cycles*, **16**, 1021.

Brasseur, G. P., J. T. Kiehl, J. F. Muller, T. Schneider, C. Granier, X. X. Tie, and D. Hauglustaine, 1998: Past and future changes in global tropospheric ozone: Impact on radiative forcing. *Geophysical Research Letters*, **25**, 3807–3810.

Butler, T. M., D. Taraborrelli, C. B. H. Fischer, H. Harder, M. Martinez, J. Williams, M. G. Lawrence, and J. Lelieveld, 2008: Improved simulation of isoprene oxidation chemistry with the ECHAM5/MESSy chemistry-climate model: lessons from the GABRIEL airborne field campaign. *Atmospheric Chemistry And Physics*, **8**, 4529–4546.

Byvoet, P., J. Balis, S. Shelley, M. Montgomery, and M. Barber, 1995: Detection of hydroxyl radicals upon interaction of ozone with aqueous-media or extracellular surfactant - the role of trace iron. *Archives Of Biochemistry And Biophysics*, **319**, 464–469.

Calfapietra, C., G. Mugnozza, D. Karnosky, F. Loreto, and T. Sharkey, 2008: Isoprene emissions rates under elevated CO_2 and O_3 in two field-grown aspen clones differing in their sensitivity to O_3. *New Phytologist*, **179**, 55–61.

Carslaw, N., D. J. Creasey, D. Harrison, D. E. Heard, M. C. Hunter, P. J. Jacobs, M. E. Jenkin, J. D. Lee, A. C. Lewis, M. J. Pilling, S. M. Saunders, and P. W. Seakins, 2001: OH and HO2 radical chemistry in a forested region of north-western greece. *Atmospheric Environment*, **35**, 4725–4737.

Carver, G., P. Brown, and O. Wild, 1997: The ASAD atmospheric chemistry integration package and chemical reaction database. *Computer Physics Communications*, **105**, 197–215.

Chaves, M. M., J. P. Maroco, and J. S. Pereira, 2003: Understanding plant responses to drought - from genes to the whole plant. *Functional Plant Biology*, **30**, 239–264.

Chipperfield, M. P., 2006: New version of the TOMCAT/SLIMCAT off-line chemical transport model: Intercomparison of stratospheric tracer experiments. *Quarterly Journal Of The Royal Meteorological Society*, **132**, 1179–1203.

Claeys, M., B. Graham, G. Vas, W. Wang, R. Vermeylen, V. Pashynska, J. Cafmeyer, P. Guyon, M. Andreae, P. Artaxo, and W. Maenhaut, 2004: Formation of secondary aerosols through photooxidation of isoprene. *Science*, **303**, 1173–1176.

Collins, W. J., N. Bellouin, M. Doutriaux-Boucher, N. Gedney, P. Halloran, T. Hinton, J. Hughes, C. D. Jones, M. Joshi, S. Liddicoat, G. Martin, F. O'Connor, J. Rae, C. Senior, S. Sitch, I. Totterdell, A. Wiltshire, and S. Woodward, 2011: Development and evaluation of an Earth-System model - HadGEM2. *Geoscientific Model Development*, **4**, 1051–1075, doi:10.5194/gmd-4-1051-2011.

Cooper, O. R., D. D. Parrish, A. Stohl, M. Trainer, P. Nedelec, V. Thouret, J. P. Cammas, S. J. Oltmans, B. J. Johnson, D. Tarasick, T. Leblanc, I. S. McDermid, D. Jaffe, R. Gao, J. Stith, T. Ryerson, K. Aikin, T. Campos, A. Weinheimer, and M. A. Avery, 2010: Increasing springtime ozone mixing ratios in the free troposphere over western North America. *Nature*, **463**, 344–348.

Cox, P., 2001: Description of the "TRIFFID" dynamic global vegetation model. Hadley Centre Tech. Note 24, Met Office, Bracknell, United Kingdom, 17 pp. [Available online at www.metoffice.gov.uk/research/hadleycentre/pubs/HCTN/HCTN_24.pdf].

Cox, P., R. Betts, C. Bunton, R. Essery, P. Rowntree, and J. Smith, 1999: The impact of new land surface physics on the GCM simulation of climate and climate sensitivity. *Climate Dynamics*, **15**, 183–203.

Cox, P. M., R. A. Betts, C. D. Jones, S. A. Spall, and I. J. Totterdell, 2000: Acceleration of global warming due to carbon-cycle feedbacks in a coupled climate model. *Nature*, **408**, 184–187.

Cox, P. M., C. Huntingford, and R. J. Harding, 1998: A canopy conductance and photosynthesis model for use in a GCM land surface scheme. *Journal Of Hydrology*, **212**, 79–94.

Crutzen, P., M. Lawrence, and U. Poschl, 1999: On the background photochemistry of tropospheric ozone. *Tellus Series A-Dynamic Meteorology and Oceanography*, **51**, 123–146.

Davies, T., M. Cullen, A. Malcolm, M. Mawson, A. Staniforth, A. White, and N. Wood, 2005: A new dynamical core for the Met Office's global and regional modelling of the atmosphere. *Quarterly Journal Of The Royal Meteorological Society*, **131**, 1759–1782.

Delwiche, C. and T. Sharkey, 1993: Rapid appearance of 13C in biogenic isoprene when $13CO_2$ is fed into intact leaves. *Plant Cell Environment*, **16**, 587–591.

Denman, K., G. Brasseur, A. Chidthaisong, P. Ciais, P. Cox, R. Dickinson, D. Hauglustaine, H. C., E. Holland, D. Jacob, U. Lohmann, S. Ramachandran, P. da Silva Dias, S. Wofsy, and X. Zhang, 2007: Couplings between changes in the climate system and biogeochemistry. *Climate Change 2007: The Physical Science Basis. Contribution of Working Group I to the Fourth Assessment Report of the Intergovernmental Panel on Climate Change.*, D. Solomon, S. amd Qin, M. Manning, Z. Chen, M. Marquis, K. Averyt, M. Tignor, and H. Miller, eds., Cambridge University Press, Cambridge, United Kingdom and New York, NY, USA., 499–587.

Dentener, F., T. Keating, and H. Akimoto, 2010: (eds.) Hemispheric transport of air pollution. Part a: Ozone and particulate matter. Economic Commission For Europe, United Nations, Geneva.

Derwent, R., D. Stevenson, W. Collins, and C. Johnson, 2004: Intercontinental transport and the origins of the ozone observed at surface sites in Europe. *Atmospheric Environment*, **38**, 1891–1901.

Duncan, B. and I. Bey, 2004: A modeling study of the export pathways of pollution from Europe: Seasonal and interannual variations (1987-1997). *Journal of Geophysical Research-Atmospheres*, **109**, D08301.

Ederli, L., S. Pasqualini, P. Batini, and M. Antonielli, 1997: Photoinhibition and oxidative stress: effects on xanthophyll cycle, scavenger enzymes and abscisic acid content in tobacco plants. *Journal Of Plant Physiology*, **151**, 422–428.

Edwards, J. M. and A. Slingo, 1996: Studies with a flexible new radiation code .1. choosing a configuration for a large-scale model. *Quarterly Journal Of The Royal Meteorological Society*, **122**, 689–719.

EEA, 1999: Environmental assessment report No. 2. Environment in the European Union at the turn of the century. European Environment Agency, Copenhagen, 446pp.

Emberson, L. D., P. Bueker, M. R. Ashmore, G. Mills, L. S. Jackson, M. Agrawal, M. D. Atikuzzaman, S. Cinderby, M. Engardt, C. Jamir, K. Kobayashi, N. T. K. Oanh, Q. F. Quadir, and A. Wahid, 2009: A comparison of North American and Asian exposure-response data for ozone effects on crop yields. *Atmospheric Environment*, **43**, 1945–1953.

Emberson, L. D., G. Wieser, and M. R. Ashmore, 2000: Modelling of stomatal conductance and ozone flux of Norway spruce: comparison with field data. *Environmental Pollution*, **109**, 393–402.

Emmons, L., D. Hauglustaine, J.-F. Muller, M. Carroll, G. Brasseur, D. Brunner, J. Staehelin, V. Thouret, and A. Marenco, 2000: Data composites of airborne observations of tropospheric ozone and its precursors. *Journal of Geophysical Research - Atmospheres*, **105**, 20497–20538.

Emmons, L. K., S. Walters, P. G. Hess, J. F. Lamarque, G. G. Pfister, D. Fillmore, C. Granier, A. Guenther, D. Kinnison, T. Laepple, J. Orlando, X. Tie, G. Tyndall,

C. Wiedinmyer, S. L. Baughcum, and S. Kloster, 2010: Description and evaluation of the Model for Ozone and Related chemical Tracers, version 4 (MOZART-4). *Geoscientific Model Development*, **3**, 43–67.

Essery, R., M. Best, and P. Cox, 2001: MOSES 2.2 technical documentation. Hadley Centre Tech, Note 30, Met Office, Bracknell, United Kingdom, 30 pp. [Available online at www.metoffice.gov.uk/research/hadleycentre/pubs/HCTN/HCTN_30.pdf].

Essery, R. L. H., M. J. Best, R. A. Betts, P. M. Cox, and C. M. Taylor, 2003: Explicit representation of subgrid heterogeneity in a GCM land surface scheme. *Journal Of Hydrometeorology*, **4**, 530–543.

Farage, P., S. Long, L. E.G., and N. Baker, 1991: The sequence of change within the photosynthetic apparatus of wheat following short-term exposure to ozone. *Plant Physiology (Rockville)*, **95**, 529–535.

FederalRegister, 2008: No. 60. national ambient air quality standards for ozone. Vol. 73. Federal Register. March 27, 200816436-16512.

Felzer, B., J. Reilly, J. Melillo, D. Kicklighter, M. Sarofim, C. Wang, R. Prinn, and Q. Zhuang, 2005: Future effects of ozone on carbon sequestration and climate change policy using a global biogeochemical model. *Climate Change*, **73**, 345–373.

Field, C., R. Jackson, and H. Mooney, 1995: Stomatal responses to increased CO_2: implications from the plant to the global-scale. *Plant Cell Environment*, **18**, 1214–1255.

Fiore, A. M., F. J. Dentener, O. Wild, C. Cuvelier, M. G. Schultz, P. Hess, C. Textor, M. Schulz, R. M. Doherty, L. W. Horowitz, I. A. MacKenzie, M. G. Sanderson, D. T. Shindell, D. S. Stevenson, S. Szopa, R. Van Dingenen, G. Zeng, C. Atherton, D. Bergmann, I. Bey, G. Carmichael, W. J. Collins, B. N. Duncan, G. Faluvegi, G. Folberth, M. Gauss, S. Gong, D. Hauglustaine, T. Holloway, I. S. A. Isaksen, D. J. Jacob, J. E. Jonson, J. W. Kaminski, T. J. Keating, A. Lupu, E. Marmer, V. Montanaro, R. J. Park, G. Pitari, K. J. Pringle, J. A. Pyle, S. Schroeder, M. G. Vivanco, P. Wind, G. Wojcik, S. Wu, and A. Zuber, 2009: Multimodel estimates of intercontinental source-receptor relationships for ozone pollution. *Journal of Geophysical Research-Atmospheres*, **114**, D04301.

Fiscus, E. L., F. L. Booker, and K. O. Burkey, 2005: Crop responses to ozone: uptake, modes of action, carbon assimilation and partitioning. *Plant Cell And Environment*, **28**, 997–1011.

Flexas, J., M. Ribas-Carbo, A. Diaz-Espejo, J. Galmes, and H. Medrano, 2008: Mesophyll conductance to CO_2: current knowledge and future prospects. *Plant Cell And Environment*, **31**, 602–621.

Folberth, G., D. Hauglustaine, J. Lathiere, and F. Brocheton, 2006: Interactive chemistry in the Laboratoire de Meteorologie Dynamique general circulation model: model descirption and impact analysis of biogenic hydrocarbons on tropsopheric chemistry. *Atmospheric Chemistry And Physics*, **6**, 2273–2319.

Forster, P., V. Ramaswamy, P. Artaxo, T. Berntsen, R. Betts, D. Fahey, J. Haywood, J. Lean, D. Lowe, G. Myhre, J. Nganga, R. Prinn, G. Raga, M. Schulz, and R. V. Dorland, 2007: Changes in Atmospheric Constituents and in Radiative Forcing. *Climate Change 2007: The Physical Science Basis. Contribution of Working Group I to the Fourth Assessment Report of the Intergovernmental Panel on Climate Change*, S. Solomon, D. Qin, M. Manning, Z. Chen, M. Marquis, K. Averyt, M.Tignor, and H. Miller, eds., Cambridge University Press, Cambridge, United Kingdom and New York, NY, USA.

Fowler, D., M. Amann, R. Anderson, M. Ashmore, P. Cox, M. Depledge, D. Derwent, P. Grennfelt, N. Hewitt, O. Hov, M. Jenkin, F. Kelly, P. Liss, M. Pilling, J. Pyle, J. Slingo, and D. Stevenson, 2008: (eds.) ground level ozone in the 21st century: Future trends, impacts and policy implications. RS Policy Document 15/08. ISBN: 978-0-85403-713-1.

Franzaring, J., P. Hoegy, and A. Fangmeier, 2008: Effects of free-air CO_2 enrichment on the growth of summer oilseed rape (brassica napus cv. campino). *Agriculture Ecosystems & Environment*, **128**, 127–134.

Fuhrer, J., 2009: Ozone risk for crops and pastures in present and future climates. *Naturwissenschaften*, **96**, 173–194.

Fuhrer, J. and B. Achermann, 1994: Critical Levels for Ozone: A UN-ECE Workshop Report. *Critical Levels for Ozone: A UN-ECE Workshop Report.*, Liebefeld-Bern, Switzerland. Nr. 16.

Fuhrer, J., A. Grimm, W. Tschannen, and H. Shariatmadari, 1992: The response of spring wheat (Triticum-Aestivum L) to ozone at higher elevations .2. changes in yield, yield components and grain quality in response to ozone flux. *New Phytologist*, **121**, 211–219.

Galbally, I. and C. Roy, 1980: Destruction of ozone at the Earth's surface. *Quarterly Journal Of The Royal Meteorological Society*, **106**, 599–620.

Ganzeveld, L., L. Bouwman, E. Stehfest, D. P. van Vuuren, B. Eickhout, and J. Lelieveld, 2010: Impact of future land use and land cover changes on atmospheric chemistry-climate interactions. *Journal Of Geophysical Research-Atmospheres*, **115**, D23301.

Ganzeveld, L., G. Eerdekens, G. Feig, H. Fischer, H. Harder, R. Konigstedt, D. Kubistin, M. Martinez, F. X. Meixner, H. A. Scheeren, V. Sinha, D. Taraborrelli, J. Williams, J. V.-G. de Arellano, and J. Lelieveld, 2008: Surface and boundary layer exchanges of volatile organic compounds, nitrogen oxides and ozone during the GABRIEL campaign. *Atmospheric Chemistry And Physics*, **8**, 6223–6243.

Ganzeveld, L. and J. Lelieveld, 1995: Dry deposition parameterization in a chemistry general circulation model and its influence on the distribution of reactive trace gases. *Journal of Geophysical Research - Atmospheres*, **100**, 20999–21012.

Gauss, M., G. Myhre, I. S. A. Isaksen, V. Grewe, G. Pitari, O. Wild, W. J. Collins, F. J. Dentener, K. Ellingsen, L. K. Gohar, D. A. Hauglustaine, D. Iachetti, J. F. Lamarque, E. Mancini, L. J. Mickley, M. J. Prather, J. A. Pyle, M. G. Sanderson, K. P. Shine, D. S. Stevenson, K. Sudo, S. Szopa, and G. Zeng, 2006: Radiative forcing since preindustrial times due to ozone change in the troposphere and the lower stratosphere. *Atmospheric Chemistry And Physics*, **6**, 575–599.

Gedney, N., P. Cox, R. Betts, O. Boucher, C. Huntingford, and P. Stott, 2006: Detection of a direct carbon dioxide effect in continental river runoff records. *Nature*, **439**, 835–838.

Gedney, N., P. M. Cox, and C. Huntingford, 2004: Climate feedback from wetland methane emissions. *Geophysical Research Letters*, **31**, L20503.

Giannakopoulos, C., 1998: *Modelling the impact of physical and removal processes on tropospheric chemistry*. Ph.D. thesis, University of Cambridge, Cambridge, England.

Giannakopoulos, C., T. P. Chipperfield, K. S. Law, and J. A. Pyle, 1999: Validation and intercomparison of wet and dry deposition schemes using Pb-210 in a global

three-dimensional off-line chemical transport model. *Journal Of Geophysical Research-Atmospheres*, **104**, 23761–23784.

Giorgi, F. and W. L. Chameides, 1985: The rainout parameterization in a photochemical model. *Journal Of Geophysical Research-Atmospheres*, **90**, 7872–7880.

Greenberg, J., A. Guo, D. Klessig, and F. Ausubel, 1994: Programmed cell-death in plants - a pathogen-triggered response activated coordinately with multiple defense functions. *Cell*, **77**, 551–563.

Greenberg, J. P., A. B. Guenther, G. Petron, C. Wiedinmyer, O. Vega, L. V. Gatti, J. Tota, and G. Fisch, 2004: Biogenic VOC emissions from forested Amazonian landscapes. *Global Change Biology*, **10**, 651–662.

Guenther, A., C. Hewitt, D. Erickson, R. Fall, C. Geron, T. Graedel, P. Harley, L. Klinger, M. Lerdau, W. McKay, T. Pierce, B. Scholes, R. Steinbrecher, R. Tallamraju, J. Taylor, and P. Zimmerman, 1995: A global model of natural organic compound emissions. *Journal of Geophysical Research-Atmospheres*, **100**, 8873–8892.

Guenther, A., T. Karl, P. Harley, C. Wiedinmyer, P. Palmer, and C. Geron, 2006: Estimates of global terrestrial isoprene emissions using MEGAN (Model of Emissions of Gases and Aerosols from Nature). *Atmospheric Chemistry And Physics*, **6**, 3181–3210.

Guenther, A., P. Zimmerman, P. Harley, R. Monson, and R. Fall, 1993: Isoprene and monoterpene emission rate variability - model evaluations and sensitivity analyses. *Journal Of Geophysical Research-Atmospheres*, **98**, 12609–12617.

Hao, W., M. Liu, and P. Crutzen, 1990: Estimates of annual and regional releases of CO_2 and other trace gases to the atmosphere from fires in the tropics, based on the FAO statistics for the period 1975–1980. *Fire in the Tropical Biota: Ecosystem Processes and Global Challenges*, J. Goldammer, ed., Volkswagen Fdn., Springer–Verlag, New York, volume 84 of *Ecological Studies: Analysis and Synthesis*, 440–462, 3rd Symp. on Fire Ecology, Freiburg Univ., Freiburg Breisgau, Fed Rep Ger., May, 1989.

Harley, P., R. Monson, and M. Lerdau, 1999: Ecological and evolutionary aspects of isoprene emission from plants. *Oecologia*, **118**, 109–123.

Harmens, H., G. Mills, L. D. Emberson, and M. R. Ashmore, 2007: Implications of climate change for the stomatal flux of ozone: A case study for winter wheat. *Environmental Pollution*, **146**, 763–770.

Hauglustaine, D. A. and G. P. Brasseur, 2001: Evolution of tropospheric ozone under anthropogenic activities and associated radiative forcing of climate. *Journal Of Geophysical Research-Atmospheres*, **106**, 32337–32360.

Heagle, A. S., 1989: Ozone and crop yield. *Annual Review Of Phytopathology*, **27**, 397–423.

Heald, C. L., M. J. Wilkinson, R. K. Monson, C. A. Alo, G. Wang, and A. Guenther, 2009: Response of isoprene emission to ambient CO_2 changes and implications for global budgets. *Global Change Biology*, **15**, 1127–1140.

Heck, W. and E. Colwing, 1997: The need for a long term cumulative secondary ozone standard - an ecological perspective. Environmental Manager January.

Heck, W., W. Cure, J. Rawlings, L. Zaragoza, A. Heagle, H. Heggestad, R. Kohut, L. Kress, and P. Temple, 1984: Assessing impacts of ozone on agricultural crops .2. crop yield functions and alternative exposure statistics. *Journal Of The Air Pollution Control Association*, **34**, 810–817.

Hofzumahaus, A., F. Rohrer, K. Lu, B. Bohn, T. Brauers, C.-C. Chang, H. Fuchs, F. Holland, K. Kita, Y. Kondo, X. Li, S. Lou, M. Shao, L. Zeng, A. Wahner, and Y. Zhang, 2009: Amplified trace gas removal in the troposphere. *Science*, **324**, 1702–1704.

Holland, M., G. Mills, F. Hayes, A. Buse, L. Emberson, H. Cambridge, S. Cinderby, A. Terry, and M. Ashmore, 2002: Economic assessment of crop yield losses from ozone exposure. report to UK Department of Environment, Food and Rural Affairs under contract 1/2/170. Centre for Ecology and Hydrology, Bangor.

Holstag, A. A. M. and B. A. Boville, 1993: Local versus nonlocal boundary-layer diffusion in a global climate model. *Journal Of Climate*, **6**, 1825–1842.

Hough, A., 1988: The calculation of photolysis rates for use in global tropospheric modelling studies. *AERE Rep. R-13259*, H.M. Stationary Office, London.

Hudman, R., D. Jacob, O. Cooper, M. Evans, C. Heald, R. Park, F. Fehsenfeld, F. Flocke, J. Holloway, G. Hubler, K. Kita, M. Koike, Y. Kondo, A. Neuman, J. Nowak, S. Oltmans, D. Parrish, J. Roberts, and T. Ryerson, 2004: Ozone production in transpacific Asian pollution plumes and implications for ozone air quality in California. *Journal of Geophysical Research-Atmospheres*, **109**, D23S10.

Hurtt, G., L. Chini, S. Frolking, R. Betts, J. Feddema, G. Fischer, J. Fisk, K. Hibbard, R. A. Houghton, A. Janetos, C. Jones, G. Kindermann, T. Kinoshita, K. Klein Goldewijk, K. Riahi, E. Shevliakova, S. Smith, E. Stehfest, A. Thomson, P. Thornton, D. van Vuuren, and Y. Wang, 2011: Harmonization of Land-Use scenarios for the Period 1500-2100:600 Years of Global Gridded Annual Land-Use Transitions, Wood Harvest and Resulting Secondary Lands. *Climatic Change*, **109**, 117–161.

IPCC, 2007: Summary for Policymakers. *Climate Change 2007: The Physical Science Basis. Contribution of Working Group I to the Fourth Assessment Report of the Intergovernmental Panel on Climate Change*, S. Solomon, D. Qin, M. Manning, Z. Chen, M. Marquis, K. Averyt, M. Tignor, and H. Miller, eds., Cambridge University Press, Cambridge, United Kingdom and New York, NY, USA.

Jacob, D., 1999: *Introduction to Atmospheric Chemistry*. Princeton University Press, Princeton, New Jersey, USA.

Jacob, D., J. Logan, and P. Murti, 1999: Effect of rising Asian emissions on surface ozone in the United States. *Geophysical Research Letters*, **26**, 2175–2178.

Jacobson, M., 2002: *Atmospheric Pollution: History, Science and Regulation*. Cambridge University Press, Cambridge, United Kingdom and New York, NY, USA.

Jaffe, D., 2011: Relationship between surface and free tropospheric ozone in the western U.S. *Environmental Science & Technology*, **45**, 432–438.

Jager, H., M. Unsworth, L. De Temmerman, and P. Mathy, 1992: Effects of air pollutants on agricultural crops in europe, results of the european open-top chambers project. in: Air pollution research report no. 46. Number 46, directorate-General for Science, Research and Development, Brussels, Belgium. Report No. 46.

— 1996: Effects of Air Pollutants on Agricultural crops in Europe: results of the European Open-Top chambers project. Air Pollution Series of the Environmental Research

Programme of the Commission of the European Communities, Directorate-General for Science, Research and Development, Brussels, Belgium. Report No. 46.

Jenkin, M., S. Saunders, and P. M.J., 1997: The tropospheric degradation of volatile organic compounds: A protocol for mechanism development. *Atmospheric Environment*, **31**, 81–104.

Johns, T., C. Durman, H. Banks, M. Roberts, A. McLaren, J. Ridley, C. Senior, K. Williams, A. Jones, G. Rickard, S. Cusack, W. Ingram, M. Curucifix, D. Sexton, M. Joshi, B.-W. Dong, H. Spencer, R. Hill, J. Gregory, A. Keen, A. Pardaens, J. Lowe, A. Bodas-Salcedo, S. Stark, and Y. Searl, 2006: The New Hadley Centre Climate Model (HadGEM1): Evaluation of Coupled Simulations. *Journal Of Climate*, **19**, 1327–1353.

Jones, C. D., J. K. Hughes, N. Bellouin, S. C. Hardiman, G. S. Jones, J. Knight, S. Liddicoat, F. M. O'Connor, R. J. Andres, C. Bell, K.-O. Boo, A. Bozzo, N. Butchart, P. Cadule, K. D. Corbin, M. Doutriaux-Boucher, P. Friedlingstein, J. Gornall, L. Gray, P. R. Halloran, G. Hurtt, W. J. Ingram, J.-F. Lamarque, R. M. Law, M. Meinshausen, S. Osprey, E. J. Palin, L. Parsons Chini, T. Raddatz, M. G. Sanderson, A. A. Sellar, A. Schurer, P. Valdes, N. Wood, S. Woodward, M. Yoshioka, and M. Zerroukat, 2011: The HadGEM2-ES implementation of CMIP5 centennial simulations. *Geoscientific Model Development*, **4**, 543–570, doi:10.5194/gmd-4-543-2011.

Jones, H. G., 1998: Stomatal control of photosynthesis and transpiration. *Journal Of Experimental Botany*, **49**, Soc Exptl Biol.

Karl, T., A. Guenther, R. J. Yokelson, J. Greenberg, M. Potosnak, D. R. Blake, and P. Artaxo, 2007: The tropical forest and fire emissions experiment: Emission, chemistry, and transport of biogenic volatile organic compounds in the lower atmosphere over Amazonia. *Journal Of Geophysical Research-Atmospheres*, **112**, D18302.

Karlsson, P. E., J. Uddling, S. Braun, M. Broadmeadow, S. Elvira, B. S. Gimeno, D. Le Thiec, E. Oksanen, K. Vandermeiren, M. Wilkinson, and L. Emberson, 2004: New critical levels for ozone effects on young trees based on AOT40 and simulated cumulative leaf uptake of ozone. *Atmospheric Environment*, **38**, UNECE.

Karnosky, D. F., K. S. Pregitzer, D. R. Zak, M. E. Kubiske, G. R. Hendrey, D. Weinstein, M. Nosal, and K. E. Percy, 2005: Scaling ozone responses of forest trees to the ecosystem level in a changing climate. *Plant Cell And Environment*, **28**, 965–981.

Kiehl, J. T., T. L. Schneider, R. W. Portmann, and S. Solomon, 1999: Climate forcing due to tropospheric and stratospheric ozone. *Journal Of Geophysical Research-Atmospheres*, **104**, 31239–31254.

Klein Goldewijk, K., A. Beusen, and P. Janssen, 2010: Long term dynamic modelling of global population and built-up area in a spatially explicit way: HYDE 3.1. *Holocene*, **20**, 565–573.

Kley, D., A. Volz, and F. Mülheims, 1988: Ozone measurements in historic perspective. *Tropospheric Ozone: Regional and Global Interactions*, I. S. A. Isaksen, ed., D. Reidel, Norwell, Mass., 63–72.

Krol, M., P. J. van Leeuwen, and J. Lelieveld, 1998: Global OH trend inferred from methylchloroform measurements. *Journal Of Geophysical Research-Atmospheres*, **103**, 10697–10711.

Krupa, S., M. Nosal, and A. Legge, 1998: A numerical analysis of the combined open-top chamber data from the USA and Europe on ambient ozone and negative crop responses. *Environmental Pollution*, **101**, 157–160.

Kuhn, U., M. O. Andreae, C. Ammann, A. C. Araujo, E. Brancaleoni, P. Ciccioli, T. Dindorf, M. Frattoni, L. V. Gatti, L. Ganzeveld, B. Kruijt, J. Lelieveld, J. Lloyd, F. X. Meixner, A. D. Nobre, U. Poeschl, C. Spirig, P. Stefani, A. Thielmann, R. Valentini, and J. Kesselmeier, 2007: Isoprene and monoterpene fluxes from Central Amazonian rainforest inferred from tower-based and airborne measurements, and implications on the atmospheric chemistry and the local carbon budget. *Atmospheric Chemistry And Physics*, **7**, 2855–2879.

Lack, A. and D. Evans, 2005: *Plant Biology*. Taylor and Francis Group, Abingdon, UK.

Lamarque, J. F., T. C. Bond, V. Eyring, C. Granier, A. Heil, Z. Klimont, D. Lee, C. Liousse, A. Mieville, B. Owen, M. G. Schultz, D. Shindell, S. J. Smith, E. Stehfest, J. Van Aardenne, O. R. Cooper, M. Kainuma, N. Mahowald, J. R. McConnell, V. Naik, K. Riahi, and D. P. van Vuuren, 2010: Historical (1850-2000) gridded anthropogenic and biomass burning emissions of reactive gases and aerosols: methodology and application. *Atmospheric Chemistry And Physics*, **10**, 7017–7039.

Lamarque, J. F., P. Hess, L. Emmons, L. Buja, W. Washington, and C. Granier, 2005: Tropospheric ozone evolution between 1890 and 1990. *Journal Of Geophysical Research-Atmospheres*, **110**, D08304.

Lathiere, J., D. A. Hauglustaine, N. De Noblet-Ducoudre, G. Krinner, and G. A. Folberth, 2005: Past and future changes in biogenic volatile organic compound emissions simulated with a global dynamic vegetation model. *Geophysical Research Letters*, **32**, L20818.

Law, K., P. Plantevin, D. Shallcross, H. Rogers, J. Pyle, C. Grouhel, V. Thouret, and A. Marenco, 1998: Evalutation of modeled O_3 using Measurement of Ozone by Airbus In-Service Aircraft (MOZAIC) data. *Journal of Geophysical Research-Atmospheres*, **103**, 25721–25737.

Law, K. S. and J. A. Pyle, 1993a: Modeling trace gas budgets in the troposphere .1. ozone and odd nitrogen. *Journal Of Geophysical Research-Atmospheres*, **98**, 18377–18400.

— 1993b: Modeling trace gas budgets in the troposphere .2. CH_4 and CO. *Journal Of Geophysical Research-Atmospheres*, **98**, 18401–18412.

Lawrence, M. G., P. Jockel, and R. von Kuhlmann, 2001: What does the global mean OH concentration tell us? *Atmospheric Chemistry And Physics*, **1**, 37–49.

Lelieveld, J., T. Butler, J. Crowley, T. Dillon, H. Fischer, L. Ganzeveld, H. Harder, M. Lawrence, M. Martinez, D. Taraborrelli, and J. Williams, 2008: Atmospheric oxidation capacity sustained by a tropical forest. *Nature*, **452**, 737–740.

Lenschow, D., D. Pearson Jr, and B. Boba Stankov, 1982: Measurements of ozone vertical flux to ocean and forest. *Journal of Geophysical Research - Atmospheres*, **87**, 8833–8837.

Levis, S., C. Wiedinmyer, G. B. Bonan, and A. Guenther, 2003: Simulating biogenic volatile organic compound emissions in the community climate system model. *Journal Of Geophysical Research-Atmospheres*, **108**, 4659.

Li, X. S., Z. S. He, X. M. Fang, and X. J. Zhou, 1999: Distribution of surface ozone concentration in the clean areas of China and its possible impact on crop yields. *Advances in Atmospheric Sciences*, **16**, 154–158.

Lin, C. Y. C., D. J. Jacob, and A. M. Fiore, 2001: Trends in exceedances of the ozone air quality standard in the continental United States, 1980-1998. *Atmospheric Environment*, **35**, 3217–3228.

Linvill, D., W. Hooker, and B. Olson, 1980: Ozone in Michigans environment 1876-1880. *Monthly Weather Review*, **108**, 1883–1891.

Liu, S., X. Mo, Z. Lin, Y. Xu, J. Ji, G. Wen, and J. Richey, 2010: Crop yield responses to climate change in the Huang-Huai-Hai Plain of China. *Agricultural Water Management*, **97**, 1195–1209.

Logan, J. A., 1999: An analysis of ozonesonde data for the troposphere: Recommendations for testing 3-D models and development of a gridded climatology for tropospheric ozone. *Journal Of Geophysical Research-Atmospheres*, **104**, 16115–16149.

Lombardozzi, D., S. Levis, G. Bonan, and J. P. Sparks, 2012: Predicting photosynthesis and transpiration responses to ozone: decoupling modeled photosynthesis and stomatal conductance. *Biogeosciences*, **9**, 3113–3130, doi:10.5194/bg-9-3113-2012.

Loreto, F., M. Mannozzi, C. Maris, P. Nascetti, F. Ferranti, and P. S., 2001: Ozone quenching properties of isoprene and its antioxidant role in leaves. *Plant Physiology*, **126**, 993–1000.

Loreto, F. and V. Velikova, 2001: Isoprene produced by leaves protects the photosynthetic apparatus against ozone damage, quenches ozone products, and reduces lipid peroxidation of cellular membranes. *Plant Physiology*, **127**, 1791–1787.

Louis, J. F., 1979: Parametric model of vertical eddy fluxes in the atmosphere. *Boundary-Layer Meteorology*, **17**, 187–202.

Loveland, T., B. Reed, J. Brown, D. Ohlen, Z. Zhu, L. Yang, and J. Merchant, 2000: Development of a global land cover characteristics database and IGBP DISCover from 1km AVHRR data. *International Journal of Remote Sensing*, **21**, 1303–1330.

LRTAPConvention, 2004: Manual on methodologies and criteria for modelling and mapping critical loads and levels and air pollution effects, risks and trends. International Cooperative Programme on Mapping and Modelling under the UNECE Convention on Long-Range-Transboundary Air Pollution.

Maccarrone, M., G. Veldink, and J. F. G. Vliegenthart, 1992: Thermal-injury and ozone stress affect soybean lipoxygenases expression. *FEBS Letters*, **309**, 225–230.

Marenco, A., H. Gouget, P. Nedelec, J. Pages, and F. Karcher, 1994: Evidence of a long-term increase in tropospheric ozone from Pic Du Midi data series - consequences - positive radiative forcing. *Journal Of Geophysical Research-Atmospheres*, **99**, 16617–16632.

Martin, G., M. Ringer, V. Pope, A. Jones, J. Dearden, and T. Hinton, 2006: The Physical Properties of the Atmosphere in the New Hadley Centre Global Environmental Model (HadGEM1). Part I: Model Description and Global Climatology. *Journal Of Climate*, **19**, 1274–1301.

Martin, G. M., N. Bellouin, W. J. Collins, I. D. Culverwell, P. R. Halloran, S. C. Hardiman, T. J. Hinton, C. D. Jones, R. E. McDonald, A. J. McLaren, F. M. O'Connor, M. J. Roberts, J. M. Rodriguez, S. Woodward, M. J. Best, M. E. Brooks, A. R. Brown, N. Butchart, C. Dearden, S. H. Derbyshire, I. Dharssi, M. Doutriaux-Boucher, J. M. Edwards, P. D. Falloon, N. Gedney, L. J. Gray, H. T. Hewitt, M. Hobson, M. R. Huddleston, J. Hughes, S. Ineson, W. J. Ingram, P. M. James, T. C. Johns, C. E. Johnson, A. Jones, C. P. Jones, M. M. Joshi, A. B. Keen, S. Liddicoat, A. P. Lock, A. V. Maidens, J. C. Manners, S. F. Milton, J. G. L. Rae, J. K. Ridley, A. Sellar, C. A. Senior, I. J. Totterdell, A. Verhoef, P. L. Vidale, A. Wiltshire, and H. D. Team, 2011: The HadGEM2 family of Met Office Unified Model climate configurations. *Geoscientific Model Development*, **4**, 723–757, doi:10.5194/gmd-4-723-2011.

Matichuk, R. I., P. R. Colarco, J. A. Smith, and O. B. Toon, 2007: Modeling the transport and optical properties of smoke aerosols from African savanna fires during the Southern African regional science initiative campaign (SAFARI 2000). *Journal Of Geophysical Research-Atmospheres*, **112**, D08203.

Michelsen, H., R. Salawitch, P. Wennberg, and J. Anderson, 1994: Production of o(^{1}d) from photolysis of O_3. *Geophysical Research Letters*, **21**, 2227–2230.

Mickley, L. J., D. J. Jacob, and D. Rind, 2001: Uncertainty in preindustrial abundance of tropospheric ozone: Implications for radiative forcing calculations. *Journal Of Geophysical Research-Atmospheres*, **106**, 3389–3399.

Mickley, L. J., P. P. Murti, D. J. Jacob, J. A. Logan, D. M. Koch, and D. Rind, 1999: Radiative forcing from tropospheric ozone calculated with a unified chemistry-climate model. *Journal Of Geophysical Research-Atmospheres*, **104**, 30153–30172.

Mills, G., A. Buse, B. Gimeno, V. Bermejo, M. Holland, L. Emberson, and H. Pleijel, 2007: A synthesis of AOT40-based response functions and critical levels of ozone for agricultural and horticultural crops. *Atmospheric Environment*, **41**, 2630–2643.

Mills, G., F. Hayes, D. Simpson, L. Emberson, D. Norris, H. Harmens, and P. Buker, 2011a: Evidence of widespread effects of ozone on crops and (semi-)natural vegetation in europe (1990-2006) in relation to AOT40-and flux-based risk maps. *Global Change Biology*, **17**, 592–613, doi:10.1111/j.1365-2486.2010.02217.x.

Mills, G., H. Pleijel, S. Braun, P. Buker, V. Bermejo, E. Calvo, H. Danielsson, L. Emberson, I. Fernandez, L. Grunhage, H. Harmens, F. Hayes, P. Karlsson, and D. Simpson, 2011b: New stomatal flux-based critical levels for ozone effects on vegetation. *Atmospheric Environment International*, **45**, 5064–5068, doi:10.1016/j.atmosenv.2011.06.009.

Monfreda, C., N. Ramankutty, and J. A. Foley, 2008: Farming the planet: 2. geographic distribution of crop areas, yields, physiological types, and net primary production in the year 2000. *Global Biogeochemical Cycles*, **22**, GB1022.

Monson, R. and R. Fall, 1989: Isoprene emission from Aspen leaves - influence of environment and relation to photosynthesis and photorespiration. *Plant Physiology*, **90**, 267–274.

Monson, R., C. Jaeger, W. Adams, E. Driggers, G. Silver, and R. Fall, 1992: Relationships among isoprene emission rate, photosynthesis, and isoprene synthase activity as influenced by temperature. *Plant Physiol.*, **98**, 1175–1180.

Monson, R. K., N. Trahan, T. N. Rosenstiel, P. Veres, D. Moore, M. Wilkinson, R. J. Norby, A. Volder, M. G. Tjoelker, D. D. Briske, D. F. Karnosky, and R. Fall, 2007: Isoprene emission from terrestrial ecosystems in response to global change: minding the gap between models and observations. *Philosophical Transactions Of The Royal Society A-Mathematical Physical And Engineering Sciences*, **365**, 1677–1695.

Monteith, J., 1973: *Principles of Environmental Physics*. American Elsevier, New York, USA.

Moxim, W. J., H. Levy, and P. S. Kasibhatla, 1996: Simulated global tropospheric PAN: Its transport and impact on no_x. *Journal Of Geophysical Research-Atmospheres*, **101**, 12621–12638.

Musselman, R. C. and W. J. Massman, 1999: Ozone flux to vegetation and its relationship to plant response and ambient air quality standards. *Atmospheric Environment*, **33**, 65–73.

Naik, V., C. Delire, and D. J. Wuebbles, 2004: Sensitivity of global biogenic isoprenoid emissions to climate variability and atmospheric CO_2. *Journal Of Geophysical Research-Atmospheres*, **109**, D06301.

Niinemets, U., A. Arneth, U. Kuhn, R. Monson, and M. Penuelas, J. ad Staudt, 2010a: The emission factor of volatile isoprenoids: stress, acclimation, and developmental responses. *Biogeosciences*, **7**, 2203–2223.

Niinemets, U., R. K. Monson, A. Arneth, P. Ciccioli, J. Kesselmeier, U. Kuhn, S. M. Noe, J. Penuelas, and M. Staudt, 2010b: The leaf-level emission factor of volatile isoprenoids: caveats, model algorithms, response shapes and scaling. *Biogeosciences*, **7**, 1809–1832.

Niinemets, U., J. Tenhunen, P. Harley, and R. Steinbrecher, 1999: A model of isoprene emission based on energetic requirements for isoprene synthesis and leaf photosynthetic properties for Liquidambar and Quercus. *Plant, Cell and Environment*, **22**, 1319–1335.

Nussbaum, S. and J. Fuhrer, 2000: Difference in ozone uptake in grassland species between open-top chambers and ambient air. *Environmental Pollution*, **109**, 463–471.

O'Connor, F., C. Johnson, O. Morgenstern, M. Sanderson, P. Young, W. Collins, and J. Pyle, 2011: Evaluation of the new UKCA climate-composition model. part ii. the troposphere. *Geoscientific Model Development*, **in preparation**.

Pacifico, F., S. Harrison, C. Jones, and S. Sitch, 2009: Isoprene emissions and climate. *Atmospheric Environment*, **43**, 6121–6135.

Pacifico, F., S. P. Harrison, C. D. Jones, A. Arneth, S. Sitch, G. P. Weedon, M. P. Barkley, P. I. Palmer, D. Serça, M. Potosnak, T.-M. Fu, A. Goldstein, J. Bai, and G. Schurgers, 2011: Evaluation of a photosynthesis-based biogenic isoprene emission scheme in JULES and simulation of isoprene emissions under present-day climate conditions. *Atmospheric Chemistry and Physics*, **11**, 4371–4389, doi:10.5194/acp-11-4371-2011.

Paoletti, E. and N. E. Grulke, 2005: Does living in elevated CO_2 ameliorate tree response to ozone? a review on stomatal responses. *Environmental Pollution*, **137**, Int Union Forest Res.

Parrella, J. P., D. J. Jacob, Q. Liang, Y. Zhang, L. J. Mickley, B. Miller, M. J. Evans, X. Yang, J. A. Pyle, N. Theys, and M. Van Roozendael, 2012: Tropospheric bromine chemistry: implications for present and pre-industrial ozone and mercury. *Atmospheric Chemistry And Physics*, **12**, 6723–6740.

Parrish, D. D., K. C. Aikin, S. J. Oltmans, B. J. Johnson, M. Ives, and C. Sweeny, 2010: Impact of transported background ozone inflow on summertime air quality in a California ozone exceedance area. *Atmospheric Chemistry And Physics*, **10**, 10093–10109.

Pavelin, E. G., C. E. Johnson, S. Rughooputh, and R. Toumi, 1999: Evaluation of pre-industrial surface ozone measurements made using Schonbein's method. *Atmospheric Environment*, **33**, 919–929.

Pegoraro, E., A. Rey, E. G. Bobich, G. Barron-Gafford, K. A. Grieve, Y. Malhi, and R. Murthy, 2004: Effect of elevated CO_2 concentration and vapour pressure deficit on isoprene emission from leaves of populus deltoides during drought. *Functional Plant Biology*, **31**, 1137–1147.

Pell, E. J., C. D. Schlagnhaufer, and R. N. Arteca, 1997: Ozone-induced oxidative stress: Mechanisms of action and reaction. *Physiologia Plantarum*, **100**, 264–273.

Penuelas, J. and J. Llusia, 2002: Linking photorespiration, monoterpenes and thermotolerance in *Quercus*. *New Phytologist*, **155**, 227–237.

Penuelas, J., J. Llusia, D. Asensio, and S. Munne-Bosch, 2005: Linking isoprene with plant thermotolerance, antioxidants and monoterpene emissions. *Plant, Cell and Environment*, **28**, 278–286.

Pinelli, P. and D. Tricoli, 2004: A new approach to ozone plant fumigation: the web-O_3-Fumigation. Isoprene response to a gradient of ozone stress in leaves of *Quercus pubescens*. *Forest*, **2**, 100–108.

Pleijel, H., H. Danielsson, K. Ojanpera, L. De Temmerman, P. Hogy, M. Badiani, and P. E. Karlsson, 2004: Relationships between ozone exposure and yield loss in European

wheat and potato - a comparison of concentration- and flux-based exposure indices. *Atmospheric Environment*, **38**, 2259–2269.

Pope, V. and R. Stratton, 2002: The process governing horizontal resolution sensitivity in a climate model. *Climate Dynamics*, **19**, 211–236.

Poschl, U., R. Von Kuhlmann, N. Poisson, and P. Crutzen, 2000: Development and intercomparison of condensed isoprene oxidation mechanisms for global atmospheric modelling. *Journal of Atmospheric Chemistry*, **37**, 29–52.

Possell, M., J. Heath, C. Nicholas Hewitt, E. Ayres, and G. Kerstiens, 2004: Interactive effects of elevated CO_2 and soil fertility on isoprene emissions from Quercus robur. *Global Change Biology*, **10**, 1835–1843.

Possell, M., C. N. Hewitt, and D. J. Beerling, 2005: The effects of glacial atmospheric CO_2 concentrations and climate on isoprene emissions by vascular plants. *Global Change Biology*, **11**, 60–69.

Prather, M., D. Ehhalt, F. Dentener, R. Derwent, E. Dlugokencky, E. Holland, I. Isaksen, J. Katima, V. Kirchhoff, P. Matson, P. Midgley, and W. M., 2001: Atmospheric chemistry and greehouse gases. *Climate Change 2001: The Scientific Basis*, J. T. Houghton, Y. Ding, D. J. Griggs, M. Noguer, P. J. van der Linden, X. Dai, K. Maskell, and C. A. Johnson, eds., Cambridge University Press, Cambridge, United Kingdom and New York, NY, USA., 881.

Prather, M. J., 1986: Numerical advection by conservation of 2nd-order moments. *Journal Of Geophysical Research-Atmospheres*, **91**, 6671–6681.

Price, C. and D. Rind, 1993: What determines the cloud -to-ground lightning fraction in thunderstorms? *Geophysical Research Letters*, **20**, 463–466.

Priestley, A., 1993: A quasi-conservative version of the semi-Lagrangian advection scheme. *Monthly Weather Review*, **121**, 621–629.

Prinn, R., R. Weiss, B. Miller, J. Huang, F. Alyea, D. Cunnold, P. Fraser, D. Hartley, and P. Simmonds, 1995: Atmospheric trends and lifetime of CH_3CCL_3 and global OH concentrations. *Science*, **269**, 187–192.

Ramankutty, N. and J. Foley, 1999: Estimating historical changes in land cover: North American croplands from 1850 to 1992. *Global Ecology and Biogeography*, **8**, 381–396.

Ranieri, A., G. DUrso, C. Nali, G. Lorenzini, and G. F. Soldatini, 1996: Ozone stimulates apoplastic antioxidant systems in pumpkin leaves. *Physiologia Plantarum*, **97**, 381–387.

Rap, A., P. M. Forster, A. Jones, O. Boucher, J. M. Haywood, N. Bellouin, and R. R. De Leon, 2010: Parameterization of contrails in the UK Met Office climate model. *Journal Of Geophysical Research-Atmospheres*, **115**, D10205.

Reidmiller, D., A. Fiore, D. Jaffe, D. Bergmann, C. Cuvelier, F. Dentener, B. Duncan, G. Folberth, M. Gauss, S. Gong, P. Hess, J. Jonson, T. Keating, A. Lupu, E. Marmer, R. Park, M. Schultz, D. Shindell, S. Szopa, M. Vivanco, O. Wild, and Z. A., 2009: The influence of foreign vs. North American emissions on surface ozone in the US. *Atmospheric Chemistry And Physics*, **9**, 5027–5042.

Richards, J., 1990: Land transformation. *The Earth as transformed by human action*, B. Turner, R. Clark, W.C. Kates, J. Richards, J. Matthews, and W. Meyer, eds., Cambridge University Press, Cambridge, United Kingdom and New York, NY, USA., 163–178.

Roelofs, G. J., J. Lelieveld, and R. vanDorland, 1997: A three-dimensional chemistry general circulation model simulation of anthropogenically derived ozone in the troposphere and its radiative climate forcing. *Journal Of Geophysical Research-Atmospheres*, **102**, 23389–23401.

Rossow, W. B. and R. A. Schiffer, 1999: Advances in understanding clouds from ISCCP. *Bulletin Of The American Meteorological Society*, **80**, 2261–2287.

Roy, S. D., G. Beig, and S. D. Ghude, 2009: Exposure-plant response of ambient ozone over the tropical Indian region. *Atmospheric Chemistry And Physics*, **9**, 5253–5260.

Sacks, W. J., D. Deryng, J. A. Foley, and R. N., 2010: Crop planting dates: an analysis of global patterns. *Global Ecology and Biogeography*, **19**, 607–620, doi:10.1111/j.1466-8238.2010.00551.

Sanadze, G., 2004: Biogenic isoprene (a review). *Russian Journal of Plant Physiology*, **51**, 729–741.

Sanderson, M., W. Collins, C. Johnson, and R. Derwent, 2006: Present and future acid deposition to ecosystems: The effect of climate change. *Atmospheric Environment*, **40**, 1275–1283.

Sanderson, M. G., C. D. Jones, W. J. Collins, C. E. Johnson, and R. G. Derwent, 2003: Effect of climate change on isoprene emissions and surface ozone levels. *Geophysical Research Letters*, **30**, 1936.

Sandroni, S. and D. Anfossi, 1994: Historical data of surface ozone at tropical latitudes. *Science Of The Total Environment*, **148**, 23–29.

Sandroni, S., D. Anfossi, and S. Viarengo, 1992: Surface ozone levels at the end of the 19th-century in South-America. *Journal Of Geophysical Research-Atmospheres*, **97**, 2535–2539.

Schroeder, J. I., G. J. Allen, V. Hugouvieux, J. M. Kwak, and D. Waner, 2001: Guard cell signal transduction. *Annual Review Of Plant Physiology And Plant Molecular Biology*, **52**, 627–658.

Seinfeld, J. and S. Pandis, 1998: *Atmospheric Chemistry and Physics: from Air Pollution to Climate Change*. J. Wiley.

Sharkey, T., F. Loreto, and C. Delwiche, 1991: High-carbon dioxide and sun shade effects on isoprene emission from Oak and Aspen tree leaves. *Plant Cell And Environment*, **14**, 333–338.

Sharkey, T., A. Wiberley, and A. Donohue, 2007: Isoprene Emission from Plants: Why and How. *Annals of Botany*, **101**, 5–18.

Sharkey, T. D. and S. S. Yeh, 2001: Isoprene emission from plants. *Annual Review Of Plant Physiology And Plant Molecular Biology*, **52**, 407–436.

Shindell, D., J. C. I. Kuylenstierna, E. Vignati, R. van Dingenen, M. Amann, Z. Klimont, S. C. Anenberg, N. Muller, G. Janssens-Maenhout, F. Raes, J. Schwartz, G. Faluvegi, L. Pozzoli, K. Kupiainen, L. Hoeglund-Isaksson, L. Emberson, D. Streets, V. Ramanathan, K. Hicks, N. T. K. Oanh, G. Milly, M. Williams, V. Demkine, and D. Fowler, 2012: Simultaneously mitigating near-term climate change and improving human health and food security. *Science*, **335**, 183–189.

Shindell, D. T., G. Faluvegi, and N. Bell, 2003: Preindustrial-to-present-day radiative forcing by tropospheric ozone from improved simulations with the GISS chemistry-climate GCM. *Atmospheric Chemistry And Physics*, **3**, 1675–1702.

Shindell, D. T., B. P. Walter, and G. Faluvegi, 2004: Impacts of climate change on methane emissions from wetlands. *Geophysical Research Letters*, **31**, L21202.

Sillman, S., 1999: The relation between ozone, NO_x and hydrocarbons in urban and polluted rural environments. *Atmospheric Environment*, **33**, 1821–1845.

Singh, H. B., 1987: Reactive nitrogen in the troposphere. *Environmental Science & Technology*, **21**, 320–327.

Sitch, S., P. M. Cox, W. J. Collins, and C. Huntingford, 2007: Indirect radiative forcing of climate change through ozone effects on the land-carbon sink. *Nature*, **448**, 791–U4.

Smith, R., D. Fowler, M. Sutton, C. Flechard, and F. Coyle, 2000: Regional estimation of pollutant gas dry deposition in the UK: model description, sensitivity analysis and outputs. *Atmospheric Environment*, **34**, 3757–3777.

Soldberg, S. and A. Lindskog, 2005: The development of european surface ozone. implications for a revised abatement policy. EMEP/CCC-Report 1/.

Sommariva, R., S. S. Brown, J. M. Roberts, D. M. Brookes, A. E. Parker, P. S. Monks, T. S. Bates, D. Bon, J. A. de Gouw, G. J. Frost, J. B. Gilman, P. D. Goldan, S. C. Herndon, W. C. Kuster, B. M. Lerner, H. D. Osthoff, S. C. Tucker, C. Warneke, E. J. Williams, and M. S. Zahniser, 2011: Ozone production in remote oceanic and industrial areas derived from ship based measurements of peroxy radicals during texaqs 2006. *Atmospheric Chemistry And Physics*, **11**, 2471–2485.

Spracklen, D. V., S. R. Arnold, and C. M. Taylor, 2012: Observations of increased tropical rainfall preceded by air passage over forests. *Nature*, **489**, 282–5.

Stavrakou, T., J.-F. Muller, I. De Smedt, M. Van Roozendael, G. van der Werf, L. Giglio, and A. Guenther, 2009: Evaluating the performance of pyrogenic and biogenic emissions inventories against one decade of space-based formaldehyde columns. *Atmospheric Chemistry And Physics*, **9**, 1037–1060.

Stevenson, D. S., F. J. Dentener, M. G. Schultz, K. Ellingsen, T. P. C. van Noije, O. Wild, G. Zeng, M. Amann, C. S. Atherton, N. Bell, D. J. Bergmann, I. Bey, T. Butler, J. Cofala, W. J. Collins, R. G. Derwent, R. M. Doherty, J. Drevet, H. J. Eskes, A. M. Fiore, M. Gauss, D. A. Hauglustaine, L. W. Horowitz, I. S. A. Isaksen, M. C. Krol, J. F. Lamarque, M. G. Lawrence, V. Montanaro, J. F. Muller, G. Pitari, M. J. Prather, J. A. Pyle, S. Rast, J. M. Rodriguez, M. G. Sanderson, N. H. Savage, D. T. Shindell, S. E. Strahan, K. Sudo, and S. Szopa, 2006: Multimodel ensemble simulations of present-day and near-future tropospheric ozone. *Journal Of Geophysical Research-Atmospheres*, **111**, D08301.

Stocker, D., D. Stedman, K. Zeller, W. Massman, and D. Fox, 1993: Fluxes of nitrogen oxides and ozone measured by Eddy correlation over a shortgrass prairie. *Journal of Geophysical Research - Atmospheres*, **98**, 12619–12630.

Stockwell, D. Z. and M. P. Chipperfield, 1999: A tropospheric chemical-transport model: Development and validation of the model transport schemes. *Quarterly Journal Of The Royal Meteorological Society*, **125**, 1747–1783.

Stockwell, D. Z., C. Giannakopoulos, P. H. Plantevin, G. D. Carver, M. P. Chipperfield, K. S. Law, Y. A. Pyle, D. E. Shallcross, and K. Y. Wang, 1999: Modelling NO_x from lightning and its impact on global chemical fields. *Atmospheric Environment*, **33**, 4477–4493.

Stohl, A., 2001: A 1-year lagrangian "climatology" of airstreams in the Northern Hemisphere troposphere and lowermost stratosphere. *Journal of Geophysical Research-Atmospheres*, **106**, 7263–7279.

Tan, D., I. Faloona, J. B. Simpas, W. Brune, P. B. Shepson, T. L. Couch, A. L. Sumner, M. A. Carroll, T. Thornberry, E. Apel, D. Riemer, and W. Stockwell, 2001: HO_x budgets in a deciduous forest: Results from the PROPHET summer 1998 campaign. *Journal Of Geophysical Research-Atmospheres*, **106**, 24407–24427.

Thornley, J. and I. Johnson, 1990: *Plant and Crop Modelling*. Oxford University Press, Oxford, UK.

Thornton, J. A., P. J. Wooldridge, R. C. Cohen, M. Martinez, H. Harder, W. H. Brune, E. J. Williams, J. M. Roberts, F. C. Fehsenfeld, S. R. Hall, R. E. Shetter, B. P. Wert,

and A. Fried, 2002: Ozone production rates as a function of NO_x abundances and HO_x production rates in the nashville urban plume. *Journal Of Geophysical Research-Atmospheres*, **107**, 4146.

Tiedtke, M., 1989: A comprehensive mass flux scheme for cumulus parameterization in large-scale models. *Monthly Weather Review*, **117**, 1779–1800.

Tiiva, P., R. Rinnan, T. Holopainen, S. Morsky, and J. Holopainen, 2007: Isoprene emissions from boreal peatland microcosms; effects of elevated ozone concentration in an open field experiment. *Atmospheric Environment*, **41**, 3819–3828.

Tjoelker, M., J. Volin, J. Oleksyn, and P. Reich, 1995: Interaction of ozone pollution and light effects on photosynthesis in a forest canopy experiment. *Plant Cell And Environment*, **18**, 895–905.

Tognetti, R., J. D. Johnson, M. Michelozzi, and A. Raschi, 1998: Response of foliar metabolism in mature trees of Quercus pubescens and Quercus ilex to long-term elevated CO_2. *Environmental And Experimental Botany*, **39**, 233–245.

Tong, D. Q., R. Mathur, D. W. Kang, S. C. Yu, K. L. Schere, and G. Pouliot, 2009a: Vegetation exposure to ozone over the continental United States: Assessment of exposure indices by the Eta-CMAQ air quality forecast model. *Atmospheric Environment*, **43**, 724–733.

Tong, D. Q., N. Z. Muller, H. D. Kan, and R. O. Mendelsohn, 2009b: Using air quality modeling to study source-receptor relationships between nitrogen oxides emissions and ozone exposures over the United States. *Environment International*, **35**, 1109–1117.

Tuovinen, J. P., D. Simpson, L. Emberson, M. Ashmore, and G. Gerosa, 2007: Robustness of modelled ozone exposures and doses. *Environmental Pollution*, **146**, 578–586.

Turner, I., R. Moss, and D. Skole, 1993: Relating land use and global land cover change. a proposal for an IGBP-HDP Core Project. IGBP Report no. 24, HDP Report no. 5. The International Geosphere-Biosphere Programme: A study of global change and the Human Dimensions of Global Environmental Change Programme, Stockholm.

USEPA, 1996: Air quality criteria for ozone and other photochemical oxidants, vol. ii. epa-600/p-93/00bf. Epa-600/p-93/00bf, US Environmental Protection Agency, National

Center for Environmental Assessment, US Environmental Protection Agency, National Center for Environmental Assessment, Research Triangle Park, NC.

— 2010a: National ambient air quality standards for ozone: Proposed rules, federal register, vol. 75, no. 11. Http://www.epa.gov/air/ozonepollution/fr/20100119.pdf.

— 2010b: National Ambient Air Quality Standards (NAAQS) ozone O_3 Standards. Http://www.epa.gov/ttn/naaqs/standards/ozone/s_o3_index.html.

van der Werf, G. R., J. T. Randerson, L. Giglio, G. J. Collatz, P. S. Kasibhatla, and A. F. Arellano, Jr., 2006: Interannual variability in global biomass burning emissions from 1997 to 2004. *Atmospheric Chemistry And Physics*, **6**, 3423–3441.

Van Dingenen, R., F. J. Dentener, F. Raes, M. C. Krol, L. Emberson, and J. Cofala, 2009: The global impact of ozone on agricultural crop yields under current and future air quality legislation. *Atmospheric Environment*, **43**, 604–618.

Velikova, V., A. Edreva, and F. Loreto, 2004: Endogenous isoprene protects *Phragmites australis* leaves against singlet oxygen. *Physiologia Plantarum*, **122**, 219–225.

Velikova, V., T. Tsonev, P. Pinelli, G. Alessio, and F. Loreto, 2005: Localized ozone fumigation system for studying ozone effects on photosynthesis, respiration, electron transport rate and isoprene emission in field-grown mediterranean oak species. *Tree Physiology*, **25**, 1523–1532.

Volz, A. and D. Kley, 1988: Evaluation of the Montsouris series of ozone measurements made in the 19th-century. *Nature*, **332**, 240–242.

Wang, K. Y., J. A. Pyle, M. G. Sanderson, and C. Bridgeman, 1999: Implementation of a convective atmospheric boundary layer scheme in a tropospheric chemistry transport model. *Journal Of Geophysical Research-Atmospheres*, **104**, 23729–23745.

Wang, K. Y. and D. E. Shallcross, 2000: Modelling terrestrial biogenic isoprene fluxes and their potential impact on global chemical species using a coupled LSM-CTM model. *Atmospheric Environment*, **34**, 2909–2925.

Wang, X. P. and D. L. Mauzerall, 2004: Characterizing distributions of surface ozone and its impact on grain production in China, Japan and South Korea: 1990 and 2020. *Atmospheric Environment*, **38**, 4383–4402.

Wang, Y. H. and D. J. Jacob, 1998: Anthropogenic forcing on tropospheric ozone and OH since preindustrial times. *Journal Of Geophysical Research-Atmospheres*, **103**, 31123–31135.

Wayne, R., 2000: *Chemistry of Atmospheres*. Oxford University Press, Oxford, UK.

Wellburn, F. A. M. and A. R. Wellburn, 1996: Variable patterns of antioxidant protection but similar ethene emission differences in several ozone-sensitive and ozone-tolerant plant selections. *Plant Cell And Environment*, **19**, 754–760.

Wesely, M., 1989: Parameterization of Surface Resistances to Gaseous Dry Deposition in Regional Scale Numerical Models. *Atmospheric Environment*, **23**, 1293–1304.

Wesely, M., D. Cook, and R. Williams, 1981: Field measurements of small ozone fluxes to snow, wet bare soil, and lake water. *Boundary Layer Meteorology*, **20**, 459–471.

WHO, 2000: Air Quality Guidelines for Europe, Reg. Publ. Eur. Ser., WHO Reg. Off. Eur. Copenhagen, 2nd ed., 91, 288 pp.,.

Wild, O., 2007: Modelling the global tropospheric ozone budget: exploring the variability in current models. *Atmospheric Chemistry And Physics*, **7**, 2643–2660.

Wild, O., A. M. Fiore, D. T. Shindell, R. M. Doherty, W. J. Collins, F. J. Dentener, M. G. Schultz, S. Gong, I. A. MacKenzie, G. Zeng, P. Hess, B. N. Duncan, D. J. Bergmann, S. Szopa, J. E. Jonson, T. J. Keating, and A. Zuber, 2012: Modelling future changes in surface ozone: a parameterized approach. *Atmospheric Chemistry and Physics*, **12**, 2037–2054, doi:10.5194/acp-12-2037-2012.

Wild, O., P. Pochanart, and H. Akimoto, 2004: Trans-Eurasian transport of ozone and its precursors. *Journal of Geophysical Research-Atmospheres*, **109**, D11302.

Wilkinson, M. J., R. K. Monson, N. Trahan, S. Lee, E. Brown, R. B. Jackson, H. W. Polley, P. A. Fay, and R. Fall, 2009: Leaf isoprene emission rate as a function of atmospheric CO_2 concentration. *Global Change Biology*, **15**, 1189–1200.

Young, P. J., A. Arneth, G. Schurgers, G. Zeng, and J. A. Pyle, 2009: The CO_2 inhibition of terrestrial isoprene emission significantly affects future ozone projections. *Atmospheric Chemistry And Physics*, **9**, 2793–2803.

Zhang, L., J. Brook, and R. Vet, 2003: A revised parameterization for gaseous dry deposition in air-quality models. *Atmospheric Chemistry And Physics*, **3**, 2067–2082.

Zhang, Q., D. G. Streets, G. R. Carmichael, K. B. He, H. Huo, A. Kannari, Z. Klimont, I. S. Park, S. Reddy, J. S. Fu, D. Chen, L. Duan, Y. Lei, L. T. Wang, and Z. L. Yao, 2009: Asian emissions in 2006 for the NASA INTEX-B mission. *Atmospheric Chemistry And Physics*, **9**, 5131–5153.

Zhao, C., Y. H. Wang, Q. Yang, R. Fu, D. Cunnold, and Y. Choi, 2010: Impact of East Asian summer monsoon on the air quality over China: View from space. *Journal Of Geophysical Research-Atmospheres*, **115**, D09301.